Title

Mechanosensing uses the intricate internal organization of bacteria to regulate surface behaviors

Author

Patino, Ramiro

Publication Date

2024

Mechanosensing uses the intricate internal organization of bacteria to regulate surface behaviors

by
Ramiro Patino

DISSERTATION
Submitted in partial satisfaction of the requirements for degree of
DOCTOR OF PHILOSOPHY

in

Biomedical Sciences

in the

GRADUATE DIVISION
of the
UNIVERSITY OF CALIFORNIA, SAN FRANCISCO

Approved:

DocuSigned by:
Carol Gross
F2413DA7F84F46A...

Carol Gross
Chair

DocuSigned by:
Joanne N. Engel
DocuSigned by:
Hiten D. Madhani
DocuSigned by:
William F. DeGrado
582727E949C7441...

Joanne N. Engel
Hiten Madhani
William F. DeGrado

Committee Members

For Corey and Nacho,

Who give me the strength to never give up.

Thank you.

ACKNOWLEDGEMENTS

Getting a PhD has challenged me in many ways I never imagined. I have not only grown as a scientist, but I have become a better version of myself during my PhD journey. This personal evolution could not have been possible without the amazing support group that I have built throughout the years. I am eternally grateful to those who have believed in me since the very beginning. Their encouragement and support has taken me out of very dark places. Again, thank you.

A special shoutout to my past self. As my PhD journey is coming to an end, I realize that I overcame substantial challenges to get into graduate school. From moving to the US, to not fully knowing the language, to moving across the country to start my PhD adventure, my past self took a leap of faith every single time, despite being terrified. Thank you for managing and thriving in those hardships, past self.

I want to thank Joanne Engel for guiding my PhD training and for always believing in me, even when I do not. I was blessed by having a PhD advisor who values open and honest communication. By always actively listening to my concerns and reaching compromises, Joanne really helped me find my voice, which was actively hiding in a void before joining the lab. I want to also thank Joanne for allowing to be my authentic self since the first day I started working in her laboratory. Observing how Joanne navigates the world as a proud member of the LGBTQ+ community has been inspiring. Thanks to Joanne, I have learned

to embrace my queer and Latino identities. So, Joanne has taught me many valuable life lessons, in addition to helping me thrive as a scientist.

I thank the members of the Engel lab, past and present, for making the lab a fun place to do science. Although the lab is divided by research topic (*Pseudomonas* and *Chlamydia* sides), I feel we are a big family joined by a shared curiosity to solve complex scientific problems. Every lab member has always been there for me, even when I just want to chat about drag queens. I will always have so many amazing memories of the lab thanks to all of you: Yuki, Henriette, Cheri, Jessica, Ellie, Clara, Khavong, and Kate. I will also have cherished memories of Carol, our now retired lab assistant. She kept the lab running so smoothly and was a joy to be around. I especially thank Yuki and Henriette. They are amazing people. Compassionate, supportive, attentive, creative, you name it. They are all-stars. Thank you for teaching so much about lab and life. Undoubtedly, their support was key for my training. I will be forever grateful to them. Special mention to Cheri, who gave me countless free therapy sessions and song recommendations.

Collaborating with brilliant scientists has been one of the best things about my PhD journey. I thank Alex Persat, Lorenzo Tala, and Marco Kuhn for the long-standing collaboration that led to amazing contributions to the field of bacterial mechanosensing. The stimulating scientific conversations with all of you helped me grow as a scientist. Special thanks to Marco. His drive to solve scientific problems is contagious and motivated me while working on our sensory adaptation manuscript.

My thesis committee Carol Gross, Hiten Madhani, and Bill DeGrado have been amazing cheerleaders. During our thesis committee meetings, they provided insightful comments to advance my research forward. At a moment when I was feeling low about my project, their enthusiasm about my results reignited the flame of scientific curiosity that allowed me to complete my co-first author manuscript.

At UCSF, I have found amazing friends and colleagues who have taught me so much about life and science. For starters, friends from my PhD cohort have been there for me when I struggled with imposter syndrome in the beginning. It was also great to explore San Francisco with them shortly after I moved from Texas/Mexico. Lexi, Ryan B., Bryan M., Anthony, Karen W., Camille, Sara Sunshine, Nich Gentry, Stephen – thank you for helping me navigate the early days of grad school and beyond. I will never forget how welcomed you all made me feel. Trainees in integrative microbiology program, past and present, have also been a great support system. Thank you to Dror, Rosa, Alison, Dinara, Lauren, Bevin,

As a brown and queer person, grad school was not designed for me. Finding a group of motivated, resilient, and outspoken POC and queer graduate students at UCSF motivated me to get involved and contribute to change the culture. Big thanks to the SACNISTAS who were there supporting me when I was clueless about how to be a leader for the chapter. Veronica, Dana, Dina, Donovan, Elise, Melissa – your leadership and dedication is inspiring. Special thanks to Robbie Diaz and D'Anne Duncan for trusting me and teaching me how to be a better advocate for diversity, equity, and inclusion.

I thank my gay “Barbies” for showing me a good time outside the lab. From going to the beach in warm days to dancing the night away, every moment has shown me how fun it can be to be in San Francisco and to be gay. Every “Barbie” adventure also helped me to learn something about myself and to not lose my mind (PhDs are hard!). Although some barbies have moved away from San Francisco, they were there for me when I needed them the most and I will always value their friendship. Wil, Pawel, Kevin, Eric, Leo, Mikey, Omar P., Andy R., Pierce, Kiet, Bo – thanks to all of you for being such loyal friends!

I would not have made it to UCSF without the amazing mentors from the University of Texas Rio Grande. I must thank Robert Dearth seeing something in me and accepting me into the NIH Research Initiative for Scientific Enhancement (RISE) Program. Coming from a poor background, it was impossible to find volunteer research opportunities. The RISE program made it possible for me to gain the skills I needed for graduate school and to get paid. This program was also reason I ended up in the lab of Teresa Feria. Thank you, Dr. Feria, for believing in me. You provided endless opportunities to gain skills that were useful in graduate school. I will forever be grateful for your mentorship, which continues until this day. When I started my research career at UTRGV, I was clueless about opportunities outside Texas. Mirayda Torres-Avila motivated me and pushed me to apply to the 2014 SACNAS conference. This conference changed my life. As my first national conference, it showed me that there are endless opportunities for research around the US. Indeed, I believe this conference is the reason I was accepted in an

undergraduate research program at UCLA. I will always treasure that experience. Patricia Johnson, thank you for taking a chance on me by accepting me in your lab. Francie Mercer, thank you for being an empathetic mentor who really cared about my success.

Family is everything to me. I could not have embarked in a journey to become a scientist without the full support of my family. My Dad, also named Ramiro, always worked hard to make sure that me and three siblings always had a roof, food, and an education. My dad's work ethic has always inspired me. My Mom, Juany, has always been there to support me. I thank you, Mom, for doing your best every day to make sure I am doing well. I know that I did not meet my extended family expectations. They expected me to drop my professional dreams to ensure that my family could move to the US. Mom and Dad, thank you for pushing me to pursue my dreams. I will forever be grateful for having both of you in my life. Monica, Javier, and Johan – thank you for being great siblings even when we are so far away. I appreciate you all!

Now, I want to thank my amazing partner, Corey, for dealing with me during this journey. I have no words to express my gratitude towards you. You have supported me through very dark times in my life. You go above and beyond to care for me and make sure I do not lose my mind. For that, I appreciate you dearly. You have been a ray of light in my life since we met in 2018. After all these years together, I feel our bond grows stronger and stronger, especially when we go through challenging times. I am looking forward to sharing many more years with you. I love you!

Lastly, I want to thank my baby doggy son, Nacho. Although I was very reluctant to have a dog, I have learned so much about life by raising you. It seems like yesterday when you were so tiny you could barely walk, and now you are a moody ween. I will always value all our moments together. Coming home from a stressful day to an excited and lovey Nacho makes my worries fade away in an instant.

STATEMENT REGARDING AUTHOR CONTRIBUTIONS

Chapter 2 contains a reprint of a *Proceedings of the National Academy of Sciences* article: Marco J. Kühn, Lorenzo Talà, Yuki Inclan, Ramiro Patino, Xavier Pierrat, Iscia Vos, Zainebe Al-Mayyah, Henriette Macmillan, Jose Negrete, Joanne N. Engel, Alexandre Persat. (2021). Mechanotaxis directs *Pseudomonas aeruginosa* twitching motility. Vol. 118, No. 30: e2101759118.

Marco J. Kühn and Lorenzo Talà designed and performed the majority of the biological experiments and drafted the manuscript under guidance of Alexandre Persat. Yuki Inclan also performed experiments under the guidance of Joanne N. Engel. Ramiro Patino, Xavier Pierrat, Iscia Vos, Zainebe Al-Mayyah, Henriette Macmillan, Jose Negrete contributed with new reagents and analytical tools under the guidance of Alexandre Persat and Joanne N. Engel. For the paper, I contributed with molecular biology expertise to design and generate bacterial strains required for the research under the guidance of Joanne N. Engel. I also contributed with stimulating conversations while revising the manuscript before publication under the guidance of Joanne N. Engel.

Chapter 3 contains a reprint of a *The EMBO Journal* article:

Marco J. Kühn, Henriette Macmillan, Lorenzo Talà, Yuki Inclan, Ramiro Patino, Xavier Pierrat, Zainebe Al-Mayyah, Joanne N. Engel, Alexandre Persat. (2023). Two antagonistic response regulators control *Pseudomonas aeruginosa* polarization during mechanotaxis. 42:e112165.

Marco J. Kühn designed and performed the majority of the biological experiments and drafted the manuscript under guidance of Alexandre Persat. Yuki Inclan, Henriette Macmillan, and Ramiro Patino generated new reagents and analytical tools as well as performed experiments under the guidance of Joanne N. Engel. Lorenzo Talà, Xavier Pierrat, Zainebe Al-Mayyah generated new reagents and analytical tools as well as performed experiments under the guidance of Alexandre Persat. For the paper, I contributed with molecular biology expertise to design and generate bacterial strains required for the research under the guidance of Joanne N. Engel. I also developed and optimized a protocol to measure activity of a bacterial transcriptional reporter using flow cytometry. Figure S3.11B shows data obtained using this protocol. I also contributed with stimulating conversations while revising the manuscript before publication under the guidance of Joanne N. Engel.

Chapter 4 is a manuscript draft submitted for publication:

Ramiro Patino, Marco J. Kühn, Henriette Macmillan, Yuki Inclan, Ivan Chavez, John Von Dollen, Jeffrey R. Johnson, Danielle L. Swaney, Nevan J. Krogan, Alexandre Persat, Joanne N. Engel. Spatial control of sensory adaptation modulates mechanosesing in *Pseudomonas aeruginosa*. Submitted to biorxiv.

I conceived, designed, and performed the experiments and wrote the manuscript under the guidance of Joanne N. Engel. Henriette Macmillan assisted with the optimization of the protocol for methylation immunoblots. Ivan Chavez assisted with performing some experiments related to methylation immunoblots. Marco J. Kühn performed the microscopy experiments under the guidance of Alexandre Persat. Yuki Inclan prepared

samples for Mass Spectrometry (MS) and interpreted the data. Under the guidance of Nevan J. Krogan, John Von Dollen and Jeffrey R. Johnson ran the MS samples while Danielle Swaney performed analysis on the resulting data set.

Chapter 5 is unpublished work using transcriptomics to test whether a medically important Acinetobacter species has a surface-dependent transcriptional response that may be involved in upregulating virulence. I conceived and designed the experiments described under the guidance Joanne N. Engel. I prepared the samples for RNA-sequencing and analyzed resulting data set. Chaz Langelier assisted with the Illumina deep sequencing and analysis of the resulting data.

Mechanosensing uses the intricate internal organization of bacteria to regulate surface behaviors.

Ramiro Patino

ABSTRACT

Bacteria use conserved signal transduction pathways, called sensory systems, to sense environmental stimuli. Most of our understanding of sensory systems in bacteria, however, comes from the chemotaxis system of *Escherichia coli*, which senses chemical gradients to control the direction of flagellar-based motility (chemosensing). Importantly, bacteria can also sense mechanical stimuli to actively shape their physiology. An in-depth mechanistic understanding of mechanosensory systems, when compared to their chemosensory counterparts, is however lacking. This dissertation presents work towards understanding mechanosensing in the important opportunistic human pathogen *Pseudomonas aeruginos*a. This Gram-negative bacterium uses Type IV pili (TFP), retractile polarly localized appendages, to sense mechanical forces generated during surface contact at one cell pole. We and others have demonstrated that spatially resolved mechanical stimuli transmitted by TFP activates the Pil-Chp mechanosensory system. Upon surface contact, TFP transmits mechanical stimuli to the Pil-Chp receptor, PilJ, thereby altering the autophosphorylation state of ChpA and thus the phosphorylation of PilG and PilH, the antagonistic Pil-Chp response regulators.

PilG and PilH inversely control two outputs of the Pil-Chp system in *P. aeruginosa*: cAMP production and twitching motility. Sensing of surface contact by the Pil-Chp system activates the membrane bound CyaB adenylate cyclase, which catalyzes the production

of the second messenger, cyclic adenosine monophosphate (cAMP). cAMP binds to the Vfr transcription factor, leading to altered transcription of >200 genes involved in acute virulence as well as selected TFP regulatory proteins. Signal processing through PilG and PilH is critical for surface-dependent cAMP production. PilG promotes cAMP production and upregulation of the surface dependent transcriptional program while PilH has the opposite effect.

The Pil-Chp mechanosensory system is required for twitching motility, partially independently of cAMP levels. In Chapter 2, we demonstrate that *P. aeruginosa* actively directs twitching in the direction of mechanical input from TFP, in a process called mechanotaxis. The Pil-Chp system controls the balance of forward and reverse twitching motility of single cells in response to the mechanical inputs. We show that the Pil-Chp response regulators PilG and PilH control the polarization of the TFP extension motor PilB. PilG localizes to both poles, but shows greater accumulation at the leading pole, where it stimulates polarization favoring forward migration. In contrast, PilH, is primarily cytoplasmic, thereby globally antagonizing PilG. Subcellular segregation of PilG and PilH efficiently orchestrates their antagonistic functions, ultimately enabling rapid reversals upon perturbations. The distinct localization of response regulators establishes a signaling landscape known as local-excitation, global-inhibition in higher order organisms.

In Chapter 3, we demonstrate that PilG and PilH enable dynamic cell polarization by coupling their antagonistic functions on TFP extension. By precisely quantifying the localization of fluorescent protein fusions, we show that phosphorylation of PilG by the

histidine kinase ChpA controls PilG polarization. Although PilH is not inherently required for twitching reversals, upon phosphorylation, PilH becomes activated and breaks the local positive feedback established by PilG so that forward-twitching cells can reverse. To spatially resolve mechanical signals, the Pil-Chp system thus locally transduces signals with a main output response regulator, PilG. To respond to signal changes, Chp uses its second regulator, PilH, to break the local feedback.

In Chapter 4, we report the mechanism of sensory adaptation in the Pil-Chp mechanosensory system. Bacterial sensory adaptation has primarily been studied in flagellar-mediated chemotaxis, where reversible methylation of sensory receptors by a methyltransferase and a methylesterase "tune" their sensitivity of signaling. The Pil-Chp system encodes the PilK methyltransferase, predicted to methylate PilJ, and the ChpB methylesterase, predicted to demethylate PilJ; however, whether sensory adaptation occurs in response to surface contact remained underexplored. Using biochemistry, genetics, and cell biology, we discovered that PilK and ChpB are segregated to opposing cell poles as *P. aeruginosa* explore surfaces. By coordinating the localization of both enzymes, we found that the Pil-Chp response regulators influence local PilJ methylation *in vivo*. We propose a model in which spatially resolved mechanical inputs transmitted by TFP not only alter PilG and PilH signaling mechanisms but locally controls PilJ methylation to modulate twitching motility reversal rates and surface-dependent cAMP production. Despite decades of chemosensory adaptation studies, our work has uncovered an unrecognized mechanism that bacteria use to achieve adaptation to mechanical sensory stimuli.

Acinetobacter species are opportunistic pathogens that are ubiquitous throughout the environment and are emerging as a public health threat around the world due to their widespread multidrug resistance. Intriguingly, many *Acinetobacter* strains encode homologs of the *P. aeruginosa* Pil-Chp mechanosensory system. In Chapter 5, we demonstrate that *A. nosocomialis* strain M2, a pathogenic member of the *Acinetobacter calcoaceticus-baumannii* complex, has a robust surface-dependent transcriptional response. We speculate that the homologous Pil-Chp mechanosensory system is responsible for the surface-dependent transcriptional response that we report in this dissertation.

Overall, this dissertation demonstrates that mechanosensing through the Pil-Chp system takes advantage of the intricate internal organization of bacteria to sense spatially resolved mechanical information. As medically *Acinetobacter* species exhibit a surface transcriptional response, defining the mechanosensing mechanism of *Acinetobacter* species represents an exciting area of investigation. Understanding the mechanisms of bacterial mechanosensing may lead to the generation of desperately needed therapeutics to treat multi-drug resistant infections, such as the ones typically caused by *P. aeruginosa* and medically relevant *Acinetobacter* species.

TABLE OF CONTENTS

LIST OF FIGURES

CHAPTER 2

CHAPTER 3

CHAPTER 4

CHAPTER 5

LIST OF TABLES

CHAPTER 4

CHAPTER 5

COMMON ABBREVIATIONS

Acb: *Acinetobacter calcoaceticus-baumannii*.

AnM2: *Acinetobacter nosocomialis* strain M2.

cAMP: cyclic adenosine monophosphate.

Chp: Pil-Chp mechanosensory system.

GOF: gain-of-function.

Hpt: histidine phosphotransfer domain.

iSCAT: interferometric scattering microscopy

LBD: ligand binding domain.

LOF: loss-of-function.

MCP: methyl-accepting chemotaxis protein.

MCS: mechanochemical signaling.

MDR: multi-drug resistant.

mNG: mNeonGreen.

REC: receiver domain.

SAINT: significance analysis of interactome.

SDS-PAGE: sodium dodecyl-sulfate polyacrylamide gel.

T3SS: type 3 secretion system.

TFP: type IV pili.

Vfr: virulence factor regulator.

WT: wild type.

CHAPTER ONE

INTRODUCTION

Bacteria use conserved signal transduction pathways to sense environmental stimuli. These so-called sensory systems regulate critical cellular responses, including development, motility, biofilm formation, and production of virulence factors (He & Bauer, 2014). Although bacteria in the environment encounter a diverse array of stimuli, most of our knowledge about sensory systems in bacteria comes from studying the flagellar-mediated chemotaxis system of *Escherichia coli* (Parkinson et al., 2015). This chemotaxis system senses chemical gradients to control the direction of flagellar-based motility. For decades, the chemosensing paradigm has served as the blueprint for bacterial sensory systems in general, and as such, sensory systems are often termed chemosensory systems. This generalization could prove misleading because recent seminal studies have demonstrated that sensory systems also sense mechanical stimuli to actively shape bacterial physiology (Dufrêne & Persat, 2020). Despite these recent advances, an in-depth mechanistic understanding of mechanosensory systems, when compared to their chemosensory counterparts, is lacking.

At the molecular level, bacterial sensory systems are a variation of two-component regulatory systems (Zschiedrich et al., 2016), and their components are conserved and widespread throughout nature (Wuichet & Zhulin, 2010). We will consider each of these components in the order of signal processing, which was established by the chemosensing paradigm. To elicit biochemical responses, small chemical molecules first bind to chemoreceptors, which are also known as methyl-accepting chemotaxis proteins (MCPs), as the activity of many of them is modulated by reversible methylation (Parkinson et al., 2015). MCPs are usually transmembrane proteins, and freely diffusible chemical

inputs bind to the ligand binding domain (LBD), which is typically in the periplasmic domain (Ortega et al., 2017). LBDs are the most variable regions of chemoreceptors, thus providing specificity for diverse chemical inputs (Ortega et al., 2017). Binding of chemical inputs to the LBDs initiates a series of conformational changes that are transmitted to the conserved cytoplasmic domain of the MCPs. The MCP cytoplasmic domain consists of a 4 helix bundle, which include the methylation sites and the sites of contact to the CheW adaptor protein and the CheA histidine kinase (Alexander & Zhulin, 2007).

After MCPs sense chemical inputs, signal transmission continues through CheW and CheA. Although variations with unique signaling capabilities exist, CheW primarily serves as a structural protein to link MCPs to CheA (Parkinson et al., 2015). CheA is a sensor histidine kinase, which undergoes autophosphorylation on a conserved histidine residue in response to environmental stimuli (Zschiedrich et al., 2016). Once CheA becomes autophosphorylated, the high-energy phosphoryl group is transferred to a conserved aspartic acid residue found in the receiver domain of the CheY response regulator (Parkinson et al., 2015). Based on the phosphotransfer mechanism, CheA is one of the simplest sensor histidine kinases. There are well-documented examples of histidine kinases with multiple histidine phosphotransfer domains (Hpts), which create complex phosphorelays (Hoch, 2000). Hybrid histidine kinases, which have additional structural domains such as an in-cis receiver domain, have also been described (Zschiedrich et al., 2016).

The family of response regulators is characterized by the conserved receiver domain that undergoes a conformational change upon phosphorylation of the conserved aspartate (Bourret, 2010). Response regulators act as standalone receiver domains or are fused to output domains. In simple two-component systems, the latter scenario is commonly observed. Here, the receiver domain is often linked to a DNA binding domain that functions as a transcriptional regulator, allowing an environmental signal to be transduced into a transcriptional response (Zschiedrich et al., 2016). In contrast, standalone response regulators are usually found in chemosensory systems, where they participate in reversible protein-protein interactions upon phosphorylation. Control of response regulator phosphorylation is the culmination of the signaling processing that began with binding of chemical inputs to MCPs.

In the case of the *E. coli* flagellar-mediated chemotaxis system, which has served as the paradigm for chemosensing, CheA becomes autophosphorylated in response of chemical repellents, which increases the phosphorylation levels of the CheY response regulator, which consists only of a receiver domain (Parkinson et al., 2015). CheY~P can then bind to the base of the flagellar motor to reverse direction of flagellar rotation (Sarkar et al., 2010). This chemotactic response allows *E. coli* to swim away from harmful chemicals, ensuring survival.

During chemotaxis, *E. coli* must constantly sample its environment to navigate chemical gradients. At the biochemical level, this scenario creates a challenge for *E. coli* because the chemotaxis system must also respond to changing levels of chemical inputs within

gradients (Sourjik & Wingreen, 2012). To overcome this problem, chemosensory systems evolved a sensory adaptation branch. Bacterial sensory adaptation relies on two additional core components of chemosensory systems, a methyltransferase and a methylesterase (Sourjik & Wingreen, 2012). The constitutively active CheR methyltransferase methylates conserved glutamic acid residues found in the cytoplasmic signaling domain of MCPs (Alexander & Zhulin, 2007), while the CheB methylesterase demethylates MCPs.

The level of MCP methylation serves as an additional level of signaling control for chemosensory systems, which is not found in two-component systems. In the *E. coli* chemotaxis system (Parkinson et al., 2015), MCP methylation enhances signal transduction to CheA, increasing CheA autophosphorylation and subsequent phosphoryl group transfer to CheY, while MCP demethylation has the opposite effect. To control the level of MCP methylation, chemosensory systems use CheB as a command center. Upon sensing a chemical repellent, CheA autophosphorylation also promotes phosphorylation of the N-terminal receiver domain found in CheB, albeit at a slower rate, thereby increasing its methylesterase activity (Djordjevic et al., 1998; Kehry & Dahlquist, 1982; Lupas & Stock, 1989). Therefore, sensing a chemical repellent increases CheY phosphorylation but with a time delay, also decreases MCP methylation, leading to a time-delayed negative feedback loop that is at the heart of sensory adaptation during chemotaxis (Sourjik & Wingreen, 2012). While binding of chemical repellents to MCPs triggers an increase in CheY phosphorylation to direct flagellar motility, this event also ensures that MCP methylation and thus signaling decrease to a basal signaling state,

even in the presence of constant levels of repellent. In this way, chemotaxis system can sense increasing or decreasing levels of chemical inputs within gradients (Sourjik & Wingreen, 2012). The integration of signal processing from both branches of chemosensory systems (i.e. CheY phosphorylation and sensory adaptation) is therefore critical for chemosensing, although less is known about how these two branches function together during bacterial mechanosensing.

Bacteria also encounter mechanical forces in the environment (Persat, Nadell, et al., 2015). Mechanical forces have been implicated in regulating critical biological processes such as development in eukaryotes; however, the emerging field of bacterial mechanosensing has only recently begun uncovering how mechanical forces shape bacterial physiology (Dufrêne & Persat, 2020). Although bacteria can sense diverse mechanical stimuli, such as sheer forces, special interest has been placed on understanding how mechanical forces generated during surface contact influence bacterial physiology. This interest comes from the well documented involvement of surface contact in initiating surface motility, biofilm formation, virulence, and developmental programs in bacteria (Laventie & Jenal, 2020). Nevertheless, the mechanisms that bacteria use to sense and transduce surface contact remain elusive. Although flagellar components and membrane deformation have been implicated in the sensing of surface contact (Dufrêne & Persat, 2020; Laventie & Jenal, 2020), surface sensing mediated by type IV pili (TFP) is emerging as a model to study bacterial mechanosesing (Ellison et al., 2017; Geiger & O'Toole, 2023; Kuchma & O'Toole, 2022;

Lee et al., 2018; Luo et al., 2015; Persat, Inclan, et al., 2015) and is the focus of this dissertation.

TFP are polymeric appendages that undergo repeated cycles of extension, surface attachment, and retraction (Leighton et al., 2015). In the opportunistic pathogen *Pseudomonas aeruginosa*, TFP are preferentially assembled at one cell pole (the leading pole), where they produce forces of ~ 55 pN during TFP retraction (Koch et al., 2022). These forces propel a single *P. aeruginosa* bacterium forward in a type of surface motility called twitching (Burrows, 2012). With technological advancements in the field of microbiology and engineering, our group and others demonstrated that *P. aeruginosa* has a surface-dependent transcriptional response that depends on TFP, implicating TFP as mechanosensors (Persat, Inclan, et al., 2015).

We and others furthered implicated a sensory system, called Pil-Chp system, in the signal processing of surface-derived mechanical inputs (Lee et al., 2018; Luo et al., 2015; Persat, Inclan, et al., 2015). During attachment or retraction, TFP senses mechanical forces generated while contacting surfaces at one cell pole. The Pil-Chp MCP, PilJ, directly receives TFP-derived mechanical forces possibly through the binding of pilin subunits (Persat et al., 2015), although alternative scenarios have been proposed (Luo et al., 2015). By analogy to the chemosensing MCPs (Parkinson et al., 2015), we infer that PilJ undergoes conformational changes that alter the autophosphorylation state of ChpA, the Pil-Chp histidine kinase. ChpA is a complex hybrid histidine kinase, with a C-terminal receiver domain. In addition to the receiver domain, it encodes 6 histidine

phosphotransfer (Hpt) domains, a putative serine phosphotransfer (Spt) domain, and a putative threonine phosphotransfer (Tpt domain) (Whitchurch et al., 2004). Although phosphorelay through ChpA is incompletely understood (Silversmith et al., 2016), genetic and biochemical studies indicate that ChpA requires histidine kinase activity and its in-cis receiver domain (Bertrand et al., 2010; Leech & Mattick, 2006). *In vitro* biochemical studies utilizing purified proteins indeed highlight that ChpA can subsequently transfer high phosphoryl groups to PilG and PilH, the antagonistic Pil-Chp response regulators (Silversmith et al., 2016), although the efficiency and temporal resolution of these competing phosphorylation reactions *in vivo* is not known.

The surface dependent transcriptional program is mediated by the second messenger, cyclic adenosine monophosphate (cAMP) (Luo et al., 2015; Persat, Inclan, et al., 2015). Sensing of surface contact by the Pil-Chp system activates the membrane bound CyaB adenylate cyclase, the enzyme responsible for the majority of cAMP production in *P.* aeruginosa (Fulcher et al., 2010). A detailed molecular mechanism of CyaB activation is however lacking, but it is likely post-translational (Inclan et al., 2011; Topal et al., 2012). cAMP binds to the Vfr transcription factor, modulating the transcription of >200 genes, some of which are involved in an acute virulence program while others are involved in assembling the TFP apparatus that mediates twitching motility (Wolfgang et al., 2003). Signal processing through PilG and PilH is critical for surface-dependent cAMP production. PilG promotes cAMP production and upregulation of the surface dependent transcriptional program while PilH has the opposite effect (Fulcher et al., 2010; Persat, Inclan, et al., 2015).

The Pil-Chp system not only controls surface-dependent cAMP production but is required for twitching motility (Bertrand et al., 2010; Fulcher et al., 2010; Whitchurch et al., 2004). Although cAMP levels affect transcription of a set of TFP regulatory genes (Wolfgang et al., 2003), *P. aeruginosa* can twitch in the absence of cAMP (Buensuceso et al., 2017). Thus, the Pil-Chp system regulates twitching motility independently of cAMP levels. By analogy with the chemotaxis system, mechanical forces transmitted by TFP could dictate direction of twitching motility by altering Pil-Chp signaling.

Through studies by us and others (Inclan et al., 2016; Luo et al., 2015; Persat et al., 2015), the Pil-Chp system has emerged a mechanosensory model system, akin to the *E. coli* chemotaxis system. Therefore, defining the mechanisms used by the Pil-Chp system to sense and transduce mechanical forces will allow us to uncover fundamental mechanosensing principles that bacteria use to interact with their environment. This dissertation advances our knowledge by elucidating how the design of the Pil-Chp system enables mechanosensing in *P. aeruginosa*.

In Chapter 2 (Kühn et al., 2021), we demonstrate that *P. aeruginosa* actively directs twitching in the direction of mechanical input from TFP in a process called mechanotaxis. The Pil-Chp system controls the balance of forward and reverse twitching migration of single cells in response to the mechanical inputs. Collisions between twitching cells stimulate reversals, but Pil-Chp mutants either always or never reverse. As a result, while wild-type cells colonize surfaces uniformly, collision-blind Pil-Chp mutants jam, demonstrating a function for mechanosensing in regulating group behavior. On surfaces,

the Pil-Chp system senses mechanical forces transmitted by TFP at one pole, thereby sensing a spatially-resolved signal. As a result, the Chp response regulators PilG and PilH control the polarization of the TFP extension motor PilB. Of note, the TFP retraction motor, PilT, appears to be constitutively localized at both poles. This strategy ensures that TFP only undergo extension at the pole that receives mechanical stimuli. PilG is localized to both poles, but its localization is enhanced at the leading pole, as is PIlB. This polarized localization further stimulates polarization favoring forward migration. As PilH primarily localizes to the cytoplasm, PilH can globally antagonize PilG polarization and can induce twitching motility reversals. Subcellular segregation of PilG and PilH efficiently orchestrates their antagonistic functions, ultimately enabling rapid reversals upon spontaneous or mechanical perturbations. The distinct localization of response regulators establishes a signaling landscape known as local-excitation, global-inhibition in higher order organisms, identifying a conserved strategy to transduce spatially-resolved signals.

In Chapter 3 (Kühn et al., 2023), we further investigate how the subcellular localization of the Pil-Chp response regulators enable sensing of spatially-resolved mechanical forces. We demonstrate that PilG and PilH enable dynamic cell polarization by coupling their antagonistic functions on TFP extension. By precisely quantifying the localization of fluorescent protein fusions, we show that phosphorylation of PilG by the histidine kinase ChpA controls PilG polarization. Although PilH is not inherently required for twitching reversals, upon phosphorylation, PilH becomes activated and breaks the local positive feedback established by PilG so that forward-twitching cells can reverse. To spatially

resolve mechanical signals, the Pil-Chp system thus locally transduces signals with a main output response regulator, PilG. To respond to signal changes, Chp uses its second regulator PilH to break the local feedback. By identifying the molecular functions of two response regulators that dynamically control cell polarization, our work provides a rationale for the diversity of architectures often found in bacterial sensory systems.

To completely define how spatially resolved mechanical stimuli are transduced, we need a comprehensive understanding of the integration of the antagonistic response regulator and sensory adaptation branches of the Pil-Chp mechanosensory system. However, whether sensory adaptation occurs in response to surface contact remains underexplored. The Pil-Chp system encodes predicted methyltransferase (CheR) and methylesterase (CheB) homologs (Darzins, 1995; Fulcher et al., 2010; Whitchurch et al., 2004). The PilK methyltransferase is predicted to methylate PilJ while the ChpB methylesterase is predicted to demethylate PilJ. By analogy with the chemosensory paradigm, the methylation state of PilJ is expected to influence Pil-Chp signaling with the goal of allowing efficient mechanotaxis and cAMP production in *P. aeruginosa*. In Chapter 4, we report the mechanism of sensory adaptation in the Pil-Chp mechanosensory system. Using biochemistry, genetics, and cell biology, we discovered that PilK and ChpB are segregated to opposing cell poles as *P. aeruginosa* explore surfaces. By coordinating the localization of both enzymes, we found that the Pil-Chp response regulators influence local PilJ methylation. We propose a model in which spatially resolved mechanical inputs transmitted by TFP not only alter PilG and PilH signaling mechanisms but locally controls PilJ methylation to modulate twitching motility reversal rates and surface-dependent

cAMP production. Despite decades of chemosensory adaptation studies, our work has uncovered an unrecognized mechanism that bacteria use to achieve adaptation to mechanical sensory stimuli.

Preliminary studies have suggested that the Pil-Chp mechanosensory system is found throughout bacterial phyla, including *Acinetobacter* species (Inclan et al., 2016). *Acinetobacter* species are opportunistic pathogens that are ubiquitous throughout the environment and are emerging as a public health threat around the world due to their extensive antibiotic resistance (Weber et al., 2016). Given that members of the medically relevant *Acinetobacter calcoaceuticus-baumanii* (Acb) complex encode a homologous Pil-Chp system, in Chapter 5, we begin to test the hypothesis that the Acb complex has a surface response that may be important in human disease. We focused on *A. nosocomialis* strain M2, a human pathogen that exhibits TFP-mediated twitching motility and encodes homologs of the Pil-Chp system. Using RNA sequencing, we demonstrate here that *A. nosocomialis* strain M2 has a robust surface-dependent transcriptional response that may involve virulence factors that contribute to human infections. This study has the potential to enhance our understanding of how surface contact reshapes the transcriptome of other medically important MDR Gram-negative pathogens and may pave the way to developing new therapeutic involve virulence factors that contribute to human infections.

Overall, this dissertation demonstrates that spatially resolved mechanical forces reshaped the design of the Pil-Chp mechanosensory system. In contrast to the

chemosensing paradigm, mechanosensing through the Pil-Chp system takes advantage of the intricate internal organization of bacteria. By integrating spatially resolved mechanical information, the Pil-Chp system controls twitching motility and upregulation of an acute virulence program. These two defense mechanisms may protect *P. aeruginosa* when it transitions from flagella-mediated planktonic growth, which allows it to swim away from predators and toxins and towards nutrients, to surface-associated biofilm formation, where, although it lacks motility, it is encased in a protective matrix, shielding it from predators and harmful compounds. During early surface contact, *P. aeruginosa* has lost flagellar-mediated swimming motility but not yet been encased by a biofilm. Surface-contact-mediated mechanosensing activates twitching motility, which allows surface exploration. Mechanosensing also promotes cAMP production, which turns on a contact mediated virulence program that includes production of type III secreted toxins. These toxins target single cell predators such as amoeba in the environment and neutrophils in the human host. Our work also opens the door to an exciting area of investigation: defining the regulation of the surface transcriptional response of pathogenic *Acinetobacter* species. Understanding the mechanisms of bacterial mechanosensing may lead to the generation of desperately needed therapeutics to treat multi-drug resistant infections, like the ones typically caused by *P. aeruginosa* (Hauser, 2014) and medically relevant *Acinetobacter* species (Harding et al., 2018).

REFERENCES

Alexander, R. P., & Zhulin, I. B. (2007). Evolutionary genomics reveals conserved structural determinants of signaling and adaptation in microbial chemoreceptors. *Proceedings of the National Academy of Sciences of the United States of America*, *104*(8), 2885–2890. https://doi.org/10.1073/pnas.0609359104

Bertrand, J. J., West, J. T., & Engel, J. N. (2010a). Genetic Analysis of the Regulation of Type IV Pilus Function by the Chp Chemosensory System of Pseudomonas aeruginosa. *Journal of Bacteriology*, *192*(4), Article 4. https://doi.org/10.1128/JB.01390-09

Bertrand, J. J., West, J. T., & Engel, J. N. (2010b). Genetic Analysis of the Regulation of Type IV Pilus Function by the Chp Chemosensory System of Pseudomonas aeruginosa. *Journal of Bacteriology*, *192*(4), 994–1010. https://doi.org/10.1128/jb.01390-09

Bourret, R. B. (2010). Receiver domain structure and function in response regulator proteins. *Current Opinion in Microbiology*, *13*(2), 142–149. https://doi.org/10.1016/j.mib.2010.01.015

Buensuceso, R. N. C., Daniel-Ivad, M., Kilmury, S. L. N., Leighton, T. L., Harvey, H., Howell, P. L., & Burrows, L. L. (2017). Cyclic AMP-Independent Control of Twitching Motility in Pseudomonas aeruginosa. *Journal of Bacteriology*, *199*(16), e00188-17. https://doi.org/10.1128/JB.00188-17

Burrows, L. L. (2012). Pseudomonas aeruginosa Twitching Motility: Type IV Pili in Action. *Annual Review of Microbiology*, *66*(1), 493–520. https://doi.org/10.1146/annurev-micro-092611-150055

Darzins, A. (1995). The Pseudomonas aeruginosa pilK gene encodes a chemotactic methyltransferase (CheR) homologue that is translationally regulated. *Molecular Microbiology*, *15*(4), 703–717. https://doi.org/10.1111/j.1365-2958.1995.tb02379.x

Djordjevic, S., Goudreau, P. N., Xu, Q., Stock, A. M., & West, A. H. (1998). Structural basis for methylesterase CheB regulation by a phosphorylation-activated domain. *Proceedings of the National Academy of Sciences*, *95*(4), 1381–1386. https://doi.org/10.1073/pnas.95.4.1381

Dufrêne, Y. F., & Persat, A. (2020). Mechanomicrobiology: How bacteria sense and respond to forces. *Nature Reviews. Microbiology*, *18*(4), 227–240. https://doi.org/10.1038/s41579-019-0314-2

Ellison, C. K., Kan, J., Dillard, R. S., Kysela, D. T., Ducret, A., Berne, C., Hampton, C. M., Ke, Z., Wright, E. R., Biais, N., Dalia, A. B., & Brun, Y. V. (2017). Obstruction of pilus retraction stimulates bacterial surface sensing. *Science (New York, N.Y.)*, *358*(6362), 535–538. https://doi.org/10.1126/science.aan5706

Fulcher, N. B., Holliday, P. M., Klem, E., Cann, M. J., & Wolfgang, M. C. (2010). The Pseudomonas aeruginosa Chp chemosensory system regulates intracellular cAMP levels by modulating adenylate cyclase activity. *Molecular Microbiology*, *76*(4), 889–904. https://doi.org/10.1111/j.1365-2958.2010.07135.x

Geiger, C. J., & O'Toole, G. A. (2023). Evidence for the Type IV Pilus Retraction Motor PilT as a Component of the Surface Sensing System in Pseudomonas aeruginosa. *Journal of Bacteriology*, *205*(7), e0017923. https://doi.org/10.1128/jb.00179-23

Harding, C. M., Hennon, S. W., & Feldman, M. F. (2018). Uncovering the mechanisms of Acinetobacter baumannii virulence. *Nature Reviews. Microbiology*, *16*(2), 91–102. https://doi.org/10.1038/nrmicro.2017.148

Hauser, A. R. (2014). Pseudomonas aeruginosa virulence and antimicrobial resistance: Two sides of the same coin? *Critical Care Medicine*, *42*(1), 10.1097/CCM.0b013e3182a120cd. https://doi.org/10.1097/CCM.0b013e3182a120cd

He, K., & Bauer, C. E. (2014). Chemosensory signaling systems that control bacterial survival. *Trends in Microbiology*, *22*(7), 389–398. https://doi.org/10.1016/j.tim.2014.04.004

Hoch, J. A. (2000). Two-component and phosphorelay signal transduction. *Current Opinion in Microbiology*, *3*(2), 165–170. https://doi.org/10.1016/s1369-5274(00)00070-9

Inclan, Y. F., Huseby, M. J., & Engel, J. N. (2011). FimL Regulates cAMP Synthesis in Pseudomonas aeruginosa. *PLOS ONE*, *6*(1), e15867. https://doi.org/10.1371/journal.pone.0015867

Inclan, Y. F., Persat, A., Greninger, A., Von Dollen, J., Johnson, J., Krogan, N., Gitai, Z., & Engel, J. N. (2016). A scaffold protein connects type IV pili with the Chp chemosensory system to mediate activation of virulence signaling in Pseudomonas aeruginosa. *Molecular Microbiology*, *101*(4), 590–605. https://doi.org/10.1111/mmi.13410

Kehry, M. R., & Dahlquist, F. W. (1982). Adaptation in bacterial chemotaxis: CheB-dependent modification permits additional methylations of sensory transducer proteins. *Cell*, *29*(3), 761–772. https://doi.org/10.1016/0092-8674(82)90438-X

Koch, M. D., Black, M. E., Han, E., Shaevitz, J. W., & Gitai, Z. (2022). Pseudomonas aeruginosa distinguishes surfaces by stiffness using retraction of type IV pili. *Proceedings of the National Academy of Sciences*, *119*(20), e2119434119. https://doi.org/10.1073/pnas.2119434119

Kuchma, S. L., & O'Toole, G. A. (2022). Surface-Induced cAMP Signaling Requires Multiple Features of the Pseudomonas aeruginosa Type IV Pili. *Journal of Bacteriology*, *204*(10), e0018622. https://doi.org/10.1128/jb.00186-22

Kühn, M. J., Macmillan, H., Talà, L., Inclan, Y., Patino, R., Pierrat, X., Al-Mayyah, Z., Engel, J. N., & Persat, A. (2023). Two antagonistic response regulators control Pseudomonas aeruginosa polarization during mechanotaxis. *The EMBO Journal*, *42*(7), e112165. https://doi.org/10.15252/embj.2022112165

Kühn, M. J., Talà, L., Inclan, Y. F., Patino, R., Pierrat, X., Vos, I., Al-Mayyah, Z., Macmillan, H., Negrete, J., Engel, J. N., & Persat, A. (2021). Mechanotaxis directs Pseudomonas aeruginosa twitching motility. *Proceedings of the National Academy of Sciences*, *118*(30), e2101759118. https://doi.org/10.1073/pnas.2101759118

Laventie, B.-J., & Jenal, U. (2020). Surface Sensing and Adaptation in Bacteria. *Annual Review of Microbiology*, *74*(1), 735–760. https://doi.org/10.1146/annurev-micro-012120-063427

Lee, C. K., de Anda, J., Baker, A. E., Bennett, R. R., Luo, Y., Lee, E. Y., Keefe, J. A., Helali, J. S., Ma, J., Zhao, K., Golestanian, R., O'Toole, G. A., & Wong, G. C. L.

(2018). Multigenerational memory and adaptive adhesion in early bacterial biofilm communities. *Proceedings of the National Academy of Sciences*, *115*(17), 4471–4476. https://doi.org/10.1073/pnas.1720071115

Leech, A. J., & Mattick, J. S. (2006). Effect of site-specific mutations in different phosphotransfer domains of the chemosensory protein ChpA on Pseudomonas aeruginosa motility. *Journal of Bacteriology*, *188*(24), 8479–8486. https://doi.org/10.1128/JB.00157-06

Leighton, T. L., Buensuceso, R. N. C., Howell, P. L., & Burrows, L. L. (2015). Biogenesis of Pseudomonas aeruginosa type IV pili and regulation of their function. *Environmental Microbiology*, *17*(11), 4148–4163. https://doi.org/10.1111/1462-2920.12849

Luo, Y., Zhao, K., Baker, A. E., Kuchma, S. L., Coggan, K. A., Wolfgang, M. C., Wong, G. C. L., & O'Toole, G. A. (2015). A Hierarchical Cascade of Second Messengers Regulates Pseudomonas aeruginosa Surface Behaviors. *mBio*, *6*(1), 10.1128/mbio.02456-14. https://doi.org/10.1128/mbio.02456-14

Lupas, A., & Stock, J. (1989). Phosphorylation of an N-terminal Regulatory Domain Activates the CheB Methylesterase in Bacterial Chemotaxis. *Journal of Biological Chemistry*, *264*(29), 17337–17342. https://doi.org/10.1016/S0021-9258(18)71497-X

Ortega, Á., Zhulin, I. B., & Krell, T. (2017). Sensory Repertoire of Bacterial Chemoreceptors. *Microbiology and Molecular Biology Reviews : MMBR*, *81*(4), e00033-17. https://doi.org/10.1128/MMBR.00033-17

Parkinson, J. S., Hazelbauer, G. L., & Falke, J. J. (2015). Signaling and sensory adaptation in Escherichia coli chemoreceptors: 2015 update. *Trends in Microbiology*, *23*(5), 257–266. https://doi.org/10.1016/j.tim.2015.03.003

Persat, A., Inclan, Y. F., Engel, J. N., Stone, H. A., & Gitai, Z. (2015). Type IV pili mechanochemically regulate virulence factors in Pseudomonas aeruginosa. *Proceedings of the National Academy of Sciences of the United States of America*, *112*(24), 7563–7568. https://doi.org/10.1073/pnas.1502025112

Persat, A., Nadell, C. D., Kim, M. K., Ingremeau, F., Siryaporn, A., Drescher, K., Wingreen, N. S., Bassler, B. L., Gitai, Z., & Stone, H. A. (2015). The Mechanical World of Bacteria. *Cell*, *161*(5), 988–997. https://doi.org/10.1016/j.cell.2015.05.005

Sarkar, M. K., Paul, K., & Blair, D. (2010). Chemotaxis signaling protein CheY binds to the rotor protein FliN to control the direction of flagellar rotation in Escherichia coli. *Proceedings of the National Academy of Sciences*, *107*(20), 9370–9375. https://doi.org/10.1073/pnas.1000935107

Silversmith, R. E., Wang, B., Fulcher, N. B., Wolfgang, M. C., & Bourret, R. B. (2016). Phosphoryl Group Flow within the *Pseudomonas aeruginosa* Pil-Chp Chemosensory System. *Journal of Biological Chemistry*, *291*(34), 17677–17691. https://doi.org/10.1074/jbc.M116.737528

Sourjik, V., & Wingreen, N. S. (2012). Responding to chemical gradients: Bacterial chemotaxis. *Current Opinion in Cell Biology*, *24*(2), 262–268. https://doi.org/10.1016/j.ceb.2011.11.008

Topal, H., Fulcher, N. B., Bitterman, J., Salazar, E., Buck, J., Levin, L. R., Cann, M. J., Wolfgang, M. C., & Steegborn, C. (2012). Crystal Structure and Regulation Mechanisms of the CyaB Adenylyl Cyclase from the Human Pathogen *Pseudomonas aeruginosa*. *Journal of Molecular Biology*, *416*(2), 271–286. https://doi.org/10.1016/j.jmb.2011.12.045

Weber, B. S., Harding, C. M., & Feldman, M. F. (2016). Pathogenic Acinetobacter: From the Cell Surface to Infinity and Beyond. *Journal of Bacteriology*, *198*(6), 880–887. https://doi.org/10.1128/jb.00906-15

Whitchurch, C. B., Leech, A. J., Young, M. D., Kennedy, D., Sargent, J. L., Bertrand, J. J., Semmler, A. B. T., Mellick, A. S., Martin, P. R., Alm, R. A., Hobbs, M., Beatson, S. A., Huang, B., Nguyen, L., Commolli, J. C., Engel, J. N., Darzins, A., & Mattick, J. S. (2004). Characterization of a complex chemosensory signal transduction system which controls twitching motility in Pseudomonas aeruginosa. *Molecular Microbiology*, *52*(3), 873–893. https://doi.org/10.1111/j.1365-2958.2004.04026.x

Wolfgang, M. C., Lee, V. T., Gilmore, M. E., & Lory, S. (2003). Coordinate Regulation of Bacterial Virulence Genes by a Novel Adenylate Cyclase-Dependent Signaling Pathway. *Developmental Cell*, *4*(2), 253–263. https://doi.org/10.1016/S1534-5807(03)00019-4

Wuichet, K., & Zhulin, I. B. (2010). Origins and Diversification of a Complex Signal Transduction System in Prokaryotes. *Science Signaling*, *3*(128), ra50–ra50. https://doi.org/10.1126/scisignal.2000724

Zschiedrich, C. P., Keidel, V., & Szurmant, H. (2016). Molecular Mechanisms of Two-Component Signal Transduction. *Journal of Molecular Biology*, *428*(19), 3752–3775. https://doi.org/10.1016/j.jmb.2016.08.003

CHAPTER TWO

MECHANOTAXIS DIRECTS PSEUDOMONAS AERUGINOSA TWITCHING MOTILITY

SUMMARY

The opportunistic pathogen *Pseudomonas aeruginosa* explores surfaces using twitching motility powered by retractile extracellular filaments called type IV pili (TFP). Single cells twitch by sequential T4P extension, attachment and retraction. How single cells coordinate T4P to efficiently navigate surfaces remains unclear. We demonstrate that *P. aeruginosa* actively directs twitching in the direction of mechanical input from T4P, in a process called mechanotaxis. The Chp chemotaxis-like system controls the balance of forward and reverse twitching migration of single cells in response to the mechanical signal. Collisions between twitching cells stimulate reversals, but Chp mutants either always or never reverse. As a result, while wild-type cells colonize surfaces uniformly, collision-blind Chp mutants jam, demonstrating a function for mechanosensing in regulating group behavior. On surfaces, Chp senses T4P attachment at one pole thereby sensing a spatially-resolved signal. As a result, the Chp response regulators PilG and PilH control the polarization of the extension motor PilB. PilG stimulates polarization favoring forward migration, while PilH inhibits polarization inducing reversal. Subcellular segregation of PilG and PilH efficiently orchestrates their antagonistic functions, ultimately enabling rapid reversals upon perturbations. The distinct localization of response regulators establishes a signaling landscape known as local-excitation, global-inhibition in higher order organisms, identifying a conserved strategy to transduce spatially-resolved signals.

INTRODUCTION

Single-cell organisms have evolved motility machineries to explore their environments. For example, bacteria utilize swimming motility to propel themselves through fluids. In their natural environments, bacteria are however most commonly found associated to surfaces (Costerton et al., 1995). Many species use surface-specific motility systems such as twitching, gliding, and swarming to migrate on solid substrates (Jarrell & McBride, 2008). However, we still know very little about how cells regulate and control surface motility. In particular, the role of mechanical signals in regulating the motility of single cells remains vastly underexplored in bacteria, as well as in higher order microorganisms (Dufrêne & Persat, 2020a).

To migrate towards nutrients and light or away from predators and toxins, cells actively steer motility in response to environmental signals. For example, chemotactic systems mediate motility towards specific molecular ligands (Bi & Sourjik, 2018a; Van Haastert & Devreotes, 2004). Bacteria have a remarkably diverse set of chemotaxis systems. The canonical Che system, which has been extensively studied as a regulator of *Escherichia coli* swimming, is widely conserved among motile species including non-swimming ones (A. M. Stock et al., 2000). However, the signal inputs and the motility outputs of other bacterial chemotaxis-like systems remain incompletely understood in many species (Matilla & Krell, 2018). Finally, chemotaxis-like systems are found with alternative signaling architectures, including additional components compared to the Che system. For example, while Che controls flagella rotation by phosphorylation of a single response

regulator, other species can use up to six. The functions of these supplementary elements remain cryptic (Porter et al., 2008).

Pseudomonas aeruginosa is a major opportunistic pathogen well-adapted to growth on surfaces. *P. aeruginosa* colonizes and explores abiotic and host surfaces using twitching motility, which is powered by retractile extracellular filaments called type IV pili (TFP) (Burrows, 2012a). During twitching, single cells pull themselves by successive rounds of TFP extension, attachment and retraction (Burrows, 2012a; Merz et al., 2000a). TFP extend and retract from the cell surface by respective polymerization and depolymerization of the pilin subunit PilA at the poles (Burrows, 2012a; Merz et al., 2000a). While an understanding of the assembly mechanisms of individual filaments is beginning to emerge, we still don't know whether and how cells coordinate multiple T4P at their surface to power migration over large distances.

Genetic studies show that a chemotaxis-like system called Chp regulates twitching (Bertrand et al., 2010a). Beyond playing a role in the transcription of TFP genes, the mechanism by which Chp regulates motility remains unknown (Fulcher et al., 2010a; Whitchurch et al., 2004a). Also unlike Che which possesses a single response regulator, the Chp system possesses two response regulators, PilG and PilH, whose respective functions and mechanism of action are incompletely resolved (Darzins, 1994a) (**Figure 2.1A**). Most Chp mutants twitch aberrantly most often due to downregulation of TFP machinery, making their motility phenotypes hard to interpret (Bertrand et al., 2010a). In addition, unlike homologs from the well-studied canonical *E. coli* Che system, the Chp

methyl-accepting chemotaxis protein called PilJ has no clear chemical ligand (Darzins, 1994a; Whitchurch et al., 2004a). Several chemical compounds bias collective or single cell twitching migration in a Chp-dependent manner (Kearns et al., 2001; Limoli et al., 2019; Nolan et al., 2020; Oliveira et al., 2016). For example, single *P. aeruginosa* cells twitch up strong gradients of dimethylsulfoxide (Oliveira et al., 2016). Because most Chp mutants have strong piliation defects, it remains unclear whether chemical gradients passively bias twitching displacements or actively guide motility via chemosignaling.

We previously demonstrated that *P. aeruginosa* upregulates genes coding for virulence factors upon surface contact in a TFP- and Chp-dependent manner (Fulcher et al., 2010a; Persat, Inclan, et al., 2015a). However how Chp controls motility independently of transcription remains unresolved (Bertrand et al., 2010a; Buensuceso et al., 2017; Whitchurch et al., 2004a). The homology between Chp and Che systems suggests a tactic function for Chp. As a result, we rigorously tested the hypothesis that Chp regulates twitching motility of single cells in response to T4P mechanical input at short timescales.

RESULTS

The canonical Che system regulates bacterial swimming by transducing an input chemical signal into a motility response via flagellar rotation control (Berg, 2004). By analogy, we hypothesized that the chemotaxis-like Chp system regulates the trajectory of single twitching cells (Whitchurch et al., 2004a). Chp mutants twitch aberrantly in the traditional stab assay (**Figure S2.1A and B**)(Buensuceso et al., 2017; Fulcher et al., 2010a). These mutants also have altered cyclic AMP (cAMP) levels (**Figure S2.1C**) (Persat, Inclan, et al., 2015a). cAMP regulates the transcription of virulence genes upon surface contact, so that Chp mutants have aberrant T4P numbers (**Figure S2.1D**) (Persat, Inclan, et al., 2015a). To overcome a potential cross-talk, we decoupled the Chp-dependent, short timescale motility control from cAMP-dependent transcription by investigating single cell twitching in constitutively low or high cAMP regimes.

We first explored the functions of Chp in directing twitching motility by visualizing individual isolated motile WT (**Figure 2.1B, Movie S2.1**), Δ*cpdA*, Δ*pilH,* and Δ*pilGcpdA* cells, at the interface between a glass coverslip and an agarose pad. For these strains, which all have elevated cAMP levels (**Figure S2.1C**), we computed the linear displacements of single cells to visually highlight the balance between persistent forward motion and reversals for single cells (**Figure 2.1C**). We also computed their mean reversal frequency (**Figure 2.2A**). WT and Δ*cpdA* cells mostly move persistently forward and only occasionally reversed twitching direction (**Figure 2.1C, Figure 2.2A**). Δ*pilGcpdA* cells reversed so frequently that they appeared to “jiggle”, never committing to a single direction of twitching (**Movie S2.2, Figure 2.1C**, **Figure 2.2A**). They ultimately had very

little net migration, consistent with their reduced twitching motility in the stab assay (**Figure S2.1A**). By contrast, Δ*pilH* moved very persistently in a single direction and reversed very rarely (**Figure 2.1C, Figure 2.2A**). Likewise, Δ*pilHcyaB*, which has reduced cAMP levels compared to Δ*pilH,* had near zero reversal frequency, confirming the Chp-dependent, cAMP-independent control of twitching direction (**Figure 2.2*A***).

WT cells often reversed their twitching direction after a side collision (**Fig. 2.2B and C**, **Movie S2.3**). Δ*pilGcpdA* reversed almost always after impact, whereas Δ*pilH* almost never did (**Figure 2.2B and C, Movie S2.3**). This suggest that cell-cell contact may mechanically interrupt Chp signaling at the colliding pole, or that Chp chemically senses the surface of the other cell. To distinguish between these hypotheses, we inspected how cells reversed upon collisions with non-biological material. We produced micrometer-wide glass microfibers that we added to the twitching environment, thereby producing obstacles to the motile bacteria. Upon colliding these microfibers, WT cells often reversed twitching direction (**Figure 2.2D, Movie S2.4**). The rate of reversal upon colliding glass was indistinguishable from collisions with other cells (**Fig. 2.2E**). These observations are therefore consistent with a mechanism where cell-cell contact mechanically perturb Chp signaling.

The Chp-dependent control of reversal rates is reminiscent of the role of Frz sensory system in controlling motile collective behavior in *Myxococcus xanthus* (Blackhart & Zusman, 1985a; Thutupalli et al., 2015). We therefore explored how mutations in Chp influenced group motility. At high cell density, WT cells spread relatively evenly over the

surface (**Figure 2.2F**). In contrast, collision-blind Δ*pilH* cells jammed head-to-head, forming small groups that inefficiently moved forwards (**Figure 2.2F, Movie S2.5**). At much higher cell density, in a WT colony, the bacteria distribute evenly across the field of view and form persistent rafts at the leading edge thereby expanding the colony edge rapidly (**Figure S2.2, Movie S2.6**). Δ*pilH* colonies tend to form clusters of cells jamming into each other, forming swirls and comet-like rafts of migrating cells that quickly disperse, thereby inhibiting persistent collective migration (**Figure S2.2**, **Movie S2.6**). As a consequence, the leading edge expands more slowly compared to WT, resulting in smaller colony diameter in twitching stab assays (**Figure S2.1A**). These observations could explain the patterns observed at the edge of larger colonies (Darzins, 1994a; Meacock et al., 2021a). In summary, by controlling reversal rates upon collision, Chp-dependent mechanosensing can optimize *P. aeruginosa* collective motility.

Chp provides single *P. aeruginosa* cells with the ability to migrate persistently in one direction and to rapidly change twitching direction. PilG promotes persistent forward motility, driving migration over long distances. PilH enables directional changes particularly useful upon collisions with other bacteria.

To investigate how PilG and PilH control twitching direction, we focused on the distribution of TFP between the two poles of a cell. We imaged *P. aeruginosa* by interferometric scattering microscopy (iSCAT) to quantify TFP at each cell pole and evaluate their distributions. We found that the TFP of WT and Δ*cpdA* were nearly randomly distributed (**Figure S2.3**). In contrast, TFP of Δ*pilGcpdA* were distributed more symmetrically

compared to the random distribution and to WT. While Δ*pilH* had too many TFP for a direct comparison with other mutants, we could quantify symmetry in the less piliated Δ*pilHcyaB* background (**Figure S2.1D**). The TFP of Δ*pilHcyaB* were markedly more asymmetrically distributed than WT (**Figure S2.3**), consistent with its inability to reverse twitching direction. We conclude that the Chp system polarizes TFP to regulate twitching direction. PilG promotes unipolar TFP deployment driving persistent forward migration, while PilH promotes TFP deployment at both poles simultaneously, favoring reversals.

TFP extend and retract from the cell surface by respective polymerization and depolymerization of the pilin subunit PilA at the poles. The extension motor PilB assembles PilA monomers to extend TFP, while the retraction motors PilT and PilU disassemble filaments to generate traction forces (**Figure 2.1A**) (Burrows, 2012a; Merz et al., 2000a). We reasoned that for the Chp system to regulate T4P polarization and set a cell's twitching direction, it must control either extension or retraction at a given pole. To test this hypothesis, we investigated how the localization of extension and retraction motors regulate the deployment of TFP to direct twitching. First, we simultaneously visualized TFP distribution and motor protein subcellular localization within single cells. To this end, we generated chromosomal mNeonGreen (mNG) fluorescent protein fusions at their native loci to the extension motor PilB, to its regulator FimX (Jain, Sliusarenko, Kazmierczak, et al., 2017), and to the retraction motors PilT and PilU (**Figure 2.3A**). All fusion proteins were functional and exhibited primarily bright fluorescent foci at one or both poles, globally consistent with inducible plasmid-borne fusion proteins, with the exception of PilU which had been reported as asymmetrically localized but under different

imaging, expression and growth conditions (Chiang et al., 2005; Kazmierczak et al., 2006). We leveraged correlative iSCAT-fluorescence microscopy for simultaneous imaging of TFP and fluorescent reporter fusions (**Fig. 3B**) (Ortega Arroyo et al., 2016a). In single cells, we identified the pole with brightest fluorescent signal and the pole with most TFP. We then categorized cells into two groups: cells with more TFP at the bright pole versus cells with less TFP at the bright pole. We found that in more than 60% of cells, the poles with more TFP had the brightest PilB-mNG fluorescent signal (**Figure 2.3C**) (Chiang et al., 2005). On the other hand, we found no negative correlation between mNG-PilT or mNG-PilU signals and relative numbers of TFP, which would be expected if cells controlled TFP distribution using retraction. We conclude that PilB, but neither PilT nor PilU, control the polarized deployment of TFP.

Since most, but not all cells had more TFP at the bright PilB pole, we considered whether PilB controls the direction of twitching migration of single *P. aeruginosa* cells. To test this hypothesis, we investigated the dynamic localization of motors in single twitching cells (**Figure S4, Movie S7**). While mNG-PilT and mNG-PilU fusions were fully functional, PilB-mNG exhibited a partial twitching motility defect (**Figure S2.5**). We therefore systematically validated PilB localization results by visualization of its regulator FimX using mNG-FimX, which was fully functional (**Figure S2.5**). We tracked single cells while measuring the subcellular localization of the fusion proteins. We first categorized cells as moving and non-moving. We then measured the proportion of cells that had asymmetric and symmetric protein localizations based on a threshold of fluorescence ratio between poles. We found that PilB-mNG and mNG-FimX localizations were more asymmetric (*i.e.*

polarized) in moving cells compared to non-moving cells (**Figure 2.3D**). In addition, both fusion proteins changed localization and polarity during reversals (**Figure S2.6, Movie S2.8**) (Jain, Sliusarenko, Kazmierczak, et al., 2017). In contrast, the localization of mNG-PilT and mNG-PilU was largely symmetric across the population, without marked symmetry differences between non-moving and moving cells. Since PilB and FimX polarize in moving cells, we computed the correlation between the twitching direction and fusion protein polarization (*i.e.* the localization of their brightest polar spot). We found that more than 90% of cells moved in the direction of the bright PilB and FimX pole (**Figure 2.3E**). Thus, PilB polarization correlates more strongly with motility than with T4P number (**Figure 2.3C**). While we measure twitching for minutes, over nearly hundred T4P extension and retraction events (Talà et al., 2019a), correlative iSCAT gives a snapshot of the T4P distribution in a given cell, explaining the discrepancy between conditions. Altogether, our data shows that polarized extension and constitutive retraction controls *P. aeruginosa* twitching direction.

The Chp system regulates TFP distribution, which itself is under the control of the PilB polarization. Since TFP and Chp mediate surface sensing to regulate transcription, we hypothesize that mechanosensing also regulates the subsequent extension of additional TFP (Persat, Inclan, et al., 2015a). As a result, we tested whether TFP activity itself regulates PilB polarization. We reasoned that the longer a cell resides on a surface, the more likely it is to experience mechanical stimuli from TFP. We thus compared polarization of cell populations immediately after contact (10 min) with populations that were associated with the surface for longer times (60 min). We focused on the dynamic

localization of mNG-FimX. First, we found that in many cells, polar mNG-FimX foci relocated from pole to pole within a short timeframe after surface contact, as if they were oscillating (**Figure 2.4A, Movie S2.9**). These observations were reminiscent of oscillations in the twitching and gliding regulators observed in *M. xanthus* (Blackhart & Zusman, 1985a; Galicia et al., 2019; Guzzo et al., 2018a). The proportion of cells exhibiting these oscillations became smaller after prolonged surface contact (**Figure 2.4B, Figure S2.7A**), suggesting that surface sensing inhibits mNG-FimX oscillations and stabilizes polarization. To test whether mechanosensing with T4P induces polarization of the extension machinery, we visualized mNG-FimX in a Δ*pilA* mutant background, which also displayed oscillations (**Figure 2.4*C*, Movie S2.10**). We found that the fraction of Δ*pilA* cells that showed mNG-FimX oscillations 10 and 60 min after surface contact were equal, near 90% (**Figure 2.4D**). The distributions of oscillation frequencies between these two states were also indistinguishable (**Figure S2.7B**). Altogether, our results demonstrate that TFP-mediated mechanosensing at one pole locally recruits and stabilizes extension motors, thereby inducing a positive feedback onto their own activity. While several exogenous molecular compounds bias collective or single cell twitching migration (Kearns et al., 2001; Limoli et al., 2019; Nolan et al., 2020; Oliveira et al., 2016), our data shows chemical gradients are not necessary for active regulation of twitching.

PilB polarization sets the twitching direction of single cells, and PilG and PilH regulate T4P polarization to control reversals. We therefore investigated how the Chp system regulates PilB localization to control a cell's direction of motion. We compared the mean localization profiles of PilB-mNG and mNG-FimX in WT, Δ*pilG* and Δ*pilH* backgrounds

(**Figure 2.5A and B, Figure S2.8A**). Both fusion proteins had greater polar fluorescent signal in Δ*pilH* and lower polar signal in Δ*pilG* compared to WT (**Figure 2.5C and D**). We computed a polar localization index which measures the proportion of the signal localized at the poles relative to the total fluorescence (**Figure S2.8B**). About 50% of the mNG-FimX and PilB-mNG signal is found at the poles for WT, 70% of the signal is polar in Δ*pilH*, and most of the signal is diffuse in Δ*pilG* (**Figure 2.5E and G**). We next computed a symmetry index that quantifies the extent of signal polarization, that is how bright a pole is compared to the other, with a value of 0.5 being completely symmetric (**Figure S2.8B**). WT cells grown in liquid had a mNG-FimX and PilB-mNG symmetry index of about 0.6 (**Figure 2.5F and H**). In contrast, Δ*pilH* cells were more polarized, with a symmetry index close to 0.75. Compared to WT, mNG-FimX was more symmetric in a Δ*pilG* background (**Figure 2.5H**). We verified that the increase in expression levels in the different Chp mutants did not exacerbate PilB and FimX localization and polarization (**Figure S2.9**). In summary, we showed that PilG promotes polar recruitment and polarization of PilB and its regulator FimX, which is counteracted by PilH.

We then wondered how *P. aeruginosa* orchestrates two response regulators with opposing functions. Yeast and amoebae control cell polarization in response to environmental cues using spatially structured positive and negative feedback (Brandman & Meyer, 2008). By analogy, we considered a model wherein PilG and PilH segregate to implement positive and negative feedback at distinct subcellular locations (Inclan, Persat, Greninger, Dollen, et al., 2016a). We therefore investigated the localization of functional mNG-PilG and mNG-PilH integrated at their native chromosomal loci (**Figure 2.6A**). We

found that PilG predominantly localizes to the poles (**Figure 2.6B and C**). In contrast, PilH is mainly diffuse in the cytoplasm, with only a small fraction at the poles (**Figure 2.6B and C**). *P. aeruginosa* can therefore ensure the antagonistic functions of PilG and PilH by localizing the former to the poles and the latter to the cytoplasm.

We next analyzed the relationship between a cell's direction of migration with mNG-PilG and mNG-PilH polarization (**Figure S2.10*A*, Movie S2.11**). We found that 90% of cells moved towards their bright mNG-PilG pole, while only 50% moved towards their bright mNG-PilH, corresponding to a random orientation relative to the direction of migration (**Figure 2.6D**). By comparing the asymmetry of polar foci, we found that mNG-PilG signal was largely asymmetric in motile cells compared to the non-motile population (**Figure 2.6E**). Correlative iSCAT fluorescence highlighted that the brightest mNG-PilG polar spots had more TFP (**Figure 2.6F**). Consistent with this finding, in cells that reversed twitching direction, mNG-PilG localization switched to the new leading pole prior to reversal (**Figure S2.10B, Movie S2.12**). We found that the polar signal of mNG-PilH was mainly symmetric, both in moving and non-moving subpopulations (**Figure 2.6D**). Thus, PilG, but not PilH, actively localizes to the leading pole during twitching, recapitulating the dynamic polarization of PilB and FimX. We confirmed this by imaging the double fluorescent protein fusions mScarlet-I-PilG with mNG-FimX and mScarlet-I-PilG with PilB-mNG (**Figure S2.11, Figure S2.12A**). In both strains, the FimX/PilB and PilG colocalized at the leading pole of twitching cells (**Figure S2.12B**) and changed polarization upon reversals (**Figure S2.12C-F**). We could not however distinguish the order at which FimX and PilG changed polarity during reversals, nor could we measure differences in the delay

between motility reversal and polarity changes in single fusions (**Figure S2.13**). Therefore, T4P input at the leading pole activates PilG. Polar PilG rapidly drives a local positive feedback on T4P extension to maintain the direction of twitching. Cytoplasmic PilH stimulate reversals by inhibiting PilB polarization, permitting reassembly at the opposite pole. In summary, *P. aeruginosa* controls mechanotactic twitching using a local-excitation, global-inhibition signaling network architecture akin to chemotactic signaling in amoebae and neutrophils (**Figure S2.14**) (Levchenko & Iglesias, 2002a; Van Haastert & Devreotes, 2004).

DISCUSSION

We discovered that *P. aeruginosa* controls the direction of twitching motility in response to mechanical signals through the motility machinery itself. This migration strategy differs from the one employed in chemotactic control of swimming motility. Chemotaxis systems control the rate at which swimming cells switch the direction of rotation of their flagella, generating successive run-and-tumbles (Berg, 2004; Bi & Sourjik, 2018a) or flicks (Son et al., 2013) that cause directional changes. However, T4P must disassemble from one pole and reassemble at the opposite in order to reverse cell movement. In essence, this tactic strategy is akin to the one of single eukaryotic cells such as amoebae and neutrophils that locally remodel their cytoskeleton to attach membrane protrusions in the direction of a stimulus (Van Haastert & Devreotes, 2004). *P. aeruginosa* twitching direction is also biased by chemical gradients, suggesting that Chp also senses chemical stimuli (Kearns et al., 2001; Limoli et al., 2019; Nolan et al., 2020; Oliveira et al., 2016). Our results do not disprove that Chp controls twitching chemotactically, but provide a complementary perspective on these observations. In one scenario, a strong chemical gradient could produce a gradient in surface chemistry that causes differential adhesion of TFP between leading and lagging poles, inducing a bias in twitching direction. The relative contributions of chemical and mechanical inputs in activating the Chp system will therefore require further biophysical investigations.

Ultimately, the ability to balance persistent forward migration with reversals optimizes *P. aeruginosa* individual twitching. Reversal may occur spontaneously or upon perturbations, for example when colliding another cell. The Chp system may also promote

asymmetric piliation of upright twitching *P. aeruginosa* cells during exploratory motility (Gibiansky et al., 2010). We also found that the ability to reverse upon collision prevents jamming of groups of cells, supporting a model wherein the Chp system orchestrates collective migration (Whitchurch et al., 2004a). More generally, we anticipate that other bacteria, as well as archaeal and eukaryotic species that actively migrate on surfaces leverage mechanosensation to control reversal rates and orchestrate collective motility behaviors (Guzzo et al., 2018a).

Bacteria use dedicates sensing systems to regulate gene expression and adhesion in response to mechanical signals (Dufrêne & Persat, 2020a; Ellison et al., 2017; Hug et al., 2017; Sanfilippo et al., 2019). Beyond bacteria, eukaryotic cells also transduce mechanical signals into cellular responses, regulating an array of physiological processes including development, immunity and touch sensation (Kefauver et al., 2020). Eukaryotic cell motility is also sensitive to mechanical cues. For example, adherent mammalian cells migrate up gradients of substrate material stiffness in a process termed durotaxis (Sunyer et al., 2016). We established that single cells can actively sense their mechanical environment to control motility on the timescale of seconds. Our work thus expands our view of signals activating bacterial sensing systems and more generally highlights the role of mechanics in regulating motility, be it in bacteria, archaea or eukaryotes (Houk et al., 2012).

Altogether, Chp functions as a spatial sensor for mechanical input. Thus, chemotaxis-like systems can sense spatially-resolved mechanical signals, a feat that is still debated when

only considering diffusible molecules as input stimuli (Berg & Purcell, 1977). Phototactic systems may however be an exception by conferring cyanobacteria the ability to spatially sense gradients of light (Schuergers et al., 2016a, 2017). Accordingly, the Pix phototactic system of the cyanobacterium *Synechocystis* shares signal transduction architecture with the *P. aeruginosa* Chp system by harboring two CheY-like response regulators, PixG and PixH (Schuergers et al., 2016a, 2017). There also exists a broad range of chemotaxis-like systems with even higher degrees of architectural complexity (Porter et al., 2011a). We thus highlight that their subcellular arrangement may play important functions in the mechanism by which they regulate motility.

Finally, we revealed an unexpected commonality between bacteria, and single eukaryotic cells in the way they transduce environmental signals to control polarity (Van Haastert & Devreotes, 2004). Amoebae and neutrophils harness complex circuitry which combines positive and negative feedback loops to chemotax (Brandman & Meyer, 2008). Positive regulators activate actin polymerization locally to drive membrane protrusion in the direction of polarization. Negative regulators inhibit actin polymerization throughout the cytoplasm to limit directional changes while also permitting adaptation (Brandman & Meyer, 2008). Altogether, these cells establish a local activation-global inhibition landscape that balances directional persistence with adaptation (Levchenko & Iglesias, 2002a). By virtue of PilG and PilH compartmentalization, *P. aeruginosa* replicates the local activation-global inhibition landscape (Levchenko & Iglesias, 2002a). We have therefore uncovered a signal transduction principle permitting mechanotaxis in response to spatially-resolved signals that is conserved across kingdoms of life.

MATERIALS AND METHODS

Growth conditions and media.

For surface association experiments cells were plated on pre-heated solid LB media containing 1 % agarose standard (Carl Roth) and incubated at 37 °C for 3 hours. For twitching motility assays semi-solid tryptone media were prepared by autoclaving (5 $g.l^{-1}$ tryptone (Carl Roth), 2.5 $g.l^{-1}$ NaCl (Fisher Bioreagents), 0.5 % ($wt.vol^{-1}$) agarose standard (Carl Roth)). For fluorescence visualization under correlative fluorescence and iSCAT cells were washed with PBS (BioConcept AG) and resuspended in M9 medium (VWR) containing 0.2 % of glucose.

Strains and vector construction.

All strains used in this study are listed in Table S2.1. Plasmids and corresponding oligonucleotides are listed in Table S2.2 and Table S2.3, respectively. Gene deletions and gene fusions were constructed by two-step allelic exchange (according to (Hmelo et al., 2015a)) using the suicide vectors pEX18Amp or pEX18Gent. In-frame deletions were generated by combining approximately 500-bp fragments of the up- and downstream regions of the designated gene, leaving only a few codons (usually around six) and verified by colony PCR and sequencing. In-frame insertions were constructed in basically the same fashion. Insertion fragments with wild-type length (e.g. for complementation) were integrated into the corresponding deletion strain. Fluorophore genes were fused to the N- or C-termini of the desired gene separated by a GGGGG linker and introduced into the wild-type chromosome. Expression and integrity of fluorescent fusions were verified by Western blotting and functionality was tested by twitching motility assays (see

corresponding methods). Plasmids were constructed using standard Gibson assembly protocols (Gibson et al., 2009a) and introduced into *P. aeruginosa* cells by conjugative mating with *E. coli* S17.1 as donor. For selection of *E. coli* the following antibiotic concentrations were used: 100 µg/ml ampicillin, 10 µg.ml^{-1} gentamycin. For selection of *P. aeruginosa* the following antibiotic concentrations were used: 300 µg.ml^{-1} carbenicillin, 60 µg.ml^{-1} gentamycin.

Twitching motility stab assay.

Square plastic dishes (100x100x20 mm, Sarstedt) were filled with 50 ml of 0.5 % agarose tryptone medium and dried in a flow hood for 30 min. Single colonies grown overnight on LB agar at 37 °C were stabbed with a 10 µl pipette tip through the agarose hydrogel to the bottom of the dish without much force to prevent separation of the hydrogel from the plastic. The plates were incubated at 37 °C overnight in a plastic bag. The hydrogel was then scored around the edges with a 10 µl pipette tip and removed carefully. Twitching motility was quantified by taking two measurements of the twitching zone diameters from two to eight independent stabs. The twitching diameter of wild-type or Δ*fliC P. aeruginosa* was used as reference.

Western blot.

Cells were grown overnight in LB, diluted 1:100 in LB and grown until OD_{600} = 1. One ml of cell suspension was harvested by centrifugation and resuspended in 100 µl of 2x loading bugger (Li-Cor), 100 mM DTT (Sigma) and at least 200 U/ml nuclease (Pierce) until the sample was no longer viscous. 10 µl of each sample was run on a sodium dodecyl

sulfate-polyacrylamide gel electrophoresis (SDS-PAGE) at 200 V and transferred onto a nitrocellulose membrane (iblot 2). The membrane was incubated in PBS + 5 % milk powder for 1 h, then in 1:1000 anti-mNeonGreen antibody (Chromotek) in TBST + 5 % milk powder for 1 h, washed 3x with TBST and 1:10,000 Goat anti-Mouse IgG IRDye 800CW (Li-Cor) in TBST + 5 % milk powder for 1 h and washed 3x at room temperature. The blot was visualized with Odyssey CLx (Li-Cor).

Fluorescence microscopy image processing.

All fluorescent images were background subtracted with ImageJ (version 1.53c). Snapshot images and movies were generated with ImageJ and data were analyzed with custom scripts in Python (version 3.7.6 and 3.8.5) and MATLAB (version R2019b and R2020a), as specified in detail below. Sample sizes for each experiment are listed in Table S2.4.

Correlative interferometric scattering (iSCAT) fluorescence microscopy setup.

Our iSCAT microscope setup was previously described in (Talà et al., 2019b). For this study, we added a fluorescent channel as described in (Ortega Arroyo et al., 2016b). Briefly, we implemented a green fluorescence channel by coupling a blue laser with a wavelength of 462 nm (Lasertack, LDM-462-1400-C) to the iSCAT illumination path with a 490 nm long pass dichroic mirror (Thorlabs, DMLP490). The laser was focused on the back focal plane of the objective with a plano-convex lens (f = 500 mm, Thorlabs, LA1908-A). The fluorescent signal was then focused onto a CMOS camera (PointGrey, GS3-U3-23S6M) with a 400 mm focal length achromatic lens and a GFP filter (CWL = 525 nm,

Bandwidth = 39 nm, Thorlabs, MF525-39). A shutter was placed in the illumination path of the fluorescence channel in order to prevent unnecessary illumination. The iSCAT illumination was monitored by modulating the acousto-optic deflectors' output (Figire S2.15).

Glass coverslip and microfluidic chip preparation.

Glass coverslips (Marienfeld, 22x40 mm No 1.5) were cleaned as described in (Talà et al., 2019b). Briefly, they were washed sequentially with distilled water, ethanol, distilled water, isopropanol, distilled water, ethanol, distilled water and excess water was dried with a stream of nitrogen. For visualization, we either plasma-bonded 500 µm wide, 140 µm deep polydimethylsiloxane (PDMS) microchannels, fabricated using standard photolithography methods, or we deposited PDMS gaskets on the clean coverslips. PDMS gaskets were obtained using biopsy punches of 6 mm in diameter.

cAMP quantification using PaQa-YFP reporter.

The PaQa-YFP reporter system for cAMP measurements including a reference promoter fused to mKate2 has been previously described in detail(Persat, Inclan, et al., 2015a). Single colonies were grown overnight in LB-carbenicillin, diluted to OD_{600} 0.05 and grown until mid-exponential phase. For surface-association growth, cells were grown for 3 h at 37 °C on LB 1 % agarose and then harvested in 1 ml LB by gentle scraping. 1 µl of culture was then loaded on a 1 % agarose-PBS pad and flipped onto a glass bottom dish (MatTek) prior to visualization. Several images in phase contrast, YFP and mKate2 channels were acquired. Images were binned 2x2 and fluorescence channels were

background subtracted using a custom macro in ImageJ. Cells were segmented and the cell area and corresponding cell mean fluorescence were extracted using BacStalk (Hartmann et al., 2020b). Median PaQa-YFP to mKate2 fluorescent intensity ratios were computed with a custom Python script for each biological replicate. Each median was then normalized to the mean of the WT biological replicates of liquid cultures.

iSCAT-based quantification of type IV pili number.

Single colonies were inoculated in LB, grown overnight and diluted 1:500 or 1:1000 followed by a grow period of 2 h to obtain mid exponential phase cultures. 100 µl of the cell suspension were plated on LB 1 % agarose, grown for 3 h at 37 °C and harvested in 500 µl LB by gentle scraping. Cells were diluted to OD_{600} 0.02 prior to visualization. Both liquid and solid grown cells were either loaded on 500 µm x 140 µm PDMS microchannels or in 6 mm PDMS gaskets. Cells sticking to the surface were visualized without flow with iSCAT and movies were recorded at 10 fps for either 2 min, 1 min or 30 s. To reveal the interferometric component of the signal, each frame was processed as described in (Talà et al., 2019b). In some cases, we extracted the interferometric signal by differential processing. Briefly, we subtracted each frame at time t-1 to the frame at time t then performed the bandpass filtering and frame normalization as described in (Talà et al., 2019b). This technique allowed to drastically decrease strong background signal which revealed hidden floppy pili. However stationary pili disappeared in the process as they became part of the background. Individual movies were manually analyzed by counting the total number of pili in each cell. The residence time of each cell on the coverslip was also recorded. Finally, we computed a bootstrap median of the total pili number for each

biological replicate. To compare strains, we then took the mean of the medians for each biological replicate within one strain as well as their standard deviation.

Quantification of type IV pili distributions.

To quantify pili at both cell poles, we selected flat laying cells (all strains with Δ*fliC* background). Pili from each pole were manually counted and recorded with a custom ImageJ macro. Probabilities were computed and plotted using Python. We focused our analysis on subset populations of cells that had either two, three or four pili and counted the total number of cells in those populations as well as their corresponding pili distribution combinations (for cells with two pili: (1|1), (2|0) (Figure S2.3A), for cells with three pili: (2|1), (3|0) (Figure S2.3B) and for cells with four pili: (2|2), (3|1) and (4|0) (Figure S2.3C). We considered a cell to have symmetric pili distribution when they had 0 or 1 pilus difference between poles and we considered asymmetric distributions when cells had 2 and more pili difference between poles. We obtained a probability by dividing the cells in each pili distribution by the total number of cells of the corresponding population. We then compared these percentages with the percentages obtained by a random distribution (Figure S2.3D).

Single cell twitching behavior without fluorescence.

Cells from an exponential culture grown in LB were diluted to an OD_{600} of 0.2 in tryptone medium. The agarose pads were prepared by autoclaving tryptone medium 0.5 % agarose, cooling down to 70 °C in the autoclave followed by cooling to 55 °C for 20 min in a water bath, pouring 28 ml into round petri dishes and letting dry for 30 min in a flow

hood. Plates were then stored in a plastic bag at 4 °C for 1 day. A round pad was cut out and 1 µl of the diluted cell suspension was pipetted onto the upper side of the agarose pad (i.e. the side that was not in contact with the plastic dish bottom). We note that all of the following conditions were critical in order to reproducibly allow cells to twitch as single, isolated cells: The medium composition (see Media), autoclaving the agarose medium, cooling down and drying as specified above, the initial optical density of the droplet and pipetting on the upper side of the agarose pad. Then, without letting the droplet dry, the pad was flipped onto a microscope glass bottom dish (MatTek) and six droplets of PBS were added to the sides to prevent drying. The cells were incubated at 37 °C and imaged with phase contrast microscopy every hour at 0.2 frames per second for 5 min over 3 h. The movies were processed with a custom ImageJ macro to ensure compatibility with the downstream analysis. If necessary, drift was also corrected using the *StackReg* plugin (version July 7, 2011; (Thévenaz et al., 1998a)) in that step. Cells were then segmented and tracked using BacStalk (version 1.8, (Hartmann et al., 2020b)) to get the cell outline and position of the center of mass (CM) of each isolated bacterium for each frame. Subsequent analyses of the cell tracks were done with custom MATLAB scripts. For every analysis, cell tracks were categorized into moving and non-moving by using a speed threshold of 1 pixel per frame (here: 32.5 nm s^{-1}). The speed threshold was applied to the speed of each frame (converted from the displacement of the CM between the current and previous frame), setting the speed to 0 if below the threshold. Cells were only considered moving when the speed was unequal to zero for at least three subsequent frames over the tracked time.

In Figure 2.1B, other cells in the snapshots were cut out for clarity (unmodified images: Movie S2.1).

Spatiotemporal cumulative displacement maps.

In order to analyze twitching displacement relative to the initial cell orientation, we defined a cell orientation unit vector $\vec{t}$ from the CM to the initial leading pole (*cf*. Figure 2.1B). The initial leading pole was determined by comparing the scalar products of the unit vectors from CM to poles A and B (arbitrary classification) to the normalized displacement vector $\vec{d}$ in the first frame with a speed above the speed threshold. The vectors $\vec{t}$ and $\vec{d}$ were then used to determine direction of the cell displacement δ relative to the initial leading pole, giving it a positive sign for forward (i.e. toward initial leading pole) and a negative sign for reverse (i.e. opposite to initial leading pole) movement. The spatiotemporal displacement maps (Figure 2.1C) were generated by cumulating the direction-corrected displacement as a function of time, for 200 tracks that were between 31 and 61 frames long.

Reversal frequency of isolated cells.

To count the reversal frequency of twitching cells, the scalar product between the normalized displacement vector $\vec{d}$ and the cell orientation unit vector $\vec{t}$ was determined (*cf*. Figure 2.1B) and rounded for each frame (starting from the first frame with a speed above the speed threshold). This resulted in a series of numbers that correspond to movement of the cell toward the initial leading pole (1), toward the initial lagging pole (-1) or no movement (0) at that timepoint. Timepoints corresponding to no movement were

removed. Cells were considered moving in the same direction (relative to the initial leading pole) as long as the sign remained the same. A reversal was counted when the sign changed, however, only if at least two subsequent frames before and after the reversal had the same sign (this was done to correct for frequent sign changes when a cell was in a non-moving phase). The reversal frequency (Figure 2.2A) was calculated by dividing the sum of all considered reversals by the total tracked time over all cell tracks for each biological replicate.

Reversal frequency after collision with an obstacle (cells and glass microfibers).
Cells were prepared and movies recorded as described above. Reversal rates after collisions with other cells (Figure 2.2C) were determined in the same movies recorded for analyzing spontaneous reversals. To determine the reversal rate after collision with non-biological obstacles, we prepared glass microfibers by vortexing glass microfiber filters (GF/B, ~0.3-3 µm diameter, Whatmann) in 50 ml PBS for 5 min, concentrating the supernatant with sheared off fibers (removing as much liquid as possible), followed by 1 h sonication in a standard sonication bath. This resulted in long microfibers being broken down into lengths between 10 and 200 µm. The fiber suspension was mixed with the cell suspension to an appropriate concentration.

Because only isolated cells were tracked by BacStalk, we counted all collisions and potential subsequent reversals manually. A collision was only considered if the cell was moving for at least three frames in the same direction prior to the collision and the collision lasted for at least two frames (frame interval 5 sec). Furthermore, collisions with angles

below 20° (data Fig. 2C) or 45° (data Figure 2.2E) were not considered. The conditions to consider a collision were adapted for the comparison of cell-cell and cell-fiber collisions (Figure 2.2E) because of the difference in shape of the glass microfibers. Bigger fibers typically lift the agar pad, resulting in accelerating rather than slowing down colliding cells at low collision angles, in contrast to low-angle collision with other cells.

A reversal following a collision was considered only if it occurred within five frames after the collision ended. Freshly divided cells were not considered as they were never found to reverse after a collision, potentially due to the lack of functional pili basal bodies at the new pole. The frequency of reversals following a collision (Figure 2.2C,E) was calculated by dividing the sum of all considered reversals by the sum of all considered collisions for each biological replicate.

In the snapshots of Figure 2.2B (left), the moving and colliding cell was cut and placed at its original position into frame 10 s for clarity (unmodified images: Movie S2.3).

Dynamic localization of fluorescent protein fusions in isolated twitching cells.

All localization studies in moving cells were performed in Δ*fliC* background to ensure that cells are not moving by means of flagella. Cells and microscope dishes were essentially prepared as described above (*cf*. single cell twitching behavior without fluorescence). The cells were then incubated at 37 °C and imaged with fluorescence microscopy every hour at 0.2 – 0.5 frames per second for 2 min over 3 h. Cells were similarly segmented and tracked with BacStalk, and basic MATLAB analysis was performed as described above,

applying a speed threshold (here: 26 - 65 nm s^{-1}) in order to categorize cell tracks into moving and non-moving. Next, the positions of both cell poles were determined using the cell outline obtained from BacStalk. Poles were labeled according to their position in subsequent frames. Average fluorescence intensity was measured in an area around the coordinate of each pole with a radius $r = \frac{cell\ width}{1.8}$.

Cells were then categorized according to their ratio of average fluorescence intensity between the two poles over the whole cell track ($symmetry\ ratio = \frac{intensity\ \mathrm{dim}\ pole}{intensity\ bright\ pole}$). We defined a symmetry ratio threshold (0.69) according to the distribution for PilB-mNG, which showed two subpopulations, that we considered having symmetric and asymmetric subcellular protein localization. Cells were considered symmetric with a ratio below and asymmetric with a ratio above the threshold (Figure 2.3D and Figure 2.6E).

In order to measure if cells moved toward the dim or the bright pole (Figure 2.3E, Figure 2.6D; including cells which we considered having symmetric protein localization), we defined a unit vector $\vec{e}$ from the dim to the bright pole. We then computed an alignment factor α, which is the scalar product of the normalized displacement vector $\vec{d}$ and the fluorescence polarity vector $\vec{e}$. The alignment factor α represents in which direction the cell is moving relative to the bright pole. An alignment factor $\alpha > 0$ corresponds to movement toward the bright pole, with $\alpha = 1$ corresponding to movement exactly parallel to the cell length axis.

Kymographs were generated with BacStalk (version 1.8; (Hartmann et al., 2020b)) after normalizing the cell length to 50 pixels and resampling the fluorescence intensity data with the *interp1* function in MATLAB. Because the poles were labeled inconsistently by BacStalk, the reference pole was set manually for each frame to represent the initial leading pole.

In order to determine a potential temporal sequence of protein appearance at the new leading pole during reversals, we focused on cells that reversed and showed clear pole switching of the fluorescent foci. Those cells were identified by running a modified version of the MatLab script described above. This script was used to plot fluorescent traces of both poles (as in Figure S2.6E,F or Figure S2.10B) together with the displacement corrected for the initial leading pole (rounded to 1 and -1). The reversal delay time τ was defined as the time between the last crossover of the fluorescent intensity traces of both poles before the reversal, and the first frame with a displacement with opposite sign (defined as reversal).

Colocalization of PilG with PilB and FimX.

Double tagged strains were generated as described above using mNeonGreen fusions of FimX and PilB and mScarlet-I fusion of PilG. No spectral crossover could be observed with the corresponding second filters in single tagged strains. Although single tagged fusion proteins were functional (mNG-FimX and mScI-PilG) or partially functional (PilB-mNG) as measured by twitching stab assays (Figure S2.11), combining both tagged proteins in one strain resulted in significant twitching defects. Nevertheless, single

twitching cells could be observed with fluorescence microcopy, however, the fraction of motile cells and cell speed were decreased. Furthermore, the fluorescent signal of some fusions was decreased in the double tagged strain compared to the single tagged strain. Finally, because individual cell speed and twitching direction differed greatly, the offset of the fluorescent foci resulting from the image acquisition delay between fluorescent channels could not be corrected in a uniform and unbiased way. Given those limitation, we decided to determine colocalization during twitching manually. First, we marked cells that twitched smoothly without reversals (but sometimes with short stop-phases). We discarded cells with fluorescent signals below noise level of either tagged protein. Those cells were not considered, because the low fluorescence is likely a result of the impaired protein function and/or potential protein interaction in the double tagged strains. In the remaining fraction (~85% for mScI-PilG + PilB-mNG and (~75% for mScI-PilG + mNG-FimX), we then determined the bright fluorescent pole for both tagged proteins (always the leading pole, except for a small fraction ~5% of PilB-mNG) and determined if the bright fluorescent foci colocalized.

Type IV pili number quantification and motor proteins localization.

Overnight cultures grown in LB were diluted 1:500 to 1:1000 and grown for 3 h up to mid-exponential phase then plated for surface-association experiments as described above. Cells were harvested in 500 µl of LB by gentle scraping of the plate and loaded into PDMS gaskets. After 5 min incubation at room temperature (RT) unattached cells were washed with PBS and resuspended in M9 medium to avoid background autofluorescence of LB. Cells were visualized for 4 to 5 s with correlative iSCAT fluorescence microscopy at

100 fps in the iSCAT channel and 5 fps in the fluorescence channel. iSCAT movies were processed as described above. Further image processing and analysis was performed using custom ImageJ macros. Fluorescence images were background subtracted and iSCAT and fluorescence frames were registered using ImageJ's *Align Image by line ROI* function. The scaling factor between fluorescence and iSCAT frames was determined by the difference in effective pixel size of the two cameras. The rotation angle was computed with the two ROI lines used for registration. Pili were manually counted on iSCAT images and total fluorescence at the poles was measured on corresponding fluorescence images. Briefly, cells were selected by the user and cell poles were automatically detected by segmenting the fluorescent cell, extracting its outline, finding its center of mass (CM) and finding the points within the outline with maximum distance from the CM. The total fluorescence at the poles was then computed by measuring the mean fluorescence within a circle at the poles with a diameter corresponding to the cell width and multiplying that mean by the area of the circle. For the statistical analysis we counted how many cells had more pili at the brightest pole and how many had more pili at the dimmest pole in each biological replicate (at least 20 cells per biological replicate). We then divided that number by the total number of cells within the biological replicate and computed the mean probability across the biological replicates for each strain. Data was plotted using Python.

Frequency of bright pole oscillations.

Cells and microscope dishes were prepared and microscopy was performed essentially as described above (*cf.* dynamic protein localization). The only difference was that cells were grown and imaged in a heated chamber (37 °C) on the microscope at 0.2 frames

per second for 3 min after 10 and 60 min. Earlier timepoints were challenging to record, because of drift and autofocus issues, that usually diminished after a few minutes after preparing the microscope slide.

To count how often the brightest fluorescence signal of a fusion protein switched from one pole to the opposite pole, a similar analysis as for the dynamic protein localization was applied to measure the average fluorescence intensity of both poles over time. Then, a series of numbers (1 or -1) was generated that corresponds to a pole (arbitrary but same over the whole track) being the bright pole (1) or the dim pole (-1) for each frame. Similar to counting reversals, a bright pole switch was counted when the sign changed. Here, no additional filters were applied. The frequency of bright pole switches (Figure S2.7) was calculated for each cell by dividing the sum of all bright pole switches by the tracked time.

Motor protein and response regulator localization in immobilized cells.

Cells were grown, visualized and analyzed as described above (*cf*. PaQa-YFP reporter quantification). To characterize the spatial localization of the protein fusions, we segmented each cell in phase contrast and extracted their fluorescence profiles using BacStalk. Fluorescent profiles correspond to the mean pixel value of a transversal section of the cell along the mid-cell axis (Figure S2.8A). To compare cells with different expression levels, profiles were normalized by the total fluorescence of the cell (corresponding to the area under the red curve in Figure S2.8A) and rescaled by the cell length. We then computed mean profiles and standard deviations for every biological

replicate. To quantify the extent of polar localization, we computed a polar localization index. To calculate this index, we integrated the fluorescence intensity at the poles defined by a circle having a diameter of a single cell width (normalized by the cell length, pink areas a and b in Figure S2.8B). We corrected this value by subtracting the fluorescence at the poles of the diffused portion of the signal corresponding to the cytoplasmic median fluorescence (hatched areas c and d in Figure S2.8B). The polar localization index was computed by dividing this value by the sum of the pole areas. A value of 0 correspond to a totally diffused protein whereas a value of 1 correspond to a totally polar protein. Similarly, we computed a symmetry index by taking the ratio between the maximum polar total fluorescence and the sum of the polar total fluorescence. A value of 0.5 corresponds to a perfectly symmetric bipolar localization whereas a value of 1 corresponds to a perfectly unipolar localization. To compare strains, we computed the mean and standard deviation across biological replicates using a custom MatLab script.

Localization of the extension motor under arabinose induction.

Cells harboring the PilB-mNG expression plasmid were grown overnight in LB gentamycin. Cells were diluted 1:1000 in LB gentamycin and arabinose was added in the following concentrations: 0 %, 0.03 % and 0.1 %. The diluted cultures were grown for 3 h at 37 °C with 290 rpm shaking. Samples were then prepared, visualized and analyzed as described above.

ACKNOWLEDGEMENTS

LT, ZAM, IV, XP, AP are supported by the SNSF Projects grant number 310030_189084. MJK is supported by the EMBO postdoctoral fellowship ALTF 495-2020. JNE, YI, RP, HM and are supported by an NIH R01 grant number AI129547 and by the Cystic Fibrosis Foundation (495008).

REFERENCES

Berg, H. C. (2004). *E. coli in Motion* (H. C. Berg, Ed.). Springer New York. https://doi.org/10.1007/b97370

Berg, H. C., & Purcell, E. M. (1977). Physics of chemoreception. *Biophysical Journal*, *20*(2), Article 2. https://doi.org/10.1016/S0006-3495(77)85544-6

Bertrand, J. J., West, J. T., & Engel, J. N. (2010). Genetic Analysis of the Regulation of Type IV Pilus Function by the Chp Chemosensory System of Pseudomonas aeruginosa. *Journal of Bacteriology*, *192*(4), Article 4. https://doi.org/10.1128/JB.01390-09

Bi, S., & Sourjik, V. (2018). Stimulus sensing and signal processing in bacterial chemotaxis. *Current Opinion in Microbiology*, *45*, 22–29. https://doi.org/10.1016/j.mib.2018.02.002

Blackhart, B. D., & Zusman, D. R. (1985). “Frizzy” genes of Myxococcus xanthus are involved in control of frequency of reversal of gliding motility. *Proceedings of the National Academy of Sciences*, *82*(24), 8767–8770. https://doi.org/10.1073/pnas.82.24.8767

Brandman, O., & Meyer, T. (2008). Feedback Loops Shape Cellular Signals in Space and Time. *Science*, *322*(5900), 390–395. https://doi.org/10.1126/science.1160617

Buensuceso, R. N. C., Daniel-Ivad, M., Kilmury, S. L. N., Leighton, T. L., Harvey, H., Howell, P. L., & Burrows, L. L. (2017). Cyclic AMP-Independent Control of Twitching Motility in Pseudomonas aeruginosa. *Journal of Bacteriology*, *199*(16). https://doi.org/10.1128/JB.00188-17

Burrows, L. L. (2012). Pseudomonas aeruginosa Twitching Motility: Type IV Pili in Action. *Annual Review of Microbiology*, *66*(1), 493–520. https://doi.org/10.1146/annurev-micro-092611-150055

Chiang, P., Habash, M., & Burrows, L. L. (2005). Disparate Subcellular Localization Patterns of Pseudomonas aeruginosa Type IV Pilus ATPases Involved in Twitching Motility. *Journal of Bacteriology*, *187*(3), Article 3. https://doi.org/10.1128/JB.187.3.829-839.2005

Costerton, J. W., Lewandowski, Z., Caldwell, D. E., Korber, D. R., & Lappin-Scott, H. M. (1995). Microbial biofilms. *Annual Review of Microbiology*, *49*(1), 711–745. https://doi.org/10.1146/annurev.mi.49.100195.003431

Darzins, A. (1994). Characterization of a Pseudomonas aeruginosa gene cluster involved in pilus biosynthesis and twitching motility: Sequence similarity to the chemotaxis proteins of enterics and the gliding bacterium Myxococcus xanthus. *Molecular Microbiology*, *11*(1), Article 1. https://doi.org/10.1111/j.1365-2958.1994.tb00296.x

Dufrêne, Y. F., & Persat, A. (2020). Mechanomicrobiology: How bacteria sense and respond to forces. *Nature Reviews Microbiology*, *18*(4), Article 4. https://doi.org/10.1038/s41579-019-0314-2

Ellison, C. K., Kan, J., Dillard, R. S., Kysela, D. T., Ducret, A., Berne, C., Hampton, C. M., Ke, Z., Wright, E. R., Biais, N., Dalia, A. B., & Brun, Y. V. (2017). Obstruction of pilus retraction stimulates bacterial surface sensing. *Science*, *358*(6362), 535–538. https://doi.org/10.1126/science.aan5706

Fulcher, N. B., Holliday, P. M., Klem, E., Cann, M. J., & Wolfgang, M. C. (2010). The Pseudomonas aeruginosa Chp chemosensory system regulates intracellular

cAMP levels by modulating adenylate cyclase activity. *Molecular Microbiology*, *76*(4), Article 4. https://doi.org/10.1111/j.1365-2958.2010.07135.x

Galicia, C., Lhospice, S., Varela, P. F., Trapani, S., Zhang, W., Navaza, J., Herrou, J., Mignot, T., & Cherfils, J. (2019). MglA functions as a three-state GTPase to control movement reversals of Myxococcus xanthus. *Nature Communications*, *10*(1), Article 1. https://doi.org/10.1038/s41467-019-13274-3

Gibiansky, M. L., Conrad, J. C., Jin, F., Gordon, V. D., Motto, D. A., Mathewson, M. A., Stopka, W. G., Zelasko, D. C., Shrout, J. D., & Wong, G. C. L. (2010). Bacteria Use Type IV Pili to Walk Upright and Detach from Surfaces. *Science*, *330*(6001), 197–197. https://doi.org/10.1126/science.1194238

Gibson, D. G., Young, L., Chuang, R.-Y., Venter, J. C., Hutchison, C. A., & Smith, H. O. (2009). Enzymatic assembly of DNA molecules up to several hundred kilobases. *Nature Methods*, *6*(5), Article 5. https://doi.org/10.1038/nmeth.1318

Guzzo, M., Murray, S. M., Martineau, E., Lhospice, S., Baronian, G., My, L., Zhang, Y., Espinosa, L., Vincentelli, R., Bratton, B. P., Shaevitz, J. W., Molle, V., Howard, M., & Mignot, T. (2018). A gated relaxation oscillator mediated by FrzX controls morphogenetic movements in Myxococcus xanthus. *Nature Microbiology*, *3*(8), Article 8. https://doi.org/10.1038/s41564-018-0203-x

Hartmann, R., Teeseling, M. C. F. van, Thanbichler, M., & Drescher, K. (2020). BacStalk: A comprehensive and interactive image analysis software tool for bacterial cell biology. *Molecular Microbiology*, *114*(1), 140–150. https://doi.org/10.1111/mmi.14501

Hmelo, L. R., Borlee, B. R., Almblad, H., Love, M. E., Randall, T. E., Tseng, B. S., Lin, C., Irie, Y., Storek, K. M., Yang, J. J., Siehnel, R. J., Howell, P. L., Singh, P. K., Tolker-Nielsen, T., Parsek, M. R., Schweizer, H. P., & Harrison, J. J. (2015). Precision-engineering the Pseudomonas aeruginosa genome with two-step allelic exchange. *Nature Protocols*, *10*(11), Article 11. https://doi.org/10.1038/nprot.2015.115

Houk, A. R., Jilkine, A., Mejean, C. O., Boltyanskiy, R., Dufresne, E. R., Angenent, S. B., Altschuler, S. J., Wu, L. F., & Weiner, O. D. (2012). Membrane Tension Maintains Cell Polarity by Confining Signals to the Leading Edge during Neutrophil Migration. *Cell*, *148*(1), Article 1. https://doi.org/10.1016/j.cell.2011.10.050

Hug, I., Deshpande, S., Sprecher, K. S., Pfohl, T., & Jenal, U. (2017). Second messenger–mediated tactile response by a bacterial rotary motor. *Science*, *358*(6362), Article 6362. https://doi.org/10.1126/science.aan5353

Inclan, Y. F., Persat, A., Greninger, A., Dollen, J. V., Johnson, J., Krogan, N., Gitai, Z., & Engel, J. N. (2016). A scaffold protein connects type IV pili with the Chp chemosensory system to mediate activation of virulence signaling in Pseudomonas aeruginosa. *Molecular Microbiology*, *101*(4), 590–605. https://doi.org/10.1111/mmi.13410

Jain, R., Sliusarenko, O., Kazmierczak, B. I., Jacobs-Wagner, C., Jones, C., & Sanchez, D. (2017). Interaction of the cyclic-di-GMP binding protein FimX and the Type 4 pilus assembly ATPase promotes pilus assembly. *PLOS Pathogens*, *13*(8), e1006594. https://doi.org/10.1371/journal.ppat.1006594

Jarrell, K. F., & McBride, M. J. (2008). The surprisingly diverse ways that prokaryotes move. *Nature Reviews Microbiology*, *6*(6), Article 6. https://doi.org/10.1038/nrmicro1900

Kazmierczak, B. I., Lebron, M. B., & Murray, T. S. (2006). Analysis of FimX, a phosphodiesterase that governs twitching motility in Pseudomonas aeruginosa. *Molecular Microbiology*, *60*(4), Article 4. https://doi.org/10.1111/j.1365-2958.2006.05156.x

Kearns, D. B., Robinson, J., & Shimkets, L. J. (2001). Pseudomonas aeruginosa Exhibits Directed Twitching Motility Up Phosphatidylethanolamine Gradients. *Journal of Bacteriology*, *183*(2), Article 2. https://doi.org/10.1128/JB.183.2.763-767.2001

Kefauver, J. M., Ward, A. B., & Patapoutian, A. (2020). Discoveries in structure and physiology of mechanically activated ion channels. *Nature*, *587*(7835), Article 7835. https://doi.org/10.1038/s41586-020-2933-1

Levchenko, A., & Iglesias, P. A. (2002). Models of Eukaryotic Gradient Sensing: Application to Chemotaxis of Amoebae and Neutrophils. *Biophysical Journal*, *82*(1), 50–63. https://doi.org/10.1016/S0006-3495(02)75373-3

Limoli, D. H., Warren, E. A., Yarrington, K. D., Donegan, N. P., Cheung, A. L., & O'Toole, G. A. (2019). Interspecies interactions induce exploratory motility in Pseudomonas aeruginosa. *eLife*, *8*, e47365. https://doi.org/10.7554/eLife.47365

Matilla, M. A., & Krell, T. (2018). The effect of bacterial chemotaxis on host infection and pathogenicity. *FEMS Microbiology Reviews*, *42*(fux052). https://doi.org/10.1093/femsre/fux052

Meacock, O. J., Doostmohammadi, A., Foster, K. R., Yeomans, J. M., & Durham, W. M. (2021). Bacteria solve the problem of crowding by moving slowly. *Nature Physics*, *17*(2), Article 2. https://doi.org/10.1038/s41567-020-01070-6

Merz, A. J., So, M., & Sheetz, M. P. (2000). Pilus retraction powers bacterial twitching motility. *Nature*, *407*(6800), Article 6800. https://doi.org/10.1038/35024105

Nolan, L. M., McCaughey, L. C., Merjane, J., Turnbull, L., & Whitchurch, C. B. Y. 2020. (2020). ChpC controls twitching motility-mediated expansion of Pseudomonas aeruginosa biofilms in response to serum albumin, mucin and oligopeptides. *Microbiology*, *166*(7), 669–678. https://doi.org/10.1099/mic.0.000911

Oliveira, N. M., Foster, K. R., & Durham, W. M. (2016). Single-cell twitching chemotaxis in developing biofilms. *Proceedings of the National Academy of Sciences*, *113*(23), Article 23. https://doi.org/10.1073/pnas.1600760113

Ortega Arroyo, J., Cole, D., & Kukura, P. (2016a). Interferometric scattering microscopy and its combination with single-molecule fluorescence imaging. *Nature Protocols*, *11*(4), 617–633. https://doi.org/10.1038/nprot.2016.022

Ortega Arroyo, J., Cole, D., & Kukura, P. (2016b). Interferometric scattering microscopy and its combination with single-molecule fluorescence imaging. *Nature Protocols*, *11*(4), Article 4. https://doi.org/10.1038/nprot.2016.022

Persat, A., Inclan, Y. F., Engel, J. N., Stone, H. A., & Gitai, Z. (2015). Type IV pili mechanochemically regulate virulence factors in Pseudomonas aeruginosa. *Proceedings of the National Academy of Sciences of the United States of America*, *112*(24), Article 24. https://doi.org/10.1073/pnas.1502025112

Porter, S. L., Wadhams, G. H., & Armitage, J. P. (2008). Rhodobacter sphaeroides: Complexity in chemotactic signalling. *Trends in Microbiology*, *16*(6), 251–260. https://doi.org/10.1016/j.tim.2008.02.006

Porter, S. L., Wadhams, G. H., & Armitage, J. P. (2011). Signal processing in complex chemotaxis pathways. *Nature Reviews Microbiology*, *9*(3), 153–165. https://doi.org/10.1038/nrmicro2505

Sanfilippo, J. E., Lorestani, A., Koch, M. D., Bratton, B. P., Siryaporn, A., Stone, H. A., & Gitai, Z. (2019). Microfluidic-based transcriptomics reveal force-independent bacterial rheosensing. *Nature Microbiology*, *4*(8), 1274–1281. https://doi.org/10.1038/s41564-019-0455-0

Schuergers, N., Lenn, T., Kampmann, R., Meissner, M. V., Esteves, T., Temerinac-Ott, M., Korvink, J. G., Lowe, A. R., Mullineaux, C. W., & Wilde, A. (2016). Cyanobacteria use micro-optics to sense light direction. *eLife*, *5*(FEBRUARY2016), 1–16. https://doi.org/10.7554/eLife.12620

Schuergers, N., Mullineaux, C. W., & Wilde, A. (2017). Cyanobacteria in motion. *Current Opinion in Plant Biology*, *37*, 109–115. https://doi.org/10.1016/j.pbi.2017.03.018

Son, K., Guasto, J. S., & Stocker, R. (2013). Bacteria can exploit a flagellar buckling instability to change direction. *Nature Physics*, *9*(8), Article 8. https://doi.org/10.1038/nphys2676

Stock, A. M., Robinson, V. L., & Goudreau, P. N. (2000). Two-Component Signal Transduction. *Annual Review of Biochemistry*, *69*(1), Article 1. https://doi.org/10.1146/annurev.biochem.69.1.183

Sunyer, R., Conte, V., Escribano, J., Elosegui-Artola, A., Labernadie, A., Valon, L., Navajas, D., García-Aznar, J. M., Muñoz, J. J., Roca-Cusachs, P., & Trepat, X. (2016). Collective cell durotaxis emerges from long-range intercellular force transmission. *Science*, *353*(6304), 1157–1161. https://doi.org/10.1126/science.aaf7119

Talà, L., Fineberg, A., Kukura, P., & Persat, A. (2019a). Pseudomonas aeruginosa orchestrates twitching motility by sequential control of type IV pili movements. *Nature Microbiology*, *4*(5), 774–780. https://doi.org/10.1038/s41564-019-0378-9

Talà, L., Fineberg, A., Kukura, P., & Persat, A. (2019b). Pseudomonas aeruginosa orchestrates twitching motility by sequential control of type IV pili movements. *Nature Microbiology*, *4*(5), Article 5. https://doi.org/10.1038/s41564-019-0378-9

Thévenaz, P., Ruttimann, U. E., & Unser, M. (1998). A pyramid approach to subpixel registration based on intensity. *IEEE Transactions on Image Processing: A Publication of the IEEE Signal Processing Society*, *7*(1), 27–41. https://doi.org/10.1109/83.650848

Thutupalli, S., Sun, M., Bunyak, F., Palaniappan, K., & Shaevitz, J. W. (2015). Directional reversals enable Myxococcus xanthus cells to produce collective one-dimensional streams during fruiting-body formation. *Journal of The Royal Society Interface*, *12*(109), Article 109. https://doi.org/10.1098/rsif.2015.0049

Van Haastert, P. J. M., & Devreotes, P. N. (2004). Chemotaxis: Signalling the way forward. *Nature Reviews Molecular Cell Biology*, *5*(8), Article 8. https://doi.org/10.1038/nrm1435

Whitchurch, C. B., Leech, A. J., Young, M. D., Kennedy, D., Sargent, J. L., Bertrand, J. J., Semmler, A. B. T., Mellick, A. S., Martin, P. R., Alm, R. A., Hobbs, M., Beatson, S. A., Huang, B., Nguyen, L., Commolli, J. C., Engel, J. N., Darzins, A., & Mattick, J. S. (2004). Characterization of a complex chemosensory signal transduction system which controls twitching motility in Pseudomonas aeruginosa. *Molecular Microbiology*, *52*(3), Article 3. https://doi.org/10.1111/j.1365-2958.2004.04026.x

FIGURE 2.1

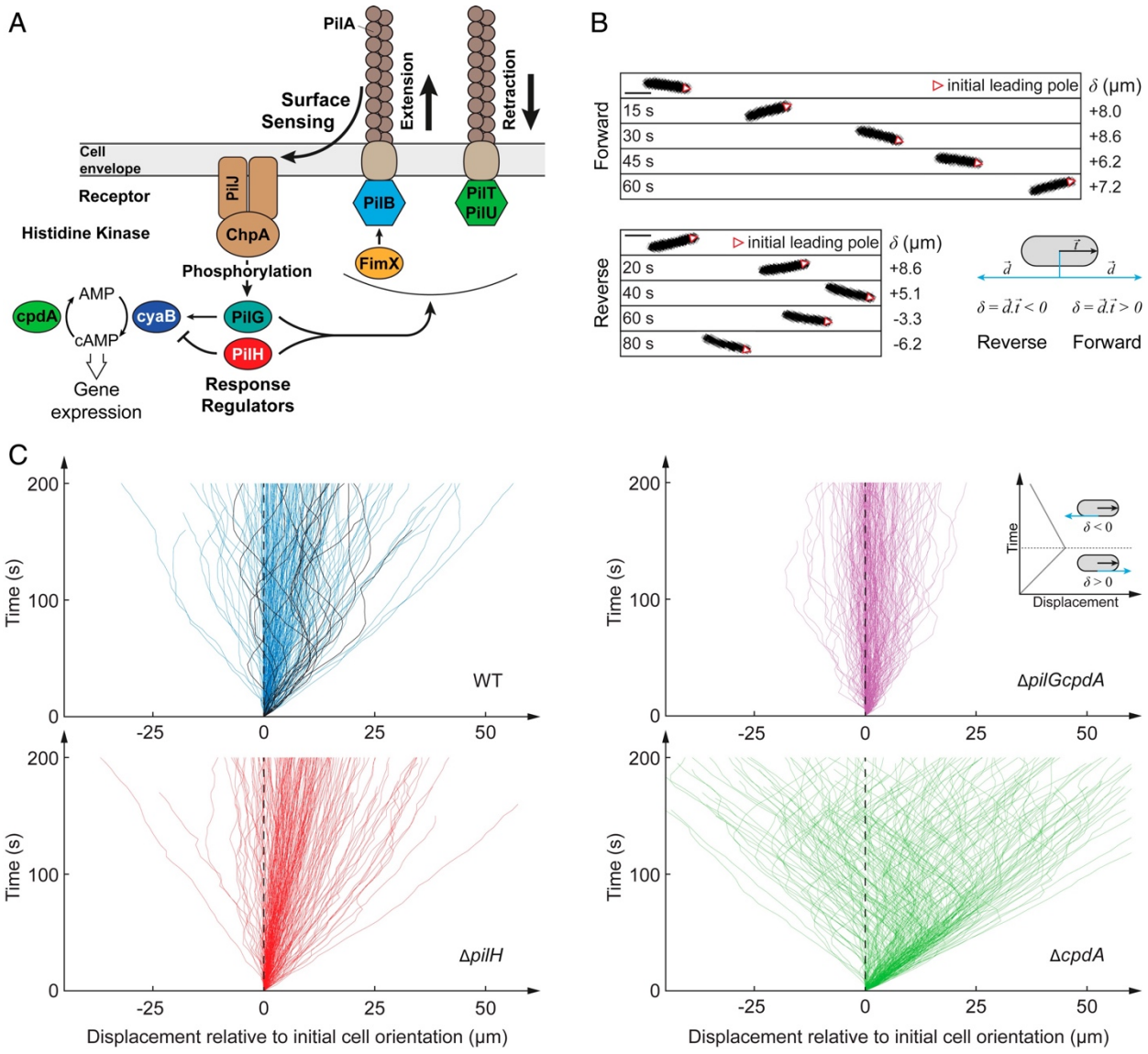

FIGURE 2.1. The Chp system regulates the twitching trajectories of individual *P. aeruginosa* cells.

(A) Schematic representation of the major components of the T4P and Chp system.

(B) Phase contrast snapshots of forward and reverse migration of twitching cells. $\vec{t}$ is a unit vector oriented along the cell body in the initial direction of motion. $\vec{d}$ is the unit displacement vector. δ is the dot product $\vec{d}.\vec{t}$, which quantifies displacements relative to the initial direction of motility. The red triangle indicates the initial leading pole of the bacterium. Scale bar, 2 μm. (Figure caption continued on the next page.)

(Figure caption continued from the previous page.) (C) Graphs of cumulative net displacement as a function of time, highlighting the forward and reverse twitching behavior of Chp mutants. Each curve corresponds to an individual cell trajectory. Tracks of reversing WT cells are highlighted in black. At any given time, a curve oriented toward the top right corresponds to a cell moving forward, while a curve oriented toward top left corresponds to reverse movement (*cf*. inset). Δ*pilGcpdA* constantly reverses twitching direction while Δ*pilH* cells persistently move forward.

FIGURE 2.2

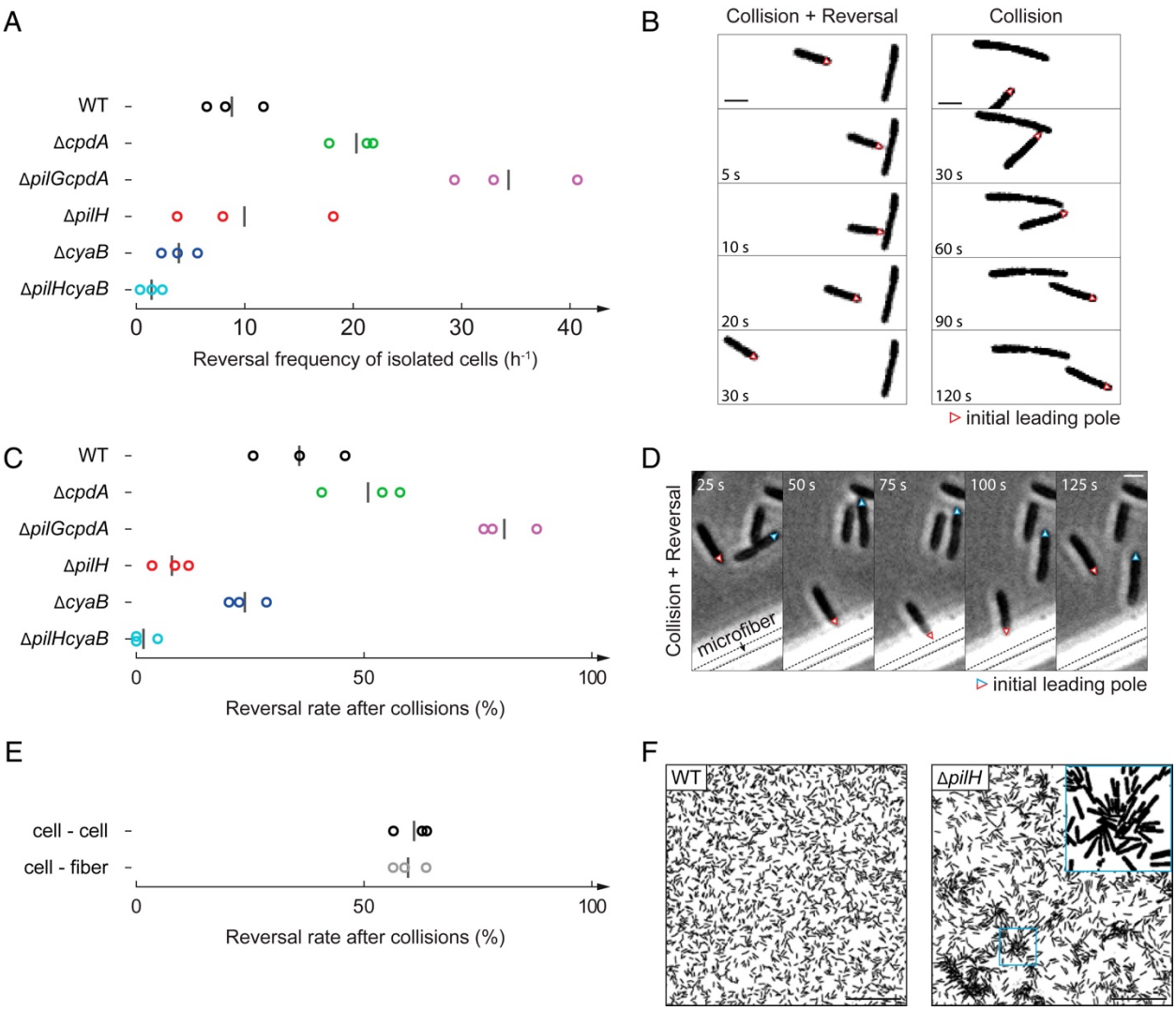

FIGURE 2.2. **The Chp system controls reversals of twitching *P. aeruginosa* cells.**

(A) Quantification of reversal rates in Chp and cAMP mutants. Δ*pilGcpdA* has highest reversal frequency. Δ*pilH* has a two-fold lower reversal frequency than Δ*cpdA*. Circles correspond to biological replicates, black bars represent their mean.

(B) Snapshots of WT reversing upon collision with another cell (left). The same sequence for a Δ*pilH* cell, failing to reverse upon collision (right). The red triangle indicates the initial leading pole of the bacterium. Scale bar, 2 μm.

(C) Fraction of cells reversing upon collision with another cell. About half of WT cells reverse after collision, Δ*pilH* almost never reserves after collision, and Δ*pilGcpdA* almost always reverses. Circles correspond to biological replicates, black bars represent their mean. (Figure caption continued on the next page.)

(Figure caption continued from the previous page.) (D) Phase contrast image sequence of WT cells reversing upon collision with glass microfibers and other cells. The dashed lines indicate the position of the fiber. Scale bar, 2 μm.

(E) Fraction of WT cells reversing upon collision with another cell and with a glass microfiber. 60% of cells reverse after collision irrespective of the type of obstacle. Circles correspond to biological replicates, black bars represent their mean.

(F) While WT is able to move efficiently at high density, the reduced ability of Δ*pilH* to reverse upon collision leads to cell jamming and clustering. Scale bar, 50 μm. Background strain: PAO1 Δ*fliC*.

FIGURE 2.3

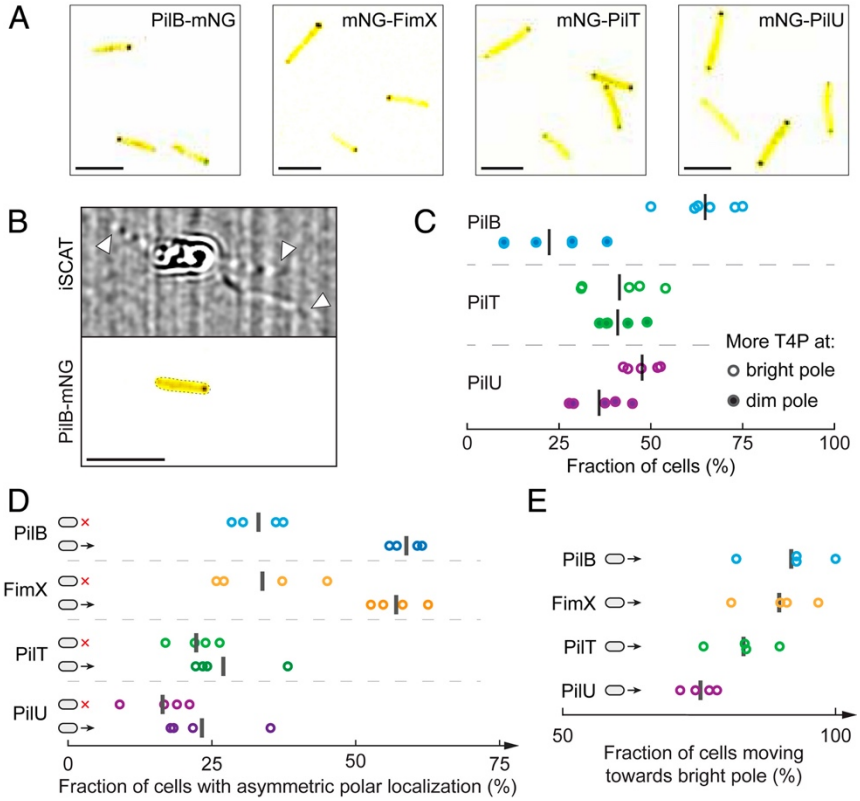

FIGURE 2.3. The localization of the extension motor PilB sets the direction of twitching and the polarization of T4P activity.

(A) Snapshot of chromosomal fluorescent protein fusions to the extension motor PilB, its regulator FimX, and the retraction motors PilT and PilU. Scale bars, 5 μm.

(B) Simultaneous imaging of PilB-mNG and T4P by correlative iSCAT fluorescence. White arrowheads indicate T4P. Scale bar, 5 μm.

(C) Fraction of cells with more T4P at bright *vs* dim fluorescent pole. Most cells have more T4P at the bright PilB-mNG pole. We could not distinguish a T4P depletion at the bright retraction motor poles. Each circle is the mean fraction for one biological replicate. Black bars correspond to their mean across replicates.

(D) Comparison of the symmetry of polar fluorescence between moving and non-moving cells. PilB and FimX signal is more asymmetric in moving cells, which is not the case for PilT and PilU.

(E) Fraction of cells twitching in the direction of their brightest pole. Circles correspond the fraction of each biological replicate, black bars represent their mean.

FIGURE 2.4

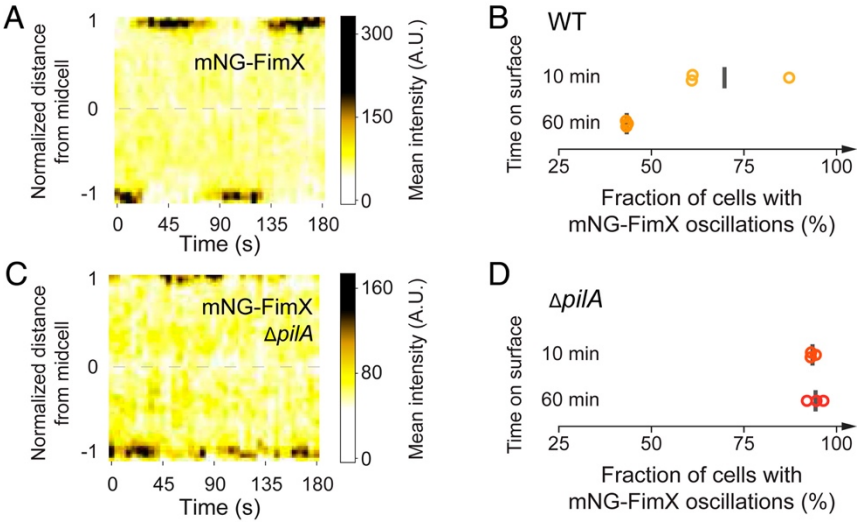

FIGURE 2.4. Mechanical input signal from T4P controls the polarization of FimX, the activator of the extension motor PilB.

(A) Kymograph of mNG-FimX fluorescence in a non-moving cell 10 min after surface contact. The bright fluorescent focus sequentially disappears from one pole to appear at the opposite to establish oscillations.

(B) Fraction of cells that showed pole to pole oscillations in WT and Δ*pilA*. The proportion of oscillating WT reduces as they remain on the surface, conversely increasing the proportion of stably polarized cells.

(C) Kymograph of mNG-FimX fluorescence in a Δ*pilA* background 60 min after surface contact. Scale bar, 5 μm.

(D) Most Δ*pilA* cells maintain oscillatory fluctuations in mNG-FimX polar localization.

FIGURE 2.5

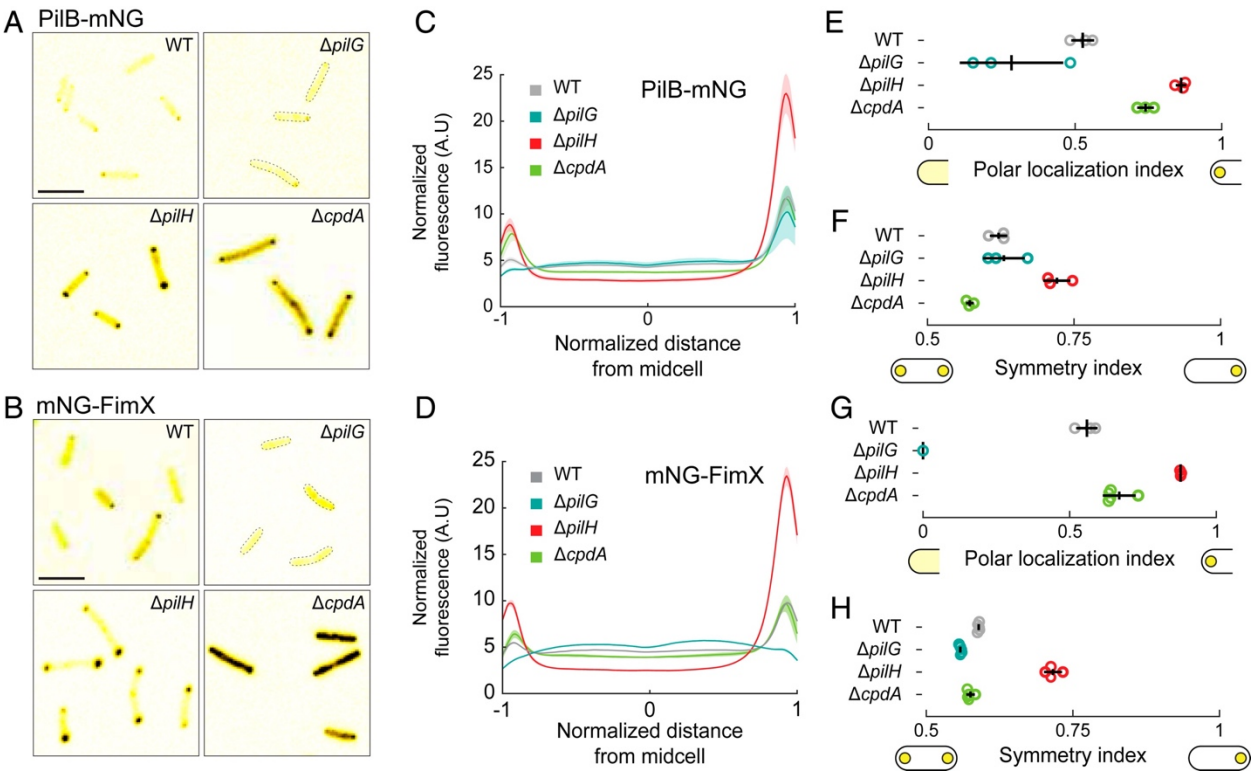

FIGURE 2.5. PilG and PilH control the polarization of T4P extension machinery.

Snapshots of PilB-mNG (A) and mNG-FimX (B) fluorescence in WT, Δ*pilG*, Δ*pilH* and Δ*cpdA* background. Scale bar, 5 μm.

(C, D) Normalized fluorescence profiles along the major cell axis of the motor protein PilB and its activator FimX (Figure S2.8A). Solid lines: mean normalized fluorescence profiles across biological replicates. Shaded area: standard deviation across biological replicates.

(E, G) Polar localization index of PilB-mNG and mNG-FimX respectively, quantifying the extent of polar signal compared to a diffused configuration (Figure S2.8B). An index of 0 and 1 respectively correspond to completely diffuse and polar signals. Relative to WT and Δ*cpdA*, polar localization is higher in Δ*pilH* and lower in in Δ*pilG*.

(F, H) Symmetry index of PilB-mNG and mNG-FimX respectively, representing the ratio of the brightest pole fluorescence to the total polar fluorescence. 0.5 and 1 respectively correspond to a symmetric bipolar and a unipolar localization. Δ*pilH* has higher symmetry index than WT and Δ*cpdA*. Circles: median of each biological replicate. Black bars: (vertical) mean and (horizontal) standard deviation across biological replicates.

FIGURE 2.6

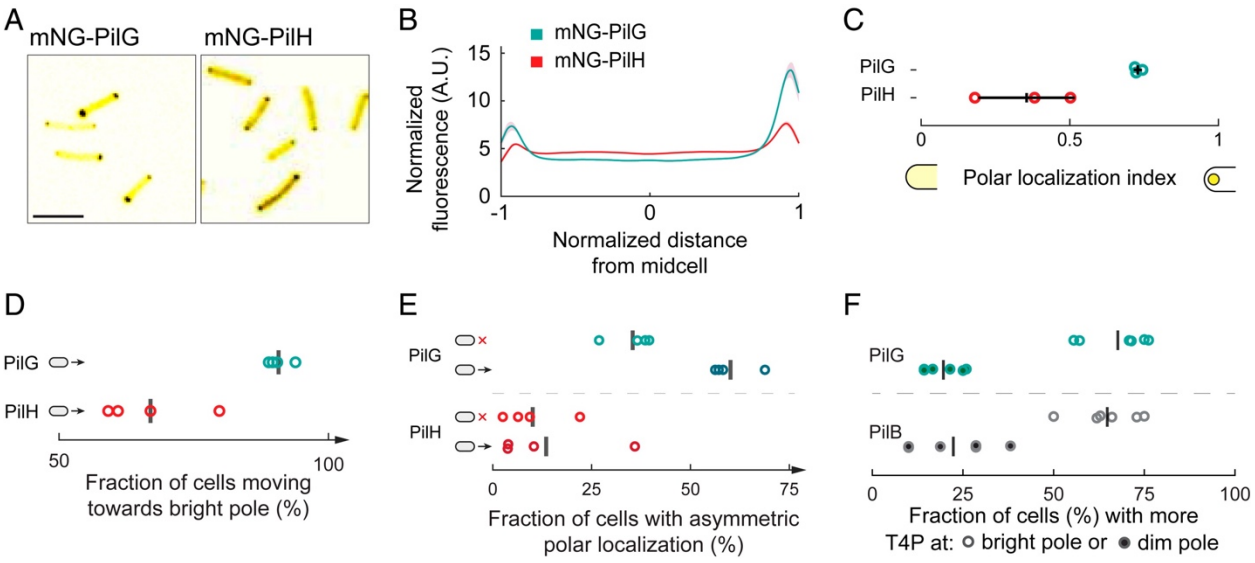

FIGURE 2.6. PilG and PilH dynamic localization establish a local-excitation, global-inhibition signaling landscape.

(A) Snapshots of mNG-PilG and mNG-PilH fluorescence. Scale bar, 5 μm.

(B) Comparison of mNG-PilG and mNG-PilH normalized mean fluorescent profiles.

(C) The polar localization index of mNG-PilG is relatively large showing PilG is mostly polar. In contrast, mNG-PilH has a low polar localization index and is thus mostly cytoplasmic. Circles: median of each biological replicate. Black bars: (vertical) mean and (horizontal) standard deviation across biological replicates.

(D) Protein polarization relative to the twitching direction. Cells predominantly move towards the brighter mNG-PilG pole. The fraction for mNG-PilH is close to 50 %, corresponding to a random polarization relative to the direction of motion. Black bars: mean across biological replicates.

(E) Comparison of the symmetry of the polar fluorescent foci of moving cells with non-moving cells for mNG-PilG and mNG-PilH fusion proteins. There is an enrichment for mNG-PilG polar asymmetry in moving cells, but no differences in mNG-PilH. Black bars: mean across biological replicates.

(F) Fraction of cells with more T4P at bright *vs* dim mNG-PilG fluorescent pole. Most cells have more T4P at the bright mNG-PilG pole, similar to PilB (data from Figure 2.3C in gray as reference). Each circle is the mean fraction for one biological replicate. Black bars correspond to their mean across replicates.

FIGURE S2.1

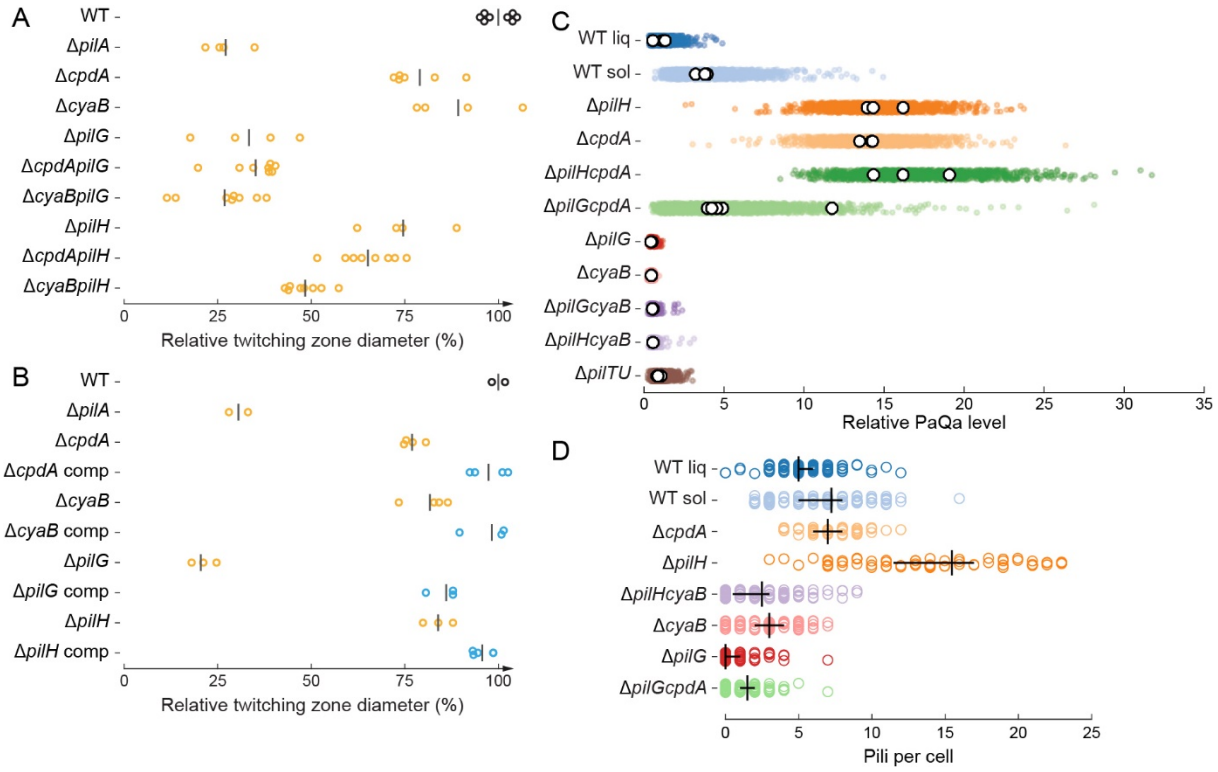

FIGURE S2.1. Quantification of twitching motility by the stab assay, cAMP levels and piliation of Chp mutants.

(A) Twitching motility as measured by the subsurface stab assay of marker-free in-frame deletions of selected Pil and Chp genes. The diameter of the zone for any given mutant is normalized by the mean twitching diameter of WT (background strain PAO1 Δ*fliC*). Each circle corresponds to a single colony. Black bars correspond to the mean of the replicates.

(B) Twitching zone diameters of the in-frame deletion mutants and their complemented versions. Yellow circles correspond to the in-frame deletions, blue circles correspond to the complemented mutants. Black bars correspond to the mean diameter of the replicates. Complementation of each of the in-frame deletion mutants restored the twitching zone diameter to WT levels (background strain PAO1).

(C) cAMP levels measured by PaQa-YFP reporter fluorescence. Colored circles represent single cells, white circles correspond to median of biological replicates. All levels are normalized by the mean fluorescence intensity of the liquid-grown WT across biological replicates. All strains except WT sol are grown in liquid culture.

(D) Quantification of T4P number in Chp and cAMP mutants by iSCAT. Each circle corresponds to the T4P number of an individual cell. Black vertical bars correspond to the

(Figure caption continued on the next page.)

(Figure caption continued from the previous page.) boostrap mean of biological replicates, horizontal bars to their bootstrap 95 % confidence interval. All strains except WT sol are grown in liquid culture.

FIGURE S2.2

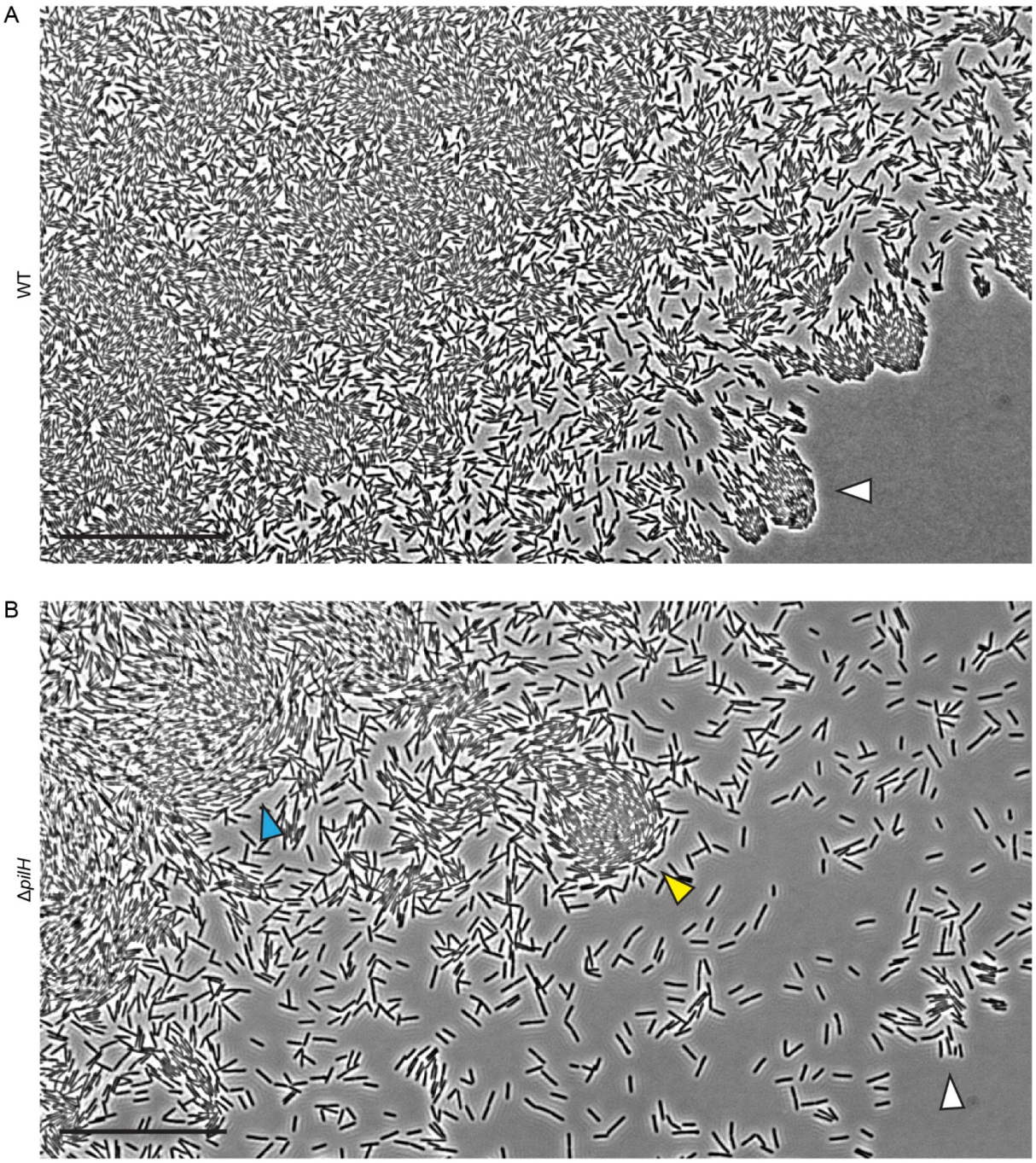

FIGURE S2.2. Colony edge expansion of twitching WT and Δ*pilH* cells.

Both leading edges expand toward the lower right.

(A) WT cells spread evenly and form persistent rafts (white triangle) at the leading edge.
(Figure caption continued on the next page.)

(Figure caption continued from the previous page.) (B) Δ*pilH* cells form transient comet-shaped rafts (yellow triangle) and swirls (blue triangle) due to their inability to reverse. At the leading edge, rafts don't persist (white triangle), resulting in slower expansion at the macroscopic scale (*cf*. Figure S2.1). In conditions that only allow cells to move in groups, donut-shaped swirls have been reported for Δ*pilH*, that likely arise from the inability to reverse as well (Darzins, 1994b). Scale bar, 50 μm. Images correspond to Movie S6.

FIGURE S2.3

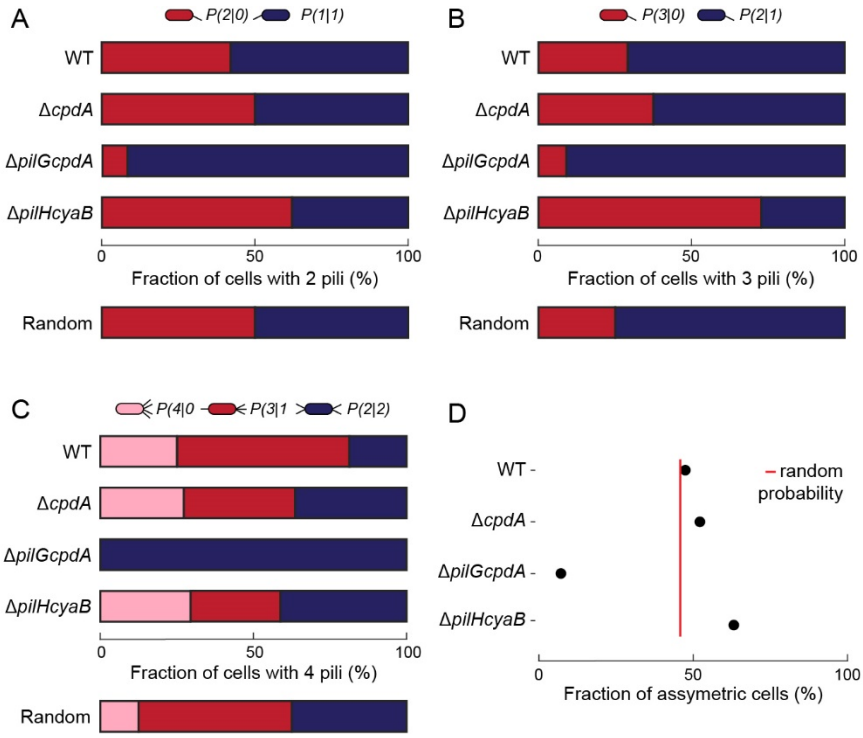

FIGURE S2.3. Chp controls T4P polar distribution in single cells.

We imaged single cells using iSCAT to quantify T4P at each pole. For cells that had two (A), three (B) and four (C) T4P, we calculated the percentage of any given T4P distribution. P(*n*/*m*) corresponds to the fraction of cells that have *n* T4P at one pole and *m* T4P at the opposite pole. For each T4P number, red corresponds to the most asymmetric distribution and blue to the most symmetric as illustrated above the graphs. As a reference, we computed the expected fractions if T4P were to be distributed randomly (shown below the mutants). WT and Δ*cpdA* T4P distributions are close to random. However, the distributions tend to shift toward complete symmetry in Δ*pilGcpdA* and complete asymmetry for Δ*pilHcyaB* and are independent of cAMP levels as these mutants have similar levels.

(D) Cumulative fraction of the population with assymetric pili distribution in cells with two, three and four pili. Δ*pilG* mostly have symmetric T4P distribution whereas Δ*pilH* tend to polarize T4P to one pole. All cells are liquid-grown.

FIGURE S2.4

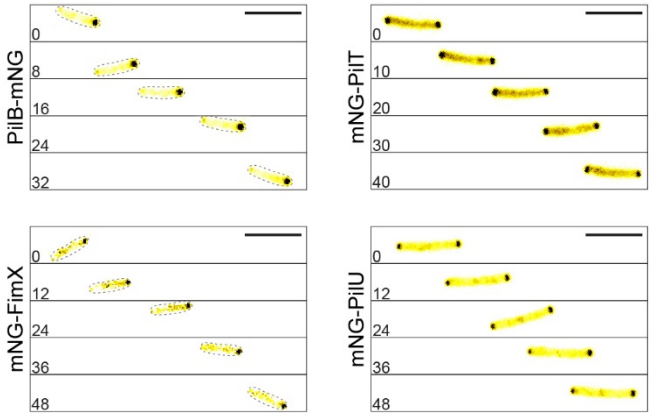

FIGURE S2.4. **Timeseries of snapshots of fluorescent fusion proteins in single cells twitching forward.**

PilB and FimX localize more prominently to the leading pole, while PilT and PilU tend to localize more symmerically to both poles. Images correspond to Movie S7. Scale bar, 5 μm.

FIGURE S2.5

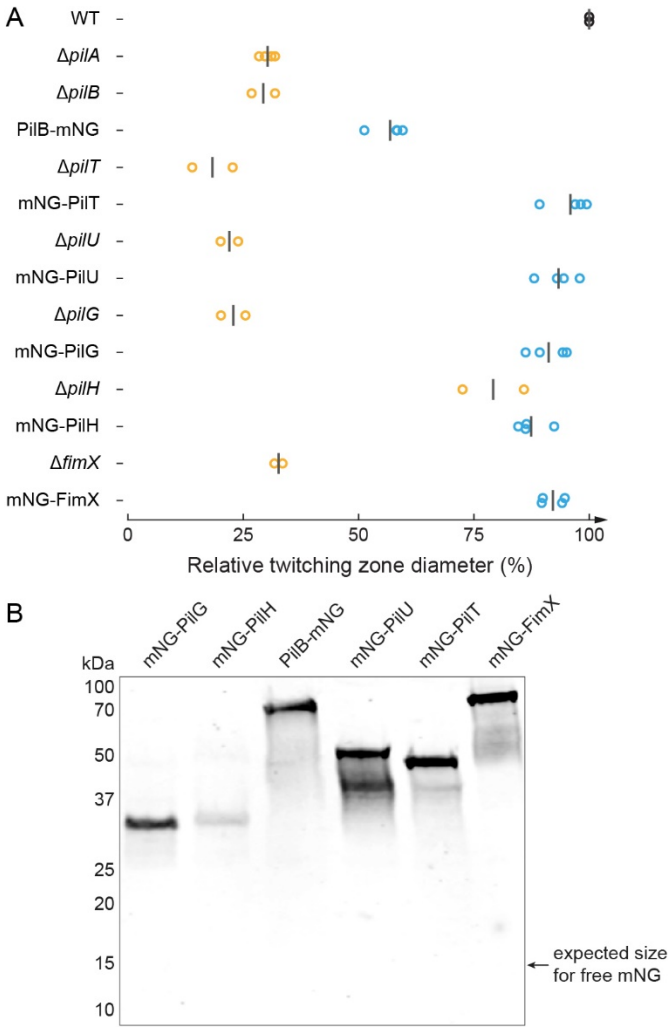

FIGURE S2.5. Functional characterization of fluorescent protein fusions to T4P motors and response regulators.

(A) Twitching diameters (relative to WT) as measured by the subsurface stab assay. Yellow circles correspond to in-frame deletions, blue circles correspond to chromosomally localized fluorescent fusions, black bars correspond to the mean of diameter of twitching zones.

(B) Western blot of all mNG fluorescent fusions used in this study to verify expression levels and production of full-length protein fusion. Free mNG was not detected.

FIGURE S2.6

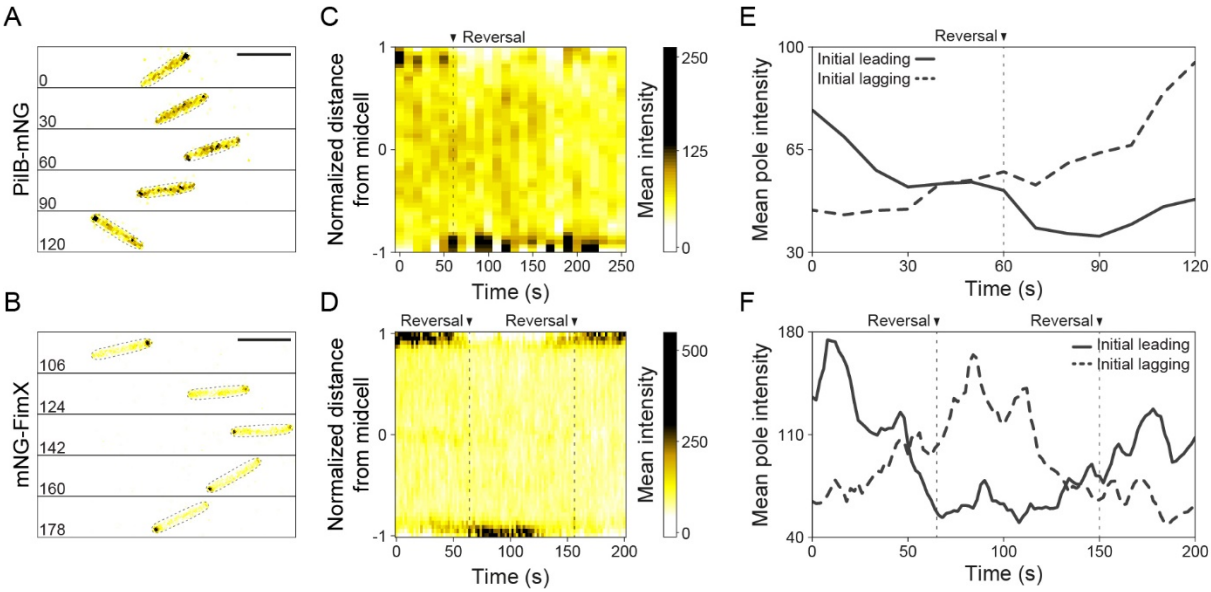

FIGURE S2.6. PilB-mNG and mNG-FimX switch polarization toward the new leading pole during twitching reversals.

Snapshots of fluorescence image sequences of reversing PilB-mNG (A) and mNG-FimX (B) cells (corresponding to Movie S2.8).

(C and D) Corresponding kymographs during reversal showing relocalization of the fluorescent fusion proteins.

(E and F) Fluorescent intensity traces of the leading and lagging poles during the visualization. The dynamic localization behaviour of FimX during reversals is qualitatively similar to the one described previously (Jain, Sliusarenko, Kazmierczak, et al., 2017). Scale bar, 5 μm.

FIGURE S2.7

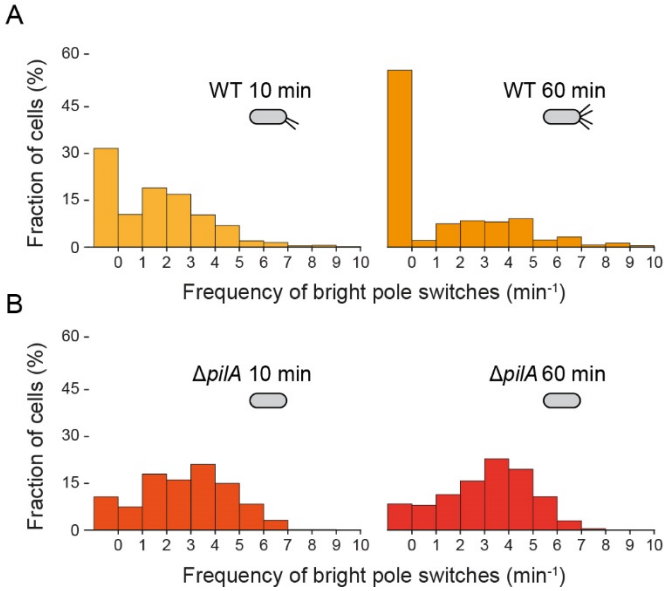

FIGURE S2.7. Frequency distributions of mNG-FimX oscillations upon surface contact is T4P-dependent.

(A) Distributions of bright foci mean switching frequency in WT 10 min (left) and 60 min (right) after surface contact. Right after surface contact, 70% of the population shows pole-to-pole mNG-FimX switches, which goes down to 50% after 1 h on the surface.

(B) Distributions of bright focus spot switching frequency in Δ*pilA*. Most cells show pole-to-pole switches. There is no change in the distribution of switching frequencies between cell populations that have been in contact with the surface for 10 min and 60 min.

FIGURE S2.8

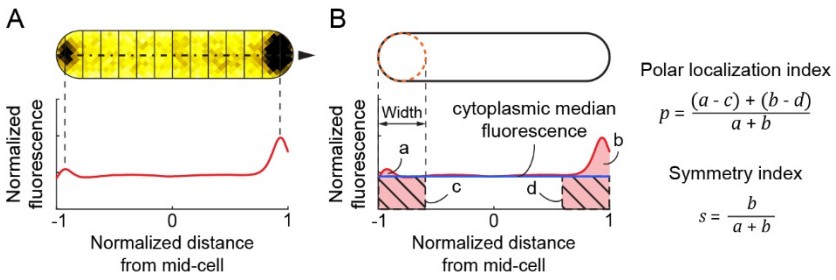

FIGURE S2.8. **Computation of fluorescent profile, polar localization and symmetry incides.**

(A) Fluorescence profiles were computed with BacStalk by taking the cross-sectional mean pixel value along the cell (dashed line). To correct the profile for differences in expression levels between cells, each was normalized by the total fluorescence intensity of the cell, represented by the area under the red curve. The cell length was also normalized so that the poles are located at -1 and 1 *x*-coordinates.

(B) Computation of the polar localization and the symmetry indices. The pole areas (pink areas a and b) were defined by the width of the cell. The hatched areas c and d correspond to the pole areas if the protein-fusion was diffused with fluorescence levels identical to the cytoplasmic median fluorescence of the profile (blue line). To extract the polar localization index for each cell, we subtracted the diffused total fluorescence (c and d) to the actual pole total fluorescence (a and b) and divided this value by the total fluorescence at the poles (a + b). The symetry index for each cell was computed as the total fluorescence of the brightest pole b divided by the sum of the total fluorescence of the two poles a + b.

FIGURE S2.9

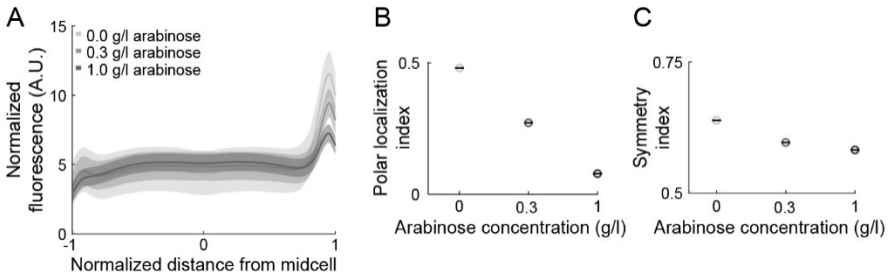

FIGURE S2.9. PilB-mNG polar localization and polarization as a function of expression level.

We induced the expression of PilB-mNG on a low-copy plasmid with arabinose in a Δ*pilB* background.

(A) Mean profiles (solid lines) and standard deviation (grey areas) of a population of liquid grown cells in which PilB-mNG was induced for 3 h at three different arabinose concentrations. When normalized, the profiles flatten with increasing inducer concentration. We attribute this to the accumulation of the motor protein in the cytoplasm after T4P machineries are saturated at the poles.

(B and C) As a result, the polar localization and symmetry indices of PilB-mNG decrease with increased concentration of inducer.

FIGURE S2.10

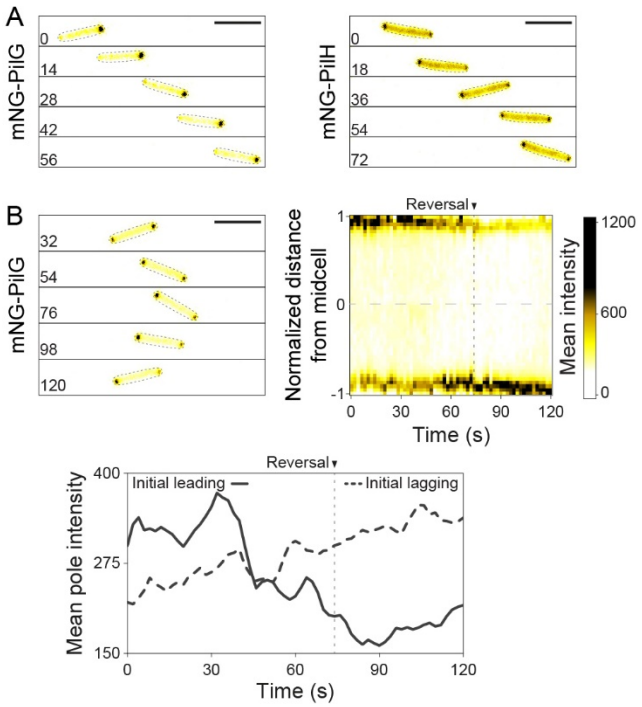

FIGURE S2.10. mNG-PilG and mNG-PilH localization during twitching and reversals.

(A) Snapshots of mNG-PilG and mNG-PilH fluorescent fusions in isolated twitching cells. PilG tends to localize more prominently to the leading pole, while PilH predominantly localizes to the cytoplasm and can be enriched at both poles without marked polarization. Snapshots taken from Movie S2.11.

(B) Snapshots of a fluorescence image sequence of a reversing cell expressing mNG-PilG at its native locus (taken from Movie S2.12), and corresponding kymograph and fluorescent intensity traces.

FIGURE S2.11

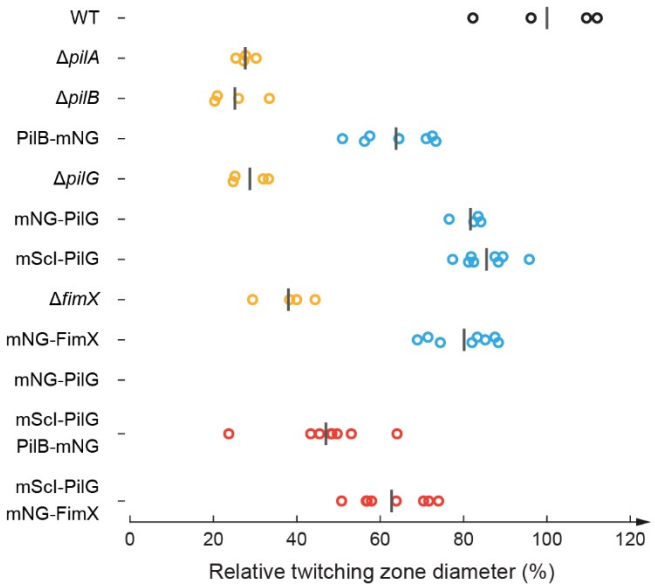

FIGURE S2.11. Functional characterization of double-tagged fluorescent protein fusion strains.

Twitching diameters (relative to WT) as measured by the subsurface stab assay. Yellow circles correspond to in-frame deletions, blue circles correspond to chromosomally localized fluorescent fusions, red circles represent the double-tagged strains, black bars correspond to the mean diameter of twitching zones.

FIGURE S2.12

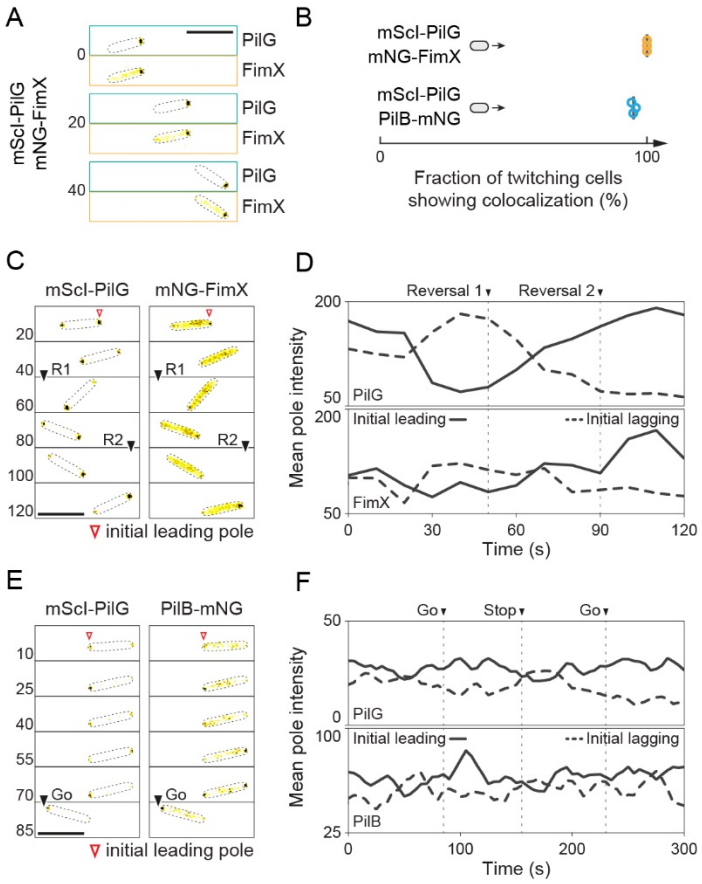

FIGURE S2.12. PilG colocalizes both with FimX and PilB in smooth twitching and reversing cells.

(A) Snapshots of a fluorescence image sequence of a smooth twitching mScI-PilG + mNG-FimX double tagged cell.

(B) Fraction of smooth twitching cells showing colocalization of PilG with FimX and PilB at the leading pole. The brighter signal was always located at the leading pole, except for the small fraction of mScI-PilG + PilB-mNG cells showing no colocalization, in which the PilB-mNG signal was located at the lagging pole. Circles correspond to the fraction of each biological replicate, black bars represent their mean.

(C and E) Snapshots of fluorescence image sequences of a reversing mScI-PilG + mNG-FimX cell (C) and a mScI-PilG + PilB-mNG cell twitching with intermittent stops (E).

(D and F) Corresponding fluorescent intensity traces showing relocalization of both fluorescent fusion proteins at the same time. A three-point moving average was applied to the fluorescent intensities in panel F. Scale bar, 5 μm.

FIGURE S2.13

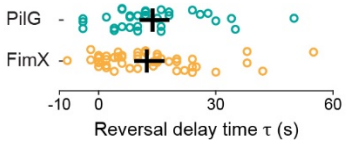

FIGURE S2.13. The delay between protein polarity switch and twitching reversal is indistinguishable between mNG-PilG and mNG-FimX.

The reversal delay time τ is the time between the last crossover of the fluorescent intensity traces of both poles (similar to Figure S2.6E,F or Figure S2.10B) before the reversal and the time point of the reversal. τ was determined in single tagged fluorescent strains.

FIGURE S2.14

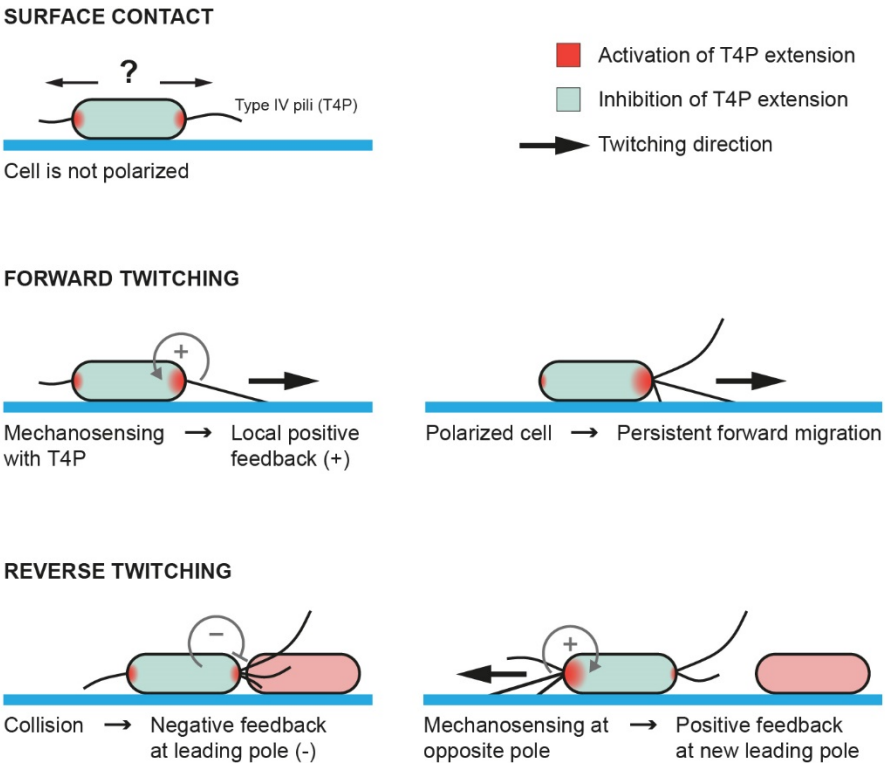

FIGURE S2.14. Mechanotaxis model.

After initial contact a cell explores its surrounding with random T4P distribution at both poles. Upon T4P tip attachment, Chp mechanosensing induces a positive feedback on T4P motors to favor extension at the same pole leading to polarization of the cell and persistent forward motion. After collision (or loss of T4P attachment/retraction) at the leading pole, a negative feedback down regulates T4P activity. T4P at the opposite pole can then attach and generate a positive feedback that reverses cell polarization and lead to persistent reverse twitching.

FIGURE S2.15

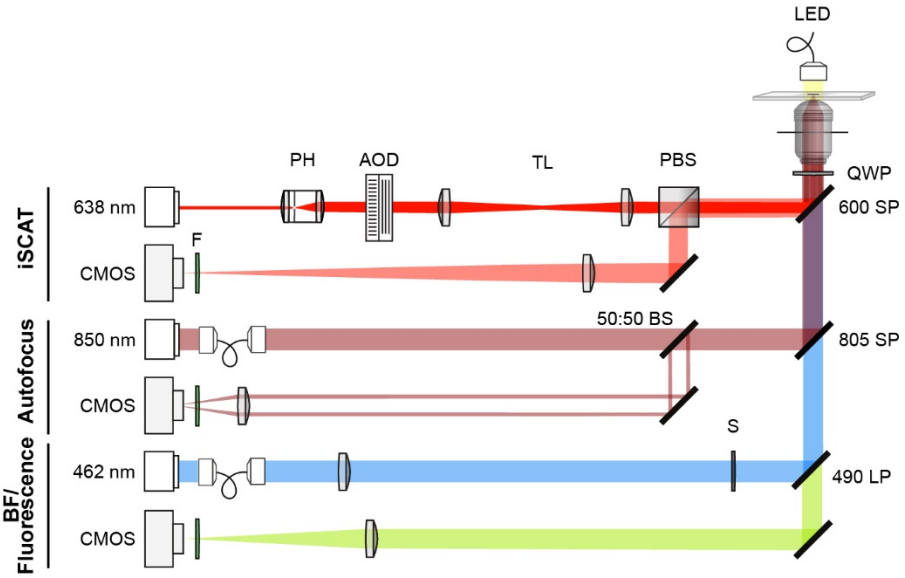

FIGURE S2.15. Optical layout of the correlative iSCAT fluorescence setup.

The setup is a modified version of the one described in (Talà et al., 2019b) in which we added a fluorescent channel. Briefly, the fluorescence channel consists in a 462 nm blue laser spatially filtered by an optical fiber and focused to the back focal plane of the objective with a 500 mm lens and a 490 nm long pass dichroic mirror. A shutter (S) allows clipping of the beam to reduce light exposure. The fluorescent signal emitted by the sample is directed to a CMOS camera with a 400 mm imaging lens. Appropriate filters (F) were used to prevent unwanted signal reaching the detectors (iSCAT: 635 band pass (BP), Bright field/fluorescence: 525 BP, Autofocus: 850 BP).

ADDITIONAL SUPPLEMENTAL MATERIAL

Table S2.1 to S2.4, Legends for Movie S2.1 to Movie S2.12, and Movie S2.1 to Movie S2.12. can be found in the full supplemental material found at:

https://doi.org/10.1073/pnas.2101759118

ahttps://www.pnas.org/doi/full/10.1073/pnas.2101759118#supplementary-materials

CHAPTER THREE

TWO ANTAGONISTIC RESPONSE REGULATORS CONTROL PSEUDOMONAS AERUGINOSA POLARIZATION DURING MECHANOTAXIS

SUMMARY

The opportunistic pathogen *Pseudomonas aeruginosa* adapts to solid surfaces to enhance virulence and infect its host. Type IV pili (TFP), long and thin filaments that power surface-specific twitching motility, allow single cells to mechanosense surfaces. Cells use T4P mediated-mechanosensing to control the direction of twitching motility. In this process, they establish a local positive feedback that polarizes TFP distribution to the sensing pole. A complex chemotaxis-like system called Chp mediates this response. The signalling mechanism allowing for transduction of this spatially-resolved signal is however incompletely understood. Here we demonstrate that the two Chp response regulators PilG and PilH enable dynamic cell polarization by coupling their antagonistic functions on TFP extension. By precisely quantifying the localization of fluorescent protein fusions, we show that phosphorylation of PilG by the histidine kinase ChpA controls PilG polarization. Although PilH is not inherently required for twitching reversals, upon phosphorylation, PilH becomes activated and breaks the local positive feedback established by PilG so that forward-twitching cells can reverse. To spatially resolve mechanical signals, Chp thus locally transduces signals with a main output response regulator, PilG. To respond to signal changes, Chp uses its second regulator PilH to break the local feedback. By identifying the molecular functions of two response regulators that dynamically control cell polarization, our work provides a rationale for the diversity of architectures often found in non-canonical chemotaxis systems.

INTRODUCTION

Bacteria use mechanosensing to rapidly adapt to life on surfaces (Dufrêne & Persat, 2020b; Persat, Nadell, et al., 2015). Mechanosensory systems regulate virulence, adhesion, biofilm formation and surface-specific motility (Laventie et al., 2019; O'Toole & Wong, 2016; Siryaporn et al., 2014; Wolfgang et al., 2003a). The opportunistic pathogen *Pseudomonas aeruginosa* senses surfaces using extracellular filaments called type IV pili (TFP) (Koch et al., 2022a; Persat, Inclan, et al., 2015b). *P. aeruginosa* responds to TFP-mediated mechanosensing on two timescales. Mechanosensing controls the direction of surface-specific twitching motility within seconds in a process called mechanotaxis (Kühn et al., 2021a). It also regulates the transcription of a series of genes responsible for acute virulence and surface adaptation through the production of the second messenger cyclic adenosine monophosphate (cAMP) over minutes to hours (Bertrand et al., 2010b; Fulcher et al., 2010c; Persat, Inclan, et al., 2015b; Wolfgang et al., 2003a).

To power surface-specific twitching motility, TFP successively extend, attach and retract, thereby pulling a cell forward (Burrows, 2012b; Merz et al., 2000b). During twitching, individual *P. aeruginosa* cells can move forward persistently and reverse spontaneously or upon collision (Kühn et al., 2021a). To twitch forward, *P. aeruginosa* localizes the TFP extension motor PilB to the cell pole facing the direction of motion. We refer to this asymmetric protein and T4P localization as polarization.

During mechanotaxis, TFP generate mechanical signal input, possibly upon surface attachment or during extension/retraction. A chemotaxis-like system called Chp relays

TFP signals to cellular components that ultimately control twitching and cAMP levels (Darzins, 1994c; Whitchurch et al., 2004c). One output response is the deployment of additional TFP which thereby establishes a positive feedback loop. In response to signal input at one pole, Chp controls the distribution of TFP extension proteins to assemble TFP at that same pole. As a result of this polarized T4P deployment, single cells twitch persistently forward (Kühn et al., 2021a). To change twitching direction spontaneously or upon collision, cells reverse polarization (**Movie S3.1**). To enforce the connection between TFP input and TFP polarization output, Chp employs two response regulators PilG and PilH that establish a local excitation - global inhibition signaling landscape (Kühn et al., 2021a). This signaling architecture is shared with higher order organisms: neutrophils, amoebae and yeast polarize via local excitation global inhibition during chemotaxis or cell division (Levchenko & Iglesias, 2002b).

While the sensory system controlling flagellar rotation in *Escherichia coli*, the Che system, serves as a model chemotaxis system to understand more complex ones, it is more of an exception than the norm. Bacteria possess a wide diversity of chemotaxis systems with different inputs, outputs and overarching signaling mechanisms. Our knowledge of the dynamic control of these diverse chemotaxis-like systems is however limited. Chp shows important functional and structural differences with the canonical Che sensory system despite strong homology (Bi & Sourjik, 2018b). First, Chp responds to a mechanical signal input from TFP. Second, the Chp complex has more components than Che. CheA, the histidine kinases of the Che system, phosphorylates a single response regulator to relay input signals to its functional target. The histidine kinase ChpA comprises six

phosphotransfer domains against just one for CheA (Whitchurch et al., 2004c). In addition, Chp possesses not one but two response regulators, PilG and PilH, with opposing functions in mechanotaxis and cAMP-dependent transcription (Bertrand et al., 2010b; Darzins, 1994c; Fulcher et al., 2010c; Kühn et al., 2021a). PilG promotes persistent forward twitching and cAMP production while PilH promotes reversals and reduces cAMP levels. However, how ChpA activates PilG and PilH to control cell polarization upon mechanosensing remains unresolved.

To guide twitching direction, TFP bind to the substrate and activate the Chp system, possibly through the interaction of the major pilin PilA and the Chp system receptor PilJ (Persat, Inclan, et al., 2015b). As a result, PilJ stimulates ChpA autophosphorylation. ChpA then activates PilG and PilH presumably by direct interaction and phosphotransfer (Silversmith et al., 2016a). PilG and PilH activate their targets, which ultimately mediate polarization of the extension motor PilB and its activator FimX (Kühn et al., 2021a), although direct interactions have yet to be rigorously identified (Jain, Sliusarenko, & Kazmierczak, 2017). PilG promotes recruitment of both PilB and FimX at the pole, while PilH inhibits it (Kühn et al., 2021a). As a consequence, TFP extend preferentially at that same pole, resulting in persistent forward twitching. Without a counterpart to PilG, i.e. in *pilH* deletion mutants, cells continue twitching in one direction without reversing (Kühn et al., 2021a).

Despite homologies and analogies with other well-studied chemotaxis systems, how antagonistic response regulators establish a stable, yet dynamic signaling landscape

remains unknown. In particular, how PilG and PilH help transduce mechanical signal input into cell polarization output that dynamically controls the direction of *P. aeruginosa* twitching is unresolved. Here, we investigate how phosphorylation by ChpA activates PilG and PilH to regulate cell polarity in response to mechanical signal input. We combined bacterial genetics with microscopy to determine the subcellular localizations and polarization of the two response regulators in their different active and inactive states. We suggest a model in which one regulator acts as primary signal relay while the other regulator only modulates the function of the first one.

RESULTS

PilG and PilH localization during surface adaptation.

To investigate how Chp activates response regulators upon surface contact, we monitored localization of functional mNeonGreen-tagged PilG and PilH as cells transition from liquid to a surface. Immediately after surface contact which reflects the state of planktonic cells that have yet to mechanosense, mNG-PilG predominantly localizes to the poles while mNG-PilH is mostly cytoplasmic (**Figure 3.1A**). Only a few cells display relatively dim PilH polar foci (**Figure S3.1A**). PilG displays pronounced asymmetrical localization, *i.e.* PilG is polarized (**Figure 3.1AB**). We quantified subcellular localization profiles of hundreds to thousands of cells in each condition from which we generate population-averaged fluorescent profiles (**Figure 3.1CF**). With these, we derive a polar localization index measuring the ratio of polar *vs* cytoplasmic localization. We found that PilG polar localization is largely insensitive to time on the surface (**Figure 3.1CD**). To quantify protein polarization (cf. **Figure 3.1B**), we defined an asymmetry index quantifying the intensity difference between the two polar spots. PilG is markedly and stably polarized, as the asymmetry index remains unchanged for 2 h on a surface (**Figure 3.1E**).

Unlike PilG, PilH is almost exclusively found in the cytoplasm early after surface contact but becomes increasingly localized to the poles after 1 and 2h of surface contact (**Figure 3.1FG**). While PilH polar localization is always lower compared to PilG, its localization index increases over time on surface (**Figure 3.1G**). PilH asymmetry index is steadily close to 0.5, *i.e.* nearly symmetric, showing PilH does not polarize (**Figure 3.1H**). In summary, PilG remains strongly polarized, only switching polarization during reversals

(Kühn et al., 2021a). PilH is largely cytoplasmic, but polar localization increases over time on surfaces without polarizing. Sustained PilG and PilH phosphorylation by ChpA during surface growth could potentially explain these changes in localization. We thus went on to identify the function of ChpA in polar localization of the two response regulators.

ChpA induces PilG polarization through phosphorylation.

PilG preferentially localizes to the leading pole of twitching cells where T4P actively extend and retract (Kühn et al., 2021a). We therefore hypothesize that in response to mechanosensing with T4P, the histidine kinase ChpA polarizes PilG by phosphorylation. To characterize the role of phosphorylation in PilG polarization, we compared the localization of mNG-PilG between a *chpA* deletion mutant and wild type (WT). In Δ*chpA*, PilG polar localization decreases but is not entirely abolished (**Figure 3.2AB**). The asymmetry index is also lower in Δ*chpA* compared to WT, showing ChpA promotes PilG polarization (**Figure 3.2C**). This is consistent with a model where ChpA promotes PilG polarization towards the leading pole in response to TFP input (Kühn et al., 2021a).

To rigorously demonstrate that phosphorylation promotes PilG polarization, we interfered with the ability of ChpA to signal to response regulators. Substituting three residues in the histidine kinase domain (D2086A, D2087A, G2088A) blocks autophosphorylation, resulting in a loss-of-function (LOF) mutant $chpA_{LOF}$ that is unable to transfer phosphate to PilG and PilH (Bertrand et al., 2010b; Silversmith et al., 2016a) but still localizes to the poles (**Figure S3.3AB**). Like Δ*chpA*, $chpA_{LOF}$ mutants neither twitch nor increase intracellular cAMP levels on surfaces (**Figure S3.4B**) (Bertrand et al., 2010b). PilG polar

localization and asymmetry indexes are much lower in *chpA*$_{LOF}$ compared to WT (**Figure 3.2BC**), showing that ChpA promotes PilG polarization by phosphorylation. ChpA$_{LOF}$ may also weakly bind PilG independent of phosphorylation as PilG polar localization is slightly higher in *chpA*$_{LOF}$ compared to Δ*chpA* (**Figure 3.2B**). We assessed whether *chpA* mutations could affect PilG localization due to cAMP-dependent transcriptional changes. We quantified the localization and polarization of mNG-PilG at low and high cAMP levels by respective deletion of the adenylate cyclase gene *cyaB* and phosphodiesterase gene *cpdA*. PilG localization was largely insensitive of cAMP levels (**Figure S3.5**). Our results therefore support a model in which TFP mechanosensing events at the leading pole stimulate ChpA to phosphorylate PilG to induce polarization.

PilG localization decreases but is not abolished in Δ*chpA* mutants, suggesting there exists an additional polar binding partner. We hypothesized that FimL, a protein that interacts with the polar hub FimV and PilG, could fulfil that role (Inclan, Persat, Greninger, Dollen, et al., 2016b). To characterize the impact of FimL on PilG polar localization, we imaged mNG-PilG in a *fimL* deletion mutant. Polar localization and asymmetry of PilG decreased in Δ*fimL* compared to WT (**Figure 3.2EF**). PilG polar localization was entirely abolished in a Δ*fimL* Δ*chpA* double deletion background (**Figure 3.2E**) showing that FimL and ChpA simultaneously recruit PilG to the poles. As in WT, loss-of-function mutation of *chpA* in Δ*fimL* background reduces PilG polar localization (**Figure S3.6AB**). However, the asymmetry index is not affected by this mutation (**Figure S3.6C**). This indicates that FimL and ChpA must act together for correct PilG polarization.

Taken together, our results specify the molecular mechanisms driving PilG polar localization and polarization. Both FimL and ChpA are required for proper polarization of PilG. FimL maintains at least non-phosphorylated PilG at the poles (Inclan, Persat, Greninger, Dollen, et al., 2016b). ChpA recruits PilG to transfer phosphate, thereby polarizing PilG and driving forward twitching (Kühn et al., 2021a).

To verify the role of phosphorylation in PilG function and localization directly, we attempted to generate a gain-of-function mutant that mimics the phosphorylated conformation of PilG by substituting the catalytic aspartate 58 to glutamate (*pilG*$_{D58E}$). We also generated an aspartate to alanine mutant yielding the loss-of-function mutant *pilG*$_{D58A}$. We assume PilG$_{D58A}$ adopts the non-phosphorylated conformation. We quantified their localization in WT (**Figure S3.7**), Δ*fimL* and *ΔchpA*. PilG$_{D58E}$ as well as PilG$_{D58A}$ are recruited to the poles by both FimL and ChpA similar to wild-type PilG (**Figure S3.8A-D**). Both mutants, however phenocopied Δ*pilG* in cAMP levels and twitching motility (**Figure S3.9**), indicating both mutants have lost function (we therefore refer to the amino acid substitutions for *pilG*, instead of $_{GOF}$ and $_{LOF}$). These observations are inconsistent with the predicted mutational effects of *pilG*$_{D58E}$. We thus failed to obtain the desired gain-of-function mutant by this method, whose limitations are however well-documented (Guzzo et al., 2018b; Smith et al., 2004). Our results suggest that PilG$_{D58E}$ may have lost functionality due to a defective interaction with downstream targets or that phosphate transfer to and from PilG may be important.

Polar recruitment of PilH depends on ChpA but not on its kinase activity.

By analogy with PilG, phosphorylation by ChpA could explain the slow increase in PilH polar localization during surface association (**Figure 3.1G**). To test this possibility, we quantified mNG-PilH localization in Δ*chpA* and $chpA_{LOF}$. We first controlled potential indirect effects of cAMP. In a Δ*cyaB* background with low cAMP, PilH polar localization was reduced compared to WT (**Figure S3.10C**). Conversely, polar localization was stronger in Δ*cpdA* with high cAMP levels. The difference in polar localization between WT and Δ*cpdA* levelled out after 2h of surface contact, as both polar localization indexes became indistinguishable (**Figure S3.10C**). PilH localization is therefore sensitive to cAMP levels. To characterize the additional role of ChpA in PilH localization independently of cAMP, we performed all subsequent mNG-PilH localization experiments in a Δ*cpdA* mutant background.

mNG-PilH polar localization is abolished in Δ*chpA* Δ*cpdA* (**Figure 3.3AB**), despite nearly identical protein levels as in Δ*cpdA* (**Figure S3.2C**) and high cAMP levels (**Figure S3.4B**). Polar localization of PilH is therefore absolutely ChpA-dependent. To address whether PilH localization depends on phosphorylation, we imaged mNG-PilH in the non-functional $chpA_{LOF}$ mutant with rescued cAMP level (Δ*cpdA* background). The polar localization index of PilH in $chpA_{LOF}$ Δ*cpdA* is close to the one in Δ*cpdA* (**Figure 3.3B**). These results show that despite depending on ChpA, polar recruitment of PilH does not depend on phosphorylation through ChpA. It is therefore possible that both non-phosphorylated and phosphorylated forms of PilH localize to the poles. We found that cAMP levels partially control polar localization of PilH. The slow increase in cAMP levels during surface contact

(Persat, Inclan, et al., 2015b) could thereby explain the increasing polar localization of PilH over time (**Figure 3.1G**).

Analogous to PilG, we generated a PilH mutant that cannot be phosphorylated by substituting the catalytic aspartate 52 with alanine to make *pilH*$_{LOF}$ (LOF, loss-of-function). *pilH*$_{LOF}$ cells twitch forward without reversing and have elevated cAMP levels similar to Δ*pilH* mutants, confirming the loss-of-function mutation (**Figure S3.11**). Substituting aspartate 52 to glutamate yields a gain-of-function (GOF) mutant, *pilH*$_{GOF}$, which is predicted to adopt an active phosphorylated conformation but loses the ability to be phosphorylated. Reversal rate measurements and cAMP levels confirmed that PilH$_{GOF}$ is functional and can complement a deletion of *pilH*, although both phenotypes are not quantitatively restored to WT levels (**Figure S3.11**).

Like wild-type PilH, PilH$_{GOF}$ slowly increases polar localization (**Figure 3.4AB**). PilH$_{LOF}$ also slowly localizes to the poles but less pronounced than PilH or PilH$_{GOF}$ (**Figure S3.12**). The slow recruitment in both PilH mutants and wild-type PilH is consistent with a scenario where polar localization of PilH is independent of phosphorylation. Like for wild-type PilH, polar localization of PilH$_{GOF}$ is ChpA-dependent but independent of ChpA's ability to autophosphorylate and transfer phosphate (**Figure 3.4CD**). This suggests that ChpA recruits both PilH and activated PilH-P to the poles. Although direct interaction between PilH forms and ChpA has yet to be demonstrated, interactions between response regulators and histidine kinases are well established in homologous chemosensory systems (Kentner & Sourjik, 2009). Regarding Chp, *in vitro* phosphorylation of purified

PilG and PilH by ChpA strongly suggests direct interaction of ChpA with both PilG and PilH (Silversmith et al., 2016a).

The signaling hierarchy between PilG and PilH impacts twitching.

The dynamic polarization of PilG during motility and localization of PilH during surface adaptation motivated us to investigate the role of phosphorylation during twitching. In response to mechanosensing, Chp controls forward twitching by polarizing PilB while still enabling spontaneous and collision-induced reversals (Kühn et al., 2021a). PilG is necessary for forward twitching while PilH is required for reversals (Kühn et al., 2021a). We tracked hundreds of isolated motile cells twitching at the interface between agarose and a glass coverslip (**Figure 3.5AB**). We computed their linear displacements which we display as spatial-temporal diagrams (**Figure 3.5C-G**), and we calculated reversal frequencies (**Figure 3.5H**). We had previously shown that *pilG* deletion mutants constitutively reverse, while *pilH* deletion mutants always move forward without reversing (Kühn et al., 2021a). Here, we found that Δ*chpA* and $chpA_{LOF}$ mutants constantly reversed twitching direction (**Figure 3.5CDH, Movie S3.2**), qualitatively recapitulating the hyper-reversing phenotype of Δ*pilG* (**Figure 3.5EH, Movie S3.2**). The inability to phosphorylate PilG and PilH thus phenocopies Δ*pilG*, not Δ*pilH*. Therefore, phosphorylation of at least PilG is required to induce persistent forward twitching.

We wondered whether PilH itself was required to trigger reversals in mutants that are already hyper-reversing. The double deletion mutant Δ*pilG* Δ*pilH* also hyper-reverses (**Figure 3.5FH, Movie S3.2**), phenocopying Δ*pilG*. This demonstrates that PilH is not

inherently required to reverse. PilH may only be required for reversals when PilG is activated by phosphorylation, *i.e.* when cells are already polarized. Our results suggest that PilH does not trigger reversals by directly inhibiting polarization of the extension motor PilB (Kühn et al., 2021a). PilH may instead interfere with PilG's function in maintaining a positive feedback that promotes TFP polarization. This finding suggests PilG is the main output regulator of the Chp phosphorylation cascade, controlling directionality of twitching, and that PilH functions antagonistically by counteracting PilG.

PilG does not directly regulate PilH localization upon surface contact.

To further refine the mechanisms of PilG's and PilH's antagonistic relationship, we investigated how they impact each other's localization. We could not distinguish a change in mNG-PilH localization in a Δ*pilG* mutant background, supporting that PilG does not regulate PilH activation (**Figure 3.6AB**). Since PilH localization is sensitive to cAMP levels, we confirmed PilG-independent localization in Δ*pilG* Δ*cpdA* whose cAMP levels are rescued to near WT levels (**Figure 3.6CD**).

PilH activation controls PilG polarization.

PilH may function antagonistically by directly inhibiting PilG. To characterize how PilH impacts PilG polarization, we quantified PilG localization in Δ*pilH*. Polar localization of PilG is increased in Δ*pilH* relative to WT and to Δ*cpdA* whose cAMP levels nearly match Δ*pilH* (**Figure 3.7AB**) (Kühn et al., 2021a). In addition, the asymmetry index of mNG-PilG is greater in Δ*pilH* than in WT (**Figure 3.7C**). Accordingly, mNG-PilG polar localization

index and asymmetry index in *pilH*$_{LOF}$ are indistinguishable from Δ*pilH* (**Figure 3.7BC**). We conclude that PilH represses PilG polar localization and polarization.

We wondered whether PilH activation by ChpA is necessary to repress PilG polarization. To decouple PilH activation from ChpA and allow native PilG activation by ChpA at the same time, we measured PilG localization in *pilH*$_{GOF}$. PilG polar localization and asymmetry in *pilH*$_{GOF}$ at 0h are much closer to Δ*pilH* and *pilH*$_{LOF}$ than to WT (cf. **Figure 3.7A-C vs D-F**). Both indexes however decrease over time on surface to eventually reach WT levels. This is consistent with a model where PilH in its active conformation reduces the polar localization of PilG and thus mitigates PilG polarization. This effect is independent of PilH-related phosphate flow since PilH$_{GOF}$ cannot get phosphorylated. In addition, this only takes effect after surface contact, which recruits PilH and PilH$_{GOF}$ to the poles, and is not an inherent property of PilH$_{GOF}$.

In summary, PilH is required for proper localization of PilG. Without PilH, PilG localization is extremely polarized, likely irreversible, explaining the unidirectional twitching phenotype observed in Δ*pilH* (Kühn et al., 2021a). Upon recruitment to the poles, PilH in its active conformation reduces polar localization of PilG. Since PilH and PilH$_{GOF}$ polar localization are ChpA-dependent, we conclude that PilH functions through ChpA. We verified that PilH requires functional ChpA but not FimL to modulate PilG polar localization (**Figure S3.13**). PilH locked in its active conformation, PilH$_{GOF}$, is sufficient to reduce PilG localization. This process does not require phosphate transfer involving PilH, disproving

the hypothesis that PilH acts as a phosphate sink for PilG and ChpA (Fulcher et al., 2010c; Silversmith et al., 2016a).

PilH activation impacts PilG phosphorylation.

Since phosphorylation stimulates PilG polarization, PilH could indirectly regulate PilG polarization by controlling PilG phosphorylation. We thus measured the fraction of phosphorylated PilG in whole-cell lysates by PhosTag™ assays in $pilH_{LOF}$ which causes strong polarization, and in $pilH_{GOF}$ which has WT-like polar localization. First, we verified that Flag-tagged PilG migrated as two bands on PhosTag™ gels (Figure S3.14A). The slower migrating band was absent in $pilG_{D58A}$ and $pilG_{D58E}$ point mutants that cannot be phosphorylated, suggesting that it represents non-phosphorylated PilG. Since $pilH_{LOF}$ and $pilH_{GOF}$ mutations affect cAMP production we verified that cAMP levels do not affect phosphorylation of PilG by measuring PilG-P in WT, Δ*cyaB* (low cAMP) and Δ*cpdA* (high cAMP) (**Figure 3.7G**). In $pilH_{LOF}$, the fraction of phosphorylated PilG is higher than in WT (**Figure 3.7H**). The fraction of phosphorylated PilG-P is relatively reduced in $pilH_{GOF}$ and in $pilH_{GOF}$ Δ*cpdA* (**Figure 3.7H**). This suggests PilH in its phosphorylated conformation reduces PilG phosphorylation without the need of phosphate flow to or from PilH. PilG phosphorylation decreases slightly on surfaces (**Figure 3.7G**), possibly due to PilH polar recruitment.

To test the model where PilH regulates PilG localization by controlling PilG phosphorylation, we quantified PilH-dependent localization of non-phosphorylatable $PilG_{D58A}$ and $PilG_{D58E}$, despite the decreased functionality of $PilG_{D58E}$. Localization of both

mutants in Δ*pilH* is indistinguishable from WT (**Figure S3.15**). Accordingly, *pilH* deletion has no effect on twitching of $pilG_{D58A}$ and $pilG_{D58E}$ (**Movie S3.3**). This confirms that PilH functions through modulation of PilG phosphorylation.

Mechanosensing shifts the balance of an ongoing competition between PilG and PilH.

We found that Chp stimulates PilG polarization, indicating that surface sensing should stimulate PilG localization. However, we observed that PilG does not change polarization during surface contact (**Figure 3.1E**). We therefore wondered how mechanical stimuli from TFP could impact Chp-dependent mechanotransduction to control reversals. To achieve this, we quantified PilG and PilH localization in Δ*pilA*. We found little difference in the overall localization patterns of response regulators between WT and Δ*pilA*. For example, PilG still localizes asymmetrically to the poles in Δ*pilA* (**Figure 3.8AB**). In WT, the polar localization decreased slightly upon surface contact, whereas in Δ*pilA* PilG polar localization remains unchanged at the level of surface-adapted WT. PilH and $PilH_{GOF}$ still get recruited to the poles upon surface contact despite the lack of PilA, albeit at a slower speed (**Figure 3.8CD, Figure S3.16AB**). In Δ*pilA* Δ*pilH*, polar localization of PilG is comparable to Δ*pilH* (**Figure 3.8EF**), indicating that PilH still regulates PilG independently of signal input from PilA, for example in liquid. Accordingly, $PilH_{GOF}$ still represses PilG polar localization in Δ*pilA*, however, the effect is slightly delayed (**Figure S3.16EF**).

While the static localization pattern of PilG is not affected by *pilA* deletion, we wondered whether dynamic localization of PilG requires signal input from PilA. As does the

extension machinery, we found that PilG oscillates from pole to pole right after surface contact, and only later stably polarizes (**Figure 3.8GH**). The rate of PilG polarization switches decreases after 1h on surface in WT as it did for FimX (Kühn et al., 2021a). However, under the same conditions, PilG sustains oscillations in a Δ*pilA* background. This suggests that mechanical input from TFP does not impact PilG polar localization quantitatively, but rather locks polarization in the direction of mechanical input. This result further confirms that PilG polarization responds to a spatially-defined mechanical input from TFP (Kühn et al., 2021a).

Consistent with this, PilG is locked at one pole in Δ*pilH* and $pilH_{LOF}$ (**Figure 3.8H**). In the double deletion mutant Δ*pilA* Δ*pilH*, PilG is also locked at one cell pole showing that PilH is required for PilG dynamic movement from pole to pole. While the competitive interaction of PilG and PilH is likely occurring at all times, our results support a model in which mechanosensing through T4P shifts the balance of PilG and PilH signaling between poles.

DISCUSSION

How cells establish and switch polarity are critical questions in biology. Polarity is an essential requirement of the physiology of many bacteria. For example, cells polarize by asymmetric localization of cellular components during motility or asymmetric division (Treuner-Lange & Søgaard-Andersen, 2014). Our results bring a high-resolution perspective on the Pil-Chp signaling network controlling reversible polarity in *P. aeruginosa* in response to mechanosensing (**Figure 3.9**). In particular, we identified the role of PilG and PilH activation in relaying information from mechanical input to a motility response. Cells sense surface contact through TFP. During attachment and retraction, TFP activate Chp through the receptor PilJ (Koch et al., 2022a; Persat, Inclan, et al., 2015b). In a simple model, PilJ stimulates ChpA autophosphorylation at that pole. Surface sensing may also selectively activate some of ChpA's many phosphotransfer domains while others may even be deactivated. ChpA then recruits PilG to transfer phosphate (Silversmith et al., 2016a), thereby polarizing the cell. This in turn stimulates TFP extension via the recruitment of at least FimX and PilB (Kühn et al., 2021a). Increased TFP deployment locally stimulates mechanosensing at that same pole, feeding a local positive feedback, which stabilizes polarization and forward motility. We showed that PilG phosphorylation by ChpA promotes polarization. PilG is however similarly polarized in liquid or without PilA-dependent signal input. PilG and PilH phosphorylation may thus be an ongoing process both in liquid and on surfaces, and surface sensing merely shifts the activation balance between PilG and PilH at one of the poles. Consistent with this scenario, we detected a slight decrease in PilG-P on surfaces (Figure 3.7G). Although PilG is always polarized, the direction of polarity frequently switches in cells that

don’t mechanosense surfaces (Figure 8GH). PilA-dependent surface sensing at one pole then stabilizes PilG polarization over time to enable persistent forward motility. This supports a model in which local activation by TFP promotes and stabilizes cell polarity, establishing the most direct molecular link between mechanical input (TFP retraction on surfaces) and cellular output (PilG polarization). Setting polarity only requires PilG, supporting the hypothesis that PilG is the main output regulator of the Chp system (Bertrand et al., 2010b; Fulcher et al., 2010c; Silversmith et al., 2016a).

Local activation of PilG alone cannot explain asymmetric activation of T4P extension. In *E. coli,* CheY-P quickly diffuses to flagellar basal bodies located throughout the cell envelope after phosphorylation (Briegel et al., 2009a; Maddock & Shapiro, 1993; Thiem et al., 2007). Conceivably, cells need to restrict diffusion of PilG-P to limit the positive feedback to the leading input pole. This could be achieved by either limiting phosphorylation to the signal input pole coupled with a short half-life of PilG-P, or by restricting diffusion of PilG once phosphorylated. We postulate FimL, which is maintained at the poles by interaction with the polar landmark protein FimV (Carter et al., 2017; Inclan, Persat, Greninger, Dollen, et al., 2016b), could be involved in restricting PilG to the mechanosensing input pole (the leading pole in motile cells). This may restrict PilG-P diffusion towards the opposite pole, while dynamic polarization of PilG-P requires other factors such as phosphorylation. Interestingly, the N-termini of FimL and ChpA are homologous and both proteins are required for proper polarization of PilG, suggesting a connection between the two proteins, for example in interacting with PilG (Inclan, Persat, Greninger, Dollen, et al., 2016b). FimL is further involved in phosphorylation-independent

asymmetry of PilG, although it is not as pronounced as phosphorylation-dependent asymmetry (Figure 3.2). While the feedback-driven asymmetry established by phosphorylation of PilG enables dynamic switching of polarity in response to mechanical signal input, the role of FimL-dependent localization of PilG remains to be clarified in future studies.

Local positive feedback promotes forward locomotion but prevents directional changes. Without a mechanism to counteract this feedback, motile cells would trap themselves in corners, and cell groups would jam during collective twitching (Kühn et al., 2021a; Meacock et al., 2021b). *P. aeruginosa* avoids locking itself into one movement direction by mitigating the positive feedback. At the molecular level, the response regulator PilH counteracts PilG to invert polarization and enable reversals of twitching direction. Multiple conflicting molecular models have been proposed for the antagonizing effect of PilH (Bertrand et al., 2010b; Fulcher et al., 2010c; Silversmith et al., 2016a). Here, we resolved the mechanism of PilH function in the Chp signaling system. We show that PilH directly regulates PilG polarization by reducing PilG phosphorylation. To reverse PilG polarization, PilH must transition to its active conformation, for which it must be phosphorylated. PilH-P may diffuse across the cytoplasmic space to create a global antagonistic effect at both poles, or PilH and PilH-P may localize to different poles generating a polarized antagonistic effect. This in turn interrupts the positive feedback perpetuated by PilG. In WT, PilH and PilH-P localize to the poles without apparent polarization, making the investigation of PilH dynamic activation in motile cells complex. Both PilH and constitutively-activated $PilH_{GOF}$ require ChpA for polar localization and for

regulating PilG. This indicates that PilH interacts with ChpA, and that once phosphorylated PilH-P inhibits PilG phosphorylation by ChpA, potentially by blocking or inhibiting the phosphotransfer domain(s) responsible for PilG phosphorylation. PilH-P may also stimulate the receiver domain of ChpA ($ChpA_{REC}$) that may function as a phosphate sink for PilG. The autodephosphorylation rate of $ChpA_{REC}$-P is order of magnitudes faster than of PilG-P or PilH-P, consistent with a sink function (Silversmith et al., 2016a).

Polar localization of PilH gradually increases during surface adaptation, however, independently from PilH phosphorylation or PilA. Instead, polar recruitment of PilH correlates well with cAMP levels (cf. Figure S3.4A and Figure S3.10C), suggesting PilH localization is regulated by transcription (Beatson et al., 2002; Wolfgang et al., 2003a). However, PilH localization doesn't correlate with mNG-PilH protein abundance (cf. Appendix Figure S3.10CE), and PilH recruitment is only delayed by constitutively low cAMP levels in Δ*cyaB* or Δ*pilA*. It is therefore unlikely that protein expression alone explains PilH polar recruitment. As both PilH and $PilH_{GOF}$ require ChpA for polar localization, the factors responsible for recruiting PilH to the pole may at least involve interaction with ChpA. In contrast, despite increasing polar recruitment of PilH, PilG polar localization and polarization are not considerably affected by surface sensing on long timescale, indicating some level of homeostasis. Polarization changes of PilG on the other hand are considerably affected by PilA-dependent surface sensing and require functional PilH. This hints at a very intricate local and dynamic interplay of PilG and PilH phosphorylation. Resolving phosphorylation of these response regulators within a cell

would provide invaluable information to resolve these connections, but this remains a technical challenge with current methods.

Chp-like systems with multiple response regulators may be involved in surface-induced and taxis-related phenotypes in other species. Chp homologs are present in a number of bacterial species, for example many gamma-proteobacteria besides *P. aeruginosa,* including *Acinetobacter baumanni*, *Stenotrophomonas maltophilia* or *Dichelobacter nodosus* amongst others (Inclan, Persat, Greninger, Dollen, et al., 2016b). In *Acinetobacter* species, TFP mediate surface motility and natural transformation. ChpA and PilG are required for motility and transformability in *A. baumanii* (Vesel & Blokesch, 2021) and motility in *A. baylyi* (Leong et al., 2017). In *A. baylyi*, PilG localizes on a line oriented along the cell body axis, a mechanism that depend on FimL (Ellison et al., 2022). PilH may also function antagonistically to PilG as in *P. aeruginosa* (Vesel & Blokesch, 2021).

The cyanobacterium *Synechocystis* uses phototaxis to direct TFP-dependent surface motility. Several chemotaxis-like systems are involved, three of which encode two response regulators as in Chp (Han et al., 2022). The response regulators PixG, PilG and TaxP2 have an N-terminal PATAN domain that is missing in PilG of *P. aeruginosa* and related systems. The PATAN domain mediates direct interaction with the T4P extension motor PilB whose localization sets twitching direction in response to light (Han et al., 2022; Schuergers et al., 2015, 2016b). The output functions of their second response regulators PixH, PilH and TaxY2 have yet to be resolved, but based on our results in *P. aeruginosa*,

one could anticipate that they counter the function of their cognate first response regulator. In *Myxococcus xanthus* a chemotaxis-like system called Frz regulates the frequency of motility reversals, in the same manner as Chp in *P. aeruginosa*. Frz controls the localization of MglA, MglB and RomR to the leading or lagging pole, thereby setting the direction of gliding and twitching motility (Blackhart & Zusman, 1985b; Carreira et al., 2022; Guzzo et al., 2018b; Kaimer & Zusman, 2016; Szadkowski et al., 2019). Here, the output response regulators FrzX and FrzZ show clear localization to opposite poles, in contrast to PilG and PilH (Guzzo et al., 2018b).

Although Chp comprises a more complex signaling network than the dominant model of chemotaxis systems, the Che system controlling flagellar rotation in *E. coli*, there are even more complex chemosensory systems in many species. They often comprise several copies of chemosensory components, including response regulators, but also of multiple sets of full chemotaxis systems. Why some species require such complexity in chemotaxis systems remains poorly understood. In *Rhodobacter sphaeroides* multiple chemotaxis systems control flagellar rotation in response to different signal inputs (Porter et al., 2011b). Remarkably, only one main response regulator actively stops the flagellar motor, while others may only modulate the effect of the main regulator, indicating a shared signaling principle with Chp (Beyer et al., 2019).

We here decoded the signaling pathway of the Chp system during mechanotaxis. Our results resolve the molecular mechanisms of signaling with two response regulators. At the same time, our model proves a rationale for the complexity of Chp by demonstrating

the necessity of each component in setting a local positive feedback while still enabling reversals. Our data therefore provides a new framework to understand more complex sensory systems in bacteria.

MATERIALS AND METHODS

Bacterial Strains, growth conditions and media.

For all experiments *P. aeruginosa* PAO1 ATCC 15692 (American Type Culture Collection) was used. For vector constructions and conjugative mating *E. coli* strains DH5α and S17.1 were used, respectively. All bacterial strains were grown in LB medium (Carl Roth) at 37 °C with 280 rpm shaking. Regular solid LB media were prepared by adding 1.5% (wt · vol^{-1}) agar (Fisher Bioreagents) and appropriate antibiotics, for selection of *E. coli* 100 $\mu g.ml^{-1}$ ampicillin or 10 $\mu g.ml^{-1}$ gentamycin, for selection of *P. aeruginosa* 300 $\mu g.ml^{-1}$ carbenicillin or 60 $\mu g.ml^{-1}$ gentamycin. For twitching and protein localization experiments semi-solid tryptone media were prepared by autoclaving (5 $g.l^{-1}$ tryptone (Carl Roth), 2.5 $g.l^{-1}$ NaCl (Fisher Bioreagents), 0.5 % ($wt.vol^{-1}$) agarose standard (Carl Roth)). For measurements of cAMP levels on solid surfaces LB plates containing 1% standard agarose were prepared by autoclaving (for the PaQa reporter), or regular 1.5% LB agar plates were used (for the PlacP1 reporter). Surface growth for PhosTag™ assays was carried out on regular 1.5% LB agar plates.

Strains and vector construction.

Strains are listed in Table S3.1, plasmids and corresponding oligonucleotides are listed in Tables S3.2 and S3.3, respectively. *Pseudomonas aeruginosa* mutants were generated as described previously (Kühn et al., 2021a). Genes were deleted or integrated by two-step allelic exchange according to (Hmelo et al., 2015b) using the suicide vectors $pEX18_{Amp}$ or $pEX18_{Gent}$. For genomic in-frame gene deletions, approximately 500 to 1000 base pair fragments of the up- and downstream regions of the designated gene were

combined by PCR amplification and subsequent Gibson assembly (Gibson et al., 2009b). Marker-free deletions were verified by PCR and sequencing. In-frame insertions were generated essentially the same way. Substitutions of wild-type genes with mutated genes (e.g. point mutants) were integrated into the corresponding deletion strains or wild type. Proteins were fluorescently labelled typically by N-terminal fusion separated by a 5xG linker, and integrated into the wild-type gene locus. Functionality was tested by monitoring single cell twitching and measurements of cAMP levels (see also (Kühn et al., 2021a)). Plasmids were constructed using standard Gibson assembly protocols (Gibson et al., 2009b) and introduced into *P. aeruginosa* cells by conjugative mating with *E. coli* S17.1 as donor.

Fluorescence microscopy.

Microscopy was performed on an inverted Nikon TiE epifluorescence microscope using NISElements (version AR 5.02.03). For phase contrast microscopy a 40× Plan APO NA 0.9 phase contrast objective was used. For fluorescence microscopy a 100× Plan APO NA 1.45 phase contrast oil objective and Semrock YFP-2427B or TxRed-A-Basic-NTE filters were used as needed. Microscope settings were kept consistent throughout all experiments to ensure comparability of fluorescent intensities. Fluorescent images were background subtracted and snapshots and movies were generated with ImageJ (version 1.53). Data were analyzed with custom scripts using Python (version 3.8.5) and MATLAB (version R2019b), as specified in detail below. Custom codes are available on Github (https://github.com/PersatLab/antagonists).

Media and cell preparation for single cell twitching experiments.

Plates were prepared by autoclaving tryptone medium supplemented with 0.5% agarose, cooling to 70 °C in the autoclave followed by cooling to 55 °C for 20 min in a water bath. 28 ml medium was poured into 90 mm petri dishes and dried in a flow hood for 30 min. Plates were always stored for one day at 4 °C in a plastic bag and used the next day or maximum after two days. Exponentially growing cells (filtered LB medium, OD_{600} = 0.2-0.8) were diluted to OD_{600} = 0.2. After prewarming the plates for 45-60 min a 16 mm round pad was cut out and 1 µl of the diluted cell suspension was pipetted onto the upper side of the agarose pad (i.e. the side that was not in contact with the plastic dish bottom). The pads were immediately flipped onto a microscope glass bottom dish (P35G-1.5-20-C, MatTek) and 4 droplets of PBS were added at the sides without touching the pad to prevent drying. The dishes were used for imaging immediately or incubated at 37 °C for later imaging.

Quantification of protein localization.

All displayed datapoints correspond to individually repeated biological replicates. Cells were prepared and imaged as described above. Although protein localization was analyzed independent of twitching direction, motile cells were imaged. Motile cells are typically visible after 1 and 2h but not at 0h. The analysis was carried out essentially as described previously (Kühn et al., 2021a). Fluorescent images of mNeonGreen fusion proteins were acquired at 0, 1 and 2h after preparation of the microscope dishes. 0h samples were taken within 1-5 minutes after the cell suspension was pipetted onto the tryptone agarose pads. Imaging settings (objective and filters, excitation power and time,

binning) were kept consistent across all experiments to ensure comparability of the fluorescent signal. Cells were segmented using phase contrast images and fluorescence profiles were extracted with BacStalk (version 1.8, (Hartmann et al., 2020a). Typically, several dozens to hundreds of cells were segmented per replicate, for total numbers of segmented cells see Table S3.4. Fluorescent profiles correspond to the mean pixel value of a transversal section of the cell along the mid-cell axis (see also (Kühn et al., 2021a)). For comparison of proteins with different expression levels the profiles were normalized by the total fluorescence of the cell and rescaled the cell length. Cells were oriented so that the dim pole is at x = -1, the bright pole at x = 1, and mid-cell at x = 0. Mean profiles and standard deviations were computed for every biological replicate.

Polar localization index.

To quantify the extent of polar localization vs cytoplasmic localization we computed a polar localization index. We defined a polar area in which we measure the polar fluorescence signal I_A and I_B of opposite poles A and B according to the ratio between cell width and cell length to account for differences in cell size ($\text{polar area} = \frac{\text{cell width}}{\text{cell length}} * 0.5$). Since the fluorescence profiles of purely cytoplasmic proteins are bell-shaped instead of flat, we applied the following correction method to accurately quantify the polar localization: As baseline profile corresponding to a polar localization index of zero, the fluorescence profile of soluble mNeonGreen expressed from plasmid pJN105-mNG (uninduced) was determined. We subtracted the average mNG baseline profile plus standard deviation from the measured profiles. The corrected integrated signal at the defined polar areas $I_{Ac} + I_{Bc}$ divided by the initial total polar fluorescence $I_A +$

I_B corresponds to the polar localization index ($polar\ localization\ index = \frac{I_{Ac}+I_{Bc}}{I_A+I_B}$). Values slightly below zero can occur with this correction for non-polarly localizing proteins due to noise. In this case, the polar localization index was set to 0. A polar localization index of 0 corresponds to completely cytoplasmic proteins whereas a value toward 1 corresponds to polarly localized proteins. Due to the applied correction method values of exactly 1 can never be reached, even for proteins that would localize exclusively at the poles. This correction method differs from the method we used previously (Kühn et al., 2021a) because we found it to be more accurate for proteins clearly localizing to the poles but to a low extent. To judge this, we compared the polar localization indexes from our previous and new analysis with the raw images as well as the fluorescent profiles (which are unaffected by this correction method). Most importantly, the polar localization indexes of proteins with weak but clearly visible polar localization (for example in Figure 3.6AB) were slightly above zero with the new analysis but below zero or zero at all timepoints with the previously used analysis. Therefore, polar localization indexes shown here can't be directly compared to the indexes published in (Kühn et al., 2021a).

Asymmetry index.

We similarly computed an asymmetry index (previously called symmetry index in (Kühn et al., 2021a)) by taking the ratio between the maximum total fluorescence I_{max} of opposite poles A and B and the sum of the polar total fluorescence $I_A + I_B$ ($asymmetry\ index = \frac{I_{max}}{I_A+I_B}$). A value of 0.5 corresponds to a perfectly symmetric bipolar localization whereas a value of 1 corresponds to a perfectly unipolar (asymmetric) localization. Note, we found that even proteins with visually symmetric polar localization

or no polar localization at all have asymmetry indexes closer to 0.55 than 0.5. This likely originates from a bias that is due to noise of the fluorescence and orienting the bright cell pole to the right by default.

Average localization pattern.

We generated average localization maps of whole cells using the demograph function of BacStalk. We selected 42 cells with similar length around 4 µm ± 0.2 µm from all segmented cells. We randomly selected one replicate for PilG and PilH that were imaged the same day. The cell lengths and fluorescent intensities were normalized and subsequently averaged using a custom ImageJ script. Note, these average maps only give a rough visual representation of protein localization and do not include all data that was acquired and used to generate quantitative localization indexes as described above.

Frequency of protein pole-to-pole switches.

Cells were prepared and fluorescence image sequences recorded essentially as described above. Cells were grown and imaged in a heated chamber (37 °C) on the microscope at 0.2 frames per second for 3 min after 10 and 70 min. We didn't image cells right after surface contact to let the agarose pad settle down to avoid drift. We measured the fluorescence signal at both poles for each cell track and each frame. We generated a series of numbers (1 or -1) corresponding to a given pole (arbitrary but same over the whole track) being the bright pole (1) or the dim pole (-1) for each frame. A pole-to-pole switch of the fluorescently labelled protein was counted every time the sign changed. The

displayed rate of pole-to-pole switches corresponds to the total detected number of switches divided by the total tracked time over all tracks per replicate.

Spatiotemporal cumulative displacement maps.

Cells were prepared and imaged as described above. The analysis was carried out as described previously (Kühn et al., 2021a). Movies of single twitching cells were recorded by phase contrast microscopy at 0.2 frames per second for 5 min at room temperature. Movies were processed with a custom ImageJ macro to ensure compatibility with the downstream analysis. Briefly, movies were cut into quadrants, drift was corrected if necessary using the StackReg plugin (version July 7, 2011; (Thévenaz et al., 1998b)), and image sequences were saved as individual tif images. BacStalk (version 1.8; (Hartmann et al., 2020a)) was used to segment and track cells. Cell tracks were analyzed with a custom MATLAB script. Briefly, we defined a cell orientation unit vector $\vec{t}$ from the center of mass (CM) to the initial leading pole. We determined the initial leading pole by comparing the scalar products of the unit vectors from CM to poles A and B (arbitrary classification) to the normalized displacement vector $\vec{d}$ in the first frame in which the cell was classified as moving (speed threshold: one pixel per frame for at least three consecutive frames). We determined the cell displacement δ relative to the initial leading pole using vectors $\vec{t}$ and $\vec{d}$. δ is positive if cells twitch forward and negative if they reverse and twitch backward. We generated spatiotemporal displacement maps by cumulating the direction-corrected displacement as a function of time.

Reversal frequency of isolated cells.

Cells were prepared and movies recorded as described above. The analysis was carried out as described previously (Kühn et al., 2021a). Briefly, for each frame (starting from the first frame in which the cell was classified as moving) the scalar product between the normalized displacement vector $\vec{d}$ and the cell orientation unit vector $\vec{t}$ was determined and rounded. This yielded a series of numbers that correspond to movement of the cell toward the initial leading pole (1), toward the initial lagging pole (-1) or no movement (0) at that timepoint (timepoints with no movement were removed). Cells were considered moving in the same direction (relative to the initial leading pole) as long as the sign remained the same, and counted reversing when a change of sign occurred. Reversals were only considered if at least two subsequent frames before and after the reversal had the same sign (to correct for frequent sign changes when a cell was close to non-moving). To calculate the reversal frequency, we divided the sum of all considered reversals by the total tracked time over all cell tracks for each biological replicate. All displayed datapoints correspond to individually repeated biological replicates.

Reversal frequency after collisions.

Cells were prepared and movies recorded as described above. The analysis was carried out as described previously (Kühn et al., 2021a). We counted cell-cell collisions and potential subsequent reversals manually using the ImageJ plugin Cell Counter. A collision was only considered if the cell was moving for at least three frames in the same direction prior to the collision and the collision lasted for at least two frames (frame interval 5 sec). Collisions with angles below roughly 20° were not considered. We considered a reversal

following a collision only if it occurred within five frames after the collision ended. Freshly divided cells were not considered. We calculated the frequency of reversals following a collision by dividing the sum of all considered reversals by the sum of all considered collisions for each biological replicate. All displayed datapoints correspond to individually repeated biological replicates.

Fluorescent labelling of pili.

Cells were essentially prepared and imaged as described above, with the exception of staining T4P prior to microscopy and increasing the fluorescence excitation power from 20 to 50%. We used a strain with mutated *pilA* (*pilA*$_{A86C}$; (Koch et al., 2021)) expressed from its chromosomal native locus. Prior to preparing the microscope slide, we labelled PilA$_{A86C}$ by supplementing the culture medium with 5 µl of the maleimide-conjugate fluorescent dye Alexa Fluor™ 488 C5 maleimide (Thermo Fischer A10254). Cells were incubated in the dark for 30 min, washed with PBS and used for fluorescence microscopy. Note, only PilA$_{A86C}$ in the extended pili are labelled during the staining process, and more non-labelled proteins get produced after the washing. Therefore, not all pili are visible in the recorded movies, and some cells may still twitch without visible pili.

cAMP quantification using PaQa-YFP and PlacP1-YFP reporter.

Single cell cyclic adenosine monophosphate (cAMP) levels were measured using the PaQa-YFP/PrpoD-mKate2 or PlacP1-YFP/POXB20-mKate2 reporter system as described previously (Persat, Inclan, et al., 2015b). *P. aeruginosa* was transformed with reporter plasmid pUCP18-PaQa-YFP/PrpoD-mKate2 and pUC18-PlacP1-YFP/POXB20-

mKate2, respectively. PaQa is a native *P. aeruginosa* promoter responsive to cAMP, whereas PrpoD is a constitutive promoter. LacP1 is a synthetic promoter responsive to cAMP, OXB20 is a strong constitutive promoter (Oxford Genetics Ltd. (UK), Sigma).

For the PaQa measurements, cells were grown overnight in LB-carbenicillin, diluted to OD_{600} = 0.05 and grown until mid-exponential phase (OD_{600} = 0.4-0.8). After dilution to OD_{600} = 0.1, liquid samples were imaged and in parallel 100 µl of the diluted culture were plated on a 1% agarose plate (LB, no antibiotics). After 3 h at 37 °C cells were harvested by adding 1.5 ml LB to the plate and gently shaking it. OD_{600} was measured and set to 0.1 for imaging. Images in YFP and mKate2 channels were acquired. Cells were segmented and mean cellular fluorescence was measured using BacStalk (Hartmann et al., 2020a). We then used a custom Python script to compute median PaQa-YFP to mKate2 fluorescent intensity ratios.

For the LacP1 measurements strains containing the reporter plasmid were grown on LB agar plates with 400 µg/ml Carbenicillin (GoldBio) at 37°C to obtain single colonies. Single colonies were grown in liquid broth in a deep well plate overnight, 37°C, shaking. Overnight cultures were diluted and grown at 37°C for 3 hours. After 3 hours a fraction of the bacteria was fixed by the addition of 4% methanol-free paraformaldehyde (PFA, Thermo Scientific) for 10 min at room temperature and the reaction was quenched by the addition of 0.3 M glycine. A second fraction of bacteria was spotted onto LB/Carbenicilin plates and grown for 2 hours, after 2 hours the spots were scraped into PBS and fixed by the addition of PFA and glycine, as above. Samples were diluted in PBS and analyzed on an LSRII flow cytometer the following day in the UCSF Parnassus Flow CoLab,

(RRID:SCR_018206). Data were exported from FlowJo and analyzed using the same custom Python script as above. We reduced the sample size from about 50000 to 1000 cells per replicate by randomizing and reducing the data from each sample separately. All displayed datapoints correspond to individual cells from at least three (up to six) individually repeated biological replicates.

Phos-tag™ SDS PAGE and immunoblotting to detect phosphorylated PilG *in vivo*.

Pseudomonas aeruginosa PAO1 and selected mutant strains expressing chromosomal 3xFlag-PilG were grown on LB agar plates at 37°C to obtain single colonies. Single colonies were grown in liquid LB broth overnight. Overnight cultures were diluted in LB broth and grown at 37°C for 3 hours. After 3 hours a fraction of the bacteria was harvested by centrifugation (10 000g, 5min, 4°C), the pellet was suspended in Laemmli sample buffer (Biorad) with 2.5% 2-mercaptoethanol and 0.1U/ul benzonase (Millipore) and frozen at -20°C. A second fraction was plated on LB plates and incubated at 37°C. After 2 hours bacteria were harvested into 1ml cold buffer (5 mM $MgCl_2$ / 50 mM KCl / 50 mM Tris pH 7.5 / 2 mM DTT) and centrifuged at 10 000xg for 5min at 4°C. Supernatants were removed and pellets suspended in cold reducing Laemmli sample buffer (Biorad) containing 0.1U/µl Benzonase (Millipore) and frozen at -20°C. Protein concentration was measured using Pierce™ 660nm Protein Assay Reagent with Ionic Detergent Compatibility Reagent. Two µg of each sample were separated by 12% SDS-PAGE with 100µM Phos-tag™ acrylamide (Wako Chemicals, Richmond, VA, USA) and 200µM $MnCl_2$. Phos-tag™ acrylamide gels were electrophoresed at a constant current of 30mA in running buffer (25 mM Tris, 192 mM glycine, 0.1% SDS, pH 8.3). Gels were incubated

in transfer buffer (25 mM Tris, 192 mM glycine, pH 8.3, 20% methanol) containing 1mM EDTA for 10min, followed by incubation in transfer buffer for an additional 20min. Gels were then transferred (100V, 60m) to PVDF membrane, blocked in TBS (20mM Tris, 150mM NaCl, pH 7.5)/5% milk and probed with monoclonal mouse anti-Flag M2 antibody (affinity isolated, catalogue number F3165, Sigma) in TBST (20mM Tris, 150mM NaCl, 0.05% Tween20, pH 7.5)/5% milk. Membranes were washed in TBST and incubated with IRDye® 680RD goat anti-mouse IgG secondary antibody (RRID AB_10956588, catalogue number 926-68070, LI-COR) and imaged on a LI-COR Odyssey system. Intensity of individual bands were generated using ImageStudioLite or EmpiriaStudio (LI-COR). Fraction PilG-P was calculated from the intensity of the PilG-P band/total intensity of PilG bands (sum of both PilG bands). All displayed datapoints correspond to individually repeated biological replicates.

Statistical tests.

To test significance, one-way ANOVA and Tukey's post hoc tests were done where required using Python (version 3.8.5). Different groups values were considered significantly different with a p-value below 0.05.

Data Availability.

This study includes no data deposited in external repositories. Custom ImageJ, Python, and MATLAB codes are available on Github (https://github.com/PersatLab/antagonists). Raw images are available from the corresponding authors upon request.

ACKNOWLEDGEMENTS

ZAM, XP, LT and AP are supported by the SNSF Projects grant number 310030_189084. MJK is supported by the EMBO postdoctoral fellowship ALTF 495-2020. JNE, YI, RP and HM are supported by an NIH R01 AI129547 and by the Cystic Fibrosis Foundation (495008).

REFERENCES

Beatson, S. A., Whitchurch, C. B., Sargent, J. L., Levesque, R. C., & Mattick, J. S. (2002). Differential Regulation of Twitching Motility and Elastase Production by Vfr in *Pseudomonas aeruginosa*. *Journal of Bacteriology*, *184*(13), 3605–3613. https://doi.org/10.1128/JB.184.13.3605-3613.2002

Bertrand, J. J., West, J. T., & Engel, J. N. (2010). Genetic Analysis of the Regulation of Type IV Pilus Function by the Chp Chemosensory System of *Pseudomonas aeruginosa*. *Journal of Bacteriology*, *192*(4), 994–1010. https://doi.org/10.1128/JB.01390-09

Beyer, Szöllössi, Byles, Fischer, & Armitage. (2019). Mechanism of Signalling and Adaptation through the Rhodobacter sphaeroides Cytoplasmic Chemoreceptor Cluster. *International Journal of Molecular Sciences*, *20*(20), 5095. https://doi.org/10.3390/ijms20205095

Bi, S., & Sourjik, V. (2018). Stimulus sensing and signal processing in bacterial chemotaxis. *Current Opinion in Microbiology*, *45*, 22–29. https://doi.org/10.1016/j.mib.2018.02.002

Blackhart, B. D., & Zusman, D. R. (1985). “Frizzy” genes of Myxococcus xanthus are involved in control of frequency of reversal of gliding motility. *Proceedings of the National Academy of Sciences*, *82*(24), 8767–8770. https://doi.org/10.1073/pnas.82.24.8767

Briegel, A., Ortega, D. R., Tocheva, E. I., Wuichet, K., Li, Z., Chen, S., Müller, A., Iancu, C. V., Murphy, G. E., Dobro, M. J., Zhulin, I. B., & Jensen, G. J. (2009). Universal architecture of bacterial chemoreceptor arrays. *Proceedings of the National*

Academy of Sciences, *106*(40), 17181–17186. https://doi.org/10.1073/pnas.0905181106

Burrows, L. L. (2012). *Pseudomonas aeruginosa* Twitching Motility: Type IV Pili in Action. *Annual Review of Microbiology*, *66*(1), 493–520. https://doi.org/10.1146/annurev-micro-092611-150055

Carreira, L. A. M., Szadkowski, D., Müller, F., & Søgaard-Andersen, L. (2022). Spatiotemporal regulation of switching front–rear cell polarity. *Current Opinion in Cell Biology*, *76*, 102076. https://doi.org/10.1016/j.ceb.2022.102076

Carter, T., Buensuceso, R. N. C., Tammam, S., Lamers, R. P., Harvey, H., Howell, P. L., & Burrows, L. L. (2017). The Type IVa Pilus Machinery Is Recruited to Sites of Future Cell Division. *mBio*, *8*(1), e02103-16. https://doi.org/10.1128/mBio.02103-16

Darzins, A. (1994). Characterization of a Pseudomonas aeruginosa gene cluster involved in pilus biosynthesis and twitching motility: Sequence similarity to the chemotaxis proteins of enterics and the gliding bacterium Myxococcus xanthus. *Molecular Microbiology*, *11*(1), 137–153. https://doi.org/10.1111/j.1365-2958.1994.tb00296.x

Dufrêne, Y. F., & Persat, A. (2020). Mechanomicrobiology: How bacteria sense and respond to forces. *Nature Reviews Microbiology*, *18*(4), 227–240. https://doi.org/10.1038/s41579-019-0314-2

Ellison, C. K., Fei, C., Dalia, T. N., Wingreen, N. S., Dalia, A. B., Shaevitz, J. W., & Gitai, Z. (2022). Subcellular localization of type IV pili regulates bacterial multicellular development. *Nature Communications*, *13*(1), 6334. https://doi.org/10.1038/s41467-022-33564-7

Fulcher, N. B., Holliday, P. M., Klem, E., Cann, M. J., & Wolfgang, M. C. (2010). The Pseudomonas aeruginosa Chp chemosensory system regulates intracellular cAMP levels by modulating adenylate cyclase activity: Regulation of cAMP by a chemosensory system. *Molecular Microbiology*, *76*(4), 889–904. https://doi.org/10.1111/j.1365-2958.2010.07135.x

Gibson, D. G., Young, L., Chuang, R.-Y., Venter, J. C., Hutchison, C. A., & Smith, H. O. (2009). Enzymatic assembly of DNA molecules up to several hundred kilobases. *Nature Methods*, *6*(5), Article 5. https://doi.org/10.1038/nmeth.1318

Guzzo, M., Murray, S. M., Martineau, E., Lhospice, S., Baronian, G., My, L., Zhang, Y., Espinosa, L., Vincentelli, R., Bratton, B. P., Shaevitz, J. W., Molle, V., Howard, M., & Mignot, T. (2018). A gated relaxation oscillator mediated by FrzX controls morphogenetic movements in Myxococcus xanthus. *Nature Microbiology*, *3*(8), Article 8. https://doi.org/10.1038/s41564-018-0203-x

Han, Y., Jakob, A., Engel, S., Wilde, A., & Schuergers, N. (2022). PATAN-domain regulators interact with the Type IV pilus motor to control phototactic orientation in the cyanobacterium Synechocystis. *Molecular Microbiology*, *117*(4), 790–801. https://doi.org/10.1111/mmi.14872

Hartmann, R., Teeseling, M. C. F., Thanbichler, M., & Drescher, K. (2020). BacStalk: A comprehensive and interactive image analysis software tool for bacterial cell biology. *Molecular Microbiology*, *114*(1), 140–150. https://doi.org/10.1111/mmi.14501

Hmelo, L. R., Borlee, B. R., Almblad, H., Love, M. E., Randall, T. E., Tseng, B. S., Lin, C., Irie, Y., Storek, K. M., Yang, J. J., Siehnel, R. J., Howell, P. L., Singh, P. K., Tolker-

Nielsen, T., Parsek, M. R., Schweizer, H. P., & Harrison, J. J. (2015). Precision-engineering the Pseudomonas aeruginosa genome with two-step allelic exchange. *Nature Protocols*, *10*(11), Article 11. https://doi.org/10.1038/nprot.2015.115

Inclan, Y. F., Persat, A., Greninger, A., Dollen, J. V., Johnson, J., Krogan, N., Gitai, Z., & Engel, J. N. (2016). A scaffold protein connects type IV pili with the Chp chemosensory system to mediate activation of virulence signaling in Pseudomonas aeruginosa. *Molecular Microbiology*, *101*(4), Article 4. https://doi.org/10.1111/mmi.13410

Jain, R., Sliusarenko, O., & Kazmierczak, B. I. (2017). Interaction of the cyclic-di-GMP binding protein FimX and the Type 4 pilus assembly ATPase promotes pilus assembly. *PLOS Pathogens*, *13*(8), e1006594. https://doi.org/10.1371/journal.ppat.1006594

Kaimer, C., & Zusman, D. R. (2016). Regulation of cell reversal frequency in Myxococcus xanthus requires the balanced activity of CheY-like domains in FrzE and FrzZ. *Molecular Microbiology*, *100*(2), 379–395. https://doi.org/10.1111/mmi.13323

Kentner, D., & Sourjik, V. (2009). Dynamic map of protein interactions in the *Escherichia coli* chemotaxis pathway. *Molecular Systems Biology*, *5*(1), 238. https://doi.org/10.1038/msb.2008.77

Koch, M. D., Black, M. E., Han, E., Shaevitz, J. W., & Gitai, Z. (2022). *Pseudomonas aeruginosa* distinguishes surfaces by stiffness using retraction of type IV pili. *Proceedings of the National Academy of Sciences*, *119*(20), e2119434119. https://doi.org/10.1073/pnas.2119434119

Koch, M. D., Fei, C., Wingreen, N. S., Shaevitz, J. W., & Gitai, Z. (2021). Competitive binding of independent extension and retraction motors explains the quantitative dynamics of type IV pili. *Proceedings of the National Academy of Sciences*, *118*(8), e2014926118. https://doi.org/10.1073/pnas.2014926118

Kühn, M. J., Talà, L., Inclan, Y. F., Patino, R., Pierrat, X., Vos, I., Al-Mayyah, Z., Macmillan, H., Negrete, J., Engel, J. N., & Persat, A. (2021). Mechanotaxis directs *Pseudomonas aeruginosa* twitching motility. *Proceedings of the National Academy of Sciences*, *118*(30), e2101759118. https://doi.org/10.1073/pnas.2101759118

Laventie, B.-J., Sangermani, M., Estermann, F., Manfredi, P., Planes, R., Hug, I., Jaeger, T., Meunier, E., Broz, P., & Jenal, U. (2019). A Surface-Induced Asymmetric Program Promotes Tissue Colonization by Pseudomonas aeruginosa. *Cell Host & Microbe*, *25*(1), 140-152.e6. https://doi.org/10.1016/j.chom.2018.11.008

Leong, C. G., Bloomfield, R. A., Boyd, C. A., Dornbusch, A. J., Lieber, L., Liu, F., Owen, A., Slay, E., Lang, K. M., & Lostroh, C. P. (2017). The role of core and accessory type IV pilus genes in natural transformation and twitching motility in the bacterium Acinetobacter baylyi. *PLOS ONE*, *12*(8), e0182139. https://doi.org/10.1371/journal.pone.0182139

Levchenko, A., & Iglesias, P. A. (2002). Models of Eukaryotic Gradient Sensing: Application to Chemotaxis of Amoebae and Neutrophils. *Biophysical Journal*, *82*(1), 50–63. https://doi.org/10.1016/S0006-3495(02)75373-3

Maddock, J. R., & Shapiro, L. (1993). Polar Location of the Chemoreceptor Complex in the Escherichia coli Cell. *Science*, *259*(5102), 1717–1723. https://doi.org/10.1126/science.8456299

Meacock, O. J., Doostmohammadi, A., Foster, K. R., Yeomans, J. M., & Durham, W. M. (2021). Bacteria solve the problem of crowding by moving slowly. *Nature Physics*, *17*(2), 205–210. https://doi.org/10.1038/s41567-020-01070-6

Merz, A. J., So, M., & Sheetz, M. P. (2000). Pilus retraction powers bacterial twitching motility. *Nature*, *407*(6800), 98–102. https://doi.org/10.1038/35024105

O'Toole, G. A., & Wong, G. C. (2016). Sensational biofilms: Surface sensing in bacteria. *Current Opinion in Microbiology*, *30*, 139–146. https://doi.org/10.1016/j.mib.2016.02.004

Persat, A., Inclan, Y. F., Engel, J. N., Stone, H. A., & Gitai, Z. (2015). Type IV pili mechanochemically regulate virulence factors in *Pseudomonas aeruginosa*. *Proceedings of the National Academy of Sciences*, *112*(24), 7563–7568. https://doi.org/10.1073/pnas.1502025112

Persat, A., Nadell, C. D., Kim, M. K., Ingremeau, F., Siryaporn, A., Drescher, K., Wingreen, N. S., Bassler, B. L., Gitai, Z., & Stone, H. A. (2015). The Mechanical World of Bacteria. *Cell*, *161*(5), 988–997. https://doi.org/10.1016/j.cell.2015.05.005

Porter, S. L., Wadhams, G. H., & Armitage, J. P. (2011). Signal processing in complex chemotaxis pathways. *Nature Reviews Microbiology*, *9*(3), 153–165. https://doi.org/10.1038/nrmicro2505

Schuergers, N., Lenn, T., Kampmann, R., Meissner, M. V., Esteves, T., Temerinac-Ott, M., Korvink, J. G., Lowe, A. R., Mullineaux, C. W., & Wilde, A. (2016). Cyanobacteria use micro-optics to sense light direction. *eLife*, *5*, e12620. https://doi.org/10.7554/eLife.12620

Schuergers, N., Nürnberg, D. J., Wallner, T., Mullineaux, C. W., & Wilde, A. (2015). PilB localization correlates with the direction of twitching motility in the cyanobacterium Synechocystis sp. PCC 6803. *Microbiology*, *161*(5), 960–966. https://doi.org/10.1099/mic.0.000064

Silversmith, R. E., Wang, B., Fulcher, N. B., Wolfgang, M. C., & Bourret, R. B. (2016). Phosphoryl Group Flow within the Pseudomonas aeruginosa Pil-Chp Chemosensory System. *Journal of Biological Chemistry*, *291*(34), 17677–17691. https://doi.org/10.1074/jbc.M116.737528

Siryaporn, A., Kuchma, S. L., O'Toole, G. A., & Gitai, Z. (2014). Surface attachment induces *Pseudomonas aeruginosa* virulence. *Proceedings of the National Academy of Sciences*, *111*(47), 16860–16865. https://doi.org/10.1073/pnas.1415712111

Smith, J. G., Latiolais, J. A., Guanga, G. P., Pennington, J. D., Silversmith, R. E., & Bourret, R. B. (2004). A search for amino acid substitutions that universally activate response regulators. *Molecular Microbiology*, *51*(3), 887–901. https://doi.org/10.1046/j.1365-2958.2003.03882.x

Szadkowski, D., Harms, A., Carreira, L. A. M., Wigbers, M., Potapova, A., Wuichet, K., Keilberg, D., Gerland, U., & Søgaard-Andersen, L. (2019). Spatial control of the GTPase MglA by localized RomR–RomX GEF and MglB GAP activities enables Myxococcus xanthus motility. *Nature Microbiology*, *4*(8), Article 8. https://doi.org/10.1038/s41564-019-0451-4

Thévenaz, P., Ruttimann, U. E., & Unser, M. (1998). A pyramid approach to subpixel registration based on intensity. *IEEE Transactions on Image Processing: A*

Publication of the IEEE Signal Processing Society, *7*(1), 27–41. https://doi.org/10.1109/83.650848

Thiem, S., Kentner, D., & Sourjik, V. (2007). Positioning of chemosensory clusters in E. coli and its relation to cell division. *The EMBO Journal*, *26*(6), 1615–1623. https://doi.org/10.1038/sj.emboj.7601610

Treuner-Lange, A., & Søgaard-Andersen, L. (2014). Regulation of cell polarity in bacteria. *Journal of Cell Biology*, *206*(1), 7–17. https://doi.org/10.1083/jcb.201403136

Vesel, N., & Blokesch, M. (2021). Pilus Production in Acinetobacter baumannii Is Growth Phase Dependent and Essential for Natural Transformation. *Journal of Bacteriology*, *203*(8), e00034-21. https://doi.org/10.1128/JB.00034-21

Whitchurch, C. B., Leech, A. J., Young, M. D., Kennedy, D., Sargent, J. L., Bertrand, J. J., Semmler, A. B. T., Mellick, A. S., Martin, P. R., Alm, R. A., Hobbs, M., Beatson, S. A., Huang, B., Nguyen, L., Commolli, J. C., Engel, J. N., Darzins, A., & Mattick, J. S. (2004). Characterization of a complex chemosensory signal transduction system which controls twitching motility in Pseudomonas aeruginosa: Chemosensory control of twitching motility in P. aeruginosa. *Molecular Microbiology*, *52*(3), 873–893. https://doi.org/10.1111/j.1365-2958.2004.04026.x

Wolfgang, M. C., Lee, V. T., Gilmore, M. E., & Lory, S. (2003). Coordinate Regulation of Bacterial Virulence Genes by a Novel Adenylate Cyclase-Dependent Signaling Pathway. *Developmental Cell*, *4*(2), 253–263. https://doi.org/10.1016/S1534-5807(03)00019-4

FIGURE 3.1

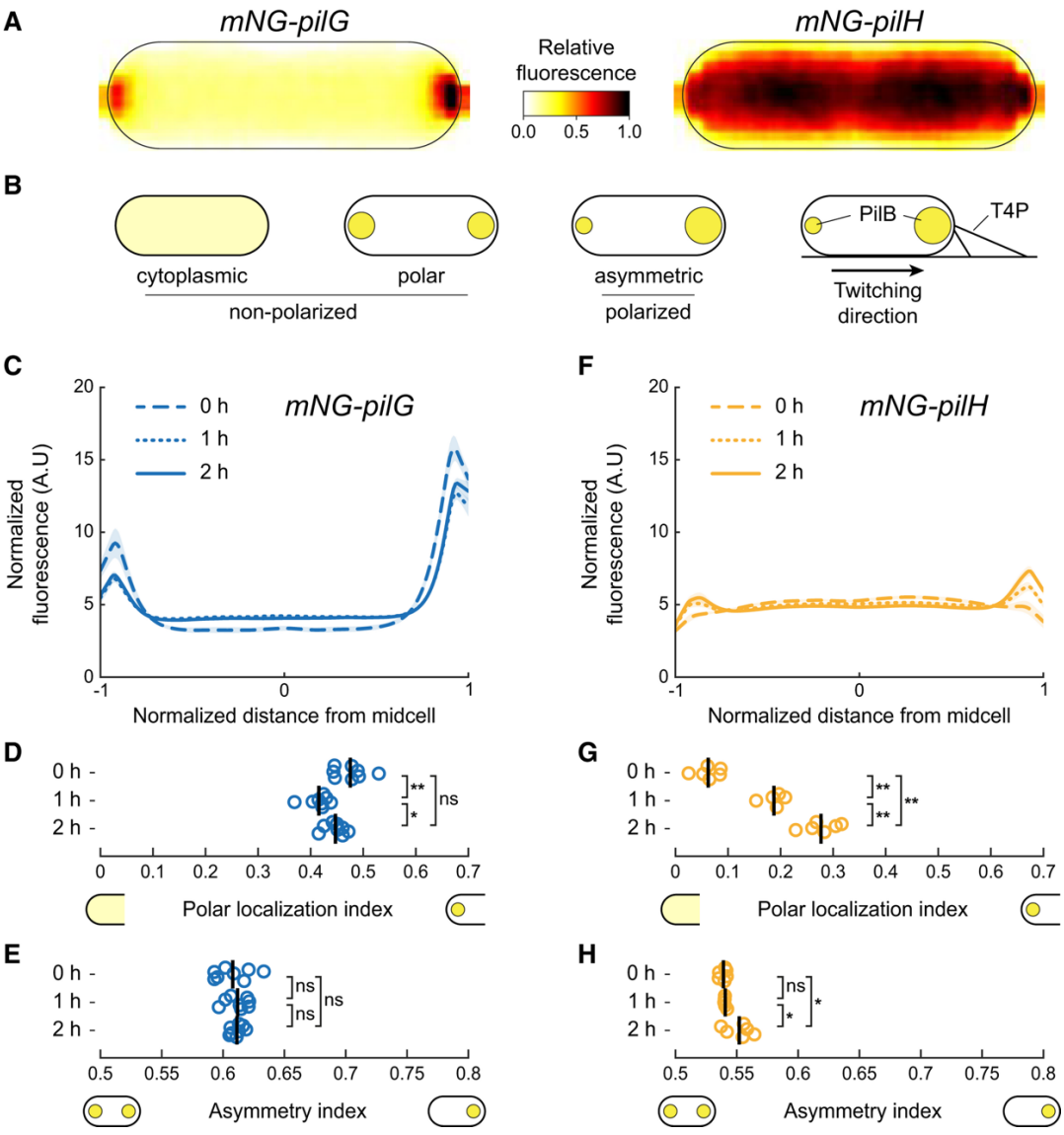

FIGURE 3.1. PilG and PilH localization during surface adaptation.

(A) Average normalized fluorescent signal over 42 cells (bright pole to the right) for mNG-PilG and mNG-PilH transferred from liquid culture to a solid substrate and imaged immediately.

(B) Schematic classification of localization patterns. The spot size indicates the relative protein concentration.

(C,F) Normalized average fluorescence profiles for mNG-PilG and mNG-PilH of hundreds to thousands of cells (cf. Table S3.4). The length of each cell is normalized so that the dim pole is positioned at x = -1, the bright pole at x = 1. (Figure caption continued on the next page.)

(Figure caption continued from the previous page.) The fluorescent profile for each cell is normalized to its total fluorescence. Solid lines: mean normalized fluorescence profiles across replicates. Shaded area, standard deviation across replicates.

(D,G) The polar localization index measures the relative fraction of the fluorescence signal at the poles compared to the cytoplasm (cf. Methods). PilG always localizes predominantly polarly. PilH is mostly cytoplasmic at 0h but becomes more polar over time.

(E,H) Quantification of protein polarization. The asymmetry index measures the difference in fluorescent intensity between poles (cf. Methods).

In D,E,G and H, each circle corresponds to the population median of one biological replicate, and the vertical bars to the mean across biological replicates. *, $p<0.05$; **, $p\leq0.001$; ns, not significant. For corresponding example images see Figure S3.1A. For corresponding fluorescence measurements see Figure S3.2A.

FIGURE 3.2

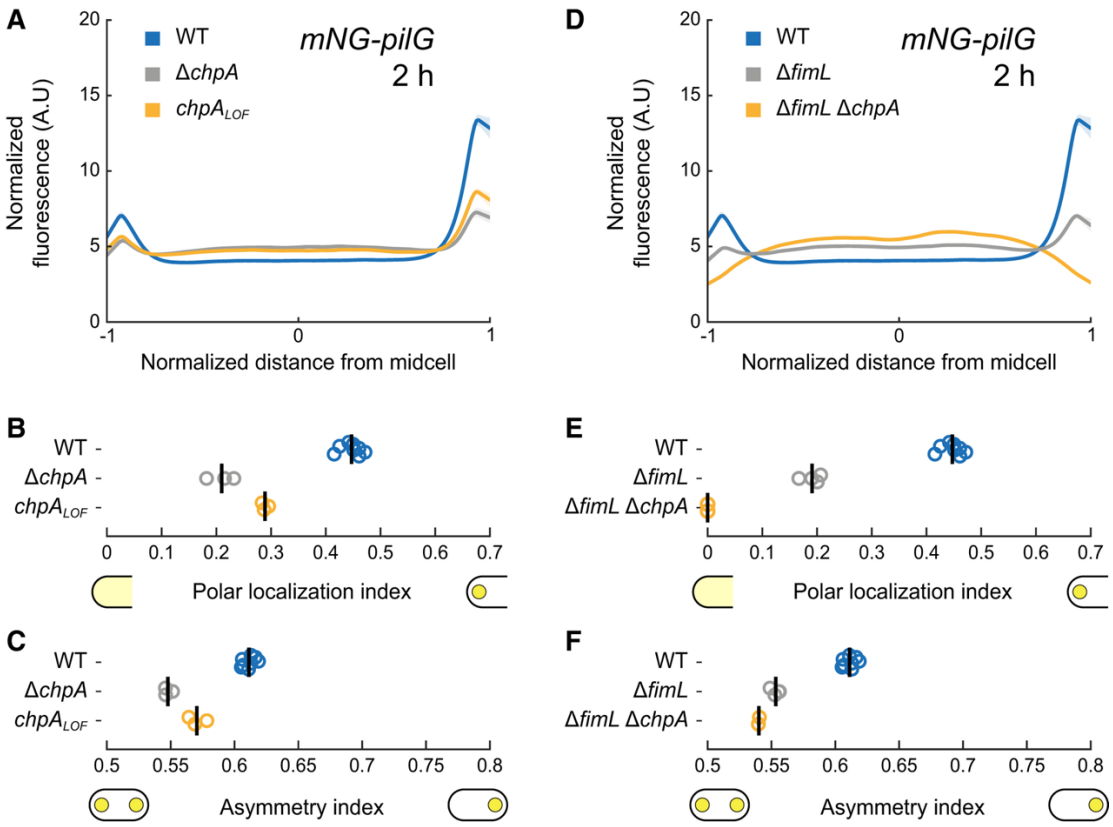

FIGURE 3.2. ChpA controls PilG polarization by phosphorylation.

(A) Fluorescence profiles of mNG-PilG in *chpA* mutants after 2 h on surfaces. Solid lines, mean normalized fluorescence profiles across biological replicates. Shaded area, standard deviation across biological replicates.

(B) Polar localization index and (C) asymmetry index measurements of ChpA- and phosphorylation-dependent localization of mNG-PilG. Both deletion of *chpA* and inhibition of phosphorylation through ChpA reduce the polar localization index of PilG as well as polarization.

(D) Polar localization profiles of mNG-PilG in Δ*fimL* and Δ*fimL* Δ*chpA* mutant after 2h on surfaces.

(E) Polar localization index shows that double deletion of *fimL* and *chpA* completely abolishes polar localization of PilG. Single deletion of *fimL* reduces but does not abolish PilG polar localization and polarization.

(F) Circles, median of each biological replicate. Vertical bars, mean across biological replicates. For corresponding mean cell fluorescence, see Figure S3.2B.

FIGURE 3.3

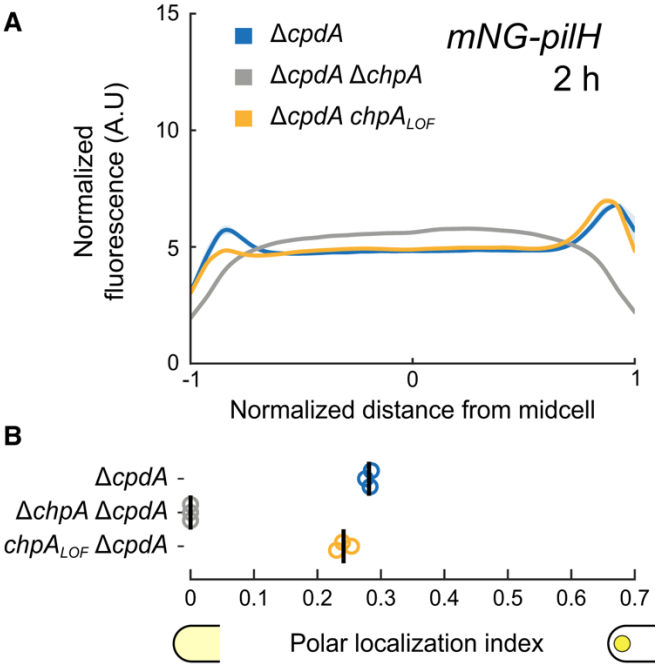

FIGURE 3.3. ChpA promotes PilH localization in a phosphorylation-independent manner.

(A) mNG-PilH fluorescence profiles in *chpA* mutants after 2 h surface growth. To avoid negative effects of low cAMP level on localization of PilH, *cpdA* was deleted in all displayed strains to rescue cAMP level to WT levels (cf. Appendix Figure S3.4B). Solid lines, mean normalized fluorescence profiles across biological replicates. Shaded area, standard deviation across biological replicates.

(B) PilH polar localization is abolished in Δ*chpA*. PilH polar localization is however maintained in $chpA_{LOF}$. Circles, median of each biological replicate. Vertical bars, mean across biological replicates. For corresponding asymmetry indexes and mean cell fluorescence see Figure S3.2C.

FIGURE 3.4

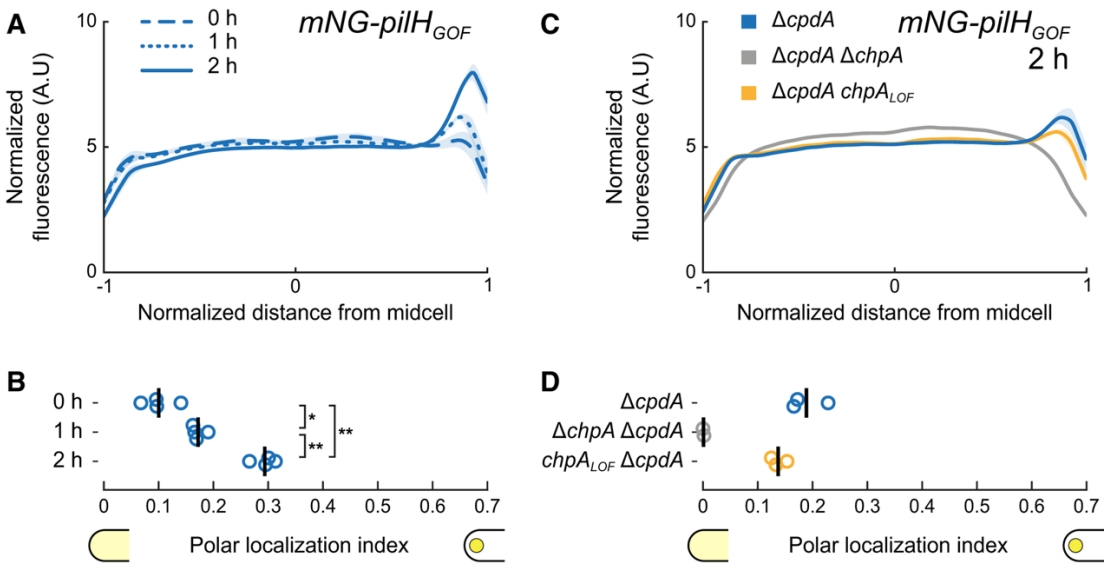

FIGURE 3.4. ChpA recruits active PilH to the pole in a phosphorylation-independent manner.

(A) Time course fluorescence profiles of mNG-PilH$_{GOF}$.

(B) Like wild-type PilH, PilH$_{GOF}$ gets recruited to the poles over time on surface.

(C) Fluorescence profiles of mNG-PilH$_{GOF}$ after 2h on surface in *chpA* mutants.

(D) Polar localization index measurements show that polar localization of mNG-PilH$_{GOF}$ depends on ChpA, but not on its kinase activity.

(A, C) Solid lines, mean normalized fluorescence profiles across biological replicates. Shaded area, standard deviation across biological replicates.

(B, D) Circles, median of each biological replicate. Vertical bars, mean across biological replicates. *, $p<0.05$; **, $p\leq0.001$; ns, not significant. For corresponding asymmetry indexes and mean cell fluorescence see Figure S3.2DE.

FIGURE 3.5

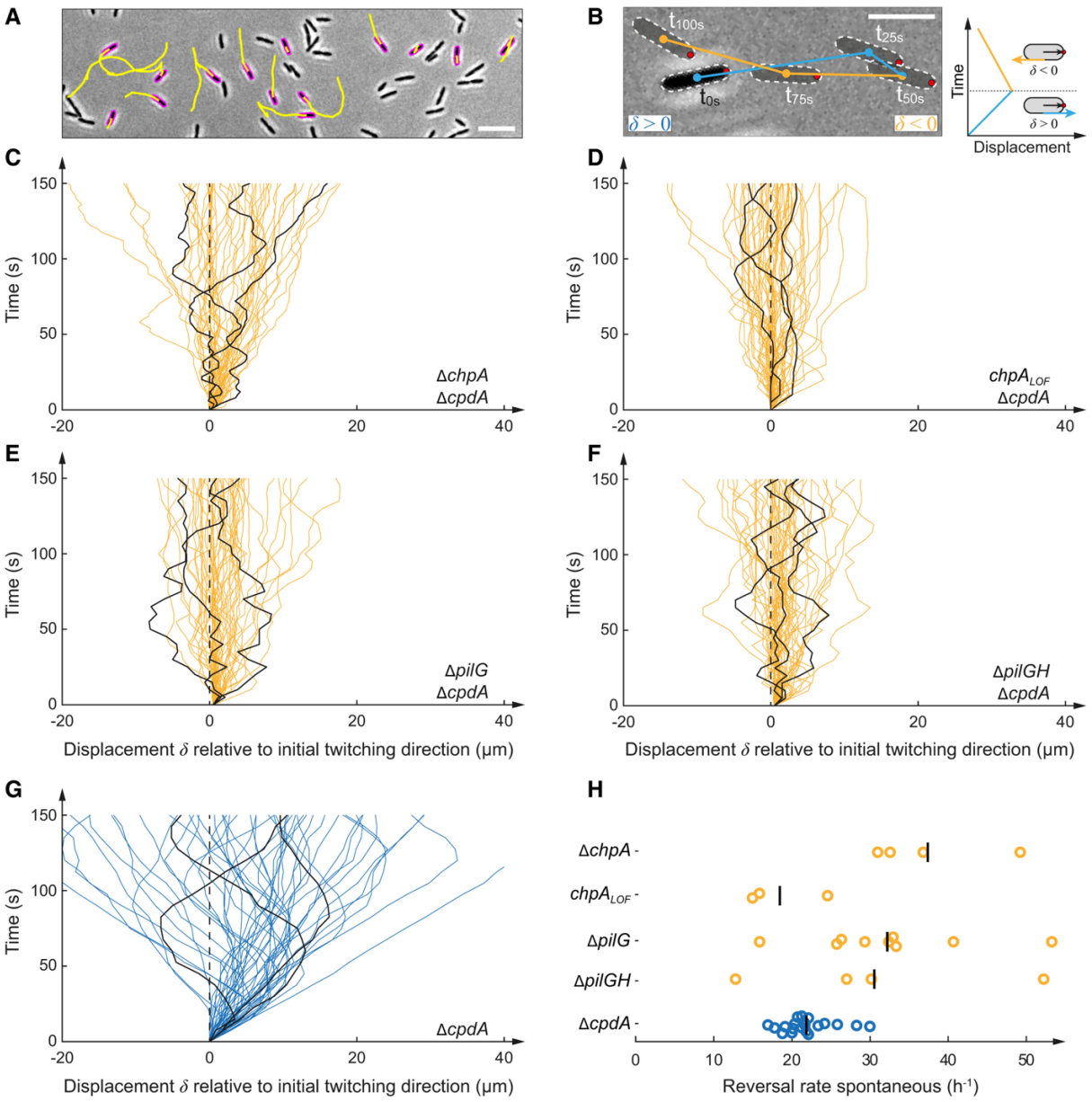

FIGURE 3.5. ChpA regulates forward and reverse twitching.

(A) Snapshot of 5 min-long twitching trajectories (yellow lines).

(B) Computation of displacement maps and reversal rates. A change in the orientation of the track relative to the initially leading pole (red dot) corresponds to a reversal.

(C-G) Displacement maps derived from 50 randomly-selected cell trajectories from three random biological replicates. Each curve corresponds to an individual trajectory. (Figure caption continued on the next page.)

(Figure caption continued from the previous page.) A curve oriented to the top right corresponds to forward twitching, a curve oriented to the top left corresponds to reverse twitching. In each graph, we highlighted three representative tracks for clarity.

(H) Corresponding spontaneous reversal rates. To bypass low cAMP levels *cpdA* was deleted in all displayed strains. We use Δ*cpdA* as reference. Deletion and loss-of-function mutation of *chpA* show a hyper-reversing phenotype, similar to deletion of *pilG*. Δ*pilG* Δ*pilH* double mutants also hyper-reverse, phenocopying Δ*pilG* and Δ*chpA*/*chpA*$_{LOF}$ mutants. For corresponding example movies see Movie S3.2.

FIGURE 3.6

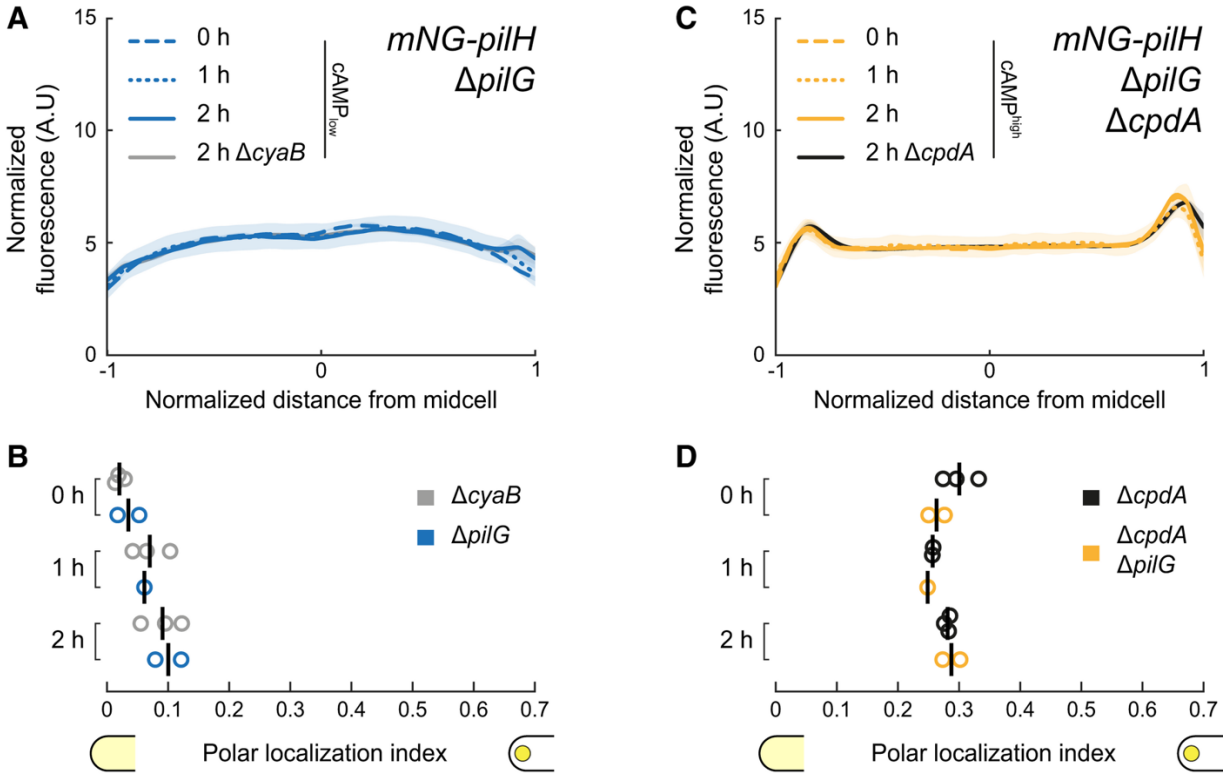

FIGURE 3.6. Localization of PilH is not directly affected by PilG.

(A) mNG-PilH fluorescence profiles in Δ*pilG* after 2h surface growth (low cAMP).

(B) Corresponding polar localization index of mNG-PilH in Δ*pilG*. Recruitment of PilH to the poles is slow but detectable in Δ*pilG*, almost identical to Δ*cyaB* which has similar cAMP levels (Figure S3.4A).

(C) mNG-PilH fluorescence profiles in Δ*pilG* Δ*cpdA* after 2h surface growth (rescued cAMP).

(D) Corresponding polar localization index of mNG-PilH in Δ*pilG* Δ*cpdA*. PilH polar recruitment is indistinguishable from Δ*cpdA*, which also has elevated cAMP levels (Figure S3.4A). Solid lines, mean normalized fluorescence profiles across biological replicates. Shaded area, standard deviation across biological replicates. Circles, median of each biological replicate. Vertical bars, mean across biological replicates. For corresponding asymmetry indexes and mean cell fluorescence see Figure S3.2F.

FIGURE 3.7

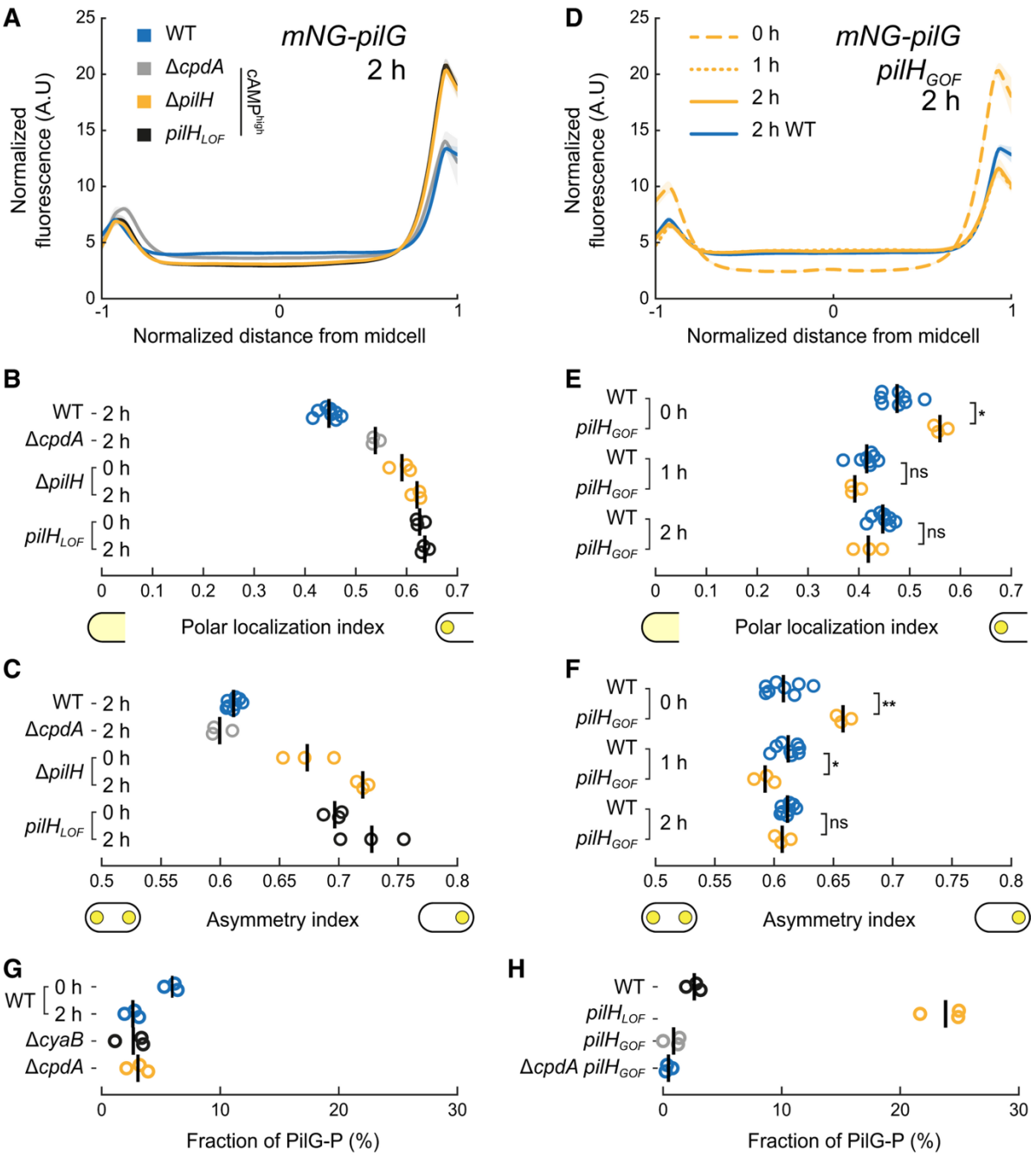

FIGURE 3.7. PilH activation modulates PilG polar localization.

(A) mNG-PilG fluorescence profiles in *pilH* mutants after 2h surface growth. We included Δ*cpdA* for comparison since both *pilH* mutations result in high cAMP levels. PilG is more polar and asymmetric in Δ*pilH* and *pilH*$_{LOF}$. (Figure caption continued on the next page.)

(Figure caption continued from the previous page.) (B) Polar localization index and (C) asymmetry index measurements of PilH-dependent localization of mNG-PilG.

(D) Time course of PilG localization in *pilH*$_{GOF}$ on surface. For clarity only the 2h profile of PilG in wild type from Figure 3.1C was included.

(E,F) Corresponding polar localization and asymmetry index measurements. In *pilH*$_{GOF}$, polar localization of PilG is comparable to Δ*pilH* and *pilH*$_{LOF}$ at 0h, but similar to wild type after 1h and 2h surface growth.

(A and D) Solid lines, mean normalized fluorescence profiles across biological replicates. Shaded area, standard deviation across biological replicates.

(B, C, E, F) Circles, median of each biological replicate. Vertical bars, mean across biological replicates. *, $p<0.05$; **, $p\leq0.001$; ns, not significant. For corresponding mean cell fluorescence see Figure S3.2G. For corresponding example micrographs see Figure S3.1B.

(G) PhosTag™ measurements of the fraction of phosphorylated Flag-PilG (PilG-P) after 2h surface growth. For WT we also show 0h data. The fraction of PilG-P decreases slightly on surfaces, consistent with slightly decreasing PilG polar localization upon surface contact (cf. Figure 3.1CD).

(H) Fraction of phosphorylated PilG after 2h surface growth in *pilH*$_{GOF}$ and *pilH*$_{LOF}$. To rule out a negative effect of lower cAMP level in *pilH*$_{GOF}$, we also deleted *cpdA* in that mutant. Circles correspond to biological replicates, black bars represent their mean. See Appendix Figure S3.14 for a representative PhosTag™ gel.

FIGURE 3.8

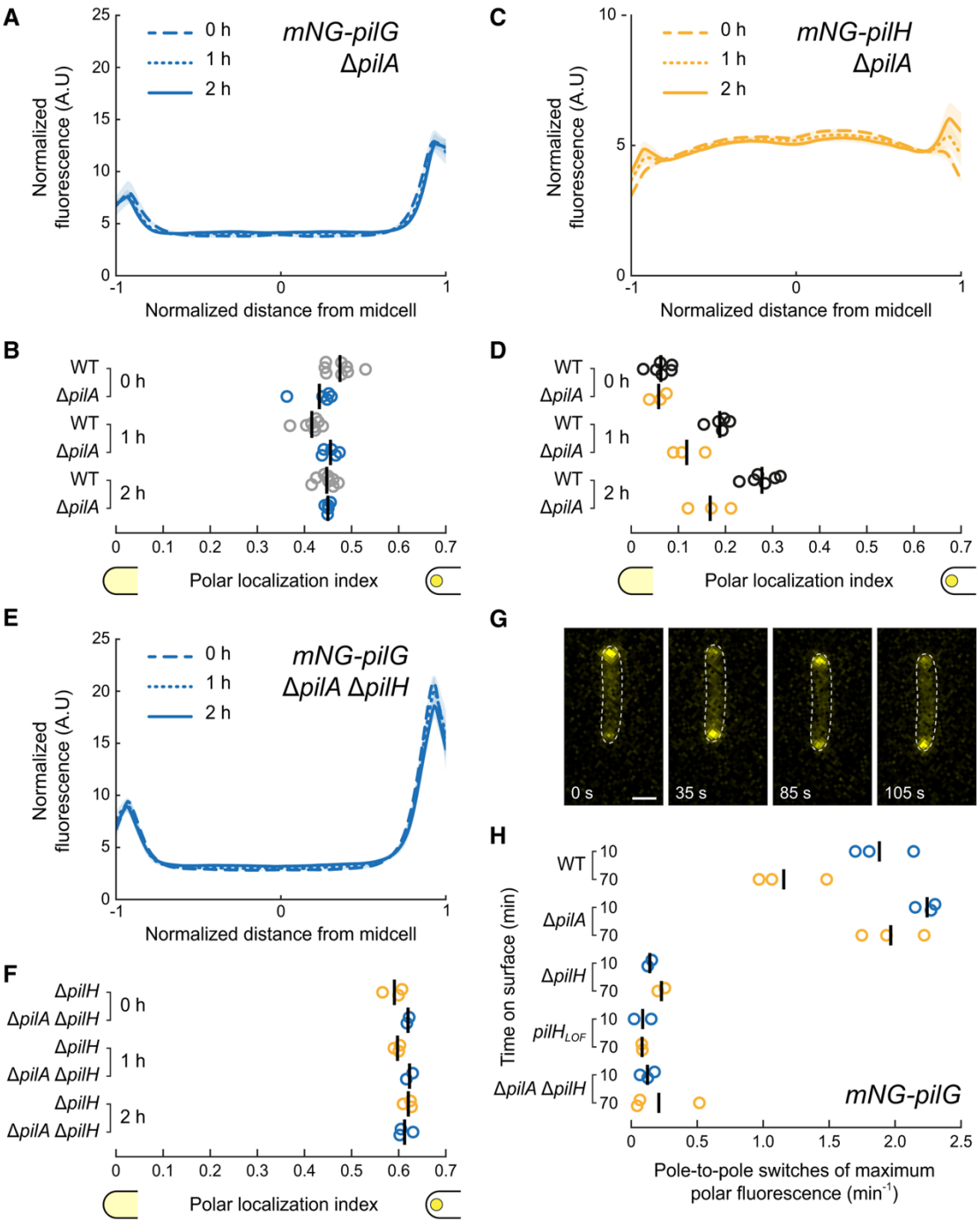

FIGURE 3.8. Mechanosensing though PilA and Chp controls dynamic PilG localization.

(A,B) Time course fluorescence profiles and polar localization indexes of mNG-PilG in Δ*pilA*. (Figure caption continued on the next page.)

(Figure caption continued from the previous page.) PilG polar localization index remains unchanged on surfaces in Δ*pilA* similar to surface-adapted WT (WT data from Figure 3.1D).

(C,D) Time course fluorescence profiles and polar localization indexes of mNG-PilH in Δ*pilA*. Like in WT, PilH gets recruited to the poles over time in Δ*pilA*, although at a slower speed (WT data from Figure 3.1G).

(E,F) Time course fluorescence profiles and polar localization indexes of mNG-PilG in Δ*pilA* Δ*pilH* (WT data from Figure 3.7B). Deletion of *pilH* affects localization of PilG despite the lack of signal input from PilA. For corresponding asymmetry indexes and mean cell fluorescence see Appendix Figure S3.17.

(G) Snapshots of a 3 min long movie (Movie S3.4) of mNG-PilG moving from pole to pole shortly after surface contact.

(H) Quantification of the rate of pole-to-pole switches of the maximum mNG-PilG signal. In Δ*pilA*, the rate remains high over time. Without PilH, independently of PilA, PilG is locked at one pole.

FIGURE 3.9

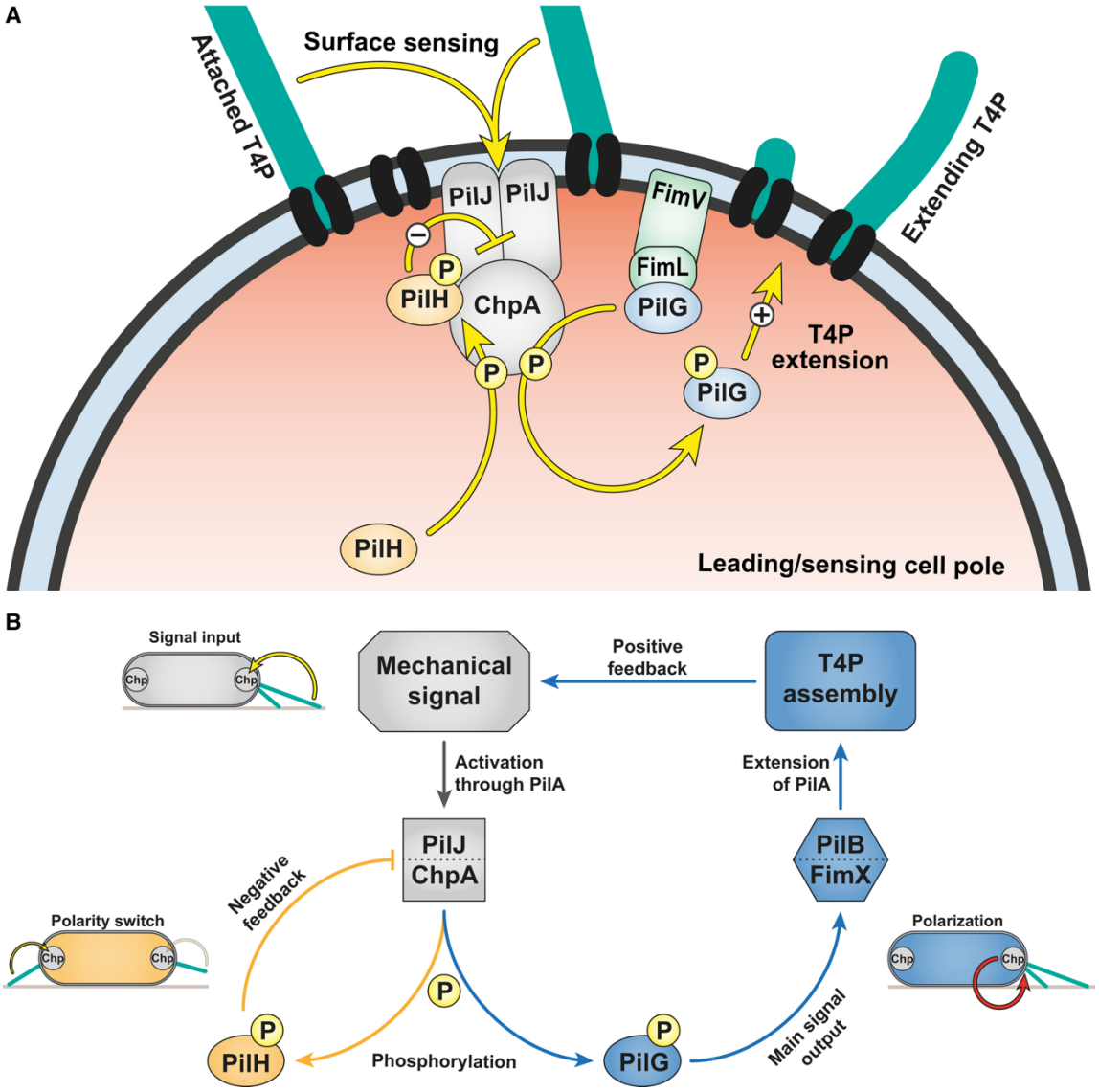

FIGURE 3.9. A model of signalling feedback in *Pseudomonas aeruginosa* mechanotaxis.

(A) Model of phosphate flow through Chp at the leading pole of twitching cells. PilG is recruited by two polar proteins, ChpA and FimL. FimL maintains PilG close to Chp, potentially to restrict diffusion. ChpA phosphorylates PilG to promote and stabilize PilG polarization. PilG locally recruits FimX and PilB to promote T4P extension (Kühn et al., 2021a). Polar localization of PilH is independent of phosphorylation. However, a conformational change induced by phosphorylation is required to activate PilH. PilH-P mitigates the polarizing effect of PilG by reducing PilG phosphorylation.

(B) Overview of the Pil-Chp regulation circuit. Chp senses a local mechanical signal when T4P attach at the leading pole of motile cells. (Figure caption continued on the next page.)

(Figure caption continued from the previous page.) Surface sensing involves interaction of T4P filament monomers PilA and Chp's receptor PilJ (Koch et al., 2022a; Persat, Inclan, et al., 2015b). As a consequence, ChpA becomes more active and phosphorylates PilG. PilG constitutes the main signal output of Chp, eventually polarizing cells by recruiting FimX and PilB to the actively sensing pole where they locally activate T4P extension. As T4P themselves are the surface sensor, this creates a positive feedback loop. ChpA also phosphorylates PilH to balance the main signal output by modulating PilG's activity and localization. PilH achieves this by decreasing PilG phosphorylation, potentially by inhibiting PilJ/ChpA. Presumably, the activity of ChpA and thus the local balance of PilG and PilH differs between sensing and non-sensing poles. Arrows depict hypothesized functional interactions, not direct protein-protein interactions.

FIGURE S3.1

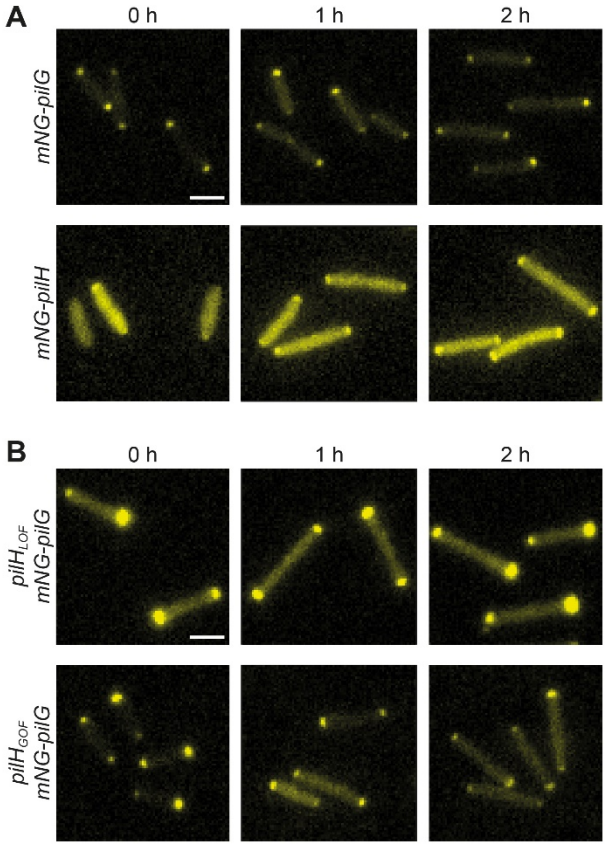

FIGURE S3.1. Example fluorescence microscopy images of mNG-PilG and mNG-PilH in cells grown on a surface.

Cells were transferred from liquid culture to solid substrates and imaged immediately (0h) and after 1h and 2h in which the cells adapt to a surface-associated lifestyle.

(A) Images correspond to data shown in Figure 3.1.

(B) Images correspond to data shown in Figure 3.7. Scale bars, 2 μm.

FIGURE S3.2

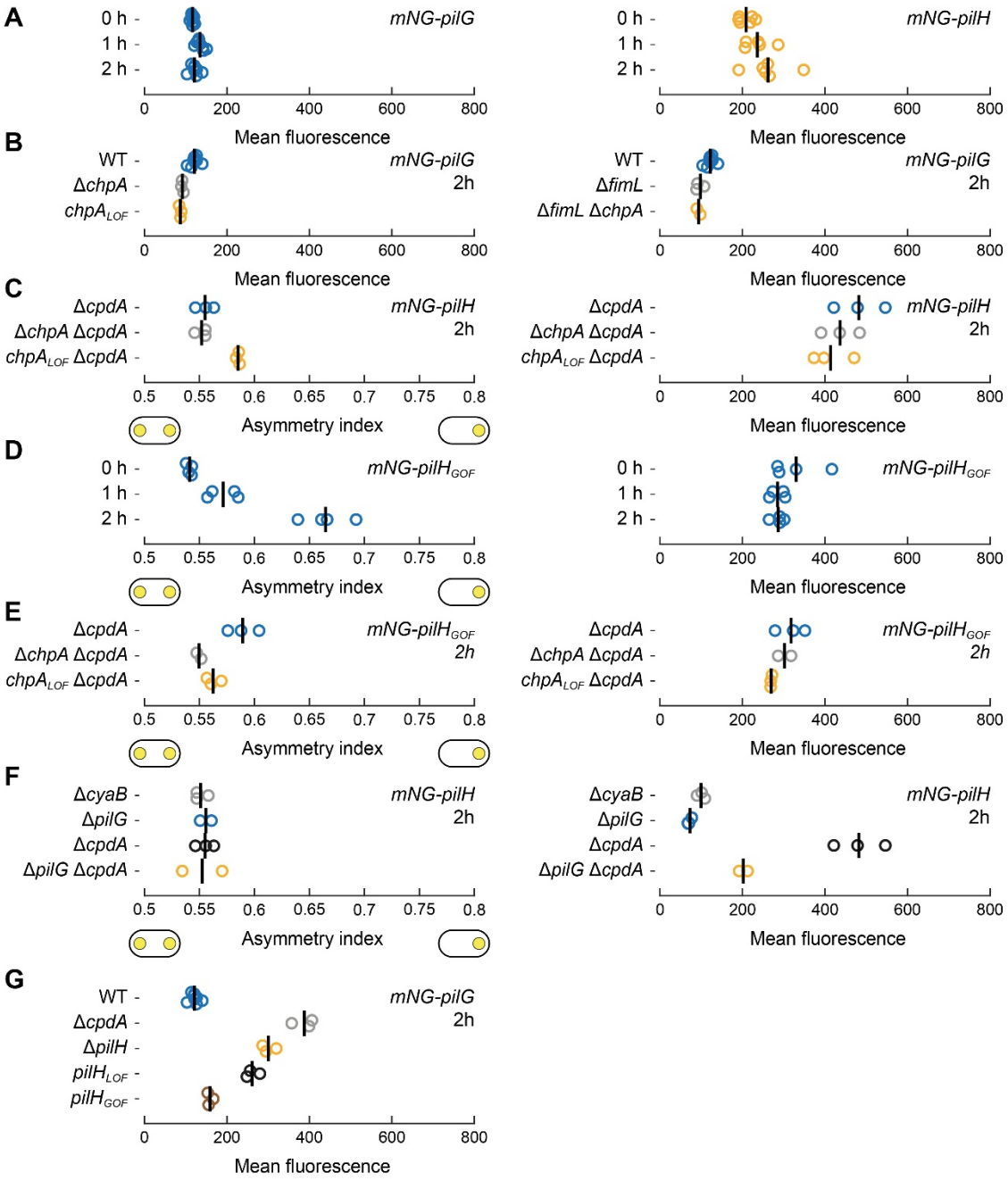

FIGURE S3.2. Mean cell fluorescence and asymmetry indexes of mNG-PilG and mNG-PilH.

Panels correspond to main figures as follows: (A) Figure 1 (B) Figure 2 (C) Figure 3 (D) Figure 3.4AB (E) Figure 3.4CD (F) Figure 3.6 (G) Figure 7. Note, for panels C and E, *cpdA* was deleted in all display strains to rescue cAMP levels and mitigate the negative effects caused by low cAMP. Circles, median of each biological replicate. Vertical bars: mean across biological replicates.

FIGURE S3.3

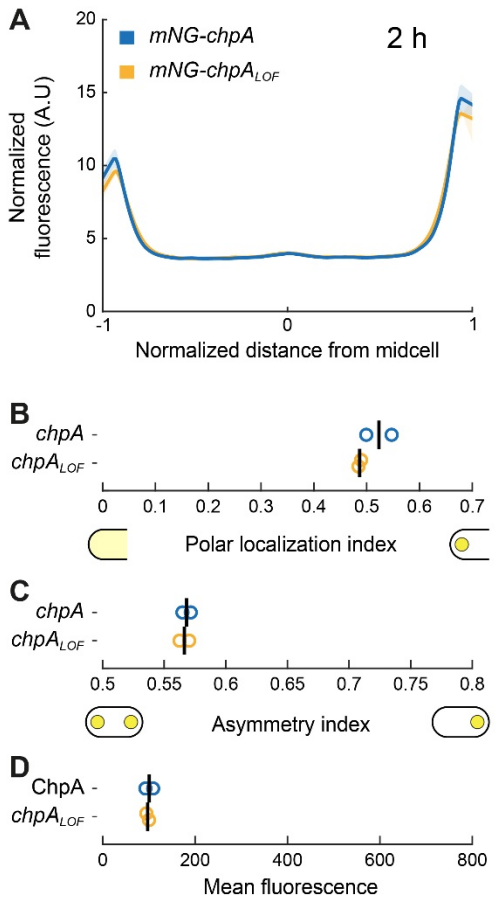

FIGURE S3.3. ChpA and ChpA$_{LOF}$ localize similarly to the poles.

(A) Average fluorescence profiles of mNG-ChpA after 2h surface growth. Note, wild-type mNG-tagged ChpA is non-functional (0 moving cells found in 97 tracked cells) like the loss-of-function mutant *chpA$_{LOF}$* (2 moving cells found in 254 tracked cells).

(B) Quantification of polar localization, (C) asymmetry index and (D) mean cellular fluorescence. Solid lines, mean normalized fluorescence profiles across biological replicates. Shaded area, standard deviation across biological replicates. Circles, median of each biological replicate. Vertical bars, mean across biological replicates.

FIGURE S3.4

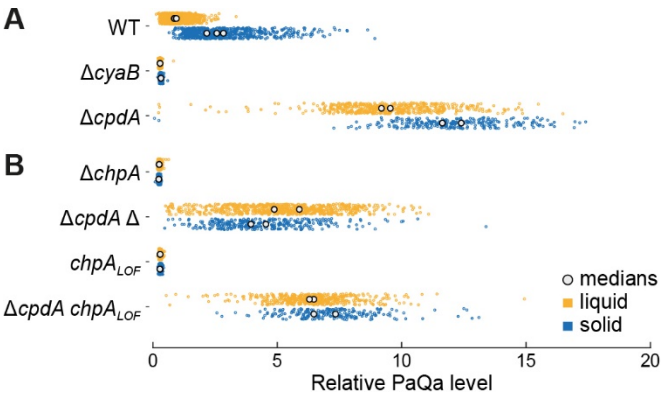

FIGURE S3.4. Quantification of cAMP levels of *chpA* mutants measured by PaQa-YFP reporter fluorescence.

(A) Relative cAMP levels measured by PaQa reporter fluorescence in deletion mutants of the cAMP production cycle. Δ*cyaB* results in constitutively low and Δ*cpdA* in constitutively high cAMP levels. The cAMP level of Δ*cpdA* increases on surfaces, likely due to increased activity of the adenylate cyclase CyaB (Fulcher et al., 2010c).

(B) Relative cAMP levels of Δ*chpA*, the histidine kinase of the Chp system, and $chpA_{LOF}$. Note, deletion of *cpdA* partially rescues the low cAMP level of *chpA* mutants, however, cAMP levels don't reach the high cAMP levels of Δ*cpdA*. Very likely, CyaB doesn't get activated in *chpA cpdA* double mutants (Fulcher et al., 2010c). Therefore, cAMP levels don't increase upon surface contact. Colored circles represent measurements of single cells, white circles correspond to medians of biological replicates. All displayed strains are in Δ*fliC* background.

FIGURE S3.5

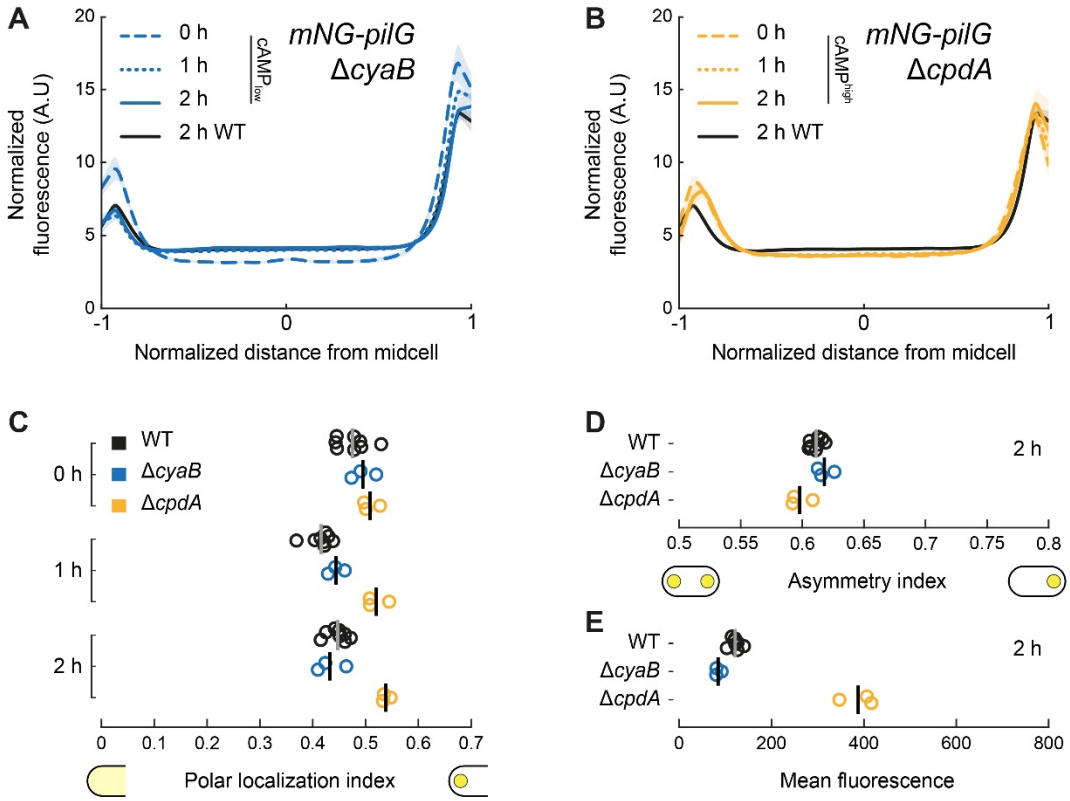

FIGURE S3.5. Time course of cAMP-dependent localization of mNG-PilG in cells grown on solid substrate.

Average fluorescence profiles of mNG-PilG in (A) low and (B) high cAMP.

Quantification of (C) polar localization, (D) asymmetry index and (E) mean cellular fluorescence.

In low cAMP (Δ*cyaB*), the localization pattern as well as the decrease of polar localization over time is almost identical to WT. Data from Figure 3.1D included for comparison (black). Note, WT refers to a strain without *cyaB* or *cpdA* deletion. In high cAMP (Δ*cpdA*), polar localization of PilG is comparable to WT at 0h; however, it remains high over time. The higher polar localization is due to increased localization to the dim pole (at x = -1, panel B) which is reflected by a slightly lower asymmetry index (D), i.e. more symmetric localization. The fluorescent signal of mNG-PilG, as a proxy for protein concentration, is largely unaffected by low cAMP; however, it is strongly increased in high cAMP. Solid lines, mean normalized fluorescence profiles across biological replicates. Shaded area, standard deviation across biological replicates. Circles, median of each biological replicate. Vertical bars, mean across biological replicates.

FIGURE S3.6

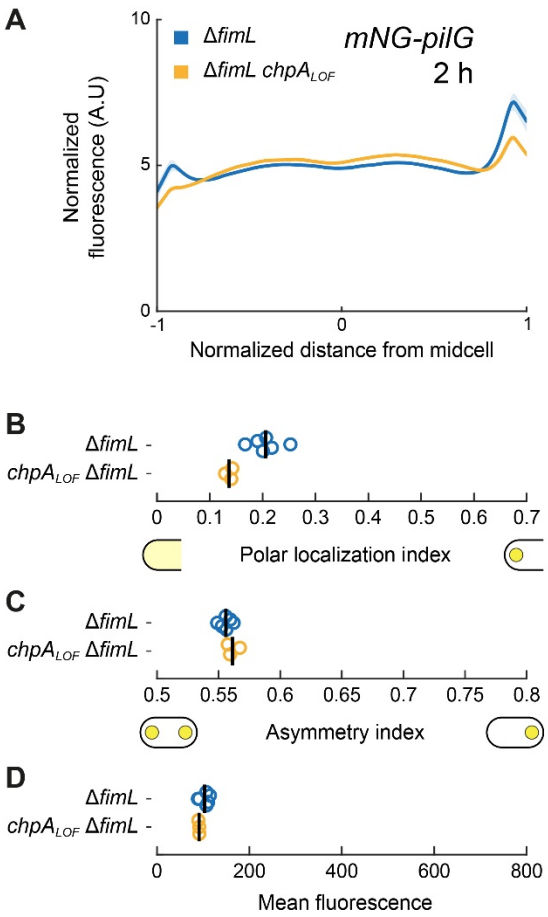

FIGURE S3.6. ChpA plays a role in recruiting PilG independently of phosphorylation.

(A) Average fluorescence profiles of mNG-PilG after 2h surface growth. In Δ*fimL*, PilG is recruited to the poles only by ChpA. Without the ability to phosphorylate, $ChpA_{LOF}$ still recruits PilG, although to a lesser extent than wild-type ChpA.

(B) Quantification of polar localization, (C) asymmetry index and (D) mean cellular fluorescence. Solid lines, mean normalized fluorescence profiles across biological replicates. Shaded area, standard deviation across biological replicates. Circles, median of each biological replicate. Vertical bars, mean across biological replicates.

FIGURE S3.7

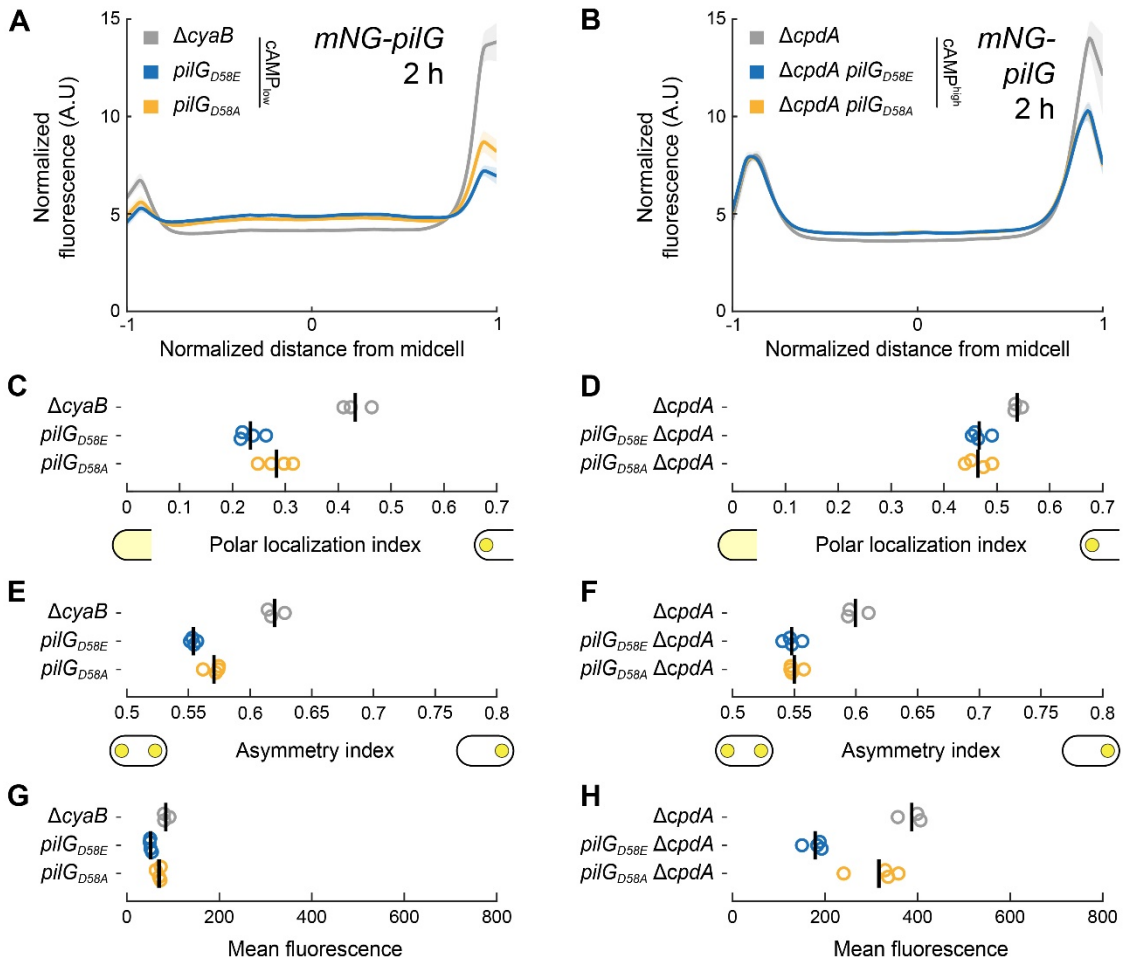

FIGURE S3.7. PilG$_{D58A}$ and PilG$_{D58E}$ similarly localize to the poles.

Average fluorescence profiles of mNG-PilG point mutants after 2h surface growth in (A) low and (B) high cAMP.

(C,D) Quantification of polar localization, (E,F) asymmetry index and (G,H) mean cellular fluorescence. Polar localization and asymmetry indexes of PilG$_{D58A}$ and PilG$_{D58E}$ are decreased compared to WT in low cAMP. Polar localization differs only slightly between the mutants, and the differences disappear in high-cAMP. Solid lines, mean normalized fluorescence profiles across biological replicates. Shaded area, standard deviation across biological replicates. Circles, median of each biological replicate. Vertical bars, mean across biological replicates.

FIGURE S3.8

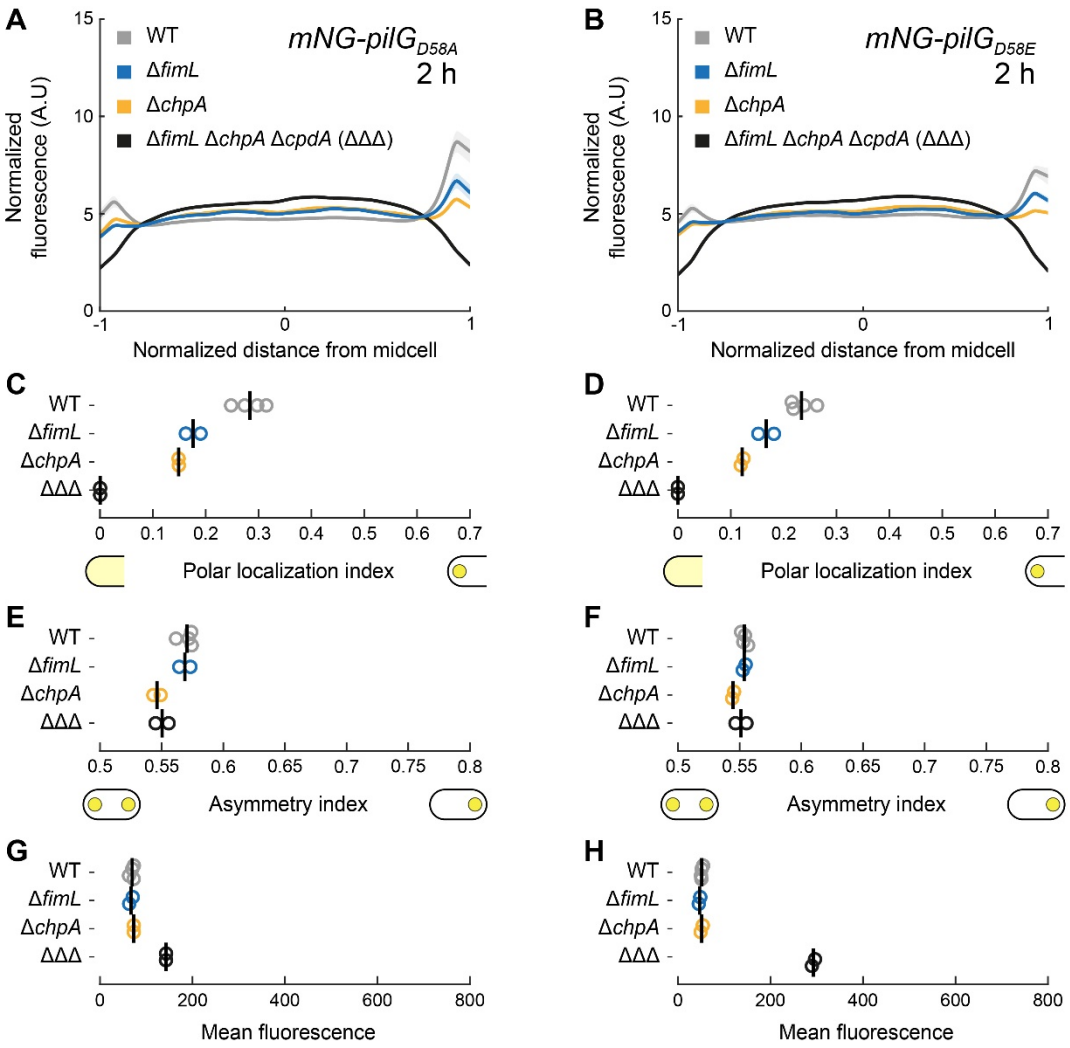

FIGURE S3.8. D58A and D58E mutations of PilG do not interfere with FimL- and ChpA-dependent recruitment.

Average fluorescence profiles of (A) mNG-PilG$_{D58A}$ and mNG-PilG$_{D58E}$ (B) after 2h surface growth. Polar localization of both point mutants similarly depends on FimL and ChpA, comparable to wild-type PilG.

(C,D) Quantification of polar localization, (E,F) asymmetry index and (G,H) mean cellular fluorescence of PilG$_{D58A}$ and mNG-PilG$_{D58E}$, respectively. ΔΔΔ refers to strain Δ*fimL* Δ*chpA* Δ*cpdA*. Solid lines, mean normalized fluorescence profiles across biological replicates. Shaded area, standard deviation across biological replicates. Circles, median of each biological replicate. Vertical bars, mean across biological replicates.

FIGURE S3.9

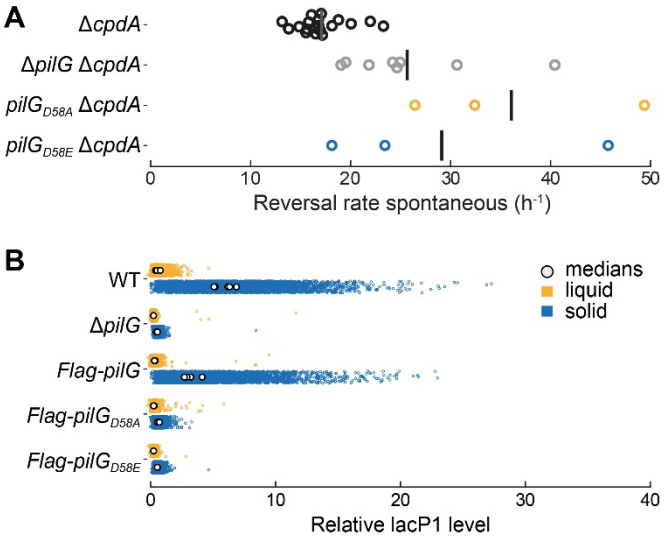

FIGURE S3.9. Reversal rates and cAMP production of *pilG$_{D58}$* point mutants.

(A) Spontaneous reversal rates of *pilG$_{D58A}$* and *pilG$_{D58E}$* mutants. To bypass low cAMP levels *cpdA* was deleted in all displayed strains. Both *pilG* mutants show increased reversals rates similar to Δ*pilG* Indicating a loss of function.

(B) Quantification of cAMP levels measured by PlacP1-YFP reporter fluorescence. Low cAMP levels of both *pilG* mutants confirm that both point mutations result in a loss of function. The Flag tag alone does not confound the cAMP measurements. Colored circles represent measurements of single cells, white circles correspond to medians of biological replicates.

FIGURE S3.10

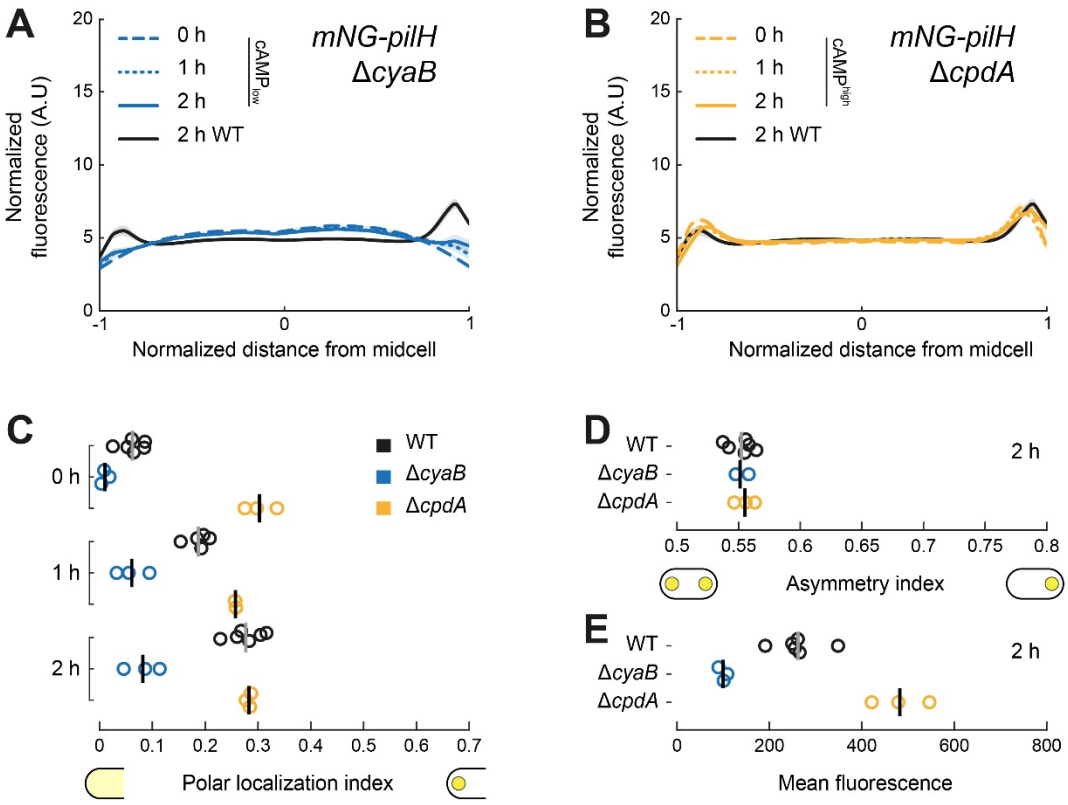

FIGURE S3.10. Time course of cAMP-dependent localization of mNG-PilH in cells grown on solid substrate.

Average fluorescence profiles of mNG-PilH in (A) low and (B) high cAMP, respectively.

Quantification of (C) polar localization, (D) asymmetry index and (E) mean cellular fluorescence. In low cAMP (Δ*cyaB*), polar localization is generally reduced, however, recruitment of PilH to the poles over time still takes place.

In high cAMP (Δ*cpdA*), polar localization is always as high as in WT after 2h surface growth. Data from Figure 1 included for comparison (black). Note, WT refers to a strain without *cyaB* or *cpdA* deletion. The fluorescent signal of mNG-PilH, as a proxy for protein concentration, is proportional to the cAMP level in *cyaB* and *cpdA* mutants (cf. Appendix Figure S4A). Solid lines, mean normalized fluorescence profiles across biological replicates. Shaded area, standard deviation across biological replicates. Circles, median of each biological replicate. Vertical bars, mean across biological replicates.

FIGURE S3.11

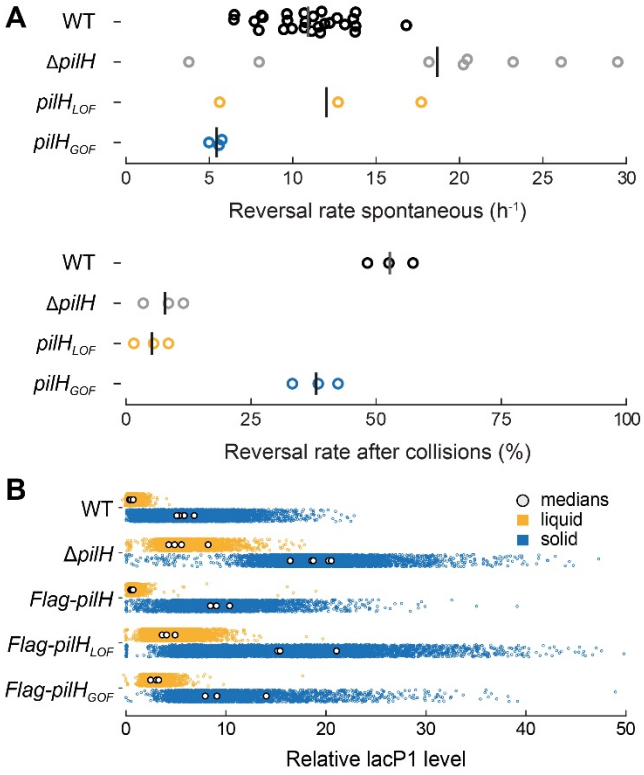

FIGURE S3.11. Reversal rates and cAMP production of loss- and gain-of-function mutants of PilH.

(A) Spontaneous reversal rates and reversal rates after collision of *pilH*$_{LOF}$ and *pilH*$_{GOF}$ mutants. Δ*pilH* and *pilH*$_{LOF}$ show low to almost no reversals (see also (Kühn et al., 2021a)). *pilH*$_{GOF}$ rescues reversal rates, however, doesn't fully restore wild-type rates. Because of high pili number in mutants with high cAMP level resulting in erratic movement of cells, spontaneous reversals rates are not measured very precisely by our algorithm. Manually counted reversal rates after collision give a better estimate. Δ*pilH* collision data from (Kühn et al., 2021a).

(B) Quantification of cAMP levels measured by PlacP1-YFP reporter fluorescence. cAMP levels of *pilH*$_{LOF}$ are comparable to Δ*pilH*, whereas *pilH*$_{GOF}$ partially rescues cAMP to intermediate levels between WT and Δ*pilH* or *pilH*$_{LOF}$. Colored circles represent measurements of single cells, white circles correspond to medians of biological replicates.

FIGURE S3.12

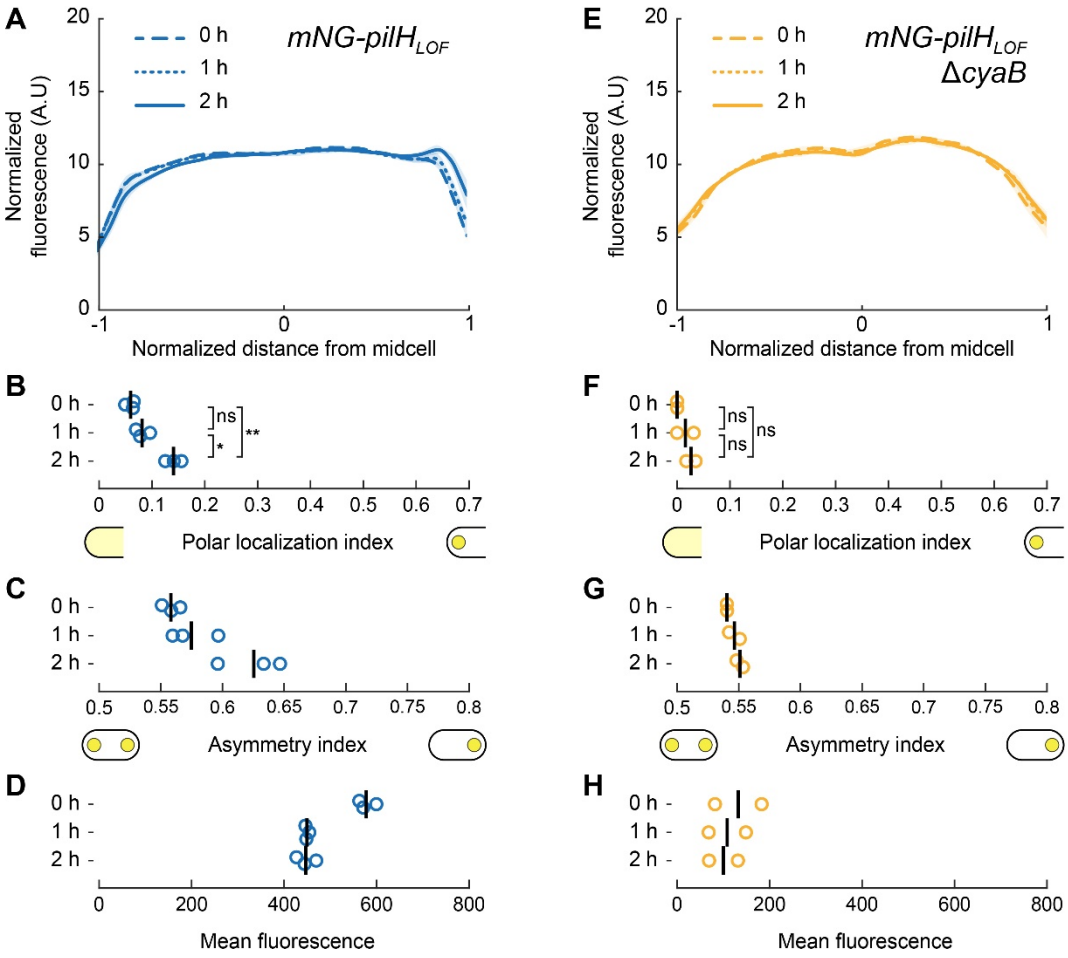

FIGURE S3.12. PilH locked in its inactive conformation is recruited to the poles upon surface contact.

(A) Time course of localization profiles of mNG-PilH$_{LOF}$ in cells grown on solid substrate.

Quantification of corresponding (B) polar localization, (C) asymmetry index and (D) mean cellular fluorescence. Like PilH$_{wt}$ and PilH$_{GOF}$, PilH$_{LOF}$ gets recruited to the poles over time (B). However, the effect is significantly less pronounced, possibly due to saturation effects because of high fluorescent signal. Note, loss-of-function mutation of *pilH* results in high cAMP like in Δ*pilH* (Appendix Figure S3.11).

(E-H) Same analysis in low cAMP (Δ*cyaB*). Polar recruitment may take place but the effect is too weak to be measured clearly (F). Solid lines, mean normalized fluorescence profiles across biological replicates. Shaded area, standard deviation across biological replicates. Circles, median of each biological replicate. Vertical bars, mean across biological replicates. *, $p<0.05$; **, $p\leq0.001$; ns, not significant.

FIGURE S3.13

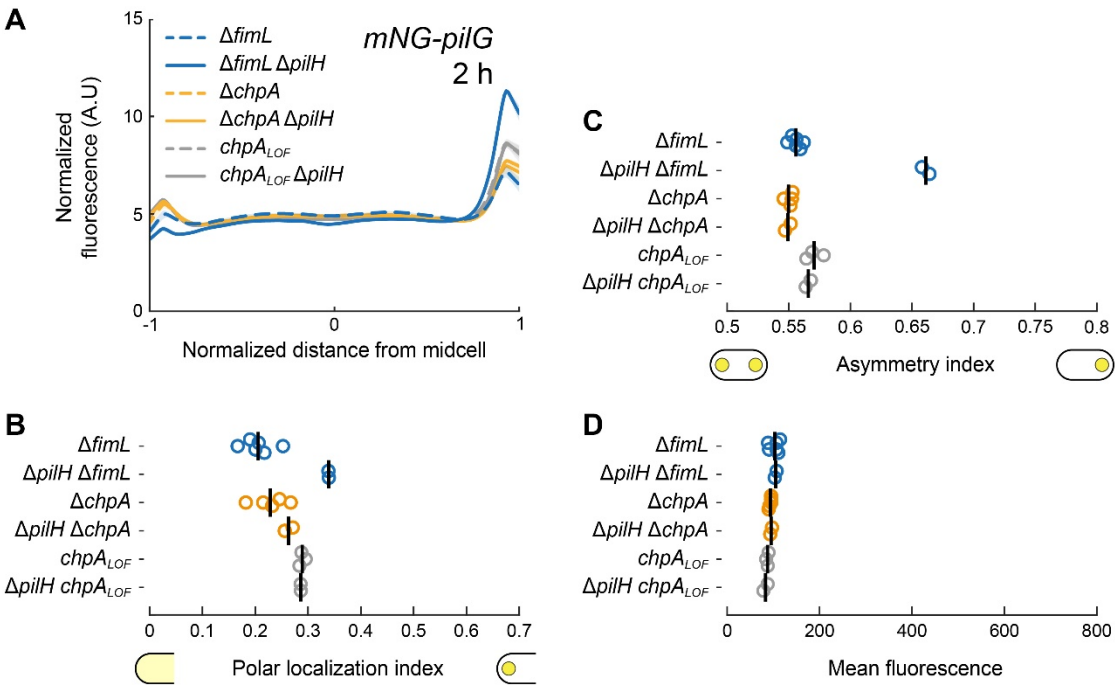

FIGURE S3.13. PilH requires functional ChpA but not FimL to modulate PilG polar localization.

(A) Average fluorescence profiles of mNG-PilG after 2h surface growth.

(B) Quantification of polar localization, (C) asymmetry index and (D) mean cellular fluorescence. PilH can repress PilG polar localization only in cells with functional ChpA (only in Δ*fimL*). Solid lines, mean normalized fluorescence profiles across biological replicates. Shaded area, standard deviation across biological replicates. Circles, median of each biological replicate. Vertical bars, mean across biological replicates.

FIGURE S3.14

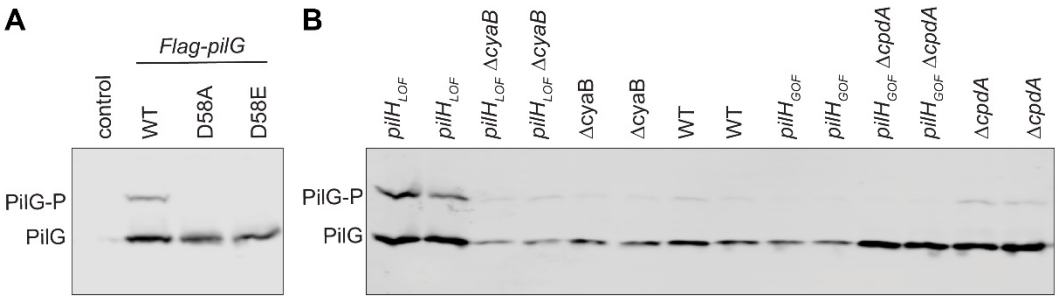

FIGURE S3.14. Example PhosTag™ western blots.

(A) Representative gel of PilG and corresponding point mutants that can't get phosphorylated. A slower migrating band corresponding to PilG-P is detected in whole cell lysates from wild type cells expressing Flag-PilG but not in cells expressing PilG with mutations in the phospho-accepting site D58. Control, wild-type PilG without Flag tag.

(B) Representative gel of PilG in PilH point mutants and mutants with altered cAMP levels (Δ*cpdA*, Δ*cyaB*), corresponding to data shown in Figure 7GH.

FIGURE S3.15

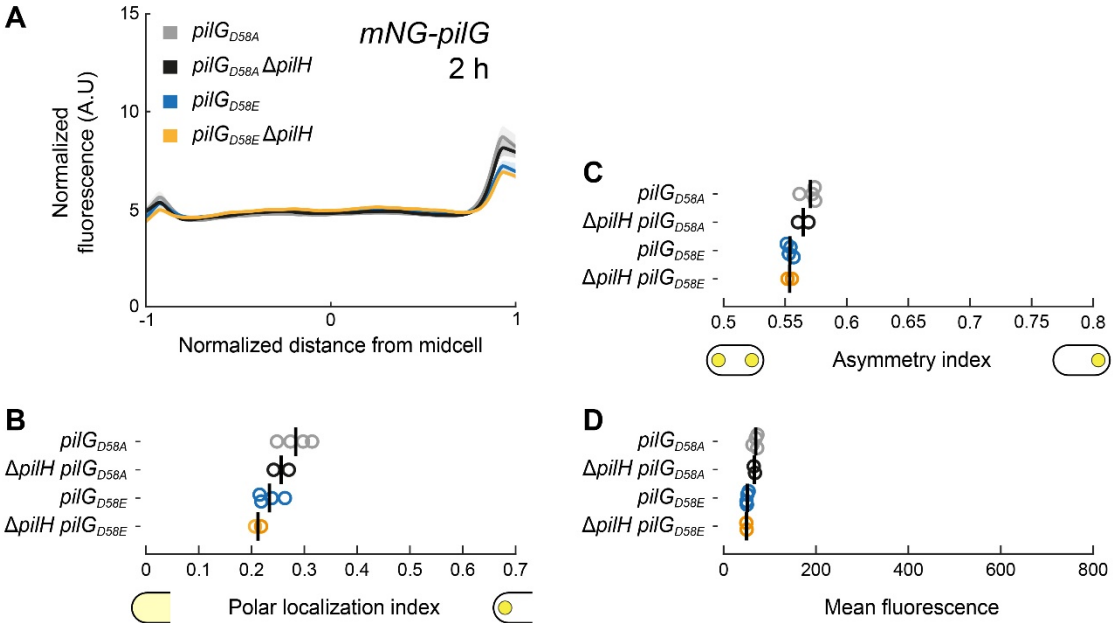

FIGURE S3.15. PilH has no effect on polar localization of non-phosphorylatable PilG mutants.

(A) Average fluorescence profiles of mNG-PilH point mutants after 2h surface growth.

(B) Quantification of polar localization, (C) asymmetry index and (D) mean cellular fluorescence. Solid lines, mean normalized fluorescence profiles across biological replicates. Shaded area, standard deviation across biological replicates. Circles, median of each biological replicate. Vertical bars, mean across biological replicates.

FIGURE S3.16

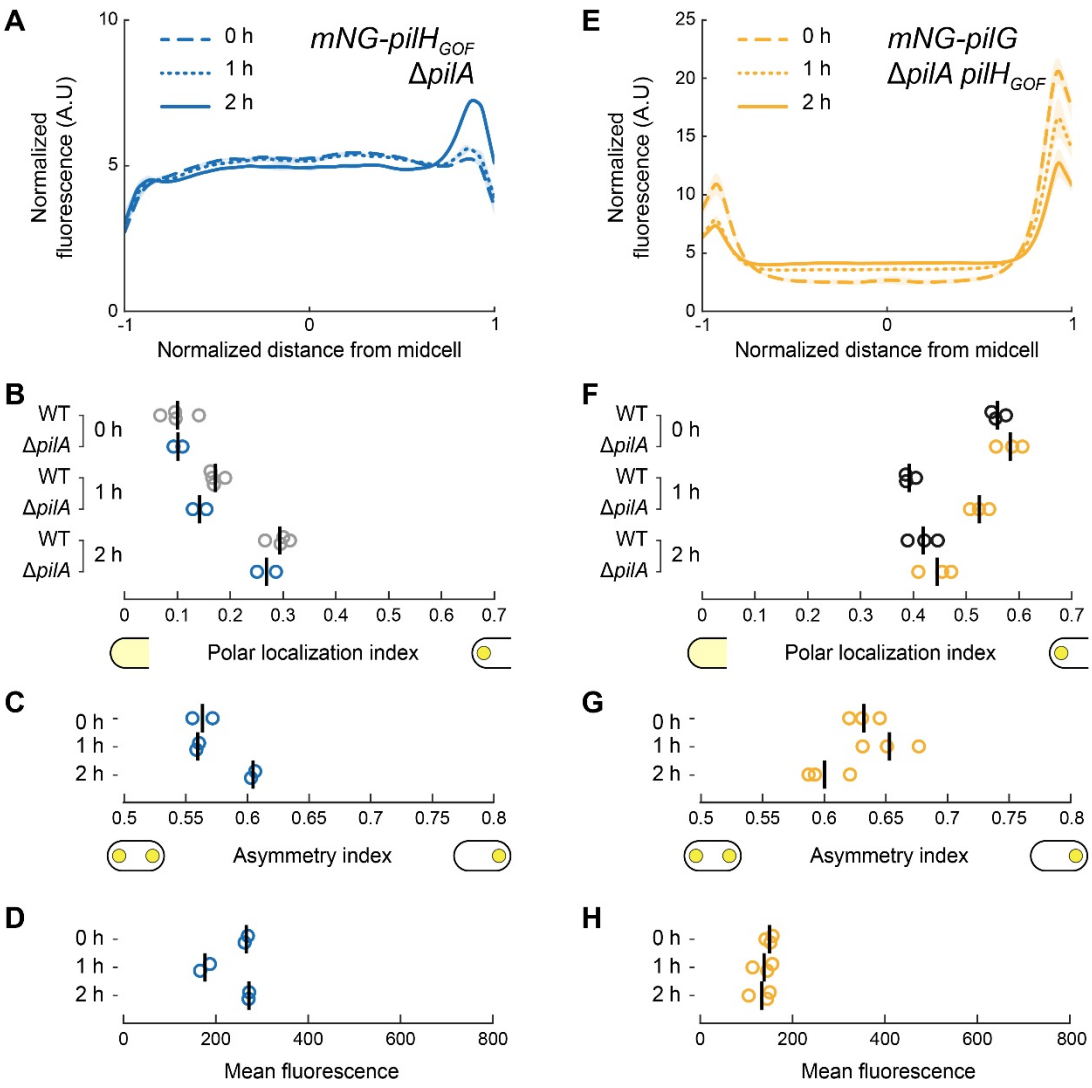

FIGURE S3.16. PilH$_{GOF}$ localization and PilH$_{GOF}$-dependent regulation of PilG in Δ*pilA*.

Time course of localization profiles of (A) mNG-PilH$_{GOF}$ in Δ*pilA* and (E) mNG-PilG in Δ*pilA pilH$_{GOF}$* in cells grown on solid substrate.

Quantification of corresponding (B), polar localization, (C) asymmetry index and (D) mean cellular fluorescence. While the overall localization is similar between WT and Δ*pilA*, the change over time is delayed in Δ*pilA* compared to WT. Solid lines, mean normalized fluorescence profiles across biological replicates. Shaded area, standard deviation across biological replicates. Circles, median of each biological replicate. Vertical bars, mean across biological replicates.

FIGURE S3.17

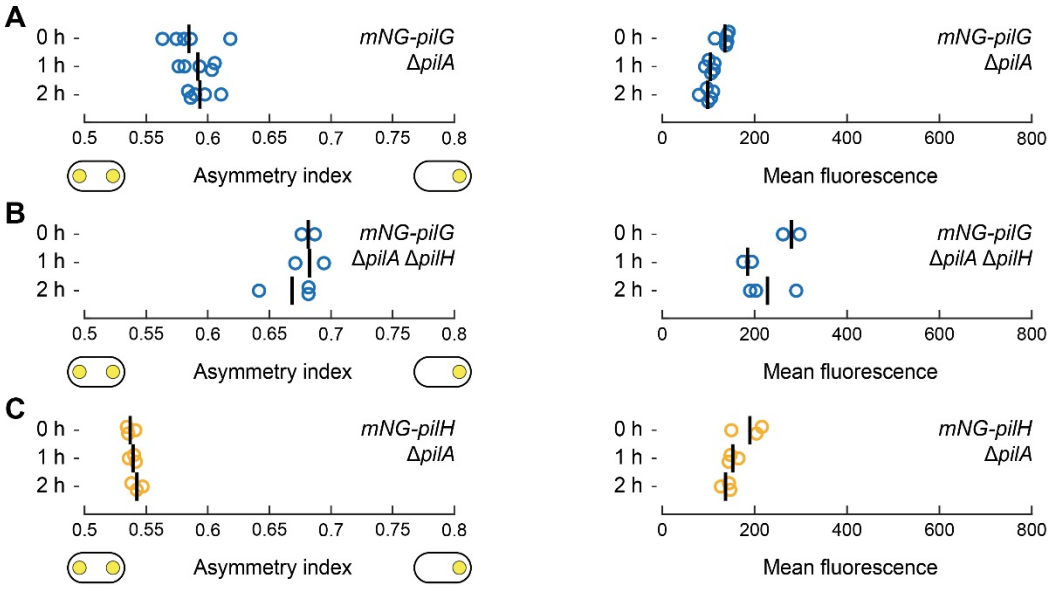

FIGURE S3.17. Asymmetry indexes and mean cell fluorescence.

Data for (A) *mNG-pilG* Δ*pilA*, (B) *mNG-pilG* Δ*pilA* Δ*pilH*, (C) *mNG-pilH* Δ*pilA* corresponding to Figure 8. Circles, median of each biological replicate. Vertical bars: mean across biological replicates.

ADDITIONAL SUPPLEMENTAL MATERIAL

Table S3.1 to S3.4, Legends for Movie S3.1 to Movie S3.4, and Movie S3.1 to Movie S3.4 can be found in the full supplemental material found at:

https://doi.org/10.15252/embj.2022112165

https://www.embopress.org/doi/full/10.15252/embj.2022112165?af=R

CHAPTER FOUR

SPATIAL CONTROL OF SENSORY ADAPTATION MODULATES MECHANOSENSING IN PSEUDOMONAS AERUGINOSA

SUMMARY

Sensory signaling pathways use adaptation to dynamically respond to changes in their environment. Here, we report the mechanism of sensory adaptation in the Pil-Chp mechanosensory system, which the important human pathogen *Pseudomonas aeruginosa* uses to sense mechanical stimuli during surface exploration. Using biochemistry, genetics, and cell biology, we discovered that the enzymes responsible for adaptation, a methyltransferase and a methylesterase, are segregated to opposing cell poles as *P. aeruginosa* explore surfaces. By coordinating the localization of both enzymes, we found that the Pil-Chp response regulators influence local receptor methylation, the molecular basis of bacterial sensory adaptation. We propose a model in which adaptation during mechanosensing spatially resets local receptor methylation, and thus Pil-Chp signaling, to modulate the pathway outputs, which are involved in *P. aeruginosa* virulence. Despite decades of bacterial sensory adaptation studies, our work has uncovered an unrecognized mechanism that bacteria use to achieve adaptation to sensory stimuli.

INTRODUCTION

Living systems must adapt to ever changing external signals to elicit proper biochemical responses (Adibi et al., 2021). For example, neurons rapidly respond to changes in the environment by adapting to a broad range of temperatures or smells (Benda, 2021). The biological process of maintaining sensitivity in different background states is known as sensory adaptation and is a general feature of sensory signaling pathways in all domains of life (De Palo & Endres, 2013).

Much of what we know about sensory adaptation in bacteria comes from extensive studies of the *Escherichia coli* chemotaxis pathway, which has served as a model system. This sensory pathway responds to and signals across several orders of magnitude of ligand concentrations without reaching saturation (Hansen et al., 2008; Mao et al., 2003). By primarily binding chemical ligands (Liu et al., 2015; Milburn et al., 1991), methyl-accepting chemotaxis proteins (MCPs, also known as chemoreceptors) signal to downstream components that promote a chemotactic response(Briegel et al., 2009b). MCPs activate a histidine kinase (CheA) that can transfer a phosphoryl group to a response regulator (CheY)(Muok et al., 2020; *Rapid Phosphotransfer to CheY from a CheA Protein Lacking the CheY-Binding Domain | Biochemistry*, n.d.). Upon phosphorylation, CheY binds to the base of the flagellar motor to change the direction of flagellar rotation, thereby controlling swimming direction (Sarkar et al., 2010).

Sensory adaptation is achieved through a negative feedback loop that involves reversible methylation of MCPs (Goy et al., 1977; Springer et al., 1977). MCP methylation is

catalyzed by the constitutively active CheR methyltransferase (Djordjevic & Stock, 1997, 1998; J. B. Stock et al., 1984), which enhances MCP signaling activity (Ninfa et al., 1991). Activated by CheA-dependent phosphorylation, like CheY, the CheB methylesterase demethylates MCPs, thereby decreasing MCP signaling activity (Lupas & Stock, 1989; A. H. West et al., 1995). By tuning MCP sensitivity and signaling activity, MCP methylation therefore serves as the molecular basis of bacterial sensory adaptation. Overall, sensory adaptation ensures that *E. coli* can robustly chemotax in response to small changes in ligand concentration that occur in chemical gradients (Alon et al., 1999; Barkai & Leibler, 1997; Yi et al., 2000).

Pseudomonas aeruginosa, an important human pathogen, relies on four sensory signaling pathways to adapt to its environment, including during human infections (Matilla et al., 2021). Two sensory pathways are involved in *P. aeruginosa* chemotaxis, while a third sensory pathway, the Wsp system, participates in biofilm formation (D'Argenio et al., 2002; Hickman et al., 2005; Matilla et al., 2021). We have recently shown that the Pil-Chp system, the fourth sensory pathway, senses mechanical stimuli generated by surface contact, thereby participating in mechanosensing (Persat, Inclan, et al., 2015c). Although all four of the sensory pathways encode predicted sensory adaptation enzymes, minimal information is available about how sensory adaptation functions during *P. aeruginosa* mechanosensing.

We have demonstrated that the Pil-Chp system responds to mechanical signals transmitted by type IV pili (TFP) upon surface contact (Persat, Inclan, et al., 2015c). TFP

are polarly localized protein filaments that undergo repeated cycles of extension, attachment, and retraction (Burrows, 2012c). By localizing TFP to one cell pole (i.e. leading pole), cells propel themselves forward in a specialized form of surface exploration called twitching motility (Burrows, 2012c). Surface contact through TFP stimulates PilJ(Koch et al., 2022b; Persat, Inclan, et al., 2015c), the Pil-Chp MCP, initiating signaling through the downstream Pil-Chp components to trigger two outputs: the polarized deployment of additional TFP and the production of the second messenger, cyclic adenosine monophosphate (cAMP) (Bertrand et al., 2010c; Fulcher et al., 2010b; Luo et al., 2015; Persat, Inclan, et al., 2015c; Whitchurch et al., 2004b).

Through deploying more TFP at one cell pole, *P. aeruginosa* can establish a local positive feedback loop that promotes twitching in the direction of mechanical stimulation (“mechanotax”) over long distances and activate a cAMP-dependent acute virulence program. Either spontaneously or upon mechanical perturbations, such as cell-cell collisions, the Pil-Chp system also inverts TFP polarity to induce reversals in twitching motility direction (Kühn et al., 2021b, 2023). The twitching motility reversals are coordinated by the spatial organization of PilG and PilH, two antagonistic CheY-like response regulators that are downstream components of the Pil-Chp system (Kühn et al., 2023). Local Pil-Chp activation at the leading pole recruits and activates PilG through phosphorylation, which drives the positive feedback loop that sustains forward movement. Accumulation of bipolarly localized PilH serves as a brake to inhibit PilG phosphorylation and enable twitching motility reversals.

The Pil-Chp regulon also encodes two predicted sensory adaptation enzymes, the methyltransferase PilK and the methylesterase ChpB (Darzins, 1995; Fulcher et al., 2010b; Whitchurch et al., 2004b). However, if and how sensory adaptation takes place in the Pil-Chp system during mechanosensing is unresolved. Here, we test the hypothesis that PilK and ChpB are bona fide sensory adaptation enzymes that control PilJ methylation and sensory adaptation during mechanosensing. We used PilK and ChpB mutants in conjunction with a method to assess PilJ methylation *in vivo* to demonstrate that PilJ undergoes reversible methylation that modulates Pil-Chp signaling. Using functional fluorescent protein fusions, we discovered that the Pil-Chp sensory adaptation enzymes are segregated to opposite cell poles in twitching *P. aeruginosa* cells. We further demonstrate that PilG and PilH dictate the localization behavior of PilK and ChpB, which is critical to control the PilJ methylation state. Our study thus reveals the mechanism of sensory adaptation during bacterial mechanosensing.

RESULTS

PilK and ChpB modulate twitching motility reversals and cAMP production.

In addition to encoding two antagonistic response regulators, PilG and PilH, the Pil-Chp operon encodes two predicted sensory adaptation enzymes, the PilK methyltransferase and ChpB methylesterase. While the response regulators have antagonistic effects on the physiological outcomes of Pil-Chp signaling (**Figure 4.1A**), limited information exists about how PilK and ChpB impact the system's two outputs: twitching motility and cAMP production(Fulcher et al., 2010b; Whitchurch et al., 2004b).

Although deletion of *pilK* and *chpB* have minimal effects on twitching motility as assayed by the subsurface stab assay (Darzins, 1995; Fulcher et al., 2010b; Whitchurch et al., 2004b)(**Figure S4.1A**), whether PilK and ChpB alter single cell twitching motility has not been explored. To address this question, we calculated the reversal frequencies of isolated Δ*pilK* and Δ*chpB* twitching cells from movies, either upon spontaneous reversals or upon collision with other bacteria (Kühn et al., 2021b, 2023). Isolated motile cells of either Δ*pilK* or Δ*chpB* exhibited slightly lower reversal frequencies than WT, with only Δ*chpB* reaching statistical significance (**Figure 4.1B, Figure S4.2A**). To further explore potential differences in the reversal rates, we examined whether the decrease in reversal frequencies observed in Δ*pilK* and Δ*chpB* were amplified in a sensitized background with elevated cAMP (Δ*cpdA*). In the absence of CpdA, *P. aeruginosa* has constitutively elevated cAMP, with a concomitant increase in the number of TFP and reversal frequency(Fuchs et al., 2010; Fulcher et al., 2010b; Inclan et al., 2011; Kühn et al., 2021b). The reversal frequency of either Δ*pilK*Δ*cpdA* or Δ*chpB*Δ*cpdA* was significantly

decreased compared to Δ*cpdA* (**Figure 4.1B, Figure S4.2A**). The decrease in reversal frequencies was not due to altered twitching motility speed, as the twitching motility speed of Δ*pilK*Δ*cpdA* and Δ*chpB*Δ*cpdA* was not statistically different compared to Δ*cpdA* (**Figure S4.2B**). We conclude that PilK and ChpB modulate the frequency of twitching motility reversals, especially when more mechanically active TFP are present.

Activation of the Pil-Chp system by mechanosensing also promotes cAMP production, albeit on the timescale of hours (Luo et al., 2015; Persat, Inclan, et al., 2015c). cAMP binds to the Vfr transcriptional activator to upregulate the transcription of >200 genes, including an acute virulence program (S. E. West et al., 1994; Wolfgang et al., 2003b). We thus used Δ*pilK* and Δ*chpB* strains to examine the role of these sensory adaptation enzymes in cAMP production over time (**Figure 4.1C**). We quantified cAMP levels from liquid-grown bacteria and from bacteria plated for up to 6 h on an agar surface, where mechanosensing occurs. In WT, cAMP levels increased upon surface contact. Maximal cAMP levels were observed at 2-3 h of surface growth and then decreased towards baseline levels at ~ 6 h of surface growth, consistent with our previously reported results (Persat, Inclan, et al., 2015c). As expected, cAMP levels were constitutively low in Δ*cyaB* (deletion of the primary adenylate cyclase)(Fulcher et al., 2010b; Persat, Inclan, et al., 2015c; Wolfgang et al., 2003b) and persistently elevated in Δ*cpdA* (deletion of the cAMP-specific phosphodiesterase)(Fuchs et al., 2010; Inclan et al., 2011; Persat, Inclan, et al., 2015c). In Δ*pilK*, cAMP levels increased upon surface contact and decreased towards baseline, similar to WT, but the peak cAMP level was slightly decreased (**Figure 4.1C**). In contrast, cAMP levels were elevated at all timepoints in Δ*chpB* as compared to WT.

However, cAMP levels still decreased towards baseline levels over time without ChpB (**Figure 4.1C**). Although sensory adaptation enzymes typically reset the physiological outcome(s) of bacterial sensory systems, our data suggest that PilK and ChpB are not required to return cAMP levels back towards pre-stimulation levels. Rather, resetting cAMP levels to the unstimulated state (i.e., liquid growth) requires the phosphodiesterase CpdA (**Figure 4.1C**), whose transcription is regulated by cAMP (Fuchs et al., 2010). We suggest instead that PilK and ChpB fine-tune cAMP production as well as reversal rates during twitching motility, likely by controlling the methylation state of the Pil-Chp receptor.

PilJ methylation increases in response to mechanosensing and is controlled by PilK and ChpB.

PilJ, the MCP of the Pil-Chp system, is required to sense and to respond to mechanical inputs generated during surface contact (Luo et al., 2015; Persat, Inclan, et al., 2015c); however, whether PilJ becomes methylated *in vivo* by the action of PilK and ChpB has never been demonstrated. We therefore tested whether PilJ methylation is detectable *in vivo* and whether PilJ methylation changes during liquid growth compared to surface growth. For these studies, the native *pilJ* gene was replaced with a *3xFlag-pilJ* fusion for detection by immunoblot analysis. Full-length 3xFlag-PilJ migrated as a single band of the expected molecular weight on conventional SDS-PAGE (**Figure S4.1B**). The chromosomally integrated 3xFlag-PilJ is functional, as demonstrated by near wild-type (WT) levels of subsurface twitching motility (**Figure S4.1A**) and cAMP production (**Figure S4.1C**). We used a well-established low-bis SDS-PAGE separation protocol to detect and quantify MCP methylation *in vivo* (hereafter referred to as methylation immunoblots)

(Boyd & Simon, 1980; DeFranco & Koshland, 1980; Engström & Hazelbauer, 1980; Feng et al., 1997; Lai et al., 2017; Sherris & Parkinson, 1981). We detected two differentially migrating species of PilJ during liquid and surface growth (**Fig S4.3A**). By analogy to the migration of *E. coli* MCPs in methylation immunoblots (Boyd & Simon, 1980; DeFranco & Koshland, 1980; Engström & Hazelbauer, 1980; Feng et al., 1997; Lai et al., 2017; Sherris & Parkinson, 1981), the slower migrating band is predicted to represent the unmethylated PilJ state, and the faster migrating band is predicted to represent a methylated form of PilJ (which we validate below). By calculating the fraction of methylated PilJ, we demonstrated that methylated PilJ was significantly increased after 2 h of surface growth compared to liquid growth ($p=0.002$; **Figure 4.1D**), suggesting that PilJ methylation increases in response to mechanical stimuli generated during surface contact.

Since surface contact promotes cAMP synthesis (Luo et al., 2015; Persat, Inclan, et al., 2015c) (**Figure 4.1C**), and many TFP and Pil-Chp genes are positively regulated by cAMP (Wolfgang et al., 2003b), we assessed whether the increase in PilJ methylation after surface growth was a secondary consequence of increased cAMP levels. The fraction of methylated PilJ did not significantly change in strains with low cAMP levels (Δ*cyaB*) or with high cAMP levels (Δ*cpdA*; **Figure 4.3B,C**). We conclude that the increase in PilJ methylation after surface contact is likely a direct response to mechanosensing, rather than a secondary effect from the increase in cAMP levels.

We next tested whether PilK and ChpB control the methylation state of PilJ and to definitively assign methylation states to the two PilJ species observed in the methylation

immunoblots. We introduced *3xFlag-pilJ* into Δ*pilK*, Δ*chpB*, and Δ*pilK*Δ*chpB* (**Figure 4.1D, Figure S4.3A**). In methylation immunoblots of Δ*pilK and* Δ*pilK*Δ*chpB*, we primarily observed a slower migrating band, which likely corresponds to unmethylated PilJ, and an almost undetectable faction of methylated PilJ. In Δ*chpB*, the faster-migrating 3xFlag-PilJ band was the most abundant species, likely corresponding to methylated PilJ, with a corresponding increase in the fraction of methylated PilJ. Thus, like the migration behavior of *E. coli* MCPs (Boyd & Simon, 1980; DeFranco & Koshland, 1980; Engström & Hazelbauer, 1980; Feng et al., 1997; Lai et al., 2017; Sherris & Parkinson, 1981), methylated PilJ migrates faster than unmethylated PilJ in this experimental setup.

To link PilK and ChpB function to their enzymatic activity, we replaced the corresponding WT *pilK* and *chpB* alleles in *3xFlag-pilJ* with the respective catalytic site mutants, based on homology to *E. coli* CheR and CheB, respectively(Djordjevic et al., 1998; Djordjevic & Stock, 1997) (*pilK*$_{R92E}$ and *chpB*$_{H184Y,}$ hereafter referred to as *pilK*$_{LOF}$ and *chpB*$_{LOF}$). Twitching motility subsurface stab assays (**Figure S4.1A**), cAMP measurements (**Figure S4.1C**), and methylation immunoblots (**Figure 4.1D**) showed that each loss-of-function (LOF) mutant phenocopied the respective *pilK* and *chpB* deletion mutant. We conclude that the enzymatic activity of PilK and of ChpB is needed to control PilJ methylation, thereby validating that PilK and ChpB are bona fide bacterial adaptation enzymes. Overall, we propose that PilK and ChpB modulate twitching motility and cAMP production by controlling PilJ methylation in response to mechanosensing.

PilK and ChpB are spatially segregated to opposite poles in twitching cells.

We have shown that the dynamic localization of PilG and PilH, the two response regulators of the Pil-Chp system, establish TFP polarity and dictate reversals(Kühn et al., 2023). We thus considered whether PilK and ChpB might also exhibit dynamic subcellular localization that could explain the mechanism by which they control PilJ methylation and modulate outcomes of Pil-Chp signaling. To test this hypothesis, we quantified static population-averaged fluorescent profiles of chromosomal ChpB-mNeonGreen (ChpB-mNG) and plasmid-expressed mNG-PilK (**Figure 4.2**). From the fluorescence profiles, we derived (i) a polar localization index, measuring the ratio of polar versus cytoplasmic localization and (ii) an asymmetry index, which quantifies the fluorescence intensity difference between the two poles(Kühn et al., 2021b, 2023).

We verified that ChpB-mNG was functional, as evidenced by WT twitching motility in sub-surface stab assays, near WT cAMP production, and expression of a full-length protein as assessed by immunoblot (**Figure 4.4**). We observed polar foci of ChpB-mNG from the moment cells encounter the surface (time = 0 h) to ~2 h of surface contact (**Figure 4.2A, C, E; Figure S4.5A**; later time points were not examined). In most cells, the fluorescent signal appeared asymmetrically localized, with a more pronounced peak in the fluorescent profile defining the bright pole (close to x = 1; **Figure 4.2C; Figure S4.5A**). Since chromosomally integrated PilK fusion strains exhibited decreased twitching motility (**Figure S4.6A**), we instead expressed mNG-PilK at low levels from a plasmid in a Δ*pilK* background. Plasmid-expressed mNG-PilK exhibited WT twitching motility and restored PilJ methylation in Δ*pilK* (**Figure S4.6B, C**), although no full-length protein species could

be detected by immunoblotting (**Figure S4.6D, E**). In contrast to chromosomal ChpB-mNG, mNG-PilK polar foci were very dim upon initial surface contact (time = 0 h) but became more visible after 2 h of surface growth, with the fluorescent signal appearing primarily at one cell pole (**Figure 4.2B, D, F; Figure S4.5A**). We observed that low cAMP levels (Δ*cyaB)* diminished polar localization of mNG-PilK and ChpB-mNG, while elevated cAMP levels (Δ*cpdA)* enhanced their polar localization (**Figure S4.7**). These results suggest that cAMP levels influence the polar localization of PilK and ChpB, without influencing the fraction of methylated PilJ (**Figure S4.3C**).

As both PilK and ChpB exhibit asymmetric polar localization, we determined whether they preferentially localize to the leading or to the lagging pole of twitching cells. For this assessment, we calculated an alignment factor between twitching direction and fluorescence asymmetry. A positive alignment factor indicates localization to the leading pole, whereas a negative alignment factor indicates localization to the lagging pole. Similar to mNG-PilG (Kühn et al., 2021b), ChpB-mNG exhibited a positive alignment factor in almost all motile cells, demonstrating preferential localization to the leading pole in twitching cells (**Figure 4.2G, I, J**). In contrast, mNG-PilK exhibited a negative alignment factor in most motile cells, showing preferential localization to the lagging pole in twitching cells (**Figure 4.2H, I, J**). We also observed that the localization of mNG-PilK and ChpB-mNG was dynamic. Upon a twitching motility reversal, mNG-PilK and ChpB-mNG fluorescent foci changed polarity to the new lagging and new leading pole, respectively (**Figure 4.2G, H; Movie S4.1** for PilK; **Movie S4.2** for ChpB). In summary, mNG-PilK and ChpB-mNG are spatially segregated to opposite poles in twitching *P. aeruginosa* cells.

By primarily localizing to the leading pole, where mechanosensing takes place, ChpB may demethylate and decrease PilJ signaling. At the opposite (lagging) pole, PilK may methylate and prime PilJ for efficient signaling once mechanosensing begins at the new leading pole.

The response regulators PilG and PilH control the PilK and ChpB localization patterns.

To understand how PilK and ChpB are spatially segregated to opposite cell poles in twitching cells, we investigated the mechanisms specifying their localization patterns. As both PilG (Kühn et al., 2021b, 2023) and ChpB (**Figure 4.2**) dynamically localize to the leading pole, we first tested whether ChpB is required for PilG asymmetric polar localization. Polar localization and asymmetry indices of mNG-PilG were unchanged in Δ*chpB* (**Figure S4.9**), indicating that PilG localization is not regulated by ChpB. Remarkably, polar localization of ChpB-mNG was lost in Δ*pilG,* resulting in a polar localization index of 0, both in high (**Figure 4.3A, C, E**) and low cAMP backgrounds (**Figure S4.10**). Moreover, ChpB asymmetric polar localization was enhanced in Δ*pilH,* in a similar manner to PilG(Kühn et al., 2023) (**Figure 4.3A, C, E, G**), while ChpB did not play a role in the localization of chromosomally expressed and functional mNG-PilH (**Figure S4.9**). Polar localization of ChpB-mNG was lost in Δ*pilG*Δ*pilH* (**Figure 4.3A, C, E**), demonstrating that PilH indirectly regulates ChpB asymmetric polar localization through PilG. Overall, these data suggest that PilG directs ChpB to the leading pole.

Given that ChpB asymmetric polar localization depends on PilG, we considered whether PilG could recruit ChpB by direct or indirect binding. We performed affinity-purification mass spectrometry on lysates prepared from bacteria transformed with a plasmid overexpressing PilG-HA as the bait, PilH-HA as a comparison bait, or from untransformed WT as a control. Protein-protein interactions were scored by SAINT from a scale of 0 to 1(H. Choi et al., 2011). ChpB was significantly enriched in affinity purified PilG-HA lysates (SAINT score 0.98), while no ChpB peptides were detectable in affinity purified PilH-HA (**Table S4.1**). Therefore, a protein-protein interaction between PilG and ChpB may account for their linked localization patterns.

We also investigated factors regulating PilK localization to the lagging pole. Since ChpB primarily localizes to the leading pole, we tested whether ChpB excludes PilK from the leading pole. The polar localization index of mNG-PilK was slightly increased without *chpB*; however, this increase in polar localization was likely due to the high cAMP levels in Δ*chpB*, as a similar increase was observed in Δ*cpdA* (**Figure 4.11A, C, E**). These data suggest that mNG-PilK can localize to the lagging pole without *chpB*. In a similar trend, ChpB-mNG localization was unchanged in Δ*pilK* (**Figure S4.11B, D, F, H**). Thus, PilK and ChpB localization patterns are largely independent. We next tested whether the PilK polar localization is regulated by the Pil-Chp response regulators, as is the case with ChpB. The polar localization of mNG-PilK was dramatically increased in Δ*pilG* and almost undetectable in Δ*pilH*, independent of cAMP levels (**Figure 4.3B, D, F; Figure S4.10B, D, F**). However, as mNG-PilK shows prominent polar localization in Δ*pilG*Δ*pilH* (**Figure 4.3B, D, F**), our data suggest that PilK can localize to the lagging pole independently of

PilG and PilH. We propose that the Pil-Chp response regulators instead ensure that PilK is segregated to the lagging pole. PilG may prevent PilK accumulation at the leading pole while PilH allows PilK localization at lagging pole in a PilG-dependent manner. Taken together, these findings indicate that PilG and PilH establish the subcellular architecture of the Pil-Chp sensory adaptation enzymes.

The ChpA histidine kinase and PilH activation affect ChpB localization.

We previously demonstrated that PilG is recruited to the cell poles (i) by its association with and phosphorylation by ChpA(Kühn et al., 2023), the Pil-Chp histidine kinase, and (ii) by FimL, a polarly localized scaffold protein(Inclan et al., 2011; Inclan, Persat, Greninger, Von Dollen, et al., 2016; Kühn et al., 2023; Whitchurch et al., 2004b). Deletion of either *chpA* or *fimL* decreases PilG polar localization by ~50%, whereas PilG polar localization is abolished in the Δ*fimL*Δ*chpA* double mutant (Kühn et al., 2023). These findings suggest that there may be two separate populations of PilG, one associated with ChpA and one associated with FimL. We therefore tested whether ChpA and FimL are required for the localization of ChpB. While *fimL* deletion had no measurable effect on ChpB localization, deletion of *chpA* abolished ChpB polar localization (**Figure 4.4A, B; Figure S4.12A, B, E**). Thus, our results suggest that only the PilG pool associated with ChpA is required for ChpB polar localization.

One explanation for the dependence on ChpA is that polar recruitment of ChpB requires phosphorylation of PilG by ChpA. To test this hypothesis, we quantified ChpB localization in a ChpA mutant, $chpA_{LOF}$, which is unable to undergo autophosphorylation and

subsequent phosphoryl group transfer to PilG(Bertrand et al., 2010c; Kühn et al., 2023). Localization of ChpB was indistinguishable from WT in *chpA*$_{LOF}$ (**Figure 4.4A, B; Figure S4.12A, B, F**). These data suggest that phosphorylation of PilG is not required for polar recruitment of ChpB.

We also assessed the role of PilG phosphorylation in ChpB polar recruitment by mutating the PilG phosphoryl group acceptor, aspartate 58, to either alanine or glutamic acid. The *pilG*$_{D58A}$ *and pilG*$_{D58}$E mutants have decreased twitching motility and cAMP production, suggesting that both point mutations diminish PilG function(Kühn et al., 2023). When we investigated ChpB localization in *pilG*$_{D58A}$ *and pilG*$_{D58}$E, ChpB polar localization was nearly undetectable in *pilG*$_{D58A}$ and greatly decreased in *pilG*$_{D58E}$ (**Figure 4.4A, C; Figure S4.12A, B, F**), even when cAMP levels are restored (Δ*cpdA*). These results further support that ChpB localization depends on PilG because PilG$_{D58A}$ and PilG$_{D58E}$ cannot properly localize to the leading pole (Kühn et al., 2023). We cannot, however, distinguish whether phosphorylation of PilG contributes to ChpB localization. Overall, we conclude that ChpA and PilG promote localization of ChpB to the leading pole, primarily in a phosphorylation independent manner.

We further investigated the role of PilH phosphorylation in the localization of ChpB-mNG using phosphorylation site mutants of PilH, *pilH*$_{D52A}$ and *pilH*$_{D52E}$ (hereafter *pilH*$_{LOF}$ *and pilH*$_{GOF}$). We have previously reported that *pilH*$_{LOF}$ *and pilH*$_{GOF}$ mimic the inactive (non-phosphorylated) and active (phosphorylated) state of PilH, respectively, as assessed by twitching motility, cAMP production, and localization assays (Kühn et al., 2023). We

observed that *pilH*$_{LOF}$ phenocopied Δ*pilH* with increased ChpB asymmetric polar localization, while ChpB-mNG localization was comparable to WT in *pilH*$_{GOF}$ (**Figure 4.4A, D, E; Figure S4.12A, G**). As PilH phosphorylation ensures that PilG dynamically localizes to the leading pole, resulting in increased PilG asymmetric localization in Δ*pilH* and *pilH*$_{LOF}$(Kühn et al., 2023), we infer that PilH~P indirectly regulates ChpB localization to the leading pole by enabling ChpB dynamic behavior.

PilG and PilH work together to exclude PilK from the leading pole.

To further investigate how the Pil-Chp response regulators segregate PilK to the lagging pole, we monitored the localization of mNG-PilK in phosphorylation mutants of PilG and PilH. Even when cAMP levels were normalized by deleting *cpdA*, PilK polar localization was increased in *pilG*$_{D58A}$ and *pilG*$_{D58E}$, with *pilG*$_{D58A}$ showing higher PilK polar localization than *pilG*$_{D58E}$ (**Figure 4.5A, C; Figure S4.12C, D, H**). This finding is consistent with both *pilG* mutants having decreased PilG function. In *chpA*$_{LOF}$, a background in which PilG cannot become phosphorylated, polar localization of PilK was also enhanced, comparable to the level of PilK polar localization observed in the *pilG* point mutants (**Figure 4.5A, C; Figure S4.12C, D, H**). Because polar localization of PilK was higher in Δ*pilG* compared to either of the PilG phosphorylation site mutants (**Figure 4.5A, C**), our data suggest that PilG phosphorylation affects the degree of PilK localization to the lagging pole.

For the PilH phosphorylation site mutants, we found that PilK polar localization was nearly abolished in *pilH*$_{LOF}$ (**Figure 4.5B, D; Figure S4.12C, D,** I), similar to the loss of PilK polar

localization in Δ*pilH* (**Figure 4.3F**). In contrast, PilK polar localization was enhanced in $pilH_{GOF}$ (**Figure 4.5B, D; Figure S4.12C, D, I**). PilK was polarly localized in Δ*pilG*, Δ*pilGpilH*$_{LOF}$, and Δ*pilGpilH*$_{GOF}$ (**Figure S4.13A-E**), demonstrating that PilH phosphorylation does not affect PilK polar localization in the absence of PilG. In summary, these results highlight that PilG, and indirectly PilH, work together to segregate PilK to the lagging pole in twitching *P. aeruginosa*.

PilG and PilH regulate PilJ receptor methylation.

To link PilJ methylation to the localization patterns of PilK and ChpB established by the Pil-Chp response regulators, we examined the PilJ methylation state in *pilG* and *pilH* mutant strains encoding the functional 3xFlag-PilJ fusion (**Figure S4.14; Figure S4.15**), using methylation immunoblots (**Figure 4.6; Figure S4.16**). In Δ*pilG*, $pilG_{D58A}$ and $pilG_{D58E}$, the fraction of PilJ methylation increased ~20-30% compared to WT levels (**Figure 4.6A; Figure S4.16A**). Similar results were observed in a Δ*cpdA* background, indicating that the increased methylation seen in *pilG* mutants is independent of cAMP levels (**Figure 4.6A; Figure S4.16A**). In the case of Δ*pilG*, the increased fraction of PilJ methylation required PilK and was enhanced in the absence of ChpB (**Figure 4.6C; Figure S4.16C**). The enhanced fraction of PilJ methylation in the absence of functional PilG is consistent with the role of PilG in recruiting ChpB to the leading pole and segregating PilK to the lagging pole (**Figure 4.3; Figure 4.4; Figure 4.5**).

In Δ*pilH* and $pilH_{LOF}$, where PilK is cytoplasmic and ChpB asymmetric polar localization is enhanced (**Figure 4.3; Figure 4.4; Figure 4.5**), the fraction of PilJ methylation was

decreased, mirroring that of Δ*pilK* and of Δ*pilH*Δ*pilK* (**Figure 4.6B, D; Figure S4.16B, D**). Compared to Δ*chpB,* PilJ methylation remained low in Δ*pilH*Δ*chpB* (**Figure 4.6D; Figure S4.16D**), suggesting that cytoplasmic PilK cannot methylate PilJ even in the absence of ChpB. In $pilH_{GOF}$ (**Figure 4.6B; Figure S4.16B**), where PilK polar localization was enhanced (**Figure 4.5B, D**), PilJ methylation was increased. These data are most consistent with a model in which PilK promotes PilJ methylation at the lagging pole, while ChpB ensures that PilJ demethylation primarily occurs at the leading pole. The spatial control of PilJ methylation would ensure that upon twitching reversals, PilJ at the new leading pole is methylated and "poised" to efficiently promote Pil-Chp signaling once mechanosensing occurs (**Figure 4.7**).

DISCUSSION

Despite decades of work that have revealed the intricate details of adaptation in bacterial chemotaxis(Vladimirov & Sourjik, 2009), our understanding of adaptation in other bacterial sensory systems that are widespread throughout nature(Wuichet & Zhulin, 2010) is limited. Here, we report the mechanism of sensory adaptation in bacterial mechanosensing, using the Pil-Chp system of *Pseudomonas aeruginosa* as a model system. By controlling the methylation state of the PilJ receptor upon mechanosensing, the PilK methyltransferase and the ChpB methylesterase modulate the two outputs of the Pil-Chp system: twitching motility and cAMP production. Using functional fluorescent fusions, we discovered that PilK and ChpB are spatially segregated to the lagging and leading poles, respectively, in twitching *P. aeruginosa* cells. In addition to the PilK and ChpB catalytic activity, we showed that the *in vivo* PilJ methylation state depends on the localization of both enzymes. We further found that the Pil-Chp response regulators not only regulate TFP polarity and dictate twitching motility reversals, but that PilG, and indirectly PilH, coordinate the spatial segregation of PilK and ChpB. Together, our results reveal how Pil-Chp sensory adaptation uses spatial control as a strategy to modulate mechanosensing in *P. aeruginosa.* Therefore, our work uncovered an unrecognized mechanism to achieve adaptation to sensory stimuli in bacteria.

Despite their small size, *P. aeruginosa* cells can sense spatial environmental information. We and others have revealed that TFP transmit mechanical stimuli derived from surfaces at the leading pole(Koch et al., 2022b; Kühn et al., 2021b; Persat, Inclan, et al., 2015c). The Pil-Chp system, while encoding core components of bacterial sensory pathways, has

evolved a complex spatial regulatory network to sense and to respond to polarized mechanical stimuli. Specifically, we demonstrated that PilG and PilH, the antagonistic response regulators of the system, exhibit spatial regulation that is critical for localized Pil-Chp signaling (Kühn et al., 2023). For example, PilG is dynamically recruited to the leading pole, mirroring the localization of the TFP mechanosensors. This “local” pool of PilG at the leading pole amplifies TFP activity and Pil-Chp signaling, which enables persistent twitching motility and production of cAMP (**Figure 4.7A**). Reversals of twitching direction are orchestrated by PilH, the antagonistic Pil-Chp response regulator. Bipolarly localized PilH inhibits the activity of local PilG pools by potentially initiating PilG relocalization to the opposite cell pole. This event triggers a twitching motility reversal and resets localized Pil-Chp signaling (**Figure 4.7B**).

Building on this previous work, we now propose that the sensory adaptation branch of the Pil-Chp system also exhibits spatial regulation to facilitate TFP-mediated mechanosensing. Unlike CheR and CheB, which are anchored to MCP arrays at the cell pole independently of the localization of flagella (Banno et al., 2004; Shiomi et al., 2002), the Pil-Chp sensory adaptation enzymes are segregated to opposite mechanosensory cell poles. PilK localization to the lagging pole ensures that this pool of PilJ is methylated and poised to respond to mechanical stimuli upon TFP polarity and twitching motility reversals. When PilG relocalizes to the lagging pole to establish a new leading pole, the increased sensitivity of methylated PilJ may amplify the signal needed to complete a twitching motility reversal and produce cAMP (**Figure 4.7C**). Our model further predicts that the inverse occurs at the opposite pole. Recruitment of ChpB by PilG at the leading

pole would dampen PilJ methylation and thus attenuate Pil-Chp signaling (**Figure 4.7D**). We propose that Pil-Chp sensory adaptation resets localized Pil-Chp signaling at each pole instead of resetting “global” signaling capabilities of MCPs, as is the case during chemotaxis (Vladimirov & Sourjik, 2009). Spatial control of PilJ methylation would enable the Pil-Chp system to optimally respond to polarized mechanical stimuli during the establishment of the leading pole. This model would also explain why PilJ methylation modulates twitching motility reversals and the amplitude of cAMP production rather than returning the system to a single baseline.

Beyond their role in the excitatory branch of the Pil-Chp system(Bertrand et al., 2010c; Fulcher et al., 2010b; Kühn et al., 2021b, 2023; Persat, Inclan, et al., 2015c; Whitchurch et al., 2004b), our experiments reveal that the response regulators PilG and PilH have taken the additional function of regulating PilJ methylation and thus sensory adaptation. In the chemotaxis system, CheB phosphorylation by activated CheA enhances CheB methylesterase activity (Lupas & Stock, 1989), thereby tilting the “global” balance of MCP methylation to achieve sensory adaptation. In the Pil-Chp system, the ChpB receiver domain lacks key residues involved in phosphotransfer (Silversmith et al., 2016b), suggesting that ChpB phosphorylation might not play a role in regulating PilJ methylation. We instead provide evidence that PilJ methylation depends on PilG, and indirectly on PilH, because these CheY-like response regulators function together to segregate the Pil-Chp sensory adaptation enzymes to opposing poles during twitching motility. This model is supported by the observation that in *pilG* and *pilH* mutants, the localization of PilK and ChpB as well as overall PilJ methylation are unregulated. Thus, the mechanisms that

ensure interactions between sensory adaptation enzymes and their cognate MCPs likely have profound effects on MCPs methylation and adaptation. Consistent with this idea, CheR and CheB in the *E. coli* chemotaxis system are recruited and anchored to the polar MCP arrays by a C-terminal pentapeptide found in MCPs (Banno et al., 2004; Bartelli & Hazelbauer, 2011; Li et al., 2021; Shiomi et al., 2002). When their cognate C-terminal pentapeptide is deleted, CheR and CheB cannot mediate an adequate sensory adaptation response during chemotaxis(Barnakov et al., 1999; Li & Hazelbauer, 2006; Okumura et al., 1998). As there is no discernible C-terminal pentapeptide in PilJ (García-Fontana et al., 2014), we infer that PilK and ChpB gained spatial control of PilJ methylation by tightly linking their localization to response regulators of the system. Our work thus provides a unique perspective on how the excitatory branch of the Pil-Chp system directly regulates sensory adaptation during *P. aeruginosa* mechanosensing. In the chemotaxis system of *Bacillus subtilis*, CheY also mediates adaptation and MCP methylation, but CheY does so indirectly by participating in a feedback loop with additional proteins (CheC and CheD) not found in the *E. coli* chemotaxis and the Pil-Chp systems (Rao et al., 2008). By relying on spatial organization and on the response regulators, we suggest that Pil-Chp sensory adaptation has achieved a mechanistic complexity that has primarily been evident in eukaryotic sensory adaptation(De Palo & Endres, 2013).

Taken together, our previous and current studies illustrate how *P. aeruginosa* has optimized the excitatory and sensory adaptation branches of the Pil-Chp system to respond to mechanical stimuli, which is required to colonize new habitats, either in its natural environment or in human tissues. The spatial regulatory network that we describe

likely ensures that the Pil-Chp system can operate independently from the other three sensory pathways found in *P. aeruginosa*, all of which encode homologous core components (Matilla et al., 2021; Ortega et al., 2017). In the case of PilK and ChpB, their spatial segregation likely arose during their evolution as they have a unique evolutionary history when compared to their chemotactic counterparts, CheR and CheB (Wuichet & Zhulin, 2010). As 90% of bacterial sensory systems encode sensory adaptation enzymes (Wuichet & Zhulin, 2010), we anticipate that spatial regulation will be increasingly recognized as a critical component of adaptation in bacterial sensory systems.

MATERIALS AND METHODS

Bacterial strains, growth conditions and media.

Pseudomonas aeruginosa PAO1 ATCC 15692 (American Type Culture Collection) was used for all experiments in this study. *Escherichia coli* strains DH5α and Stellar (Takara Bio) were used for cloning. *E. coli* strain S17.1 was used for conjugative mating with *P. aeruginosa*. All strains were grown in LB medium (Carl Roth) at 37 °C with 280 rpm shaking with the addition of appropriate antibiotics, for *E. coli* 100 $\mu g.ml^{-1}$ ampicillin/carbenicillin or 10 $\mu g.ml^{-1}$ gentamycin, for *P. aeruginosa* 300 or 400 $\mu g.ml^{-1}$ carbenicillin or 60 or 100 $\mu g.ml^{-1}$ gentamycin. Solid LB media for cell growth, cAMP measurements, and methylation immunoblots were prepared by adding 1.5% ($wt \cdot vol^{-1}$) agar (Fisher Bioreagents) and antibiotics as appropriate. For experiments that included pCuAIgent plasmid-containing strains, no inducers were added to the media.

For subsurface stab assays, 35 ml of sterile 1% LB agar were poured into tissue culture-treated plastic dishes (150 x 25 mm, Corning). The plates were allowed to solidify overnight and used the next day. Before use, plates were dried in a flow hood for 20 min. Semi-solid tryptone media for single-cell twitching and microscopy were prepared by autoclaving 5 $g.l^{-1}$ tryptone (Carl Roth), 2.5 $g.l^{-1}$ NaCl (Fisher Bioreagents), and 0.5 % ($wt.vol^{-1}$) agarose standard (Carl Roth). To reproducibly ensure single-cell twitching, the tryptone media were allowed to cool down to 70 °C in the autoclave followed by cooling to 55 °C for 20 - 30 min in a water bath and pouring 28 ml medium into 90 mm petri dishes. The plates were dried in a flow hood for exactly 30 min and stored for at least one day and no more than two days at 4 °C in a plastic bag.

Strains and vector construction.

Strains used in this study are listed in Table S4.1, plasmids in Table S4.2, and oligonucleotides in Table S4.3. Chromosomal mutants of *P. aeruginosa* were generated as described previously(Kühn et al., 2021a, 2023). Genes were deleted or integrated by two-step allelic exchange using the suicide vectors $pEX18_{Amp}$ or $pEX18_{Gent}$ following the protocol in (Hmelo et al., 2015b). For genomic in-frame gene deletions or integrations, approximately 500 to 1000 base pair fragments of the up- and downstream regions of the designated gene were combined by PCR amplification and subsequent Gibson assembly(Gibson et al., 2009b). Point mutants were created by integrating the mutated gene into the corresponding gene deletion background by allelic exchange. All mutants, marker-free deletions, and insertions were verified by PCR and sequencing. Fluorescent fusion proteins were generated by fusing mNeonGreen (mNG) to the N- or C-termini of designated genes separated by a 5x-Glycine or 4x-Glycine-1x-Serine linker. Expression and size of fluorescent fusions was verified by Western blot. Functionality was tested by measuring twitching motility in the subsurface stab assay and cAMP production. Plasmids were constructed using standard Gibson assembly(Gibson et al., 2009b) or QuikChange site directed mutagenesis protocols(Xia et al., 2015) and introduced into *P. aeruginosa* cells by conjugative mating with *E. coli* S17.1 as donor(Hmelo et al., 2015b) or by using electroporation(K.-H. Choi et al., 2006).

mNG-tagged PilK was expressed from a cumic acid-inducible plasmid that was originally designed for *Agrobacterium tumefaciens*(Pierrat, 2022). Plasmid pXP313 was used as template for vector backbone PCR amplification and the mNG-PilK fusion fragment

amplified from pMK26 was integrated by Gibson assembly to yield plasmid pMK35. The kanamycin resistance gene was exchanged with the gentamycin resistance gene (template pEX18gm) by the same approach, yielding plasmid pMK65 that was used for all plasmid-expressed mNG-PilK experiments. In addition, plasmid pMK66 was generated as an empty vector control. It was modified for easier cloning by inserting a synthetic sequence downstream of the CuO regulatory site. The insert can be excised to linearize the plasmid for Gibson assembly using restriction enzymes XhoI and XbaI.

Twitching motility subsurface stab assay.

Single *P. aeruginosa* colonies were stabbed through 1% LB agar, with appropriate antibiotics if needed, to the bottom of the dish with a sterile 10 µl pipette tip. The plates were incubated at 37 °C overnight, and the agar was carefully removed with a 10 µl inoculating loop. The diameter of the observed twitching motility zone at the bottom of the dish was measured for each biological replicate (in cm). For each biological replicate, the relative twitching motility zone was calculated as a percentage of the WT twitching motility zone.

cAMP quantification.

cAMP levels were measured using the reporter plasmid pUC18-PlacP1/POXB20 as previously described(Kühn et al., 2023). LacP1 is a synthetic cAMP responsive promoter(Fulcher et al., 2010b) and OXB20 is a strong constitutive promoter (Oxford Genetics Ltd. UK, Sigma). *P. aeruginosa* were transformed with the reporter plasmid and plated on LB agar with 400 µg.ml^{-1} Carbenicillin (GoldBio) to generate single colonies.

Single colonies were grown overnight in 500 µl of LB broth in a 96-deepwell plate at 37 °C, with shaking at 900 rpm. Overnight cultures were diluted 1:100 and grown for 3 h with shaking, as described above. To measure cAMP levels in mid-log phase liquid conditions, an aliquot of the 1:100 subculture grown for 3 h was fixed by adding methanol-free paraformaldehyde (PFA, Thermo Scientific) to a final concentration of 4% and incubated for 10 min at room temperature. The reaction was quenched by adding 2.5 M glycine (Fisher Scientific) to a final concentration of 0.3 M. Using the same 1:100 subculture, a second fraction of bacteria was spotted onto agar plates and grown for 2 h, or up to 6 h, at 37 °C. Spots were scraped, resuspended in phosphate-buffered saline (PBS; UCSF Media Production Unit) and fixed, as described above. Samples were diluted in PBS and stored at 4 °C for no more than one day before analysis. An LSRFortessa flow cytometer (BD Biosciences) located in the UCSF Parnassus Flow CoLab (RRID:SCR_018206) was used to measure yellow fluorescent protein (YFP) in at least 30,000 mKate2-positive single cells. Exported Flow Cytometry Standard (FCS) files were analyzed in FlowJo and the YFP fluorescence intensity reported as median value for each biological replicate.

Methylation immunoblots.

Single colonies of 3xFlag-PilJ encoding strains were grown overnight in 500 µl of LB broth in a 96-deepwell plate at 37 °C, with shaking at 900 rpm and with appropriate antibiotics as needed. Overnight cultures were diluted 1:100 and grown for 3 h with shaking, as described above. To quantify PilJ methylation during mid-log growth, 500 µl of the 1:100 subculture grown for 3 h was pelleted by centrifugation (10 000 x g, 5 min, 4°C). The pellet was suspended in 2X Laemmli sample buffer (Biorad) with 2.5% 2-mercaptoethanol

(Sigma) and 0.1 U/µl Pierce universal nuclease (Thermo Scientific) and frozen at -20 °C. To quantify PilJ methylation during surface growth, a second fraction of bacteria from the same 1:100 subculture grown for 3 h was spotted onto 1.5% agar plates and grown for 2 h at 37 °C. Cells were scraped, resuspended into PBS (UCSF Media Production Unit), collected by centrifugation, suspended in sample buffer, and stored as described above. Pierce™ 660nm Protein Assay Reagent with Ionic Detergent Compatibility Reagent (Thermo Scientific) was used to measure protein concentration of each whole cell lysate.

2.5 µg of each whole cell lysate was separated on 11% SDS PAGE gels containing 0.074% bis-acrylamide (low-bis SDS- PAGE). Gels were electrophoresed at 200 V in running buffer (25 mM Tris, 192 mM glycine, 0.1% SDS, pH 8.3) until the 75 kDa marker of the protein standard (5 µl of Precision Plus Protein™ Standard (Biorad)) was ~ 2 cm from the bottom of the gel. Gels were transferred (20 V, 7 min) to PVDF membranes using the iBlot™ Dry blotting system (Thermo Scientific). Membranes were blocked in TBS (20mM Tris, 150mM NaCl, pH 7.5)/5% milk overnight. Membranes were incubated with monoclonal mouse anti-Flag M2 antibody (affinity isolated, catalogue number F3165, Sigma) in TBST (20mM Tris, 150mM NaCl, 0.05% Tween20, pH 7.5)/5% milk at a final concentration of ~1 µg/ml for 1 h. Membranes were washed 3x in TBST and incubated with IRDye® 680RD goat anti-mouse IgG secondary antibody (RRID AB_10956588, catalogue number 926-68070, LI-COR) and imaged on a LI-COR Odyssey CLx system. The signal intensity of individual bands was quantified with ImageStudioLite (LI-COR). The fraction of methylated PilJ was calculated from the signal intensity of the methylated PilJ band (bottom band) divided by the signal intensity of the sum of both PilJ methylated

and unmethylated bands ($Fraction\ of\ methylated\ PilJ = \left(\frac{signal\ of\ methylated\ PilJ}{signal\ methylated+unmethylated\ PilJ}\right) x\ 100$).

Immunoblotting.

Single colonies of strains expressing mNG protein fusions were grown overnight in LB broth with appropriate antibiotics as needed at 37 °C with shaking. Overnight cultures were diluted 1:100 and grown for 3 h with shaking. 1 ml of the 1:100 subculture was harvested by centrifugation (10 000 x g, 5 min, 4°C). The pellet was suspended in 2X Laemmli sample buffer (Biorad) with 2.5% 2-mercaptoethanol (Sigma) and 0.1 U/µl Pierce universal nuclease (Thermo Scientific) and frozen at -20 °C. Pierce™ 660nm Protein Assay Reagent with Ionic Detergent Compatibility Reagent (Thermo Scientific) was used to measure protein concentration.

2.5 µg of each whole cell lysate and 2 µl of a 1:10 dilution of the Precision Plus Protein™ Standard (Biorad) were separated on Any kD™ Mini-PROTEAN TGX™ Precast SDS PAGE gels. Gels were electrophoresed at 200 V in running buffer (25 mM Tris, 192 mM glycine, 0.1% SDS, pH 8.3) for 40 min. Gels were transferred (20 V, 7 min) to PVDF membranes using the iBlot™ Dry blotting system (Thermo Scientific). Membranes were blocked in in TBS (20mM Tris, 150mM NaCl, pH 7.5)/5% milk overnight, and they were probed with a 1:500 dilution of mouse monoclonal anti-mNG antibody (catalogue number 32F6, Chromotek) in TBST (20mM Tris, 150mM NaCl, 0.05% Tween20, pH 7.5)/5% milk for 1 h. Membranes were washed 3x in TBST and incubated with IRDye® 680RD goat anti-mouse IgG secondary antibody (RRID AB_10956588, catalogue number 926-68070,

LI-COR) and imaged on a LI-COR Odyssey system. Immunoblot images were generated using ImageStudioLite (LI-COR).

Fluorescence microscopy.

Microscopy was performed on an inverted Nikon TiE epifluorescence microscope using NISElements (version AR 5.02.03). For phase contrast microscopy, a 40× Plan APO NA 0.9 phase contrast objective was used. For fluorescence microscopy, a 100× Plan APO NA 1.45 phase contrast oil objective and Semrock YFP-2427B filters were used. Microscope settings were identical throughout the study to ensure comparability of fluorescent intensities. Fluorescent images were background subtracted, and snapshots and movies were generated with ImageJ (version 1.53). Data were analyzed with custom scripts using Python (version 3.8.5) and MATLAB (version R2019b) as described previously(Kühn et al., 2023) and described further below. Custom codes are available on Github (https://github.com/PersatLab/antagonists).

Cell preparation for single cell twitching experiments.

Cells were plated on LB with appropriate antibiotics as needed and incubated overnight at 37 °C. Cells were grown to mid-exponential phase (OD_{600} = 0.2-0.8) in filtered LB medium, with appropriate antibiotics as needed, and diluted to OD_{600} = 0.2. After prewarming the tryptone agarose plates (without antibiotics or inducers for all microscopy experiments) for 45-60 min, a 16 mm round pad was cut out and 1 µl of the diluted cell suspension was pipetted onto the upper side of the agarose pad (the side that was not in contact with the plastic dish bottom). The pads were flipped immediately on a glass

bottom dish (P35G-1.5-20-C, MatTek). Four PBS droplets were pipetted to the sides without touching the pad to prevent drying. The samples were used directly for imaging or incubated at 37 °C for imaging within 2 h.

Quantification of static protein localization.

Fluorescent profiles display the mean pixel value of a transversal section of the cell along the mid-cell axis(Kühn et al., 2021a). Cells were prepared and imaged as described above. Several still images of motile cells were recorded to yield hundreds of segmented cells per replicate. Motile cells were typically visible 1 and 2 h after preparation of the sample. Image analysis was performed as described previously(Kühn et al., 2021a) and below. Fluorescent images were acquired at 0, 1 and 2 h after preparation of the microscope dishes. Cells were segmented using phase contrast images with MATLAB-based BacStalk (version 1.8)(Hartmann et al., 2020a) and fluorescence profile data was exported as csv files. For comparison of proteins with different expression levels, the profiles were normalized by the total fluorescence of the cell and rescaled to the cell length. Cells were oriented so that the dim pole is at x = -1, the bright pole at x = 1, and mid-cell at x = 0. Mean profiles and standard deviations were computed individually for each biological replicate.

Polar localization and asymmetry indexes.

To quantify the extent of polar localization vs cytoplasmic localization, a polar localization index was derived from the fluorescent profile data. A polar area was defined to measure the polar fluorescence signal I_A and I_B of opposite poles A and B. The polar area was set relative to the ratio between cell width and cell length to account for differences in cell size $(\text{polar area} = \frac{\text{cell width}}{\text{cell length}} * 0.5)$. To accurately compute polar localization indexes for proteins with weak polar localization the following correction method was applied. This was necessary because fluorescence profiles of purely cytoplasmic proteins are bell-shaped instead of flat. The fluorescence profile of soluble mNG protein expressed from plasmid pJN105-mNG (uninduced) was used as baseline profile corresponding to a polar localization index of zero(Kühn et al., 2023). The soluble mNG baseline profile plus standard deviation was subtracted from the measured profiles. The polar localization index is the corrected integrated signal at the defined polar areas $I_{Ac} + I_{Bc}$ divided by the initial total polar fluorescence $I_A + I_B$ ($polar\ localization\ index = \frac{I_{Ac}+I_{Bc}}{I_A+I_B}$). If values slightly below zero occur due to noise, the polar localization index was set to 0. A polar localization index of 0 corresponds to cytoplasmic proteins, and values toward 1 correspond to polarly localized proteins. Values of exactly 1 can never be reached with the applied correction method.

An asymmetry index was determined similarly by taking the ratio between the maximum total fluorescence I_{max} of opposite poles A and B and the sum of the polar total

fluorescence $I_A + I_B$ ($asymmetry\ index = \frac{I_{max}}{I_A+I_B}$). Values around 0.5 correspond to symmetric bipolar localization, a value of 1 corresponds to unipolar localization.

Reversal frequency of isolated cells and after collisions.

Cells were prepared and imaged with phase contrast microscopy as described above. BacStalk was used to segment cells, and image sequences with 5 s interval were recorded for 5 min. The analysis was carried out as described previously(Kühn et al., 2021a). To measure reversal rates, for each frame starting from the first frame in which the cell was classified as moving, the scalar product between the rounded normalized displacement vector $\vec{d}$ and the cell orientation unit vector $\vec{t}$ was determined. This yielded a series of numbers corresponding to cellular movement toward the initial leading pole (1), toward the initial lagging pole (-1) or no movement (0) at that timepoint. Timepoints with no movement were removed. Cell movement was considered persistently directional relative to the initial leading pole if the sign remained the same and counted as reversing when a change of sign occurred. To compensate for frequent sign changes occurring for close to non-moving cells, a reversal was only counted when at least two subsequent frames before and after the reversal had the same sign. The displayed reversal frequency is the sum of all considered reversals divided by the total tracked time over all cell tracks for each biological replicate.

Reversals after collisions were counted manually from the raw movies using the ImageJ plugin Cell Counter. A collision was only considered if the cell was moving in the same direction for at least three frames before the collision and the collision lasted for at least

two frames (frame interval 5 sec). Collisions with angles below roughly 20° were not considered. Reversals after collision were only considered if the reversal occurred within five frames after the collision ended. Freshly divided cells were not considered. The displayed reversal frequency is the sum of all considered reversals divided by the sum of all considered collisions for each biological replicate.

Quantification of dynamic protein localization.

For dynamic protein localization, image sequences were recorded similarly to still images as described above. Typically, image sequences were recorded after 2 h surface contact with an image interval of 5 s for 2-3 min. Cells were segmented and tracked in a custom code and BacStalk (version 1.8)(Hartmann et al., 2020a). Cells were categorized into moving and non-moving subpopulations by applying a speed threshold (here: 26 - 65 nm s^{-1}). The positions of both cell poles were determined using the cell outline obtained from BacStalk and poles were labeled according to their position in subsequent frames. Average fluorescence intensities I_A and I_B of opposite poles A and B were measured in an area around the coordinate of each pole with a radius $r = \frac{cell\ width}{1.8}$. Note, these intensities are not comparable to the polar intensities measured for the static localization because the polar areas are defined differently. Cells were then categorized according to their ratio of average fluorescence intensity between the two poles over the whole cell track ($symmetry\ ratio = \frac{intensity\ \mathrm{dim}\ pole}{intensity\ bright\ pole}$). The threshold between symmetric and asymmetric localization was set to 0.8 to allow enough cells in the asymmetric subpopulation for downstream analyses. Cells were considered asymmetric with a ratio below the threshold. From this asymmetric subpopulation an alignment factor was

calculated to measure if a cell moves in the direction of the dim or the bright pole. The alignment factor α is the scalar product of a unit vector $\vec{e}$ from the dim to the bright pole and the normalized displacement vector $\vec{d}$. The alignment factor α indicates in which direction the cell is moving relative to the bright pole. An alignment factor $\alpha > 0$ corresponds to movement toward the bright pole, with $\alpha = 1$ corresponding to movement exactly parallel to the cell length axis.

Affinity purification and mass spectrometry.

Experiments were performed as previously described(Inclan, Persat, Greninger, Von Dollen, et al., 2016). Briefly, LB cultures inoculated from a single colony were grown at 37 °C with vigorous aeration at 250 rpm for 6 h. One hundred microliter of the culture was spread onto 1.5% MinS media(Nicas & Iglewski, 1984) plates and grown overnight at 37 °C. Bacteria were scraped from the plate and resuspended by vortexing and rapid pipetting in 5 mL PBS, and OD_{600} was measured. Cell suspensions were diluted to OD_{600} = 3 in 2 mL PBS, centrifuged at 8000 x g, the supernatants were discarded, and cell pellets were frozen. Pellets were resuspended in 2 ml lysis buffer (50 mM Tris-HCl, pH 7.5, 150 mM NaCl, 0.5% NP- 40, 1 mg mL^{-1} lysozyme, protease inhibitor cocktail tablet [Roche], 25 U mL^{-1} benzonase [Invitrogen]). Lysates were incubated on ice for 20 min and sonicated (Branson sonicator 150) with a microtip for 10 s with 1 s manual pulsing (on setting 10, approximately 100 W), three times with minimum 1 min rest intervals on ice. Lysates were centrifuged for 20 min at 14,000 x g, and the soluble portion was decanted and incubated with 50 µl anti-HA beads (as directed by the manufacturer, EZview Red anti-HA affinity gel with antibody clone HA-7, Sigma). Beads were captured

by low speed (1000 x g) centrifugation, and the flowthrough was discarded. Bound beads were washed three times with 1 mL of wash buffer (50 mM Tris-HCl pH 7.5, 150 mM NaCl, 0.05% NP-40), vortexed briefly and centrifuged for capture. Beads were washed additionally with buffer lacking NP-40 to remove detergent. Bound material was eluted from beads with 30 µL HA peptide solution (Sigma) in TBS (100 ng/ml). Eluates were flash frozen in liquid nitrogen, thawed, and then then trypsin digested for LC-MS/MS(Jäger et al., 2011). Digested peptide mixtures were analysed on a Thermo Scientific Velos Pro ion trap MS system equipped with a Proxeon Easy nLC II high-pressure liquid chromatography and autosampler system. Each purification was performed at least four times. AP-MS samples were scored by SAINT(H. Choi et al., 2011).

Statistical tests and software.

To test significance, one-way ANOVA and Tukey's post hoc tests were done using Python (version 3.8.5). A p-value below 0.05 was considered statistically significant.

ACKNOWLEDGEMENTS

The authors would like to thank John S. (Sandy) Parkinson and Caralyn Flack for advice on the methylation immunoblots and Igor Jouline with advice on bioinformatic analysis. J.E., R.P., Y.I., H.M. were supported by funding provided by the NIH (RO1 AI129547, RO1 AI174014, R21 AI154350) and the Cystic Fibrosis Foundation (003224P221, 495008). R.P. was also funded by an NSF GRFP fellowship (1650113) and the NIH (F31 AI147544). I.C. was supported by an NSF GRFP fellowship (2034836). M.K. and A.P. were supported by funding by SNSF 310030-189084. M.K. was also supported by an EMBO postdoctoral fellowship ALTF 495-2020. D.S. was supported by NIH R01AI167412. Any opinions, findings, and conclusions or recommendations expressed in this material are those of the author(s) and do not necessarily reflect the views of the National Science Foundation.

REFERENCES

Adibi, M., Zoccolan, D., & Clifford, C. W. G. (2021). Editorial: Sensory Adaptation. *Frontiers in Systems Neuroscience*, *15*. https://www.frontiersin.org/articles/10.3389/fnsys.2021.809000

Alon, U., Surette, M. G., Barkai, N., & Leibler, S. (1999). Robustness in bacterial chemotaxis. *Nature*, *397*(6715), Article 6715. https://doi.org/10.1038/16483

Banno, S., Shiomi, D., Homma, M., & Kawagishi, I. (2004). Targeting of the chemotaxis methylesterase/deamidase CheB to the polar receptor–kinase cluster in an Escherichia coli cell. *Molecular Microbiology*, *53*(4), 1051–1063. https://doi.org/10.1111/j.1365-2958.2004.04176.x

Barkai, N., & Leibler, S. (1997). Robustness in simple biochemical networks. *Nature*, *387*(6636), Article 6636. https://doi.org/10.1038/43199

Barnakov, A. N., Barnakova, L. A., & Hazelbauer, G. L. (1999). Efficient adaptational demethylation of chemoreceptors requires the same enzyme-docking site as efficient methylation. *Proceedings of the National Academy of Sciences*, *96*(19), 10667–10672. https://doi.org/10.1073/pnas.96.19.10667

Bartelli, N. L., & Hazelbauer, G. L. (2011). Direct evidence that the carboxyl-terminal sequence of a bacterial chemoreceptor is an unstructured linker and enzyme tether. *Protein Science*, *20*(11), 1856–1866. https://doi.org/10.1002/pro.719

Benda, J. (2021). Neural adaptation. *Current Biology*, *31*(3), R110–R116. https://doi.org/10.1016/j.cub.2020.11.054

Bertrand, J. J., West, J. T., & Engel, J. N. (2010). Genetic Analysis of the Regulation of Type IV Pilus Function by the Chp Chemosensory System of Pseudomonas

aeruginosa. *Journal of Bacteriology*, *192*(4), 994–1010. https://doi.org/10.1128/jb.01390-09

Boyd, A., & Simon, M. I. (1980). Multiple electrophoretic forms of methyl-accepting chemotaxis proteins generated by stimulus-elicited methylation in Escherichia coli. *Journal of Bacteriology*, *143*(2), 809–815. https://doi.org/10.1128/jb.143.2.809-815.1980

Briegel, A., Ortega, D. R., Tocheva, E. I., Wuichet, K., Li, Z., Chen, S., Müller, A., Iancu, C. V., Murphy, G. E., Dobro, M. J., Zhulin, I. B., & Jensen, G. J. (2009). Universal architecture of bacterial chemoreceptor arrays. *Proceedings of the National Academy of Sciences*, *106*(40), 17181–17186. https://doi.org/10.1073/pnas.0905181106

Burrows, L. L. (2012). Pseudomonas aeruginosa Twitching Motility: Type IV Pili in Action. *Annual Review of Microbiology*, *66*(1), 493–520. https://doi.org/10.1146/annurev-micro-092611-150055

Choi, H., Larsen, B., Lin, Z.-Y., Breitkreutz, A., Mellacheruvu, D., Fermin, D., Qin, Z. S., Tyers, M., Gingras, A.-C., & Nesvizhskii, A. I. (2011). SAINT: Probabilistic scoring of affinity purification–mass spectrometry data. *Nature Methods*, *8*(1), Article 1. https://doi.org/10.1038/nmeth.1541

Choi, K.-H., Kumar, A., & Schweizer, H. P. (2006). A 10-min method for preparation of highly electrocompetent *Pseudomonas aeruginosa* cells: Application for DNA fragment transfer between chromosomes and plasmid transformation. *Journal of Microbiological Methods*, *64*(3), 391–397. https://doi.org/10.1016/j.mimet.2005.06.001

D'Argenio, D. A., Calfee, M. W., Rainey, P. B., & Pesci, E. C. (2002). Autolysis and Autoaggregation in Pseudomonas aeruginosa Colony Morphology Mutants. *Journal of Bacteriology*, *184*(23), 6481–6489. https://doi.org/10.1128/jb.184.23.6481-6489.2002

Darzins, A. (1995). The Pseudomonas aeruginosa pilK gene encodes a chemotactic methyltransferase (CheR) homologue that is translationally regulated. *Molecular Microbiology*, *15*(4), 703–717. https://doi.org/10.1111/j.1365-2958.1995.tb02379.x

De Palo, G., & Endres, R. G. (2013). Unraveling Adaptation in Eukaryotic Pathways: Lessons from Protocells. *PLoS Computational Biology*, *9*(10), e1003300. https://doi.org/10.1371/journal.pcbi.1003300

DeFranco, A. L., & Koshland, D. E. (1980). Multiple methylation in processing of sensory signals during bacterial chemotaxis. *Proceedings of the National Academy of Sciences*, *77*(5), 2429–2433. https://doi.org/10.1073/pnas.77.5.2429

Djordjevic, S., Goudreau, P. N., Xu, Q., Stock, A. M., & West, A. H. (1998). Structural basis for methylesterase CheB regulation by a phosphorylation-activated domain. *Proceedings of the National Academy of Sciences*, *95*(4), 1381–1386. https://doi.org/10.1073/pnas.95.4.1381

Djordjevic, S., & Stock, A. M. (1997). Crystal structure of the chemotaxis receptor methyltransferase CheR suggests a conserved structural motif for binding S-adenosylmethionine. *Structure*, *5*(4), 545–558. https://doi.org/10.1016/S0969-2126(97)00210-4

Djordjevic, S., & Stock, A. M. (1998). Chemotaxis receptor recognition by protein methyltransferase CheR. *Nature Structural Biology*, *5*(6), Article 6. https://doi.org/10.1038/nsb0698-446

Engström, P., & Hazelbauer, G. L. (1980). Multiple methylation of methyl-accepting chemotaxis proteins during adaptation of E. coli to chemical stimuli. *Cell*, *20*(1), 165–171. https://doi.org/10.1016/0092-8674(80)90244-5

Feng, X., Baumgartner, J. W., & Hazelbauer, G. L. (1997). High- and low-abundance chemoreceptors in Escherichia coli: Differential activities associated with closely related cytoplasmic domains. *Journal of Bacteriology*, *179*(21), 6714–6720.

Fuchs, E. L., Brutinel, E. D., Klem, E. R., Fehr, A. R., Yahr, T. L., & Wolfgang, M. C. (2010). In Vitro and In Vivo Characterization of the Pseudomonas aeruginosa Cyclic AMP (cAMP) Phosphodiesterase CpdA, Required for cAMP Homeostasis and Virulence Factor Regulation. *Journal of Bacteriology*, *192*(11), 2779–2790. https://doi.org/10.1128/JB.00168-10

Fulcher, N. B., Holliday, P. M., Klem, E., Cann, M. J., & Wolfgang, M. C. (2010). The Pseudomonas aeruginosa Chp chemosensory system regulates intracellular cAMP levels by modulating adenylate cyclase activity. *Molecular Microbiology*, *76*(4), 889–904. https://doi.org/10.1111/j.1365-2958.2010.07135.x

García-Fontana, C., Corral Lugo, A., & Krell, T. (2014). Specificity of the CheR2 Methyltransferase in Pseudomonas aeruginosa Is Directed by a C-Terminal Pentapeptide in the McpB Chemoreceptor. *Science Signaling*, *7*(320), ra34–ra34. https://doi.org/10.1126/scisignal.2004849

Gibson, D. G., Young, L., Chuang, R.-Y., Venter, J. C., Hutchison, C. A., & Smith, H. O. (2009). Enzymatic assembly of DNA molecules up to several hundred kilobases. *Nature Methods*, *6*(5), Article 5. https://doi.org/10.1038/nmeth.1318

Goy, M. F., Springer, M. S., & Adler, J. (1977). Sensory transduction in *Escherichia coli*: Role of a protein methylation reaction in sensory adaptation. *Proceedings of the National Academy of Sciences*, *74*(11), 4964–4968. https://doi.org/10.1073/pnas.74.11.4964

Hansen, C. H., Endres, R. G., & Wingreen, N. S. (2008). Chemotaxis in Escherichia coli: A Molecular Model for Robust Precise Adaptation. *PLoS Computational Biology*, *4*(1), e1. https://doi.org/10.1371/journal.pcbi.0040001

Hartmann, R., Teeseling, M. C. F., Thanbichler, M., & Drescher, K. (2020). BacStalk: A comprehensive and interactive image analysis software tool for bacterial cell biology. *Molecular Microbiology*, *114*(1), 140–150. https://doi.org/10.1111/mmi.14501

Hickman, J. W., Tifrea, D. F., & Harwood, C. S. (2005). A chemosensory system that regulates biofilm formation through modulation of cyclic diguanylate levels. *Proceedings of the National Academy of Sciences*, *102*(40), 14422–14427. https://doi.org/10.1073/pnas.0507170102

Hmelo, L. R., Borlee, B. R., Almblad, H., Love, M. E., Randall, T. E., Tseng, B. S., Lin, C., Irie, Y., Storek, K. M., Yang, J. J., Siehnel, R. J., Howell, P. L., Singh, P. K., Tolker-Nielsen, T., Parsek, M. R., Schweizer, H. P., & Harrison, J. J. (2015). Precision-engineering the Pseudomonas aeruginosa genome with two-step allelic exchange. *Nature Protocols*, *10*(11), Article 11. https://doi.org/10.1038/nprot.2015.115

Inclan, Y. F., Huseby, M. J., & Engel, J. N. (2011). FimL Regulates cAMP Synthesis in Pseudomonas aeruginosa. *PLOS ONE*, *6*(1), e15867. https://doi.org/10.1371/journal.pone.0015867

Inclan, Y. F., Persat, A., Greninger, A., Von Dollen, J., Johnson, J., Krogan, N., Gitai, Z., & Engel, J. N. (2016). A scaffold protein connects type IV pili with the Chp chemosensory system to mediate activation of virulence signaling in Pseudomonas aeruginosa. *Molecular Microbiology*, *101*(4), 590–605. https://doi.org/10.1111/mmi.13410

Jäger, S., Cimermancic, P., Gulbahce, N., Johnson, J. R., McGovern, K. E., Clarke, S. C., Shales, M., Mercenne, G., Pache, L., Li, K., Hernandez, H., Jang, G. M., Roth, S. L., Akiva, E., Marlett, J., Stephens, M., D'Orso, I., Fernandes, J., Fahey, M., … Krogan, N. J. (2011). Global landscape of HIV-human protein complexes. *Nature*, *481*(7381), 365–370. https://doi.org/10.1038/nature10719

Koch, M. D., Black, M. E., Han, E., Shaevitz, J. W., & Gitai, Z. (2022). Pseudomonas aeruginosa distinguishes surfaces by stiffness using retraction of type IV pili. *Proceedings of the National Academy of Sciences*, *119*(20), e2119434119. https://doi.org/10.1073/pnas.2119434119

Kühn, M. J., Macmillan, H., Talà, L., Inclan, Y., Patino, R., Pierrat, X., Al-Mayyah, Z., Engel, J. N., & Persat, A. (2023). Two antagonistic response regulators control Pseudomonas aeruginosa polarization during mechanotaxis. *The EMBO Journal*, *42*(7), e112165. https://doi.org/10.15252/embj.2022112165

Kühn, M. J., Talà, L., Inclan, Y. F., Patino, R., Pierrat, X., Vos, I., Al-Mayyah, Z., Macmillan, H., Negrete, J., Engel, J. N., & Persat, A. (2021a). Mechanotaxis directs

Pseudomonas aeruginosa twitching motility. *Proceedings of the National Academy of Sciences*, *118*(30), e2101759118. https://doi.org/10.1073/pnas.2101759118

Kühn, M. J., Talà, L., Inclan, Y. F., Patino, R., Pierrat, X., Vos, I., Al-Mayyah, Z., Macmillan, H., Negrete, J., Engel, J. N., & Persat, A. (2021b). Mechanotaxis directs *Pseudomonas aeruginosa* twitching motility. *Proceedings of the National Academy of Sciences*, *118*(30), e2101759118. https://doi.org/10.1073/pnas.2101759118

Lai, R.-Z., Han, X.-S., Dahlquist, F. W., & Parkinson, J. S. (2017). Paradoxical enhancement of chemoreceptor detection sensitivity by a sensory adaptation enzyme. *Proceedings of the National Academy of Sciences*, *114*(36), E7583–E7591. https://doi.org/10.1073/pnas.1709075114

Li, M., & Hazelbauer, G. L. (2006). The carboxyl-terminal linker is important for chemoreceptor function. *Molecular Microbiology*, *60*(2), 469–479. https://doi.org/10.1111/j.1365-2958.2006.05108.x

Li, M., Xu, X., Zou, X., & Hazelbauer, G. L. (2021). A Selective Tether Recruits Activated Response Regulator CheB to Its Chemoreceptor Substrate. *mBio*, *12*(6), e03106-21. https://doi.org/10.1128/mBio.03106-21

Liu, Y. C., Machuca, M. A., Beckham, S. A., Gunzburg, M. J., & Roujeinikova, A. (2015). Structural basis for amino-acid recognition and transmembrane signalling by tandem Per–Arnt–Sim (tandem PAS) chemoreceptor sensory domains. *Acta Crystallographica Section D: Biological Crystallography*, *71*(10), 2127–2136. https://doi.org/10.1107/S139900471501384X

Luo, Y., Zhao, K., Baker, A. E., Kuchma, S. L., Coggan, K. A., Wolfgang, M. C., Wong, G. C. L., & O'Toole, G. A. (2015). A Hierarchical Cascade of Second Messengers

Regulates Pseudomonas aeruginosa Surface Behaviors. *mBio*, *6*(1), 10.1128/mbio.02456-14. https://doi.org/10.1128/mbio.02456-14

Lupas, A., & Stock, J. (1989). Phosphorylation of an N-terminal Regulatory Domain Activates the CheB Methylesterase in Bacterial Chemotaxis. *Journal of Biological Chemistry*, *264*(29), 17337–17342. https://doi.org/10.1016/S0021-9258(18)71497-X

Mao, H., Cremer, P. S., & Manson, M. D. (2003). A sensitive, versatile microfluidic assay for bacterial chemotaxis. *Proceedings of the National Academy of Sciences*, *100*(9), 5449–5454. https://doi.org/10.1073/pnas.0931258100

Matilla, M. A., Martín-Mora, D., Gavira, J. A., & Krell, T. (2021). Pseudomonas aeruginosa as a Model To Study Chemosensory Pathway Signaling. *Microbiology and Molecular Biology Reviews: MMBR*, *85*(1), e00151-20. https://doi.org/10.1128/MMBR.00151-20

Milburn, M. V., Privé, G. G., Milligan, D. L., Scott, W. G., Yeh, J., Jancarik, J., Koshland, D. E., & Kim, S.-H. (1991). Three-Dimensional Structures of the Ligand-Binding Domain of the Bacterial Aspartate Receptor with and Without a Ligand. *Science*, *254*(5036), 1342–1347. https://doi.org/10.1126/science.1660187

Muok, A. R., Briegel, A., & Crane, B. R. (2020). Regulation of the chemotaxis histidine kinase CheA: A structural perspective. *Biochimica et Biophysica Acta (BBA) - Biomembranes*, *1862*(1), 183030. https://doi.org/10.1016/j.bbamem.2019.183030

Nicas, T. I., & Iglewski, B. H. (1984). Isolation and characterization of transposon-induced mutants of Pseudomonas aeruginosa deficient in production of exoenzyme S.

Infection and Immunity, *45*(2), 470–474. https://doi.org/10.1128/iai.45.2.470-474.1984

Ninfa, E. G., Stock, A., Mowbray, S., & Stock, J. (1991). Reconstitution of the bacterial chemotaxis signal transduction system from purified components. *Journal of Biological Chemistry*, *266*(15), 9764–9770. https://doi.org/10.1016/S0021-9258(18)92886-3

Okumura, H., Nishiyama, S., Sasaki, A., Homma, M., & Kawagishi, I. (1998). Chemotactic Adaptation Is Altered by Changes in the Carboxy-Terminal Sequence Conserved among the Major Methyl-Accepting Chemoreceptors. *Journal of Bacteriology*, *180*(7), 1862–1868. https://doi.org/10.1128/jb.180.7.1862-1868.1998

Ortega, D. R., Fleetwood, A. D., Krell, T., Harwood, C. S., Jensen, G. J., & Zhulin, I. B. (2017). Assigning chemoreceptors to chemosensory pathways in Pseudomonas aeruginosa. *Proceedings of the National Academy of Sciences of the United States of America*, *114*(48), 12809–12814. https://doi.org/10.1073/pnas.1708842114

Persat, A., Inclan, Y. F., Engel, J. N., Stone, H. A., & Gitai, Z. (2015). Type IV pili mechanochemically regulate virulence factors in Pseudomonas aeruginosa. *Proceedings of the National Academy of Sciences of the United States of America*, *112*(24), 7563–7568. https://doi.org/10.1073/pnas.1502025112

Pierrat, X. J.-Y. (2022). *Engineering synthetic adhesins for biophysical investigation and rewiring of host-microbe interactions* [EPFL]. https://doi.org/10.5075/epfl-thesis-8758

Rao, C. V., Glekas, G. D., & Ordal, G. W. (2008). The three adaptation systems of Bacillus subtilis chemotaxis. *Trends in Microbiology*, *16*(10), 480–487. https://doi.org/10.1016/j.tim.2008.07.003

Rapid Phosphotransfer to CheY from a CheA Protein Lacking the CheY-Binding Domain | Biochemistry. (n.d.). Retrieved February 12, 2024, from https://pubs.acs.org/doi/10.1021/bi001100k

Sarkar, M. K., Paul, K., & Blair, D. (2010). Chemotaxis signaling protein CheY binds to the rotor protein FliN to control the direction of flagellar rotation in Escherichia coli. *Proceedings of the National Academy of Sciences*, *107*(20), 9370–9375. https://doi.org/10.1073/pnas.1000935107

Sherris, D., & Parkinson, J. S. (1981). Posttranslational processing of methyl-accepting chemotaxis proteins in Escherichia coli. *Proceedings of the National Academy of Sciences*, *78*(10), 6051–6055. https://doi.org/10.1073/pnas.78.10.6051

Shiomi, D., Zhulin, I. B., Homma, M., & Kawagishi, I. (2002). Dual Recognition of the Bacterial Chemoreceptor by Chemotaxis-specific Domains of the CheR Methyltransferase*. *Journal of Biological Chemistry*, *277*(44), 42325–42333. https://doi.org/10.1074/jbc.M202001200

Silversmith, R. E., Wang, B., Fulcher, N. B., Wolfgang, M. C., & Bourret, R. B. (2016). Phosphoryl Group Flow within the *Pseudomonas aeruginosa* Pil-Chp Chemosensory System. *Journal of Biological Chemistry*, *291*(34), 17677–17691. https://doi.org/10.1074/jbc.M116.737528

Springer, M. S., Goy, M. F., & Adler, J. (1977). Sensory transduction in Escherichia coli: Two complementary pathways of information processing that involve methylated

proteins. *Proceedings of the National Academy of Sciences*, *74*(8), 3312–3316. https://doi.org/10.1073/pnas.74.8.3312

Stock, J. B., Clarke, S., & Koshland, D. E. (1984). [29] The protein carboxylmethyltransferase involved in *Escherichia coli* and *Salmonella typhimurium* chemotaxis. In *Methods in Enzymology* (Vol. 106, pp. 310–321). Academic Press. https://doi.org/10.1016/0076-6879(84)06031-6

Vladimirov, N., & Sourjik, V. (2009). *Chemotaxis: How bacteria use memory*. *390*(11), 1097–1104. https://doi.org/10.1515/BC.2009.130

West, A. H., Martinez-Hackert, E., & Stock, A. M. (1995). Crystal Structure of the Catalytic Domain of the Chemotaxis Receptor Methylesterase, CheB. *Journal of Molecular Biology*, *250*(2), 276–290. https://doi.org/10.1006/jmbi.1995.0376

West, S. E., Sample, A. K., & Runyen-Janecky, L. J. (1994). The vfr gene product, required for Pseudomonas aeruginosa exotoxin A and protease production, belongs to the cyclic AMP receptor protein family. *Journal of Bacteriology*, *176*(24), 7532–7542. https://doi.org/10.1128/jb.176.24.7532-7542.1994

Whitchurch, C. B., Leech, A. J., Young, M. D., Kennedy, D., Sargent, J. L., Bertrand, J. J., Semmler, A. B. T., Mellick, A. S., Martin, P. R., Alm, R. A., Hobbs, M., Beatson, S. A., Huang, B., Nguyen, L., Commolli, J. C., Engel, J. N., Darzins, A., & Mattick, J. S. (2004). Characterization of a complex chemosensory signal transduction system which controls twitching motility in Pseudomonas aeruginosa. *Molecular Microbiology*, *52*(3), 873–893. https://doi.org/10.1111/j.1365-2958.2004.04026.x

Wolfgang, M. C., Lee, V. T., Gilmore, M. E., & Lory, S. (2003). Coordinate Regulation of Bacterial Virulence Genes by a Novel Adenylate Cyclase-Dependent Signaling

Pathway. *Developmental Cell*, *4*(2), 253–263. https://doi.org/10.1016/S1534-5807(03)00019-4

Wuichet, K., & Zhulin, I. B. (2010). Origins and Diversification of a Complex Signal Transduction System in Prokaryotes. *Science Signaling*, *3*(128), ra50–ra50. https://doi.org/10.1126/scisignal.2000724

Xia, Y., Chu, W., Qi, Q., & Xun, L. (2015). New insights into the QuikChange™ process guide the use of Phusion DNA polymerase for site-directed mutagenesis. *Nucleic Acids Research*, *43*(2), e12. https://doi.org/10.1093/nar/gku1189

Yi, T.-M., Huang, Y., Simon, M. I., & Doyle, J. (2000). Robust perfect adaptation in bacterial chemotaxis through integral feedback control. *Proceedings of the National Academy of Sciences*, *97*(9), 4649–4653. https://doi.org/10.1073/pnas.97.9.4649

FIGURE 4.1

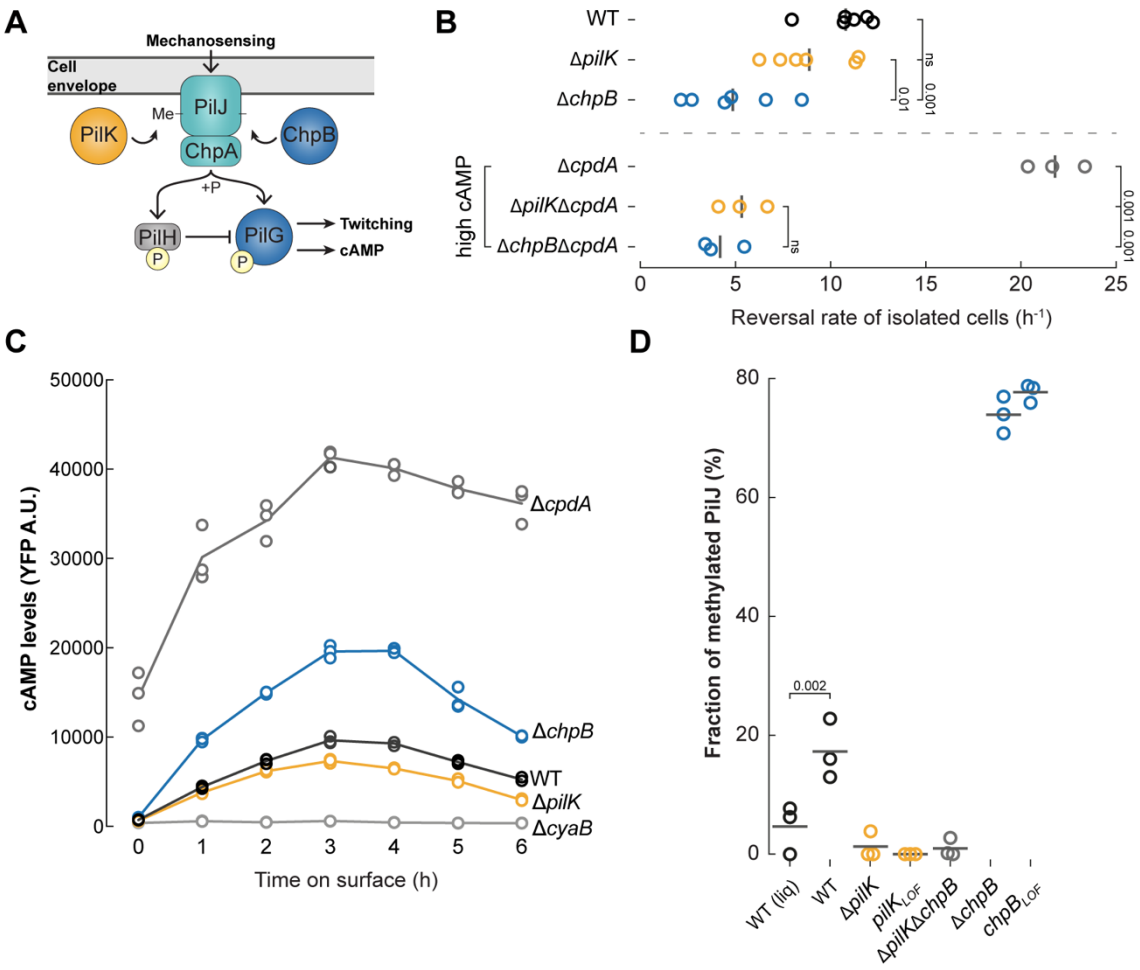

FIGURE 4.1. ChpB and PilK modulate twitching reversals and cAMP production by controlling PilJ methylation.

(A) Schematic of the Pil-Chp mechanosensory system. Mechanical stimuli are sensed by the MCP PilJ, which stimulates ChpA autophosphorylation. The phosphoryl group is transferred to PilG. PilG~P stimulates twitching motility and cAMP production. PilH~P inhibits PilG. The methyltransferase PilK and the methylesterase ChpB control PilJ methylation.

(B) PilK and ChpB modulate twitching motility reversal rates. Shown are the spontaneous reversal rates of isolated motile cells after 2 h surface growth in WT background (upper panel) or Δ*cpdA* (lower panel, with elevated cAMP levels). Circles, median of each biological replicate. Vertical bars, mean across biological replicates. Vertical numbers indicate p-values (ANOVA and Tukey's post hoc test; ns, not significant). For corresponding reversal rates after cell-cell collisions see Figure S4.2A. (Figure caption continued on the next page.)

(Figure caption continued from the previous page.) (C) PilK and ChpB fine-tune the amplitude of surface-dependent cAMP production over time. cAMP was measured with a transcriptional reporter by flow cytometry at each indicated time point for the indicated strains. A representative graph of two independent experiments, with three biological replicates per experiment, is shown. Circles, median YFP fluorescence of each biological replicate (>30,000 cells each). Each line connects the means of biological replicates. A.U., arbitrary units.

(D) PilJ methylation *in vivo*. Shown is the fraction of methylated PilJ (methylated PilJ signal/total PilJ signal) of the indicated strains expressing chromosomal 3xFLAG-PilJ. Circles, biological replicates. Horizontal bar, mean across biological replicates. P-value shown for the WT liquid vs solid comparison (ANOVA with Tukey's post hoc test). LOF, loss of function. For corresponding twitching motility assays, cAMP assays, and immunoblot images see Figure S4.1A and C and Figure S4.3A, respectively.

FIGURE 4.2

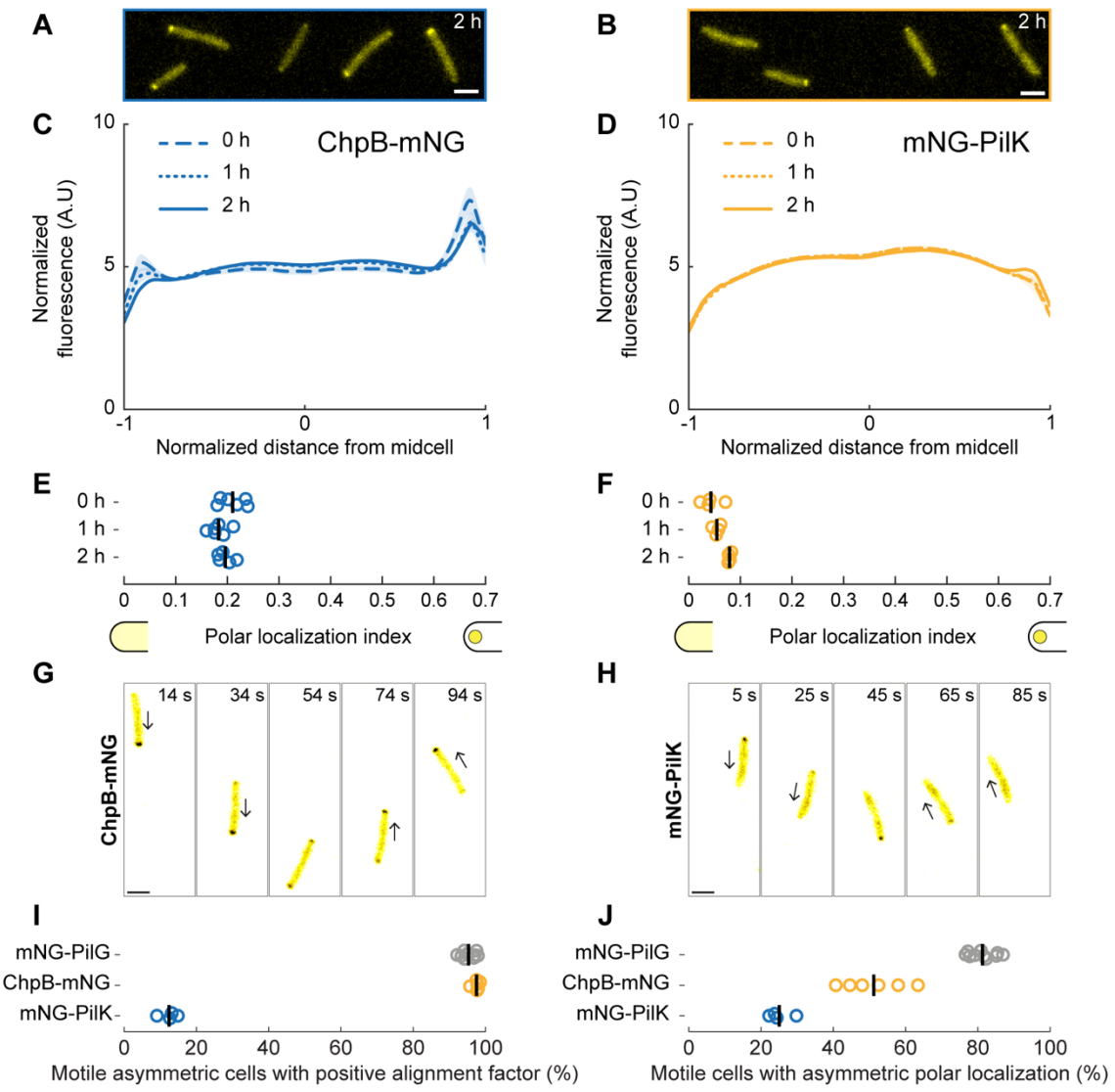

FIGURE 4.2. PilK and ChpB localize to the lagging and leading cell poles, respectively, of twitching *P. aeruginosa* cells.

(A, B) Representative fluorescence snapshots of motile cells expressing (A) chromosomal ChpB-mNG or (B) plasmid-expressed mNG-PilK in Δ*pilK* after 2 h of surface growth. Scale bar, 2 μm.

(C, D) Time course of normalized average fluorescence profiles for (C) ChpB-mNG or (D) mNG-PilK. The length of each cell is normalized so that the dim pole is positioned at x = -1, the bright pole at x = 1. The fluorescent profile for each cell is normalized by the total fluorescence. Solid lines, mean normalized fluorescence profiles across replicates. Shaded area, standard deviation across replicates. A.U., arbitrary units. (Figure caption continued on the next page.)

(Figure caption continued from the previous page.) (E, F) Corresponding polar localization index measuring the relative fraction of the fluorescence signal at the poles compared to the cytoplasm. Circles, median of each biological replicate. Vertical bars, mean across biological replicates.

(G, H) Time-lapse fluorescent snapshots of reversing cells taken from Movies 1 and 2. (G) ChpB-mNG localizes to the leading cell pole. (H) mNG-PilK localizes to the lagging cell pole. Both proteins switch poles during the twitching motility reversal. Arrows indicate direction of twitching motility.

(I) Percent of motile cells with asymmetric polar localization that are twitching in the direction of their brightest pole. In most motile cells expressing ChpB-mNG, the brightest fluorescence localizes to the leading cell pole (alignment >0), similar to mNG-PilG(Kühn et al., 2021b, 2023). Most motile cells expressing mNG-PilK have the brightest fluorescence at the lagging cell pole (alignment <0). Circles, median of each biological replicate. Vertical bars, mean across biological replicates.

(J) Percent of motile cells with asymmetric polar localization of the indicated fluorescent fusion (intensity of the dim pole ≤ 80 % compared to the bright pole). Circles, median of each biological replicate. Vertical bars, mean across biological replicates.

For corresponding asymmetry index and mean cell fluorescence measurements see Figure S4.5A.

FIGURE 4.3

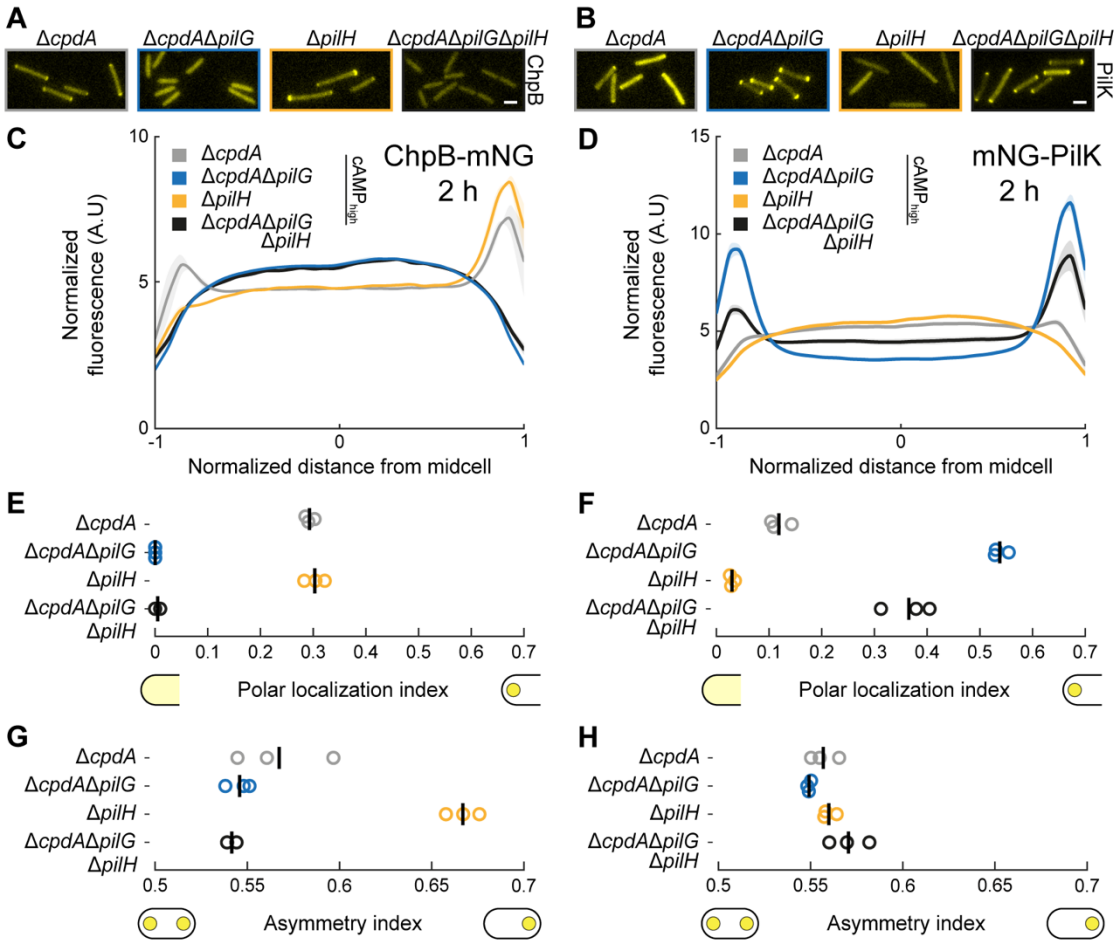

FIGURE 4.3. The response regulators PilG and PilH control the localization patterns of PilK and ChpB.

(A, B) Representative fluorescence snapshots of motile cells expressing (A) chromosomal ChpB-mNG or (B) plasmid-expressed mNG-PilK in Δ*pilK* after 2 h of surface growth. Scale bar, 2 μm.

(C, D) Fluorescence profiles of (C) ChpB-mNG or (D) mNG-PilK in Δ*pilG* and in Δ*pilH* mutants after 2 h of surface growth. *cpdA* was deleted in *pilG* mutants to eliminate potential confounding effects of low cAMP levels. Δ*pilH* has elevated cAMP. Solid lines, mean normalized fluorescence profiles across biological replicates. Shaded area, standard deviation across biological replicates. A.U., arbitrary units.

(E-H) Corresponding measurements of polar localization index and asymmetry index. Circles, median of each biological replicate. Vertical bars, mean across biological replicates.

For corresponding mean cell fluorescence measurements see Figure S4.5B.

FIGURE 4.4

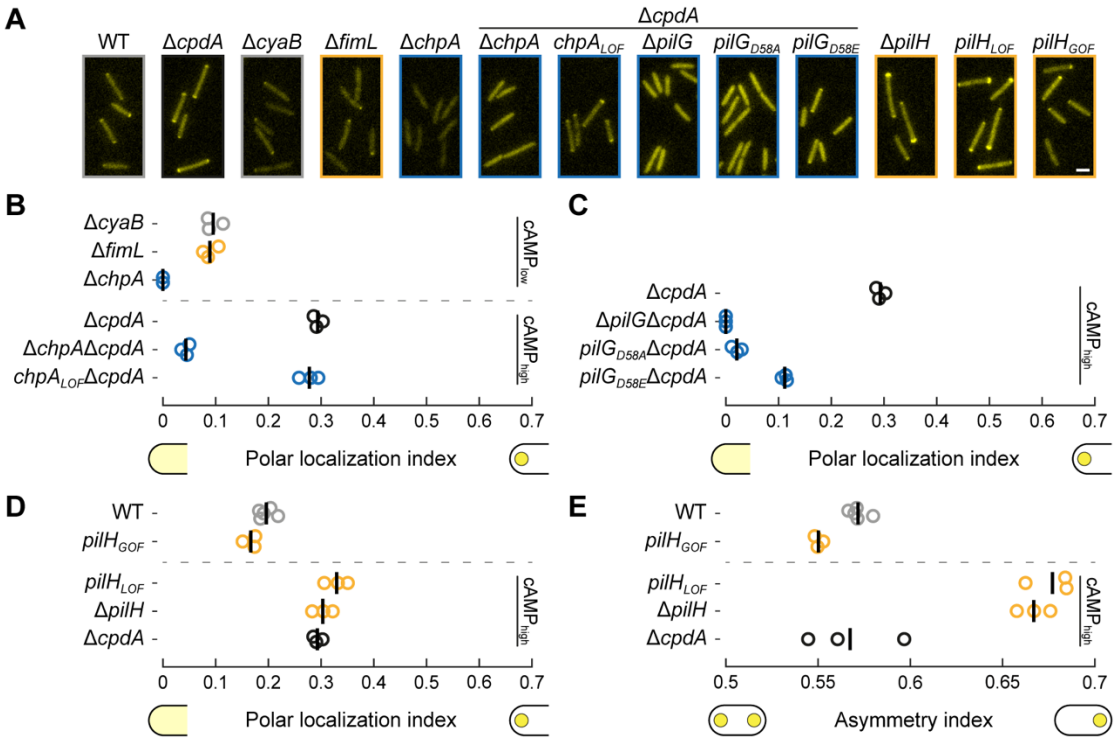

FIGURE 4.4. The ChpA histidine kinase and PilH activation affect ChpB localization.

(A) Representative fluorescence snapshots of motile cells expressing chromosomal ChpB-mNG after 2 h of surface growth. Scale bar, 2 μm. Strains constructed in Δ*cpdA* background are indicated. All other strains are in WT background.

(B-C) Polar localization index of ChpB-mNG in motile cells after 2 h of surface growth in (B) *chpA* and *fimL* mutants or in (C) *pilG* mutants. *cpdA* was deleted in *chpA* and *pilG* mutants to eliminate potential confounding effects of low cAMP levels. Circles, median of each biological replicate. Vertical bars, mean across biological replicates.

(D-E) Polar localization index and asymmetry index of motile cells expressing ChpB-mNG in *pilH* mutants after 2 h of surface growth. Circles, median of each biological replicate. Vertical bars, mean across biological replicates.

For corresponding fluorescence profiles, asymmetry index and mean cell fluorescence measurements see Figure S4.12.

FIGURE 4.5

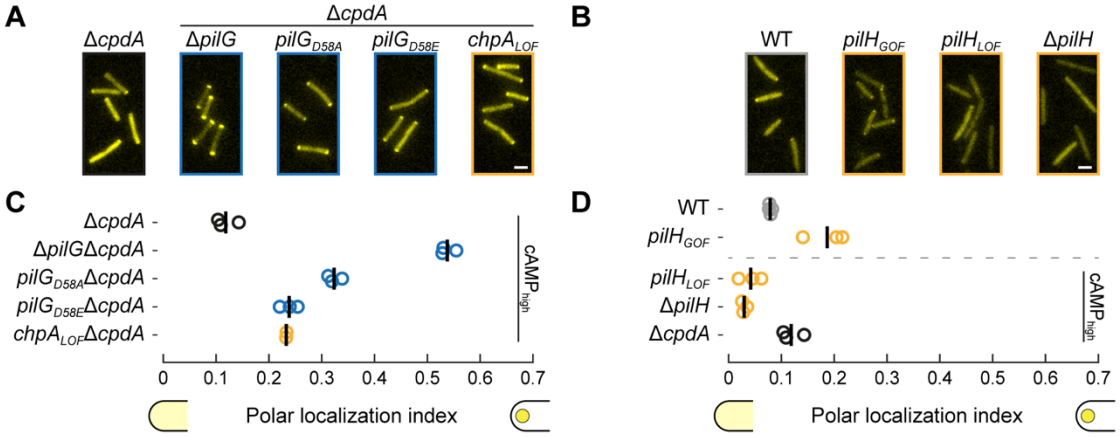

FIGURE 4.5. PilG and PilH are required to exclude PilK from the leading pole.

(A-B) Representative fluorescence snapshots of motile cells with plasmid-expressed mNG-PilK in (A) *pilG* mutants and $chpA_{LOF}$ or in (B) *pilH* mutants, all in ΔpilK background, after 2 h of surface growth. Scale bar, 2 μm.

(C-D) Polar localization index of motile cells expressing mNG-PilK in (C) *pilG* mutants and $chpA_{LOF}$ or in (D) *pilH* mutants after 2 h of surface growth. *cpdA* was deleted in *pilG* mutants and $chpA_{LOF}$ to eliminate potential confounding effects of low cAMP levels. Circles, median of each biological replicate. Vertical bars, mean across biological replicates.

For corresponding fluorescence profiles, asymmetry index and mean cell fluorescence measurements see Figure S4.12.

FIGURE 4.6

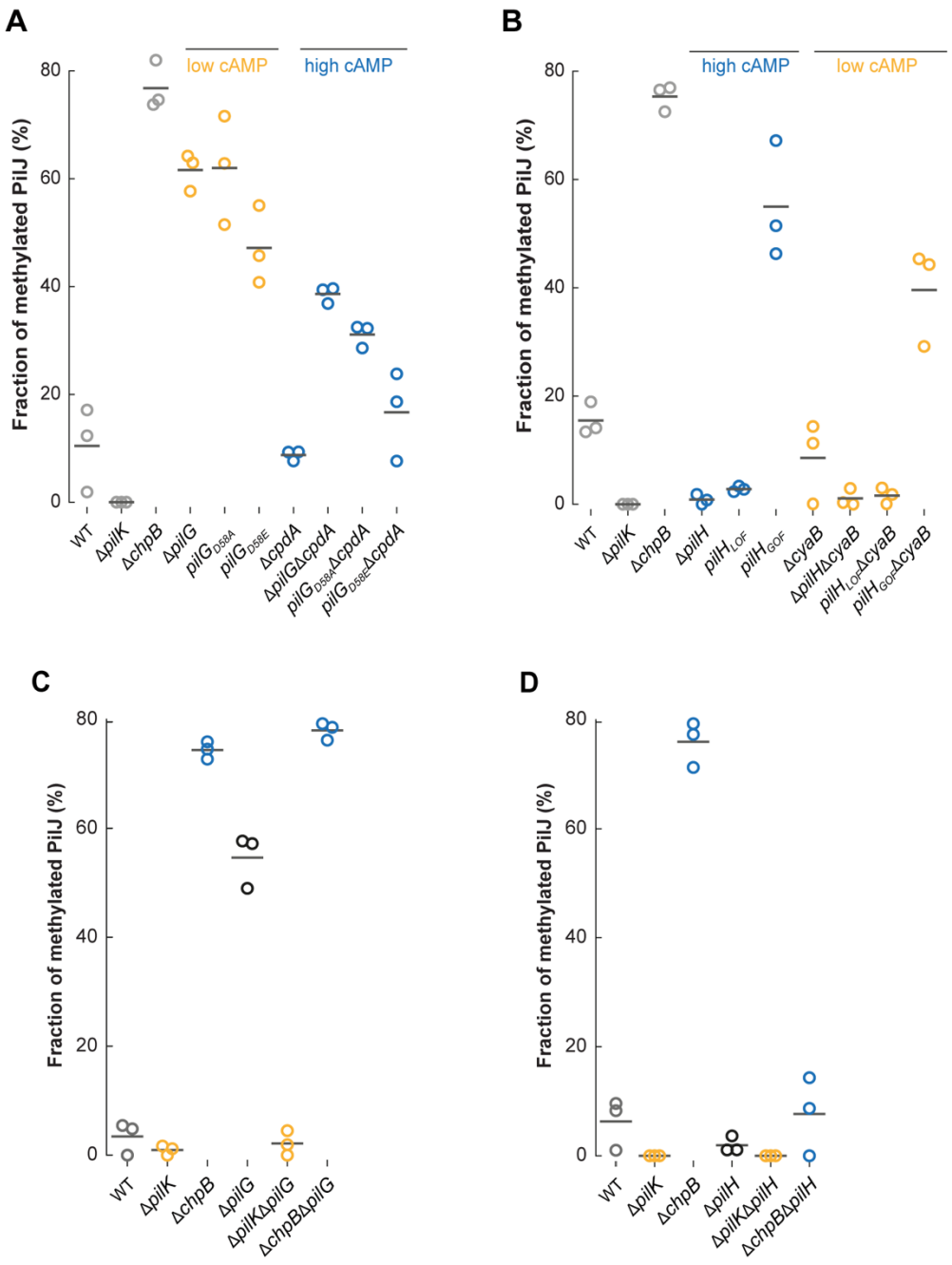

FIGURE 4.6. PilG and PilH regulate PilJ receptor methylation.

PilJ methylation was quantified as in Fig. 1A after 2 h of surface growth for (A) *pilG* mutants (B) *pilH* mutants (C) Δ*pilG*Δ*pilK* and Δ*pilG*Δ*chpB* double mutants or (D) Δ*pilH*Δ*pilK* and Δ*pilH*Δ*chpB* double mutants. (A-D) The fraction of methylated PilJ (methylated PilJ signal/total PilJ signal) is represented in the graph and was quantified from 3 biological replicates (circles). (Figure caption continued on the next page.)

(Figure caption continued from the previous page.) Horizontal bar, mean across biological replicates. LOF, loss of function. GOF, gain of function. For corresponding twitching motility assays, cAMP assays, and immunoblot images see Figure S4.14- Figure S4.16.

FIGURE 4.7

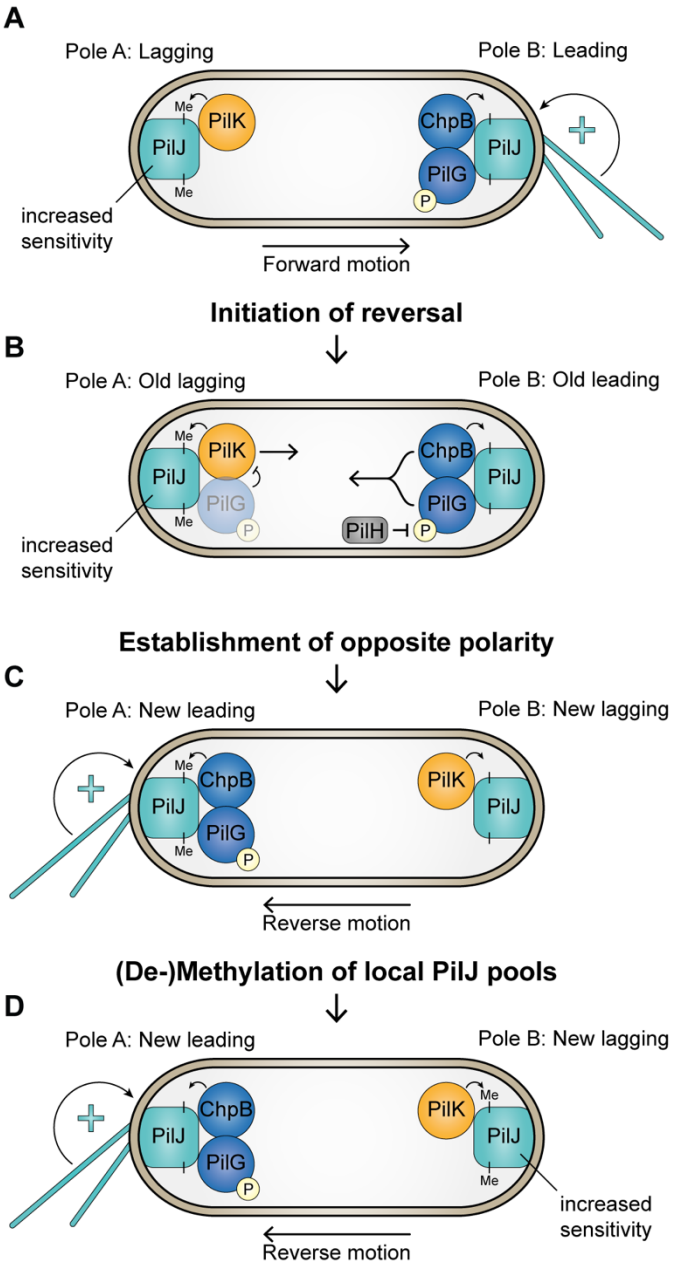

FIGURE 4.7. Spatial control of sensory adaptation modulates local signaling hubs of the Pil-Chp system during mechanosensing.

(A) PilG asymmetric localization establishes the polarity of TFP. TFP are preferentially assembled at the leading pole to propel the cell forward and transmit surface-derived mechanical signals. The mechanical signals, sensed by PilJ, initiate a positive feedback loop that continuously activates the Pil-Chp system at the leading pole(Kühn et al., 2021b, 2023). (Figure caption continued on the next page.)

(Figure caption continued from the previous page.) The lagging pole has fewer or no TFP and thus less activation of the Pil-Chp system. Leading-pole localized PilG recruits ChpB to the leading pole and excludes PilK from the leading pole, so that PilK is primarily localized to the lagging pole. This subcellular architecture ensures that the pool of PilJ at the leading pole becomes demethylated, while the pool of PilJ at the lagging pole is methylated and poised for activation upon reversal of TFP polarity and twitching motility direction.

(B) Initiation of a twitching motility reversal. By antagonizing PilG phosphorylation, PilH may trigger re-localization of PilG and ChpB from the leading pole to the lagging pole, thereby initiating a twitching motility reversal. Accumulation of PilG at the old lagging pole excludes PilK from that pole and thereby drives PilK re-localization to the old leading pole.

(C) Establishment of new leading and lagging poles. Once PilG accumulates at the old lagging pole, PilG establishes a new leading pole, in which methylated PilJ is already primed for efficient activation of the Pil-Chp system. PilG accumulation initiates TFP activity and twitching motility in the opposite direction, completing a twitching motility reversal. ChpB and PilK are now localized to the new leading and lagging pole, respectively.

(D) Inversion of the local PilJ methylation state. By localizing to the new lagging and leading pole, respectively, PilK and ChpB change the methylation state of the polar pools of PilJ, thereby resetting the sensitivity and activity of PilJ at each pole. This process ensures sensory adaptation to localized mechanical stimuli.

FIGURE S4.1

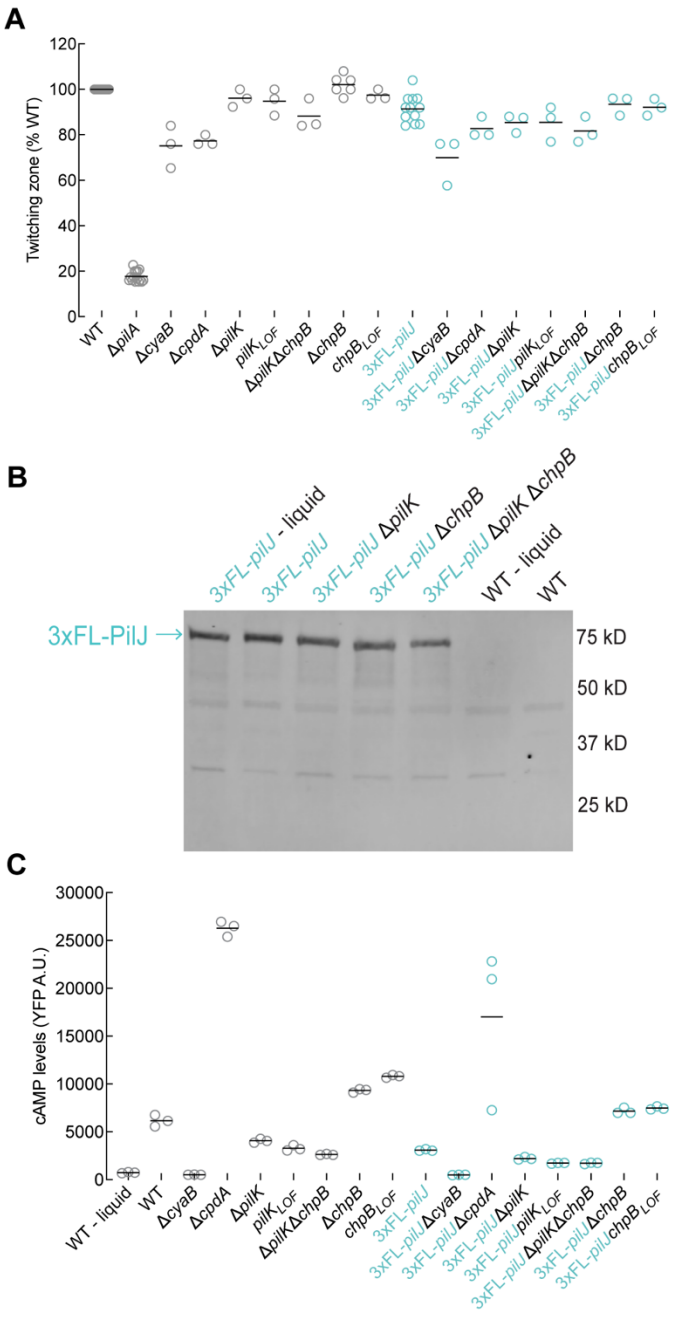

FIGURE S4.1. Phenotypic characterization of *3x-Flag-pilJ* fusion strains.

(A) Twitching motility of the indicated strains with either the WT *pilJ* or with 3xFL-*pilJ* in the chromosome was quantified by the subsurface stab assay. A representative graph of two independent experiments, with at least three biological replicates per experiment, is shown. Circles, relative twitching motility zone of each biological replicate (% of WT). Horizontal bars, mean across biological replicates. (Figure caption continued on the next page.)

(Figure caption continued from the previous page.) Δ*pilA* serves as a twitching motility deficient control.

(B) Immunoblot of whole cell lysates from strains expressing 3xFlag-PilJ (3X-FL-PilJ) from the chromosome separated by conventional SDS-PAGE and immunoblotted with anti-FLAG antibody. Whole cell lysates were prepared from cells grown to mid-log phase in liquid or from cells after 2 h of surface growth. Strains labeled WT have untagged PilJ and serve as a control for the FLAG antibody.

(C) cAMP levels of the indicated strains with either the WT *pilJ* or with 3xFL-*pilJ* grown in liquid to mid-log phase or after 2 h of surface growth. cAMP levels were quantified as in Fig 1C. A representative graph of two independent experiments, with three biological replicates per experiment, is shown. Circles, median YFP fluorescence of each biological replicate (~30,000 cells). Horizontal bars, mean across biological replicates. LOF, loss of function.

FIGURE S4.2

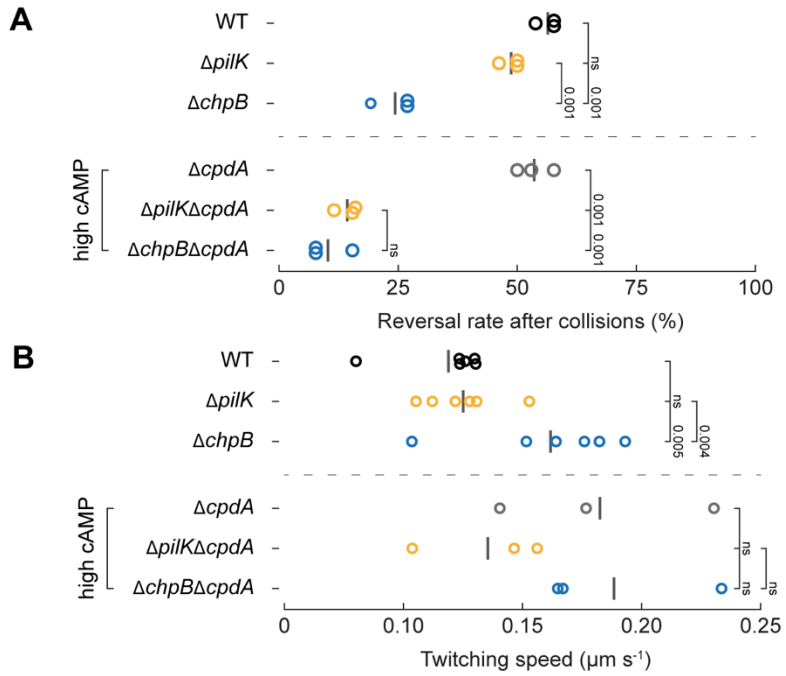

FIGURE S4.2. Effect of cAMP levels on single cell twitching reversal rate and single cell twitching speed.

(A) Manually counted reversal rates after cell-cell collisions of isolated cells after 2 h surface growth as described in Figure 4.1B. Circles, median of each biological replicate. Vertical bars, mean across biological replicates.

(B) Twitching speed of isolated motile cells was calculated using the cell tracking data from Figure 4.1B. Circles, median of each biological replicate. Vertical bars, mean across biological replicates. Vertical numbers indicate p-values (ANOVA and Tukey's post hoc test; ns, not significant).

FIGURE S4.3

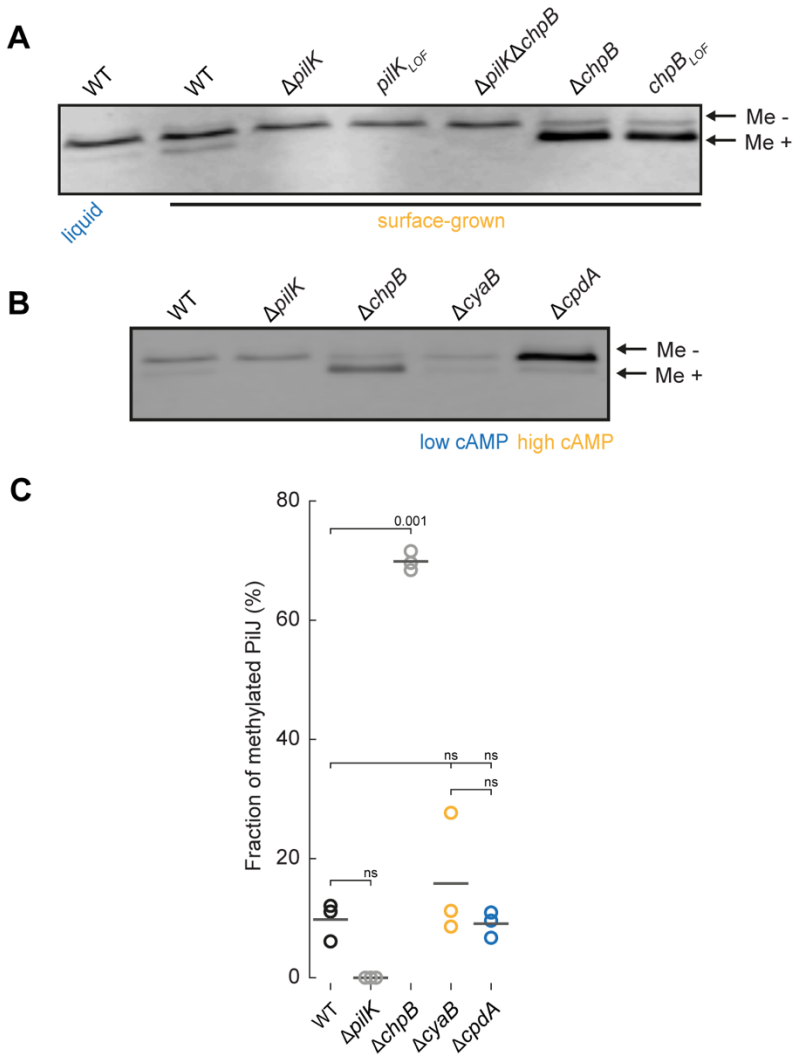

FIGURE S4.3. Role of PilK, ChpB, surface exposure, and cAMP production on PilJ methylation.

(A) PilJ methylation increases after 2 h of surface growth and requires PilK and ChpB enzymatic activity. Representative immunoblots of whole cell lysates from strains expressing chromosomal 3xFlag-PilJ separated by "low-bis" SDS-PAGE and immunoblotted with anti-FLAG antibody. Whole cell lysates were prepared from cells grown to mid-log phase in liquid or from cells after 2 h of surface growth. The slower migrating band represents unmethylated PilJ (Me -), while the faster migrating band represents methylated PilJ (Me +). LOF, loss of function.

(B,C) Methylation immunoblots (B) and fraction of PilJ methylation (C) is not affected by increased cAMP (Δ*cpdA*) or decreased cAMP (Δ*cyaB*) levels, although the absolute levels of PilJ protein are affected. The fraction of methylated PilJ (methylated PilJ signal/total PilJ signal) was quantified from 3 biological replicates (circles). (Figure caption continued on the next page.)

(Figure caption continued from the previous page.) Horizontal bar, mean across biological replicates. Numbers indicate p-values (ANOVA and Tukey's post hoc test; ns, not significant).

FIGURE S4.4

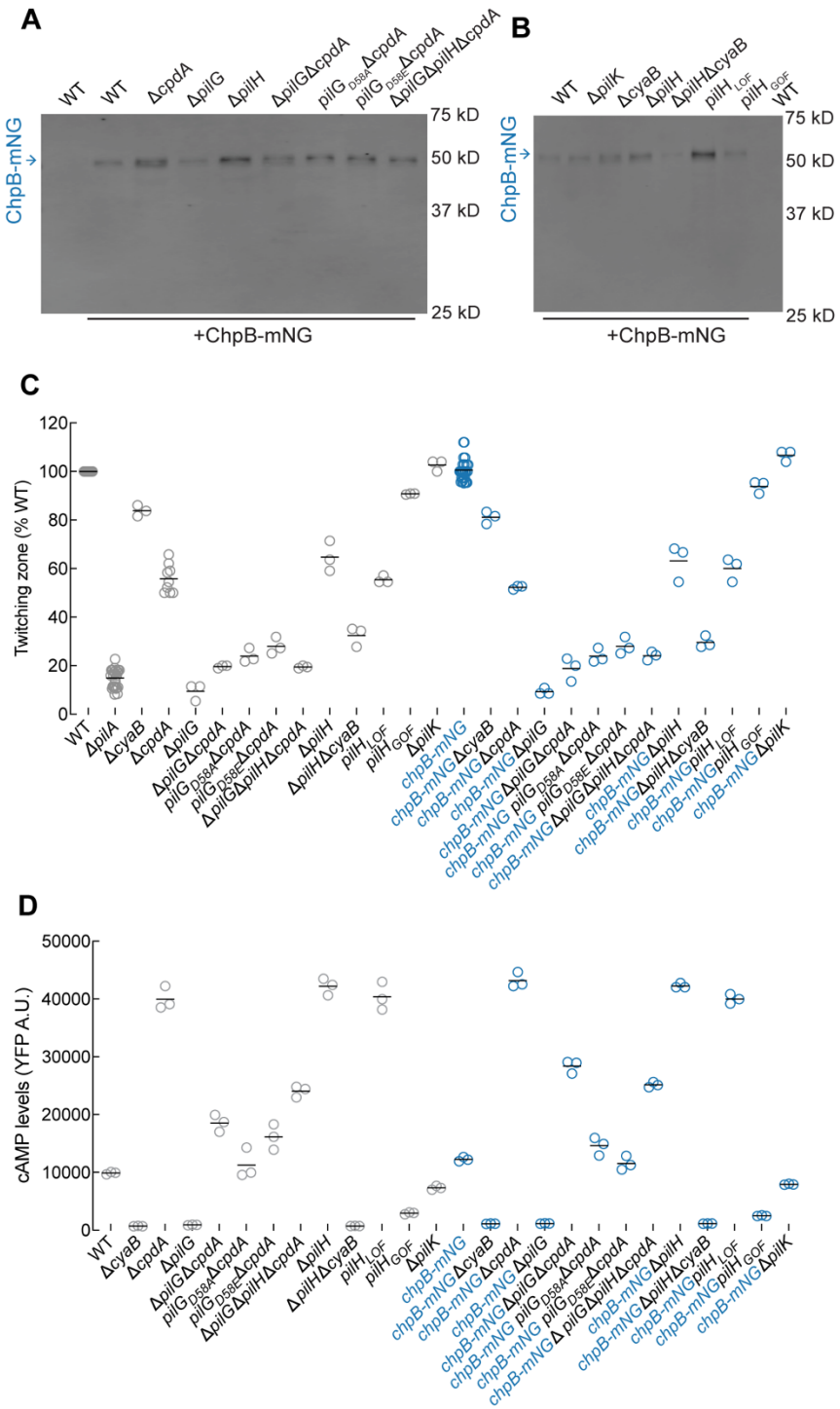

FIGURE S4.4. Phenotypic characterization of *chpB-mNG* fusion strains.

(Figure caption continued on the next page.)

(Figure caption continued from the previous page.) (A) Immunoblot of whole cell lysates from liquid grown (mid-log phase) strains encoding chromosomally expressed ChpB-mNG and probed with anti-mNG antibody. WT serves as a control for antibody specificity. Steady state levels of ChpB-mNG are increased in strains with elevated cAMP (Δ*pilH*, $pilH_{LOF}$, Δ*cpdA*) and decreased in strains with diminished cAMP (Δ*pilG,* Δ*cyaB*).

(B) Twitching motility of the indicated strains (WT *chpB* or *chpB-mNG*) was quantified by the subsurface stab assay. A representative graph of two independent experiments, with at least three biological replicates per experiment, is shown. Circles, relative twitching motility zone of each biological replicate (% WT). Horizontal bars, mean across biological replicates. Δ*pilA* serves as a twitching motility deficient control.

(C) cAMP levels of the indicated strains (WT *chpB* or *chpB-mNG*) after 2 h surface growth were quantified as in Fig 1C. A representative graph of two independent experiments, with three biological replicates per experiment, is shown. Circles, median YFP fluorescence of each biological replicate (~30,000 cells). Horizontal bars, mean across biological replicates. LOF, loss of function.

FIGURE S4.5

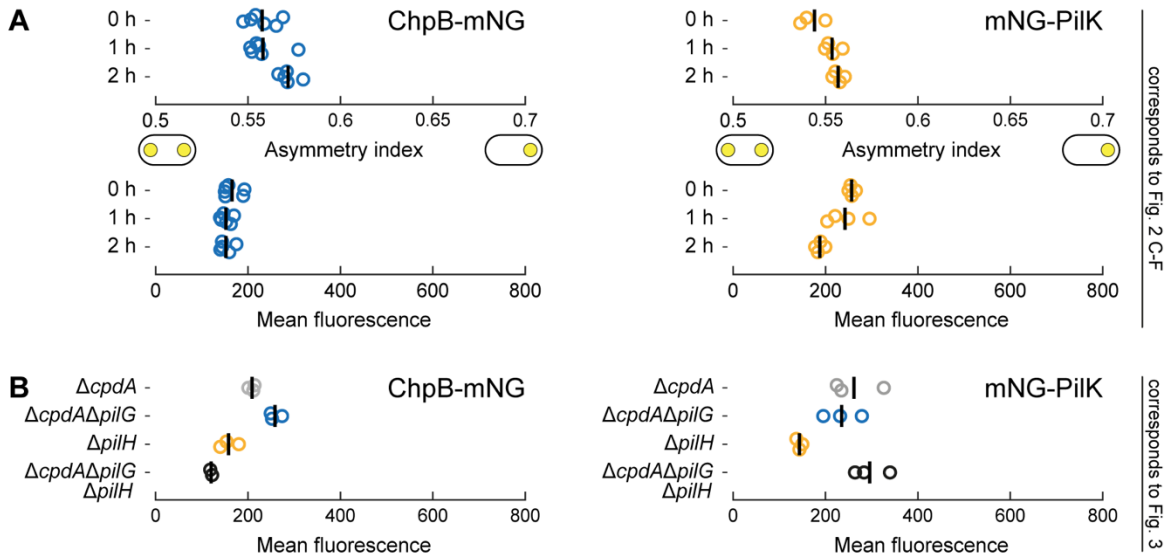

FIGURE S4.5. Asymmetry index and fluorescence measurements of PilK and ChpB.

(A, B) Mean cell fluorescence and asymmetry indexes of ChpB-mNG and mNG-PilK. ChpB-mNG is expressed chromosomally from its native locus, while mNG-PilK is expressed from a plasmid. *cpdA* was deleted in *pilG* mutants to eliminate potential confounding effects of low cAMP levels. Panels correspond to main figures as follows: (A) Fig. 2 (B) Fig. 3. Circles, median of each biological replicate. Vertical bars: mean across biological replicates.

FIGURE S4.6

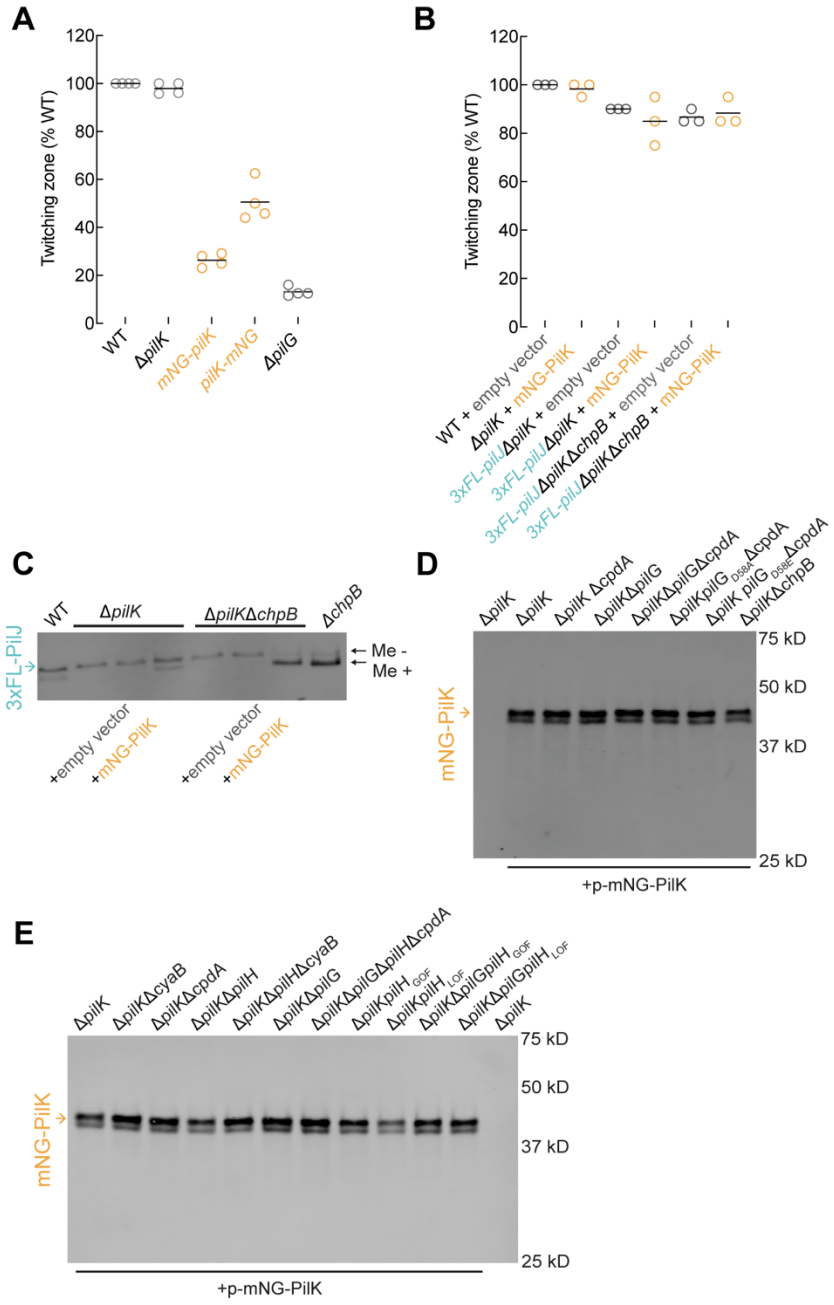

FIGURE S4.6. Phenotypic characterization of *mNG-pilK* fusion strains.

(A-B) Subsurface stab assays to measure twitching motility in (A) strains with chromosomally expressed mNG fusions of PilK and in (B) the indicated strains transformed with either empty vector or plasmid-expressed mNG-PilK. A representative graph of two independent experiments, with at least three biological replicates per experiment, is shown. (Figure caption continued on the next page.)

(Figure caption continued from the previous page.) Circles, relative twitching motility zone of each biological replicate (% of WT *P. aeruginosa* PAO1). Horizontal bars, mean across biological replicates. Δ*pilG* is shown in (A) as a twitching deficient control.

(C) Plasmid-expressed mNG-PilK restores PilJ methylation in *pilK* mutant backgrounds. PilJ methylation was assessed as in Figure 4.1D in Δ*pilK* and Δ*pilK*Δ*chpB* transformed with either empty vector or with plasmid-expressed mNG-PilK after 2 h of surface growth. WT and Δ*chpB* serve as positive controls for PilJ methylation. The slower migrating band represents unmethylated PilJ (Me-), while the faster migrating band represents methylated PilJ (Me+).

(D-E) Immunoblot of whole cell lysates from liquid grown (mid-log phase) Δ*pilK* strains transformed with plasmid-expressed mNG-PilK and probed with anti-mNG antibody. Δ*pilK* in (D-E) serves as control for antibody specificity. Expected molecular weight of plasmid expressed mNG-PilK is ~60 kD, while the observed molecular weight is ~40 kD.

FIGURE S4.7

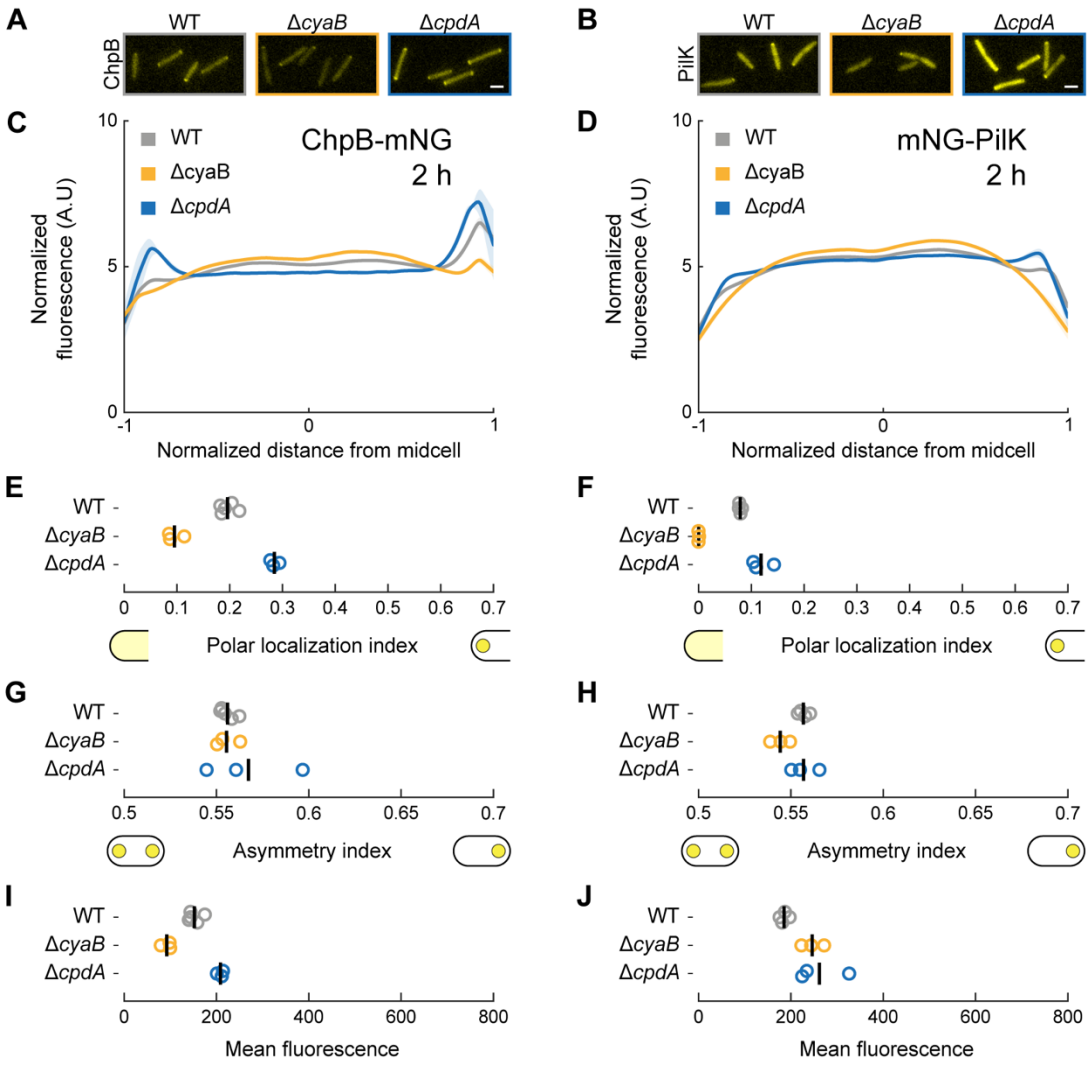

FIGURE S4.7. cAMP levels affect the polar localization of ChpB-mNG and mNG-PilK.

(A, B) Representative fluorescence snapshots of motile cells after 2 h of surface growth for (A) chromosomally expressed ChpB-mNG and (B) plasmid-expressed mNG-PilK (in Δ*pilK*). Scale bar, 2 μm.

(C, D) Fluorescence profiles of (C) ChpB-mNG or (D) mNG-PilK in low (Δ*cyaB*) or high (Δ*cpdA*) cAMP backgrounds after 2 h of surface growth. Solid lines, mean normalized fluorescence profiles across biological replicates. Shaded area, standard deviation across biological replicates.

(G-J) Corresponding measurements of polar localization index, asymmetry index, and mean cellular fluorescence. Circles, median of each biological replicate. Vertical bars, mean across biological replicates.

FIGURE S4.8

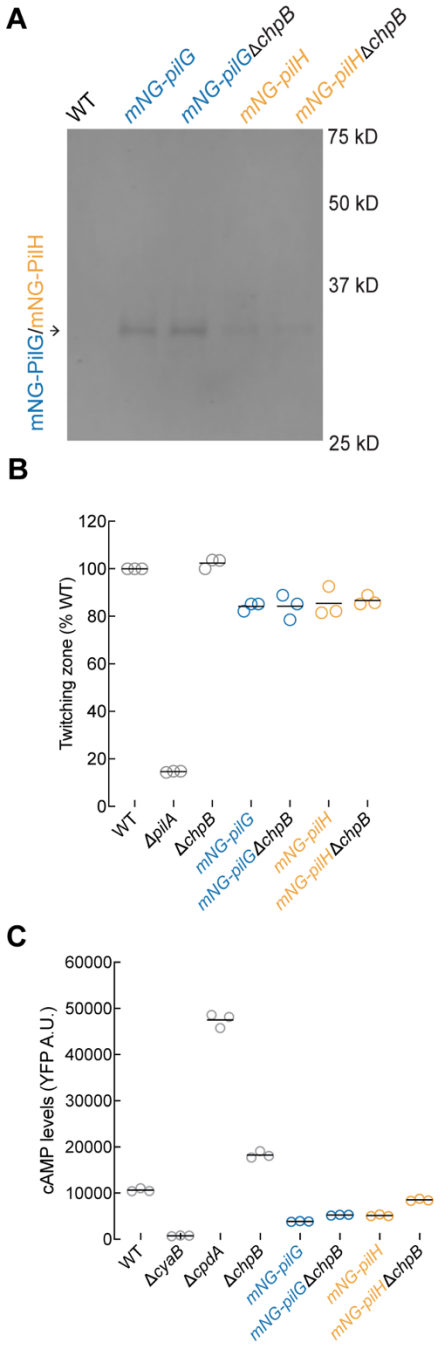

FIGURE S4.8. Phenotypic characterization of Δ*chpB* strains expressing *mNG-pilG* or *mNG-pilH*

(A) Immunoblot of whole cell lysates from liquid grown (mid-log phase) strains encoding chromosomally expressed mNG-PilG or mNG-PilH and probed with anti-mNG antibody. WT serves as a control for antibody specificity. (Figure caption continued on the next page.)

(Figure caption continued from the previous page.) As mNG-PilG and mNG-PilH have similar molecular weights, arrow points to the band representing either mNG-PilG or mNG-PilH.

(B) Subsurface stab assay to measure twitching motility in *mNG-pilG* and *mNG-pilH* fusion strains that lack c*hpB*. A representative graph of two independent experiments, with at least three biological replicates per experiment, is shown. Circles, relative twitching motility zone of each biological replicate (% of WT *P. aeruginosa* PAO1). Horizontal bars, mean across biological replicates. Δ*pilA* serves as a twitching motility deficient control.

(C) cAMP levels of *mNG-pilG* and *mNG-pilH* fusion strains in the indicated backgrounds after 2 h of surface growth were quantified as in Figure 4.1C. A representative graph of two independent experiments, with three biological replicates per experiment, is shown. Circles, median YFP fluorescence of each biological replicate (~30,000 cells). Horizontal bars, mean across biological replicates.

FIGURE S4.9

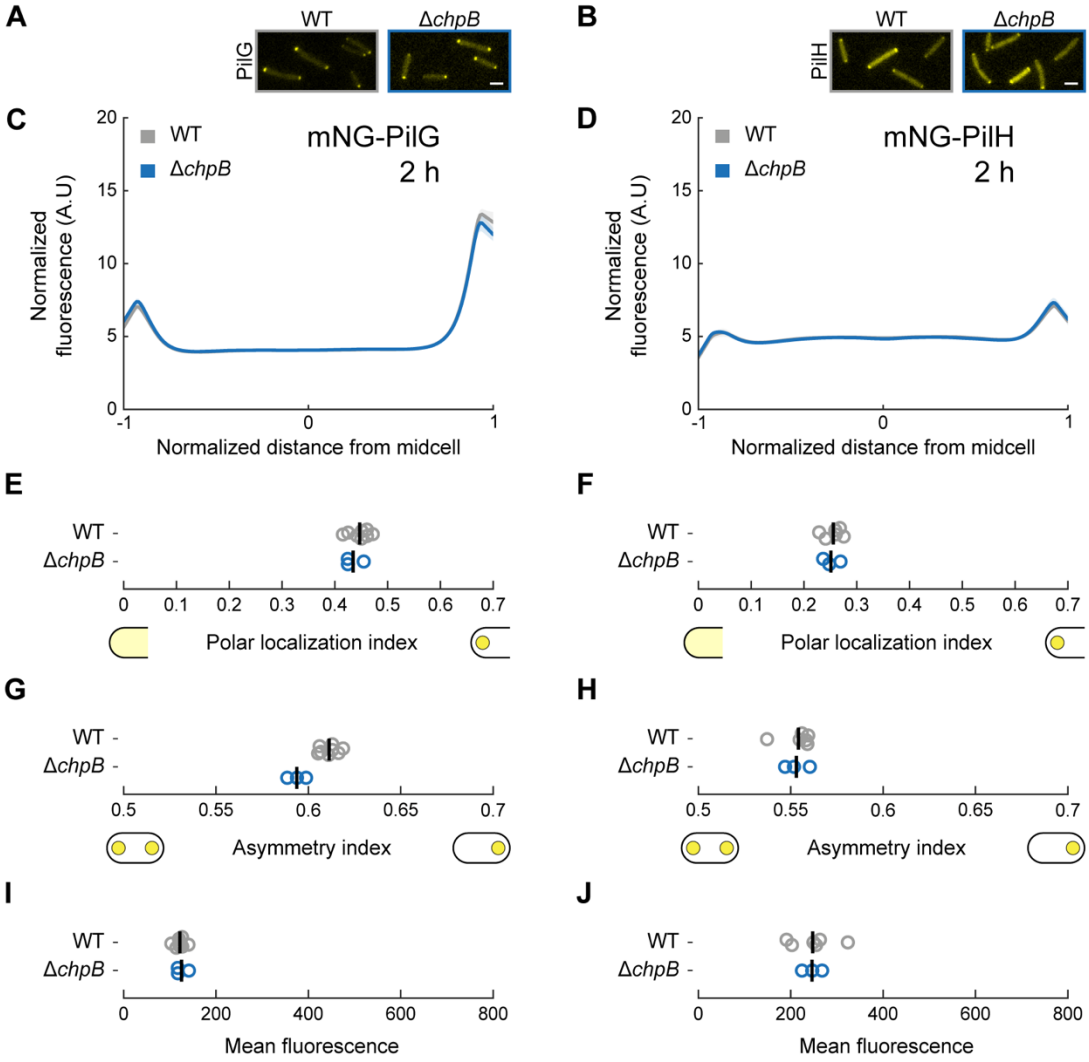

FIGURE S4.9. PilG and PilH localization is not affected by ChpB.

(A, B) Representative fluorescence snapshots of motile cells after 2 h of surface growth for (A) chromosomally expressed mNG-PilG or (B) mNG-PilH. Scale bar, 2 μm.

(C, D) Fluorescence profiles of (C) mNG-PilG or (D) mNG-PilH in Δ*chpB* after 2 h of surface growth. Solid lines, mean normalized fluorescence profiles across biological replicates. Shaded area, standard deviation across biological replicates.

(E-J) Corresponding measurements of polar localization index, asymmetry index, and mean cellular fluorescence. Circles, median of each biological replicate. Vertical bars, mean across biological replicates.

FIGURE S4.10

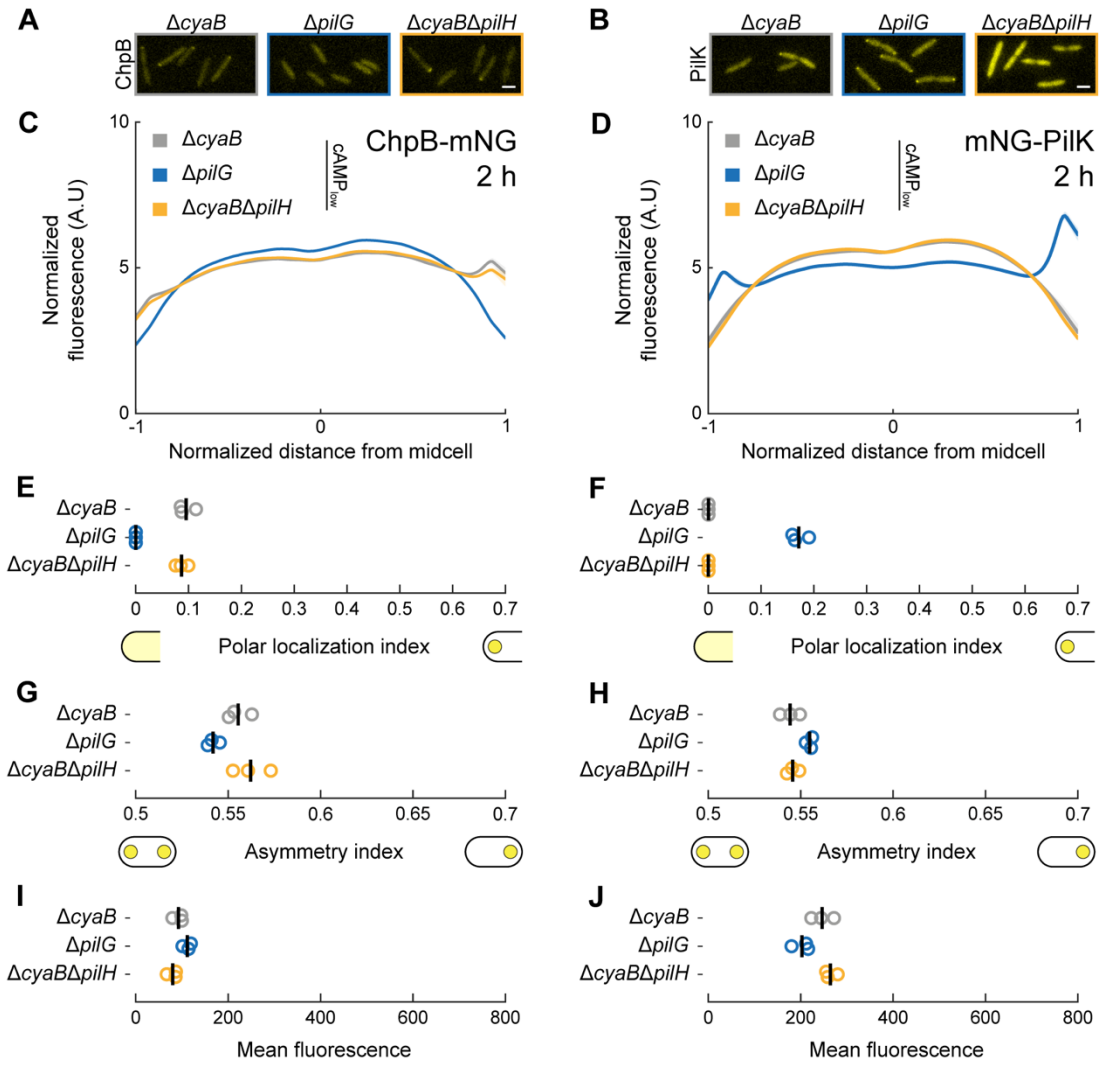

FIGURE S4.10. Regulation of ChpB and PilK polar localization by PilG and PilH is not affected by low cAMP levels.

(A, B) Representative fluorescence snapshots of motile cells after 2 h of surface growth for (A) chromosomally expressed ChpB-mNG or (B) plasmid-expressed mNG-PilK in Δ*pilK*. Scale bar, 2 μm.

(C, D) Fluorescence profiles of (C) ChpB-mNG or (D)mNG-PilK in Δ*pilG* and Δ*pilH* mutants with low cAMP levels (Δ*cyaB* where required) after 2 h of surface growth. Solid lines, mean normalized fluorescence profiles across biological replicates. Shaded area, standard deviation across biological replicates.

(E-J) Corresponding measurements of polar localization index, asymmetry index, and mean cellular fluorescence. Circles, median of each biological replicate. Vertical bars, mean across biological replicates.

FIGURE S4.11

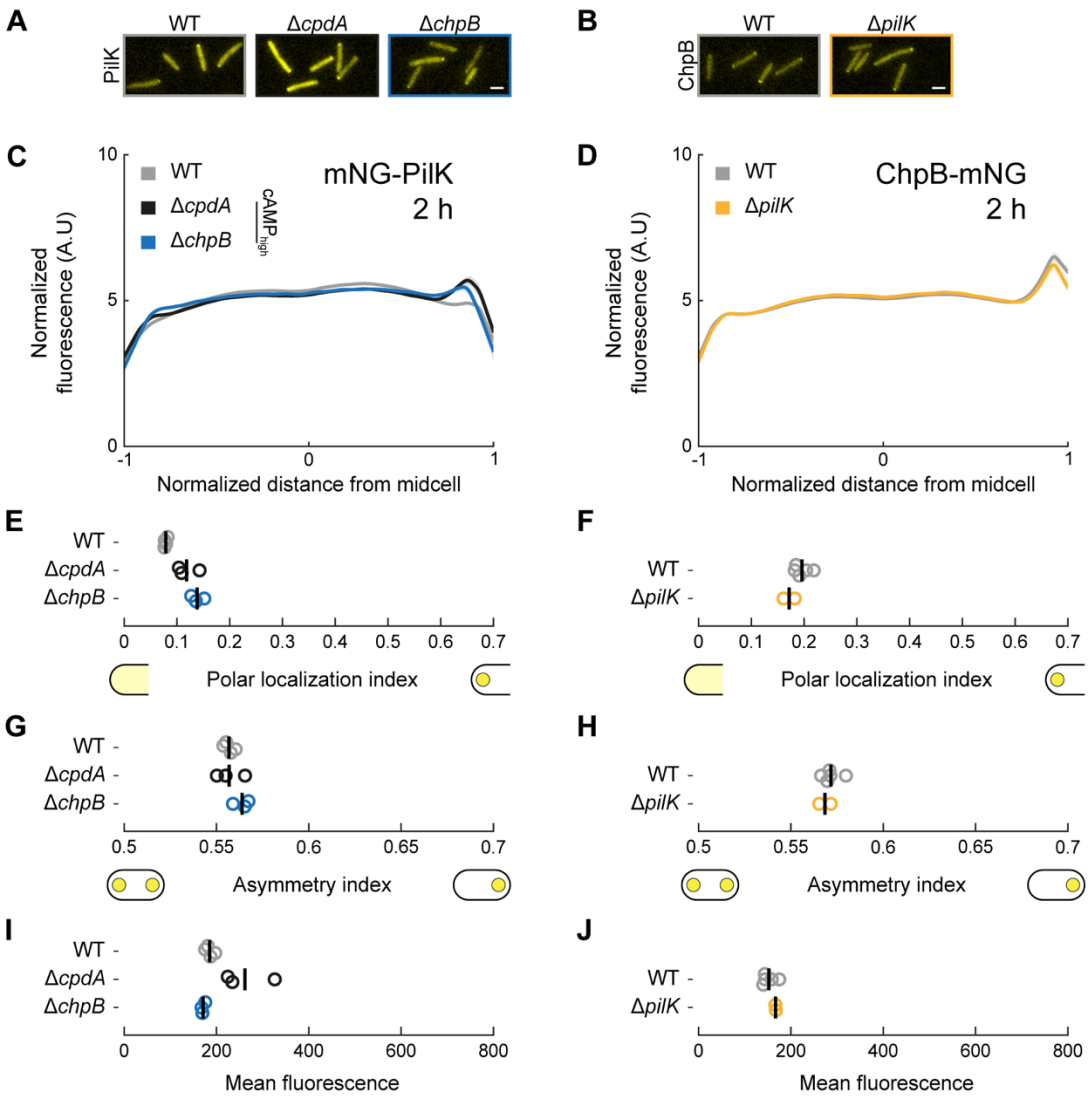

FIGURE S4.11. PilK and ChpB localization are independent of each other.

(A, B) Representative fluorescence snapshots of motile cells after 2 h of surface growth for (A) plasmid-expressed mNG-PilK in Δ*pilK* or (B) chromosomally expressed ChpB-mNG. Scale bar, 2 µm.

(C, D) Fluorescence profiles of (C) mNG-PilK in Δ*chpB* or (D) chromosomally expressed ChpB-mNG in Δ*pilK* after 2 h of surface growth. WT and D*cpdA* are shown as reference in (A, C) because cAMP levels are increased in Δ*chpB* (cf. Figure S4.1C). Solid lines, mean normalized fluorescence profiles across biological replicates. Shaded area, standard deviation across biological replicates. (Figure caption continued on the next page.)

(Figure caption continued from the previous page.) (E-J) Corresponding measurements of polar localization index, asymmetry index and mean cellular fluorescence. Circles, median of each biological replicate. Vertical bars, mean across biological replicates.

FIGURE S4.12

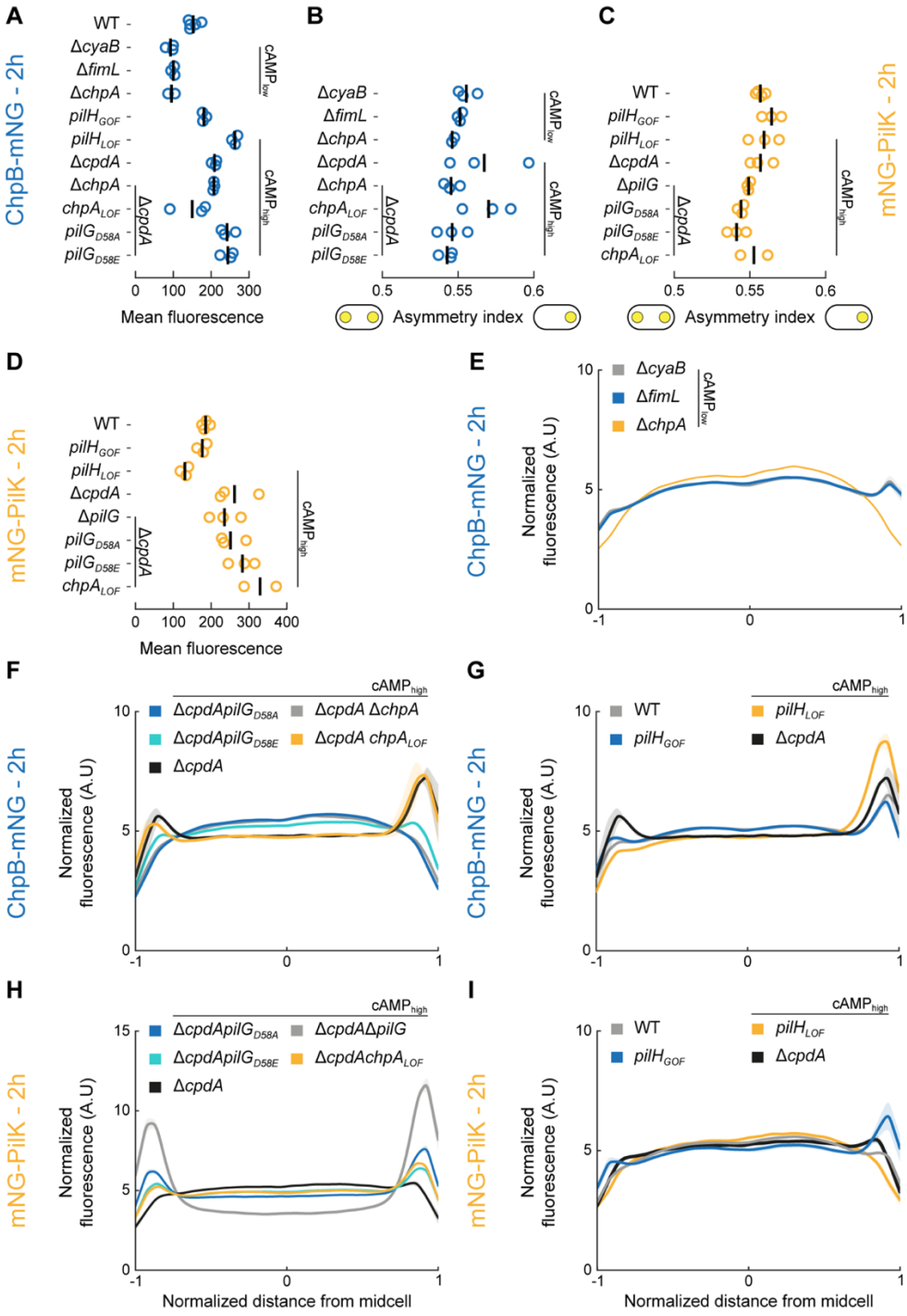

FIGURE S4.12. Fluorescence profiles, mean cell fluorescence and asymmetry indices of ChpB-mNG and mNG-PilK in indicated mutant backgrounds.

(Figure caption continued on the next page.)

(Figure caption continued from the previous page.) (A-D) Measurements of mean cellular fluorescence (A,D) and asymmetry index (B,C) for (A,B) chromosomally expressed ChpB-mNG or (C,D) plasmid-expressed mNG-PilK (in Δ*pilK*) after 2 h of surface growth, corresponding to data shown in Figure 4.4 and 4.5. Circles, median of each biological replicate. Vertical bars, mean across biological replicates.

(E-I) Fluorescence profiles of (E,F,G) chromosomally expressed ChpB-mNG or (H,I) plasmid-expressed mNG-PilK after 2 h of surface growth, corresponding to data shown in Figs 4.4 and 5.5. Solid lines, mean normalized fluorescence profiles across biological replicates. Shaded area, standard deviation across biological replicates. LOF, loss of function. GOF, gain of function.

FIGURE S4.13

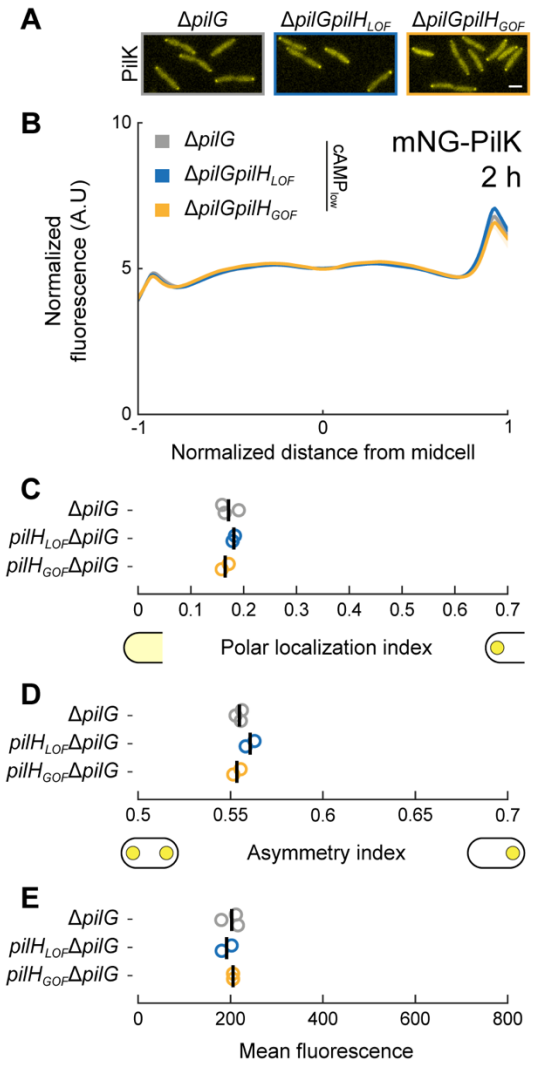

FIGURE S4.13. PilH acts on PilG to regulate PilK polar localization.

(A) Representative fluorescence snapshots of cells after 2 h of surface growth for plasmid-expressed mNG-PilK in Δ*pilK*. Scale bar, 2 μm.

(B) Fluorescence profiles of plasmid-expressed mNG-PilK in Δ*pilG,* $pilH_{LOF}$Δ*pilG,* or $pilH_{GOF}$ Δ*pilG* after 2 h of surface growth. All indicated strains also lack *pilK*. Solid lines, mean normalized fluorescence profiles across biological replicates. Shaded area, standard deviation across biological replicates. LOF, loss of function. GOF, gain of function.

(C-E) Corresponding measurements of polar localization index, asymmetry index, and mean cellular fluorescence. Circles, median of each biological replicate. Vertical bars, mean across biological replicates.

FIGURE S4.14

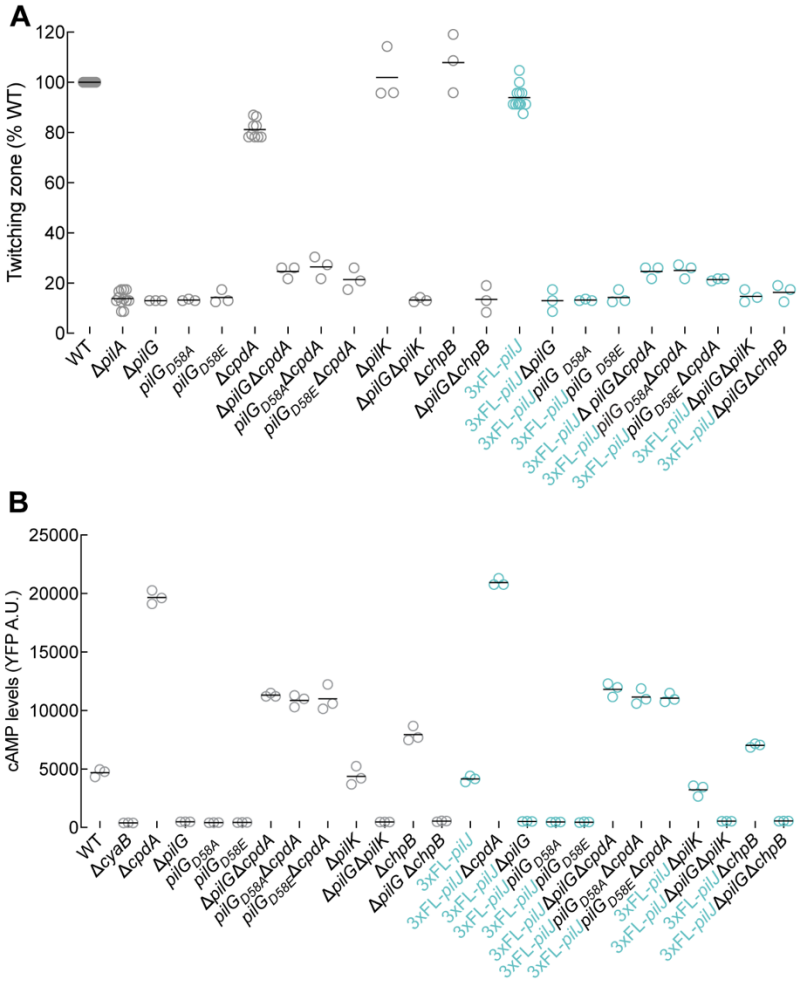

FIGURE S4.14. Phenotypic characterization of *3x-Flag-pilJ* fusion strains carrying the indicated *pilG* mutations.

(A) Twitching motility of the indicated *pilG* mutants with either the WT *pilJ* or with 3xFL-*pilJ* in the native chromosomal locus was quantified by the subsurface stab assay. A representative graph of two independent experiments, with at least three biological replicates per experiment, is shown. Circles, relative twitching motility zone of each biological replicate (% of WT). Horizontal bars, mean across biological replicates. Δ*pilA* serves as a twitching motility deficient control.

(B) cAMP levels of the indicated *pilG* mutants with either the WT *pilJ* or with 3xFL-*pilJ* in the chromosome after 2 h of surface growth were quantified as in Fig 1C. A representative graph of two independent experiments, with three biological replicates per experiment, is shown. Circles, median YFP fluorescence of each biological replicate (~30,000 cells). Horizontal bars, mean across biological replicates.
LOF, loss of function. GOF, gain of function.

FIGURE S4.15

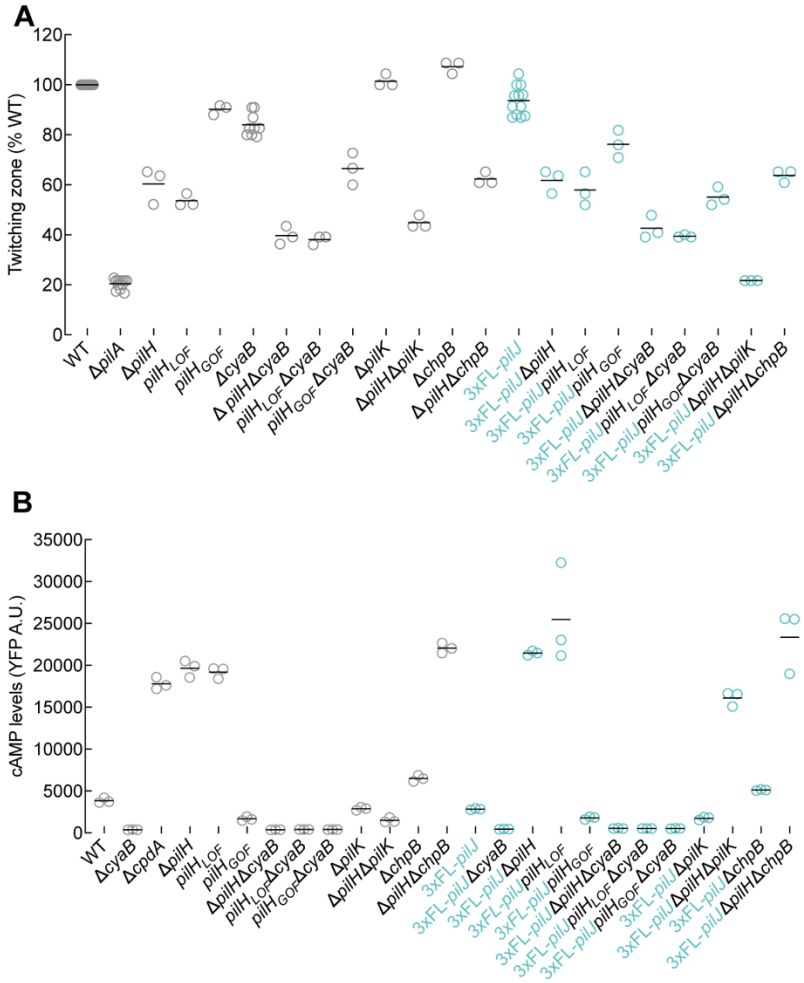

FIGURE S4.15. Phenotypic characterization of *3x-Flag-pilJ* fusion strains carrying the indicated *pilH* mutations.

(A) Twitching motility of the indicated *pilH* mutants with either the WT *pilJ* or with 3xFL-*pilJ* in the native chromosomal locus was quantified by the subsurface stab assay. A representative graph of two independent experiments, with at least three biological replicates per experiment, is shown. Circles, relative twitching motility zone of each biological replicate (% of WT). Horizontal bars, mean across biological replicates. Δ*pilA* serves as a twitching motility deficient control.

(B) cAMP levels of the indicated *pilH* mutants with either the WT *pilJ* or with 3xFL-*pilJ* in the chromosome after 2 h of surface growth were quantified as in Fig 1C. A representative graph of two independent experiments, with three biological replicates per experiment, is shown. Circles, median YFP fluorescence of each biological replicate (~30,000 cells). Horizontal bars, mean across biological replicates. LOF, loss of function. GOF, gain of function.

FIGURE S4.16

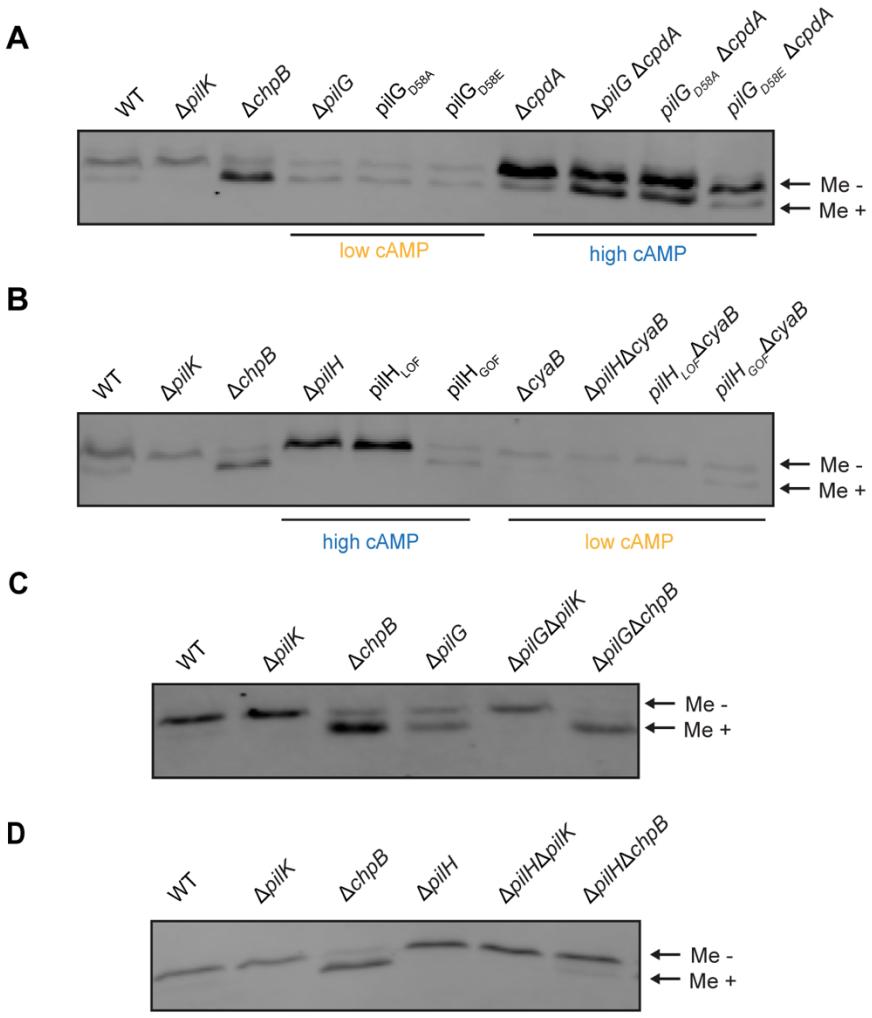

FIGURE S4.16. PilG and PilH regulate PilJ receptor methylation.

(A-D) Representative immunoblots of whole cell lysates from strains expressing chromosomal 3xFL-PilJ separated by “low-bis” SDS-PAGE and immunoblotted with anti-FLAG antibody. Whole cell lysates were prepared from cells grown after 2 h of surface growth. The slower migrating band represents unmethylated PilJ (Me -), while the faster migrating band represents methylated PilJ (Me +).

PilJ methylation was assessed for (A) *pilG* mutants, for (B) *pilH* mutants, for (C) Δ*pilG*Δ*pilK* and Δ*pilG*Δ*chpB* double mutants, or for (D) Δ*pilH*Δ*pilK* and Δ*pilH*Δ*chpB* double mutants. LOF, loss of function. GOF, gain of function.

TABLE S4.1

TABLE S4.1. AP-MS reveals a high confidence interaction between PilG and ChpB.

Bait	Prey	Counts	Replicates	Control Counts	SAINT	BFDR
PilG	PilG	373	3	0	1	0
PilG	FimV	81	3	0	1	0
PilG	FimL	28.33	3	0	1	0
PilG	ChpB	2.67	3	0	0.98	0.01
PilH	PilH	329	3	1	1	0
PilH	FimV	0	3	0	NA	NA
PilH	FimL	0	3	0	NA	NA
PilH	ChpB	0	3	0	NA	NA

Lysates from strains expressing overexpressed PilG-HA or PilH-HA were affinity purified and subjected to MS-MS. Shown are preys of interest for PilG-HA and PilH-HA. Previously characterized PilG interactions by AP-MS (PilG:FimV, PilG:FimL)(Inclan, Persat, Greninger, Von Dollen, et al., 2016) from the same experiment were included in the SAINT scoring(H. Choi et al., 2011) and are shown for comparison. SAINT scores closer to 1 and BFDR (Bayesian False Discover Rate) ≤ 0.05 suggest a high confidence interaction.

ADDITIONAL SUPPLEMENTAL MATERIAL

Supplemental material can be accessed online through ProQuest and include:

Table S4.1. Strains used in this study.

Table S4.2. Plasmids used in this study.

Table S4.3. Oligonucleotides used in this study.

Movie S4.1. The PilK methyltransferase localizes to the lagging pole of twitching *P. aeruginosa* cells. Movie recorded 2 h after surface contact. Frame interval, 5 s; scale bar, 2 μm.

Movie S4.2. The ChpB methylesterase localizes to the leading pole of twitching *P. aeruginosa* cells. Movie recorded 2 h after surface contact. Frame interval, 2 s; scale bar, 2 μm.

CHAPTER FIVE

SURFACE SENSING INDUCES A TRANSCRIPTIONAL RESPONSE IN PATHOGENIC ACINETOBACTER SPECIES

SUMMARY

Acinetobacter species are opportunistic pathogens that are ubiquitous throughout the environment and are emerging as a public health threat around the world. Medically relevant species belong to the genetically related *Acinetobacter calcoaceuticus-baumanii* (Acb) complex. Similar to the Acb complex, *Pseudomonas aeruginosa* is a Gram-negative opportunistic environmental pathogen that causes disease in critically ill patients and exhibits extensive antibiotic resistance. Our lab and others have identified three modules in *P. aeruginosa* that comprise a mechanochemical signaling (MCS) pathway that coordinately activates a virulence program in response to surface sensing. Given the similarity in lifestyles and given that they encode a predicted MCS pathway, we hypothesized that the Acb complex exhibits a surface response that may be important in human disease. Using RNA sequencing, we demonstrate here that *A. nosocomialis* strain M2, a pathogenic member of the Acb complex that exhibits TFP-mediated twitching motility, has a robust surface-dependent transcriptional response that may involve virulence factors that contribute to human infections. This study has the potential to enhance our understanding of how surface sensing reshapes the transcriptome of other medically important Gram-negative pathogens and may pave the way to developing new therapeutic involve virulence factors that contribute to human infections.

INTRODUCTION

Acinetobacter species are opportunistic pathogens that are ubiquitous throughout the environment and are emerging as a public health threat around the world due to their extensive antibiotic resistance (Weber et al., 2016). Medically relevant species belong to the genetically related *Acinetobacter calcoaceuticus-baumanii* (Acb) complex, of which *A. baumanii*, *A. nosocomialis*, and *A. pittii* are the species most frequently associated with human disease (Weber et al., 2016). Acb are an important cause of pneumonia in ventilated patients, catheter-associated blood stream and urinary tract infections in immunocompromised and hospitalized critically ill patients, and in surgical and trauma-associated soft-tissue infections in immunocompetent hosts (Weber et al., 2016).

While previously considered “low virulence” pathogens, treatment of Acb infections is becoming increasingly difficult, with up to 70% mortality rates, due to widespread antibiotic resistance. Alarmingly, 45% of isolates exhibit multi-drug resistance (MDR) or pan-resistance (Harding et al., 2018). Therefore, there is an urgent need to develop new modalities to treat and prevent MDR Acb infections. Critical for this advance is a detailed understanding of how these species cause human disease, including the identification and regulation of virulence factors. Only a few Acb virulence factors have been identified. These include surface-exposed and secreted molecules such as the polysaccharide capsule, chaperone-usher (Csu) pili, the type II secretion (T2SS) system and its effectors (the lipases Lip and LipH, as well as the CpaA metallopeptidase), and the type VI secretion system (T6SS) (Geisinger et al., 2019).

Opportunistic pathogens, such as Acb species and *Pseudomonas aeruginosa*, have developed finely tuned signal transduction pathways to rapidly adapt to changing environments, including within the human host. Similar to Acb, PA is a Gram-negative opportunistic environmental pathogen that causes disease in critically ill patients and exhibits extensive antibiotic resistance (Hauser, 2014). Our lab (Inclan et al., 2011, 2016; Persat et al., 2015; Whitchurch et al., 2004) and others (Fuchs et al., 2010; Fulcher et al., 2010; Wolfgang et al., 2003) have identified three "modules" in *P. aeruginosa* that comprise a mechanochemical signaling (MCS) pathway that coordinately activates a virulence program in response to surface contact. These modules include the (i) type IV pilus (TFP), (ii) the Pil-Chp mechanosensory system, and the adenylate cyclase (AC)/cyclic AMP (cAMP)/Virulence factor regulator (cAMP/Vfr) axis (Persat et al., 2015). We suggest that activation of the Pil-Chp mechanosensory by surface sensing and subsequent production of type III secretion system (T3SS) effectors that target predators might protect *P. aeruginosa* as it transitions from planktonic growth to surface associated biofilm formation.

We have reported that medically relevant Acb species encode a predicted homologous MCS pathway (Inclan et al., 2016), prompting speculation that Acb also utilizes the three MCS modules to coordinately regulate a surface response that may be important in human disease. However, it is unclear whether medically relevant Acb species sense surface contact to elicit cellular responses. Here, we address this question by comparing the transcriptomes of planktonically and surface grown Acb species. We employed *A. nosocomialis* strain M2 (AnM2), a genetically tractable (Tucker et al., 2014), fully

sequenced (Carruthers et al., 2013) human pathogenic Acb isolate that encodes a predicted MCS pathway, including a homologous Pil-Chp mechanosensory system. Our transcriptomic analysis revealed that after 1 h of surface growth, AnM2 exhibits a robust surface-dependent transcriptional response that might regulate virulence. These results suggest that medically relevant Acb species indeed exhibit surface-associated transcriptional programs, which might be induced by mechanical stimuli generated during surface contact.

RESULTS

Acb species encode homologs of the PA MCS system.

The functional integration of the three modules of the MCS pathway could be conserved in bacteria that thrive in diverse environmental niches, like Acb species. In support of this hypothesis, the Engel lab previously performed a bioinformatics analysis that showed the conservation of the MCS modules in other medically relevant bacteria (Inclan et al., 2016). Remarkably, AnM2 indeed encodes homologs of the three MCS modules, including key proteins of the Chp chemosensory system (PilG, PilH PilI, PilJ, and ChpA), TFP (PilA, PilB, PilT, and the assembly apparatus), the cAMP-regulated transcriptional regulator Vfr, and a predicted membrane associated CyaB. (**Table 5.1**).

Acb exhibits a surface response at the transcriptional level.

To determine whether Acb species exhibit a surface response, we used the *A. nosocomialis* strain M2 (AnM2) and employed RNAseq to quantitatively compare the transcriptomes of AnM2 grown planktonically (shaking at 37˚) to (i) liquid log (LL), (ii) stationary log (LS) phase, or of (iii) AnM2 grown to LL and then plated on a surface (1.5% LB plates) for 1 hr.

We identified 294 Surface Associated Growth (SAG) genes that are specifically upregulated and 292 genes that were specifically downregulated during 1 h surface growth compared to either LL or LS growth conditions (false discovery rate < 5% and ≥ Log_2 1.5-fold change; **Figure 1**). Our finding that transcription of these genes did not

change in LL or LS growth suggests that upregulation of these SAG genes is dependent upon surface growth rather than growth phase.

Our analysis further revealed that many of the upregulated SAG genes are involved in Acb virulence (Geisinger et al., 2019) (**Table 5.2**). The putative Acb virulence factors identified include: (i) surface appendages (pilin, Csu pili, curli pili (ii) type VI secretion system components; (iii) Chp chemosensory system response regulators; (iv) transporters associated with antibiotic resistance; and (v) multiple TonB-dependent receptor homologs that have been shown to contribute to Acb biofilm formation and virulence in a mouse model of acute pneumonia (Abdollahi et al., 2018; Smani et al., 2012).

DISCUSSION

Our transcriptomic analysis strongly supports our hypothesis that *A. nosocomialis* strain M2 (AnM2) encodes a robust surface-dependent transcriptional response that may contribute to human infections. We demonstrate that PilA (TFP), CsuAB (biofilm formation), TonB-dependent copper transporter (biofilm formation and virulence), CarO (antibiotic resistance), and Tube protein Hcp (T6SS) are SAG genes that are robustly upregulated after 1 hr and that have been associated with Acb virulence (Abdollahi et al., 2018; Geisinger et al., 2019; Weber et al., 2016). Our bioinformatics analysis furthered demonstrated that AnM2 encodes homologs of the TFP, the Pil-Chp mechanosensory system, a membrane associated AC, and Vfr. This raises the possibility that these modules of the MCS pathway might regulate the AnM2 surface response, as is the case for *P. aeruginosa*. Overall, we demonstrate, for the first time, that surface contact elicits cellular responses in a medically relevant *Acinetobacter* species.

AnM2 was selected because the following carefully considered reasons: (i) AnM2 was isolated from a human infection and is thus a human pathogenic strain, (ii) it has been sequenced (Carruthers et al., 2013), (iii) it is amenable to genetic manipulation, including transformation (Ramirez et al., 2010) and allelic exchange (Tucker et al., 2014), and (iv) it expresses TFP on its surface and demonstrates TM (Harding et al., 2013). Therefore, we are confident that our results are applicable to other members of the Acb complex, including *A. baumannii*.

Our results open to door to future investigations about the mechanism regulating the surface transcriptional response of AnM2. By analogy to *P. aeruginosa*, we propose that the MCS circuit controls the surface-dependent transcriptional program of medically relevant Acb species. We further predict that the MCS modules will be required for increased production of cAMP in response to surface sensing. It is also possible that uncharacterized mechanisms regulate this process. Either outcome is of interest as it will advance our understanding of how bacteria sense surface contact to regulate their physiology. Together, these studies have the potential to enhance our understanding Acb infections, may allow for new therapeutic approaches, and may be applicable to other medically important MDR gram negative pathogens.

MATERIAL AND METHODS

Bacterial strains, growth conditions and media.

A. nosocomialis strain M2 (AnM2) was used for all experiments in this study (Harding et al., 2013). AnM2 was grown in LB medium (Carl Roth) at 37 °C with 280 rpm shaking. Solid LB media for cell growth were prepared by adding 1.5% (wt · vol^{-1}) agar (Fisher Bioreagents).

Preparation of samples for transcriptomic analysis.

RNAseq libraries were prepared from AnM2 grown overnight in liquid LB, diluted 1:100 and grown to liquid mid log or stationary phase, and from liquid mid-log AnM2 that have been plated onto 1.5% LB plates for 1 h of surface growth. We chose these time points and growth conditions so that the transcriptional programs activated upon surface contact can be distinguished from transcriptional programs altered by growth phase. Cells were pelleted by centrifugation (10 000 x g, 5 min, 4°C), and pellet was preserved on RNA shield (Zymo Research) until RNA extraction was performed.

Transcriptome analysis.

RNA was extracted from biological triplicates and RNA seq libraries were prepared, following the manufacturer's recommendations (NEB). Following depletion of rRNA gene sequences by DASH (Gu et al., 2016), sequencing was performed on an Illumina Novaseq 6000 instrument. The data set was aligned to the AnM2 genome (NZ_CP040105) using Geneious11.1.5. Transcriptomes were compared using DESeq2 in R, and genes of interest were filtered for false discovery rate < 5% and ≥ Log_2 1.5-fold change.

ACKNOWLEDGEMENTS

The authors would like to thank Robert S. Munson Jr. for providing the *A. nosocomialis* strain M2 strain. R.P. was also funded by an NSF GRFP fellowship (1650113) and the NIH (F31 AI147544). Any opinions, findings, and conclusions or recommendations expressed in this material are those of the author(s) and do not necessarily reflect the views of the National Science Foundation.

REFERENCES

Abdollahi, S., Rasooli, I., & Mousavi Gargari, S. L. (2018). The role of TonB-dependent copper receptor in virulence of Acinetobacter baumannii. *Infection, Genetics and Evolution: Journal of Molecular Epidemiology and Evolutionary Genetics in Infectious Diseases*, *60*, 181–190. https://doi.org/10.1016/j.meegid.2018.03.001

Carruthers, M. D., Harding, C. M., Baker, B. D., Bonomo, R. A., Hujer, K. M., Rather, P. N., & Munson, R. S. (2013). Draft Genome Sequence of the Clinical Isolate Acinetobacter nosocomialis Strain M2. *Genome Announcements*, *1*(6), e00906-13. https://doi.org/10.1128/genomeA.00906-13

Fuchs, E. L., Brutinel, E. D., Jones, A. K., Fulcher, N. B., Urbanowski, M. L., Yahr, T. L., & Wolfgang, M. C. (2010). The Pseudomonas aeruginosa Vfr regulator controls global virulence factor expression through cyclic AMP-dependent and -independent mechanisms. *Journal of Bacteriology*, *192*(14), 3553–3564. https://doi.org/10.1128/JB.00363-10

Fulcher, N. B., Holliday, P. M., Klem, E., Cann, M. J., & Wolfgang, M. C. (2010). The Pseudomonas aeruginosa Chp chemosensory system regulates intracellular cAMP levels by modulating adenylate cyclase activity. *Molecular Microbiology*, *76*(4), 889–904. https://doi.org/10.1111/j.1365-2958.2010.07135.x

Geisinger, E., Huo, W., Hernandez-Bird, J., & Isberg, R. R. (2019). Acinetobacter baumannii: Envelope Determinants That Control Drug Resistance, Virulence, and Surface Variability. *Annual Review of Microbiology*, *73*, 481–506. https://doi.org/10.1146/annurev-micro-020518-115714

Gu, W., Crawford, E. D., O'Donovan, B. D., Wilson, M. R., Chow, E. D., Retallack, H., & DeRisi, J. L. (2016). Depletion of Abundant Sequences by Hybridization (DASH): Using Cas9 to remove unwanted high-abundance species in sequencing libraries and molecular counting applications. *Genome Biology*, *17*(1), 41. https://doi.org/10.1186/s13059-016-0904-5

Harding, C. M., Hennon, S. W., & Feldman, M. F. (2018). Uncovering the mechanisms of Acinetobacter baumannii virulence. *Nature Reviews. Microbiology*, *16*(2), 91–102. https://doi.org/10.1038/nrmicro.2017.148

Harding, C. M., Tracy, E. N., Carruthers, M. D., Rather, P. N., Actis, L. A., & Munson, R. S. (2013). Acinetobacter baumannii strain M2 produces type IV pili which play a role in natural transformation and twitching motility but not surface-associated motility. *mBio*, *4*(4), e00360-13. https://doi.org/10.1128/mBio.00360-13

Hauser, A. R. (2014). Pseudomonas aeruginosa virulence and antimicrobial resistance: Two sides of the same coin? *Critical Care Medicine*, *42*(1), 10.1097/CCM.0b013e3182a120cd. https://doi.org/10.1097/CCM.0b013e3182a120cd

Inclan, Y. F., Huseby, M. J., & Engel, J. N. (2011). FimL Regulates cAMP Synthesis in Pseudomonas aeruginosa. *PLOS ONE*, *6*(1), e15867. https://doi.org/10.1371/journal.pone.0015867

Inclan, Y. F., Persat, A., Greninger, A., Dollen, J. V., Johnson, J., Krogan, N., Gitai, Z., & Engel, J. N. (2016). A scaffold protein connects type IV pili with the Chp chemosensory system to mediate activation of virulence signaling in

Pseudomonas aeruginosa. *Molecular Microbiology*, *101*(4), 590–605. https://doi.org/10.1111/mmi.13410

Inclan, Y. F., Persat, A., Greninger, A., Von Dollen, J., Johnson, J., Krogan, N., Gitai, Z., & Engel, J. N. (2016). A scaffold protein connects type IV pili with the Chp chemosensory system to mediate activation of virulence signaling in Pseudomonas aeruginosa. *Molecular Microbiology*, *101*(4), 590–605. https://doi.org/10.1111/mmi.13410

Persat, A., Inclan, Y. F., Engel, J. N., Stone, H. A., & Gitai, Z. (2015). Type IV pili mechanochemically regulate virulence factors in Pseudomonas aeruginosa. *Proceedings of the National Academy of Sciences of the United States of America*, *112*(24), 7563–7568. https://doi.org/10.1073/pnas.1502025112

Ramirez, M. S., Don, M., Merkier, A. K., Bistué, A. J. S., Zorreguieta, A., Centrón, D., & Tolmasky, M. E. (2010). Naturally competent Acinetobacter baumannii clinical isolate as a convenient model for genetic studies. *Journal of Clinical Microbiology*, *48*(4), 1488–1490. https://doi.org/10.1128/JCM.01264-09

Smani, Y., McConnell, M. J., & Pachón, J. (2012). Role of fibronectin in the adhesion of Acinetobacter baumannii to host cells. *PloS One*, *7*(4), e33073. https://doi.org/10.1371/journal.pone.0033073

Tucker, A. T., Nowicki, E. M., Boll, J. M., Knauf, G. A., Burdis, N. C., Trent, M. S., & Davies, B. W. (2014). Defining gene-phenotype relationships in Acinetobacter baumannii through one-step chromosomal gene inactivation. *mBio*, *5*(4), e01313-01314. https://doi.org/10.1128/mBio.01313-14

Weber, B. S., Harding, C. M., & Feldman, M. F. (2016). Pathogenic Acinetobacter: From the Cell Surface to Infinity and Beyond. *Journal of Bacteriology*, *198*(6), 880–887. https://doi.org/10.1128/jb.00906-15

Whitchurch, C. B., Leech, A. J., Young, M. D., Kennedy, D., Sargent, J. L., Bertrand, J. J., Semmler, A. B. T., Mellick, A. S., Martin, P. R., Alm, R. A., Hobbs, M., Beatson, S. A., Huang, B., Nguyen, L., Commolli, J. C., Engel, J. N., Darzins, A., & Mattick, J. S. (2004). Characterization of a complex chemosensory signal transduction system which controls twitching motility in Pseudomonas aeruginosa. *Molecular Microbiology*, *52*(3), 873–893. https://doi.org/10.1111/j.1365-2958.2004.04026.x

Wolfgang, M. C., Lee, V. T., Gilmore, M. E., & Lory, S. (2003). Coordinate Regulation of Bacterial Virulence Genes by a Novel Adenylate Cyclase-Dependent Signaling Pathway. *Developmental Cell*, *4*(2), 253–263. https://doi.org/10.1016/S1534-5807(03)00019-4

FIGURE 5.1

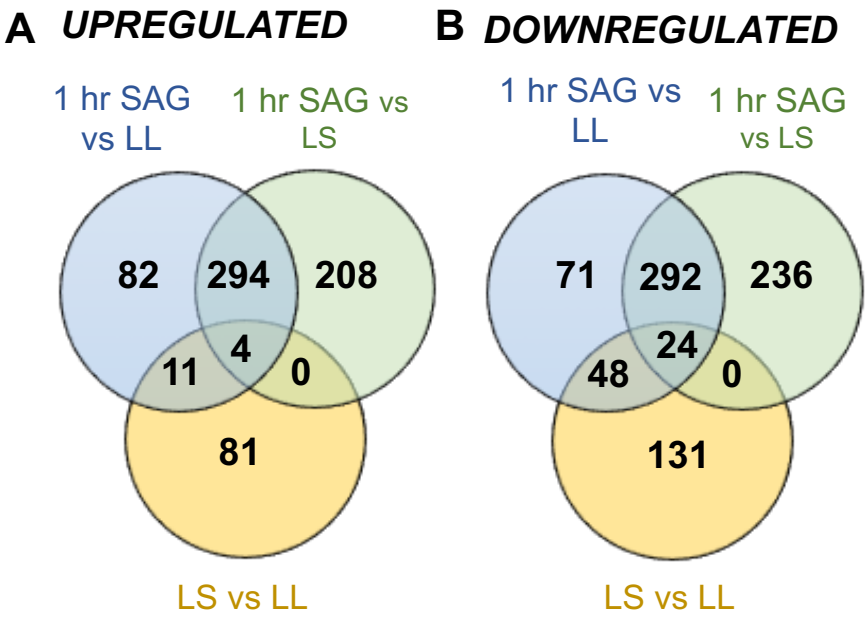

FIGURE 5.1. Acb exhibits a surface response at the transcriptional level.

Comparison of *A. nosocomialis* M2 transcriptomes that were obtained after 1 h of surface associated growth (SAG), after liquid log (LL) growth, and after liquid stationary (LS) growth.

(A) We identified 294 SAG genes that were specifically upregulated compared to LL and LS growth.

(B) We identified 292 SAG genes that were specifically downregulated compared to LL and LS growth.

TABLE 5.1

TABLE 5.1. *Acinetobacter nosocomialis* M2 encodes homologs of a mechanochemical circuit found in *Pseudomonas aeruginosa*[1].

Locus tag in *A. nosocomialis* M2	Homolog in *Pseudomonas aeruginosa* PAO1	Predicted Function
M215_06535	PilJ	Chemoreceptor
M215_06530	PilI	Scaffold protein
M215_06540	ChpA	Hybrid histidine kinase
M215_06520	PilG	Response regulator
M215_06525	PilH	Response regulator
M215_13835	CyaB	Adenylate cyclase
M215_16505	Vfr	CRP-like transcriptional regulator

[1]TFP homologs have been identified by others.

TABLE 5.2

TABLE 5.2. Potential virulence factors that are upregulated by *Acinetobacter nosocomialis* M2 upon 1 h of surface growth compared to liquid growth either in log (LL) or in stationary (LS) phase.

Predicted Function	Gene annotation	Log2 fold change (1 hr surface vs LL)	Log2 fold change (1 Hr surface vs LS)
Antibiotic susceptibility	AdeIJK	2.1/2.3/2.1	2.4/2.2/1.6
	Carbapenem-resistance associated protein (CarO)	4.5	5.5
Biofilm formation	Csu fimbrial major subunit CsuA/B	3.0	6.1
	CsuA/B family protein	2.1	4.1
	Csu biogenesis chaperone CsuC	1.9	3.0
	Curli assembly protein CsgG	3.3	4.2
Chp	Chp system Response regulators PilG and PilH	2.0/1.7	2.6/1.6
TFP	Type IV Pilus subunit (pilin)	2.4	4.0
Iron Uptake	TonB-dependent siderophore receptor	3.0	2.4
	TonB-dependent siderophore receptor	2.5	2.2
	TonB-dependent siderophore receptor	1.8	1.6
	TonB-dependent receptor	2.0	1.9
	TonB-dependent copper receptor	3.4	3.0
Type VI secretion	TssC/M/H/K	1.6/2.1/ 1.5/2.2	3.1/1.9/ 1.8/2.9
	Tube protein Hcp	2.1	3.7
	TagF	2.2	3.3
	OmpA family protein	2.3	2.9
	PAAR domain-containing protein	2.1	2.6

CHAPTER SIX

CONCLUSIONS

The human pathogen *Pseudomonas aeruginosa* uses type IV pili (TFP) to sense mechanical forces generated during surface contact at one cell pole (Persat et al., 2015). These spatially resolved mechanical stimuli activate the Pil-Chp mechanosensory system (Persat et al., 2015). Sensing of surface contact by the Pil-Chp system upregulates >200 genes involved in acute virulence as well as selected TFP regulatory proteins (Fulcher et al., 2010; Wolfgang et al., 2003). The Pil-Chp mechanosensory system is also required for twitching motility (Bertrand et al., 2010; Whitchurch et al., 2004), independently of cAMP levels (Buensuceso et al., 2017).

This dissertation work provides fundamental insights on how spatially resolved mechanical stimuli are sensed and transduced as *Pseudomonas aeruginosa* senses surface contact (Kühn et al., 2021, 2023). To direct twitching motility in the direction of mechanical input from TFP, in a process called mechanotaxis, the Pil-Chp response regulators PilG and PilH control the polarization of the TFP extension motor PilB. PilG stimulates polarization favoring forward migration, while PilH inhibits polarization inducing reversal. To spatially resolve mechanical signals, we conclude that the Pil-Chp system locally transduces signals with a main output response regulator, PilG. To respond to signal changes, Chp uses its second regulator PilH to break the local feedback.

Our investigations into the antagonistic Pil-Chp response regulators lead to fascinating and important future experiments. We report that PilG is required for recruitment of the PilB extension ATPase to the leading pole. However, the mechanism of PilB recruitment remains undefined. It is possible that PilG recruits PilB by direct or indirect binding. Future

biochemical studies can reveal insights into the PilB recruitment mechanism. It would be interesting to investigate whether the two separate pools of PilG, the one associated with ChpA and the one associated with FimL, play a district role during PilB recruitment. Because ChpA-mediated phosphorylation modulates PilG recruitment to the leading pole, suggesting that surface sensing activates Pil-Chp signaling locally, a detailed understanding of the ChpA phosphorelay is then imperative. Although we lack the reagents to study phosphotransfer at the single cell level at this time, studies that focus on dissecting the complex phosphorelay through ChpA could allow us to understand how phosphotransfer to PilG controls PilG local recruitment and downstream signaling. Similarly, understanding the Pil-Chp phosphorelay might help us understand how PilH globally antagonizes the local signaling in which PilG plays a key role. At the population level, a comprehensive time course of reversal frequencies might allow us to associate changes in reversal frequency with important *P. aeruginosa* surface behaviors.

We also define the mechanism of sensory adaptation in the Pil-Chp mechanosensory system. We discovered that PilK and ChpB, the Pil-Chp sensory adaptation enzymes, are segregated to opposing cell poles as *P. aeruginosa* explore surfaces. We propose a model in which spatially resolved mechanical stimuli transmitted by TFP locally controls PilJ methylation, the molecular basis of bacterial sensory adaptation, to modulate twitching motility and surface-dependent cAMP production. Despite decades of sensory adaptation studies, our work has uncovered an unrecognized mechanism that bacteria use to achieve adaptation to mechanical sensory stimuli.

Our model predicts that there is differential methylation of PilJ at opposite cell poles, with more PilJ methylation at the lagging pole compared to the leading pole. We emphasize, however, that reagents are not currently available to directly test this hypothesis. Our methylation immunoblots only provide a snapshot of the PilJ methylation state in the population without spatial data. Elucidating the PilJ methylation sites might provide important information about how PilJ methylation influences local signaling during mechanosensing. For example, as the fraction of methylated PilJ increases upon surface contact, it is unclear whether the amount of PilJ methylation or methylation of a specific methylation site in PilJ modulates twitching motility and cAMP production. Determining the site and function of each of the 3 to 5 predicted PilJ methylation sites can also provide a basis for structural studies to distinguish whether PilJ methylation primarily modulates receptor sensitivity or interactions with the downstream histidine kinase; scenarios that we cannot fully distinguish at this time. Importantly, our methylation immunoblots only distinguish 2 states of PilJ methylation, even though bioinformatics predicts 3-5 sites. Whether this 2-state scenario is an artifact of incomplete separation of differentially methylated PilJ species or whether only one site of PilJ is methylated at any time could be further investigated through the creation of PilJ methylation site mutants.

Our studies leave many questions for the future to address how PilK and ChpB become polarly localized. Our study suggests that PilK can localize to both poles independently of the Pil-Chp response regulators, as seen in Δ*pilG*Δ*pilH.* Therefore, the mechanism for PilK polar recruitment remains a mystery. As our methylation immunoblots emphasize the importance of PilK lagging pole localization in regulating PilJ methylation, genetic screens

might allow us to identify genes required for PilK localization to the lagging pole. The ChpB receiver domain lacks key residues involved in phosphotransfer, suggesting that phosphorylation does not play a role in ChpB activation. However, whether the ChpB receiver domain is involved in ChpB recruitment remains an open question that can illuminate how ChpB is recruited to the leading pole by PilG.

Whether integration of spatial information is a general feature of mechanosensing requires further experimental evidence. The first step to address this question is to identify and characterize additional mechanosensory systems. We now show that a medically relevant *Acinetobacter* species has a surface-dependent transcriptional response that may involve virulence factors that contribute to human infections. Therefore, it is tempting to speculate that the homologous Pil-Chp mechanosensory system that *Acinetobacter* species encode is responsible for the surface-dependent transcriptional response that we report in this dissertation. Future work should focus on validating our transcriptomic data by creating transcriptional reporters to representative classes of SAG genes to better define the kinetics of the Acb surface response and to enable subsequent genetic screens. Informative mutants of the TFP, Pil-Chp mechanosensory system, and the cAMP/Vfr genes should help in determining whether these components of the MCS pathway control the AnM2 surface-dependent transcriptional program.

In conclusion, this dissertation demonstrates that mechanosensing through the Pil-Chp system takes advantage of the intricate internal organization of bacteria to sense spatially resolved mechanical information. As medically *Acinetobacter* species exhibit a surface

transcriptional response, defining the mechanosensing mechanism of *Acinetobacter* species thus represents an exciting area of investigation. Understanding the mechanisms of bacterial mechanosensing may lead to the generation of desperately needed therapeutics to treat multi-drug resistant infections caused by *P. aeruginosa* (Hauser, 2014) and medically relevant *Acinetobacter* species (Harding et al., 2018).

REFERENCES

Bertrand, J. J., West, J. T., & Engel, J. N. (2010). Genetic Analysis of the Regulation of Type IV Pilus Function by the Chp Chemosensory System of Pseudomonas aeruginosa. *Journal of Bacteriology*, *192*(4), 994–1010. https://doi.org/10.1128/jb.01390-09

Buensuceso, R. N. C., Daniel-Ivad, M., Kilmury, S. L. N., Leighton, T. L., Harvey, H., Howell, P. L., & Burrows, L. L. (2017). Cyclic AMP-Independent Control of Twitching Motility in Pseudomonas aeruginosa. *Journal of Bacteriology*, *199*(16), e00188-17. https://doi.org/10.1128/JB.00188-17

Fulcher, N. B., Holliday, P. M., Klem, E., Cann, M. J., & Wolfgang, M. C. (2010). The Pseudomonas aeruginosa Chp chemosensory system regulates intracellular cAMP levels by modulating adenylate cyclase activity. *Molecular Microbiology*, *76*(4), 889–904. https://doi.org/10.1111/j.1365-2958.2010.07135.x

Harding, C. M., Hennon, S. W., & Feldman, M. F. (2018). Uncovering the mechanisms of Acinetobacter baumannii virulence. *Nature Reviews. Microbiology*, *16*(2), 91–102. https://doi.org/10.1038/nrmicro.2017.148

Hauser, A. R. (2014). Pseudomonas aeruginosa virulence and antimicrobial resistance: Two sides of the same coin? *Critical Care Medicine*, *42*(1), 10.1097/CCM.0b013e3182a120cd. https://doi.org/10.1097/CCM.0b013e3182a120cd

Kühn, M. J., Macmillan, H., Talà, L., Inclan, Y., Patino, R., Pierrat, X., Al-Mayyah, Z., Engel, J. N., & Persat, A. (2023). Two antagonistic response regulators control

Pseudomonas aeruginosa polarization during mechanotaxis. *The EMBO Journal*, *42*(7), e112165. https://doi.org/10.15252/embj.2022112165

Kühn, M. J., Talà, L., Inclan, Y. F., Patino, R., Pierrat, X., Vos, I., Al-Mayyah, Z., Macmillan, H., Negrete, J., Engel, J. N., & Persat, A. (2021). Mechanotaxis directs Pseudomonas aeruginosa twitching motility. *Proceedings of the National Academy of Sciences*, *118*(30), e2101759118. https://doi.org/10.1073/pnas.2101759118

Persat, A., Inclan, Y. F., Engel, J. N., Stone, H. A., & Gitai, Z. (2015). Type IV pili mechanochemically regulate virulence factors in Pseudomonas aeruginosa. *Proceedings of the National Academy of Sciences of the United States of America*, *112*(24), 7563–7568. https://doi.org/10.1073/pnas.1502025112

Whitchurch, C. B., Leech, A. J., Young, M. D., Kennedy, D., Sargent, J. L., Bertrand, J. J., Semmler, A. B. T., Mellick, A. S., Martin, P. R., Alm, R. A., Hobbs, M., Beatson, S. A., Huang, B., Nguyen, L., Commolli, J. C., Engel, J. N., Darzins, A., & Mattick, J. S. (2004). Characterization of a complex chemosensory signal transduction system which controls twitching motility in Pseudomonas aeruginosa. *Molecular Microbiology*, *52*(3), 873–893. https://doi.org/10.1111/j.1365-2958.2004.04026.x

Wolfgang, M. C., Lee, V. T., Gilmore, M. E., & Lory, S. (2003). Coordinate Regulation of Bacterial Virulence Genes by a Novel Adenylate Cyclase-Dependent Signaling Pathway. *Developmental Cell*, *4*(2), 253–263. https://doi.org/10.1016/S1534-5807(03)00019-4

Publishing Agreement

It is the policy of the University to encourage open access and broad distribution of all theses, dissertations, and manuscripts. The Graduate Division will facilitate the distribution of UCSF theses, dissertations, and manuscripts to the UCSF Library for open access and distribution. UCSF will make such theses, dissertations, and manuscripts accessible to the public and will take reasonable steps to preserve these works in perpetuity.

I hereby grant the non-exclusive, perpetual right to The Regents of the University of California to reproduce, publicly display, distribute, preserve, and publish copies of my thesis, dissertation, or manuscript in any form or media, now existing or later derived, including access online for teaching, research, and public service purposes.

DocuSigned by:
Ramiro Patino
0E409E6523804FB...
Author Signature

3/19/2024
Date